The development of new materials such MOFs for CO2 capture and alkylation of aromatic compounds.

Ugo Ravon

To cite this version:

Ugo Ravon. The development of new materials such MOFs for CO2 capture and alkylation of aromatic compounds.. Other. Université Claude Bernard - Lyon I, 2010. English. NNT : 2010LYO10009 . tel-00817254

HAL Id: tel-00817254
https://theses.hal.science/tel-00817254

Submitted on 24 Apr 2013

HAL is a multi-disciplinary open access archive for the deposit and dissemination of scientific research documents, whether they are published or not. The documents may come from teaching and research institutions in France or abroad, or from public or private research centers.

L'archive ouverte pluridisciplinaire **HAL**, est destinée au dépôt et à la diffusion de documents scientifiques de niveau recherche, publiés ou non, émanant des établissements d'enseignement et de recherche français ou étrangers, des laboratoires publics ou privés.

N° d'ordre : 9-2010 Année 2010

THESE DE L'UNIVERSITE DE LYON

Délivrée par

L'UNIVERSITE CLAUDE BERNARD LYON 1

ECOLE DOCTORALE

DIPLOME DE DOCTORAT

(Arrêté du 7 août 2006)

Soutenue publiquement le 29/01/10

Par : M Ravon Ugo

TITRE :

L'élaboration de nouveaux matériaux de type MOFs, pour le captage du CO_2 et l'alkylation de composés aromatiques.

Directeur de thèse : D.Farrusseng

JURY: Pr Daniele. S, Président
Pr Hulea. V, Rapporteur
Dr Pirngruber. G, Rapporteur
Dr Llewellyn. P, Examinateur
Dr Mirodatos. C, Examinateur
Dr Farrusseng. D, Directeur de thèse

UNIVERSITE CLAUDE BERNARD - LYON 1

Président de l'Université	**M. le Professeur L. Collet**
Vice-président du Conseil Scientifique	M. le Professeur J-F. Mornex
Vice-président du Conseil d'Administration	M. le Professeur G. Annat
Vice-président du Conseil des Etudes et de la Vie Universitaire	M. le Professeur D. Simon
Secrétaire Général	M. G. Gay

COMPOSANTES SANTE

Faculté de Médecine Lyon Est – Claude Bernard	Directeur : M. le Professeur J. Etienne
Faculté de Médecine Lyon Sud – Charles Mérieux	Directeur : M. le Professeur F-N. Gilly
UFR d'Odontologie	Directeur : M. le Professeur D. Bourgeois
Institut des Sciences Pharmaceutiques et Biologiques	Directeur : M. le Professeur F. Locher
Institut des Sciences et Techniques de Réadaptation	Directeur : M. le Professeur Y. Matillon
Département de Formation et Centre de Recherche en Biologie Humaine	Directeur : M. le Professeur P. Farge

COMPOSANTES SCIENCES ET TECHNOLOGIE

Faculté des Sciences et Technologies	Directeur : M. Le Professeur F. Gieres
UFR Sciences et Techniques des Activités Physiques et Sportives	Directeur : M. C. Collignon
Observatoire de Lyon	Directeur : M. B. Guiderdoni
Institut des Sciences et des Techniques de l'Ingénieur de Lyon	Directeur : M. le Professeur J. Lieto
Institut Universitaire de Technologie A	Directeur : M. le Professeur C. Coulet
Institut Universitaire de Technologie B	Directeur : M. le Professeur R. Lamartine
Institut de Science Financière et d'Assurance	Directeur : M. le Professeur J-C. Augros
Institut Universitaire de Formation des Maîtres	Directeur : M R. Bernard

REMERCIEMENTS

Je tiens tous d'abord à remercier **C.MIRODATOS** pour son accueil au sein de l'Institut de Recherche sur la Catalyse et l'Environnement de Lyon (IRCELyon).

J'exprime ensuite tous mes remerciements à **D.FARRUSSENG**, mon directeur de thèse, pour son aide et sa disponibilité en toutes circonstances.

Je souhaite également remercier l'ensemble de l'équipe Ingénierie et plus particulièrement **C.GAUDILLERE, S.AGUADO, A.DESMARTIN-CHOMEL, C.DANIEL, E.LANDRIVON, M.DOMINE, M.SAVONNET** et **A.CAMARATA** pour leurs aides ainsi que toutes les personnes des différents groupes et des services scientifiques de l'institut.

Introduction Générale

Dans l'industrie chimique et pétrolière, les enjeux actuels portent sur l'intensification des procédés afin de diminuer les coûts d'exploitation et d'investissement. Le génie chimique s'est considérablement développé tout au long du XX^{ème} siècle. Aussi aujourd'hui la majorité des procédés est arrivée à un certain degré de maturité. D'un autre côté, l'avènement des nanomatériaux apporte de nouvelles solutions en rupture, faisant d'eux de vrais enjeux stratégiques. Dans ce travail de thèse, nous nous sommes intéressés à développer de nouveaux matériaux en tant qu'adsorbants et catalyseurs. Du point de vue méthodologique, nous nous sommes attachés à développer des méthodes de recherches innovantes permettant d'accélérer leurs découvertes.

Ce travail fait parti du projet Européen : TOPCOMBI. Ce consortium est composé de 22 collaborateurs industriels et universitaires et a pour objectif de développer des méthodes et des outils pour accélérer la découverte de nouveaux matériaux et procédés pour l'industrie chimique. Le projet est divisé en 8 applications différentes allant de la valorisation du CH_4, C_3H_8 et glycérol jusqu'à la synthèse de nouveaux agents de blanchiment dans le domaine des lessives. Mes principaux travaux de thèse ont évolué dans le sous-projet WP23 portant sur le traitement du gaz naturel. Les partenaires impliqués étaient : ENI (It), Repsol (Es), Amtec GmbH (D), ICT-Pragues (Cz), ITQ-CSIC (Es). Le développement de nouveaux matériaux pour l'adsorption nous a permis d'ouvrir d'autres champs d'études. Ainsi, en marge du projet TopCombi, nous avons exploré les propriétés en catalyse acide de certains matériaux développés précédemment.

Les prévisions de la demande internationale d'énergétique, à savoir 1,7 % d'augmentation annuelle pour la période de 2005-2020, concerne toutes les sources d'énergie, bien que les énergies fossiles soient, et de loin, les énergies les plus utilisées et qu'elles le resteront encore pour au moins une quinzaine d'années.
De ces trois énergies, gaz naturel, pétrole et charbon, le gaz naturel est la source la plus économique et écologique. C'est pour cela que l'utilisation du gaz naturel comme source d'énergie a vu son intérêt augmenter avec l'arrivée, depuis quelques

années, de certaines restrictions environnementales principalement basées sur les déchets générés par les différentes techniques de production énergétique. Actuellement, elle n'est que peu utilisée comme tel. Cela s'explique par les difficultés rencontrées pour purifier le gaz afin de le rendre transportable et/ou consommable. En effet, selon la composition du gaz naturel et les différentes proportions des constituants, les traitements de gaz ont des coûts prohibitifs. Par conséquent les champs de petites tailles ou trop pollués étaient systématiquement abandonnés. L'un des moyens de rendre économiquement viable les différents champs de gaz naturel est de développer des procédés de séparation plus performants au niveau énergétique, avec un coût d'investissement maîtrisé. Les procédés PSA semblent répondre à ces deux critères. L'objectif de ce travail est de trouver, dans un temps réduit, des nouveaux adsorbants pour la capture du CO_2 dans le méthane avec un cahier des charges spécifique.

Le second axe de ce travail consiste à optimiser la réaction d'alkylation des composés polyaromatiques. Actuellement des travaux ont montré que cette réaction peut fonctionner par différents moyens, acides, basiques, oxydants ou radicalaires. Chaque type de réaction possède différents avantages que ce soit la conversion, la sélectivité, le site d'alkylation ou encore les solvants 'utilisables'. Bien que généralement ce type de réaction est effectué à l'aide de catalyseur acide homogène, de type $AlCl_3$ ou hétérogène, de type zéolithique. Si les réactions en catalyse hétérogène possèdent une bonne conversion même à faible température, elles ne fonctionnent que lorsque le diamètre du réactif est plus petit que la taille des pores du catalyseur. Lorsque ce n'est pas le cas, on passe par une réaction homogène qui connaît deux limitations comme la grande majorité des catalyses de ce type. i) Les déchets sont à prendre en compte, ce qui génère des problèmes de séparation. ii) la réaction ne sera pas sélective. Le but de cette partie est de trouver un composé cristallin possédant des sites acides actifs pour l'alkylation ainsi qu'une taille de pores suffisamment importante pour permettre l'alkylation de composés possédant un grand diamètre cinétique comme les composés polyaromatiques.

Dans ces deux cas, les matériaux recherchés doivent être microporeux. Aujourd'hui les types de matériaux les plus communément utilisés sont les zéolites et les charbons. Cependant, pour le traitement du gaz naturel, les adsorbants ne remplissent pas les objectifs industriels. D'autre part, pour l'alkylation, les zéolites sont limitées par leur diamètre de pores, qui empêche toute réaction avec de ‘grosses’ molécules.

Selon les problèmes posés, l’intérêt de nouveaux composés cristallins, comme les MOFs, augmente considérablement. En effet, l’un des principaux atouts de ces matériaux est la possibilité d’obtenir un composé avec différents cations et/ou ligands. Au vu de la grande diversité des cations métalliques ainsi que des ligands organiques, la diversité des MOFs est quasi-infinie. Par conséquence, il devrait être possible de trouver un composé adapté pour les deux applications. Malheureusement, au début du projet, les connaissances sur la synthèse de ces composés à l’échelle industrielle ainsi que de leurs propriétés d’adsorption étaient encore méconnues. C’est pour cela que l’un des objectifs de cette thèse consiste à mettre en place de nouvelles méthodes de synthèse pouvant être mises à l’échelle industrielle ainsi que de caractériser les propriétés d’adsorption des matériaux obtenus.

La première partie de ce travail est une synthèse bibliographique basée sur trois axes : i) un état de l’art des matériaux microporeux avec un accent sur la synthèse et la caractérisation des MOFs. ii) une détermination des besoins et des caractéristiques du traitement du gaz naturel. Quels sont les différents principes des procédés d’adsorption, ceci incluant les interactions adsorbant-adsorbat, ainsi qu’une rapide description du procédé PSA. iii) une dernière partie traitant de l’état de l’art de la réaction d’alkylation avec les différents chemins réactionnels existants, ainsi que les divers problèmes rencontrés.

La deuxième partie décrit le développement d’une méthode de criblage haut-débit afin d’accélérer la découverte de nouvelles phases de type MOFs et de trouver de nouvelles conditions de synthèses plus facilement transposables à l’échelle industrielle. Les cas d’études se sont portés sur les systèmes les plus étudiés basés sur les cations Cu^{2+}, Zn^{2+} et l’acide téréphtalique.

Ensuite, une étude sur la détermination des chaleurs d’adsorption et de la diffusivité de trois MOFs sous six gaz est effectuée. Ces résultats sont obtenus par trois techniques différentes afin de pouvoir les comparer entre elles. i) en utilisant le réacteur TAP, Temporal Analysis Product, ii) par une méthode gravimétrique, et enfin

iii) par simulation, Grand canonical Monte Carlo, réalisé par une collaboration du Pr Snurr, Northwestern University, Illinois.

La troisième partie traite des résultats obtenus lors de la synthèse de MOFs par la méthode de précipitation. Quels paramètres sont sélectionnés et quels MOFs sont obtenus. Les meilleurs candidats étant testés en adsorption CO_2/CH_4. Cette partie conclut le travail effectué sur l'adsorption.

Enfin, les deux dernières parties traitent des différents potentiels catalytiques des MOFs. D'abord de la propriété de sélectivité de cage des MOFs sur l'alkylation de Friedel Crafts. Différentes réactivités de MOFs basées sur le cluster ZnO_4 sont obtenues et comparées. Le travail porte sur la détermination des sites actifs afin d'essayer de comprendre le mécanisme réactionnel de l'alkylation sur 2 MOFs à la structure identique, MIL-53 (Al) et MIL-53 (Ga) toujours dans la réaction de Friedel-Crafts.

Chapitre I : partie bibliographique

1.1. Etat de l'art des matériaux microporeux

1.1.1. Introduction

Du fait de leurs propriétés uniques, l'intérêt des matériaux poreux à l'échelle nanométrique est sans cesse croissant. La compétitivité des procédés hétérogènes sur les procédés homogènes pousse le développement de nouveaux matériaux. C'est notamment les cas pour les procédés de purifications par voie solide et pour les procédés de catalyse hétérogènes. Au niveau des propriétés chimiques, les caractéristiques des « nano »pores génèrent des propriétés très spécifiques. En catalyse, l'activité d'un solide dépend de son nombre de sites accessibles. Donc pour un même volume, un composé poreux possède une plus grande surface et donc une plus grande réactivité qu'un composé moins poreux. D'autre part, par le seul fait d'une taille de pore adaptée l'interaction entre une molécule et le matériau peut être augmentée. Ceci se remarque lorsque la molécule et la taille des canaux du matériau sont de la même échelle de grandeur. Vu la taille moyenne d'une molécule, quelques Å, les matériaux microporeux, $Ø_{pore}$ <2nm, possèdent une réactivité spécifique par rapport aux autres composés poreux. En effet, 2 matériaux de même composition mais de porosités différentes auront des interactions différentes avec des molécules spécifiques. Pour illustrer ce phénomène, de nombreux chercheurs ont étudié ce phénomène. Everett et Derouane, ont évalué l'énergie de van der Waals et a démontré qu'elle dépendait de la distance molécule - paroi ainsi que de la taille de pores de l'adsorbant [1] [2, 3]. Du point de vue de notre démarche scientifique, que ce soit pour l'adsorption ou la catalyse, il faut favoriser les interactions entre le substrat et le matériau.

Aujourd'hui, les principaux matériaux utilisés dans ces domaines sont des silico-aluminates (zéolithes) et alumino-phosphates (AlPO). Ces oxydes cristallins ont des tailles de pores inférieures à 1nm (ultramicropore). Ceci limite leurs applications à la catalyse et séparation de petites molécules. . Depuis quelques années, l'émergence de nouveaux composés microporeux cristallins possédant une versatilité de taille de pores bien plus importante a vu le jour : les MOFs, Metal Organic Framework. Ces derniers ouvrent la porte à de nouvelles applications.

1.1.2. Zéolites

- Les aluminosilicates

Ces composés sont constitués de tétraèdres ; TO$_4$, ou T correspond à un cation comme Si^{4+} [4]. Qu'elles soient naturelles ou obtenues en condition hydrothermale, les zéolites peuvent être divisées en 2 catégories. Les polaires si le ratio Si/Al est faible (de 1 à 5), ou les apolaires si le ratio est grand (de 5 à ∞)[5]. Lorsque le ratio est faible, la charge négative provenant des atomes d'Al est compensée par de petits cations comme les alcalins ou alcalinoterreux. Pour obtenir un haut ratio, certaines zéolites sont synthétisées à l'aide de diverses molécules organiques comme des ammoniums quaternaires[6]. Ces matériaux peuvent s'obtenir avec : différentes tailles de pores, différentes polarités et acidités ; ils possèdent une bonne résistance mécanique, et une bonne stabilité thermique [7] [8].La découverte de ces composés microporeux a révolutionné la catalyse hétérogène ainsi que les méthodes de séparation de gaz.

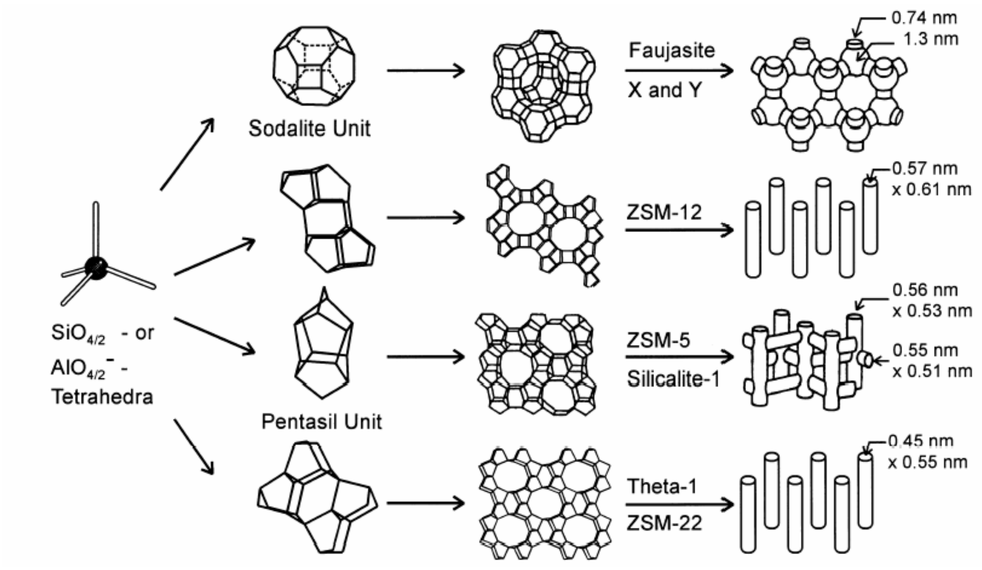

Figure 1 : Exemple de différentes structures zéolithiques provenant de tétraèdres de SiO$_4$ ou AlO$_4$ [9].

Bien que les zéolites soient constituées de tétraèdres, la façon dont ces derniers s'arrangent donne différentes structures cristallines. A ce jour, on dénombre 179 structures différentes. Les tétraèdres s'arrangent en sous unités constitutionnelles appelées Secondary Building Blocks (SBU), tels que les unités pentasil et sodalites. A l'aide de cette méthodologie, il devient possible d'imaginer quelles structures avec quelles caractéristiques poreuses pourraient exister.

- Les aliminophosphates(AlPOs)

Les AlPOs, sont eux aussi des matériaux poreux composés de tétraèdres, mais ici les cations de Silice, Si^{4+}, sont remplacés par des Al^{3+} et P^{5+}. Ces tétraèdres peuvent s'arranger de différentes manières donnant de nouvelles structures cristallines ou des structures équivalentes à celles trouvées dans les oxydes de Si, comme les FAU ou les CHA [10, 11]. Généralement Al/P=1 et les tétraèdres AlO_4^- et PO_4^+ constituent alors une charpente électriquement neutre. Comme pour les oxydes de Silice, il est possible de substituer certains tétraèdres à base de P^{5+} par un Si^{4+}, on parle de SAPO, ou par des cations à base Cr, V ou encore de Co, appelé respectivement CrAPO, VAPO ou encore CoAPO.

1.1.2.1. Classification des zéolithes par la taille de pores

- Les zéolithes à petits pores

Les couronnes des canaux (Member Ring) sont constituées de 8 atomes d'oxygènes, (8MR) avec des diamètres de pores de l'ordre de 4Å. Les zéolites de ce groupe les plus connues sont les zéolites A (LTA) et chabazite (CHA).

- Les pores de taille moyenne

Cette fois-ci, la couronne est constituée de 10 atomes, (10MR) avec des diamètres de pores de l'ordre de 5 à 6 Å. Les zéolites les plus connues sont la ZSM-5 (MFI) et la Ferrite (FER).

- Les zéolites aux larges pores

Les zéolites composant cette catégorie possèdent une couronne composée de 12 atomes, (12MR) avec un diamètre poreux de 7 Å. Les zéolites les plus connues sont la Faujasite (FAU) et la Beta (BEA).

- Les zéolites aux pores extra larges

Cette catégorie est la plus récente. La couronne est constituée avec plus de 12 atomes (12MR). En 2004, la collaboration entre IFP et l'ENS Mulhouse a donné naissance à une nouvelle zéolithe bidimensionnelle : IM-12[12]. Cette zéolithe possède 2 pores différents, 12MR et 14MR, de taille respective 9.5 * 7.1Å et 8.5 * 5.5 Å. Si une double porosité peut être un handicape pour tout ce qui concerne l'adsorption, ce composé peut être dopé au Ge avec un rapport Al/(Si+Ge) proche de 0.2 qui suggère une activité catalytique. En 2008 Kang et al [13], ont mis en évidence les effets catalytiques sur le diisopropylbenzene avec des composés possédant des forces acides différentes : B-IM-12 < Ga-IM-12 < Al-IM-12.

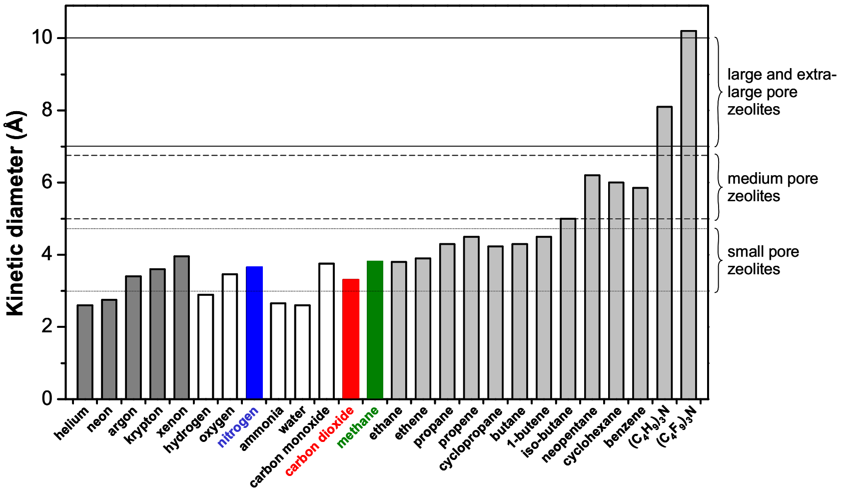

Figure 2 : Diamètre cinétique de plusieurs molécules comparé au diamètre de pores des différentes tailles de zéolites[5].

En regardant les différentes tailles de pores des zéolites, nous nous rendons compte que la taille de pore maximal de ces composés se situe autour de 10Å. Il en résulte donc bien une limitation de l'utilisation de ces composés pour toutes molécules supérieures à cet ordre de grandeur empêchant toutes réactions. La

Figure 2 illustre bien la limitation de ces composés qui pousse certains chercheurs à trouver un composé possédant une plus grande taille de pores afin d'ouvrir la voie à de nouvelle application.

1.1.2.2. La forme des cavités

La forme des cavités est aussi un paramètre important des structures cristallines, il existe beaucoup de composés qui possèdent une taille de pores identique mais une forme de cavités différente, cela provoque des réactivités d'un autre genre. Par exemple, les zéolites de petite taille de pores comme la zéolite A (LTA) et l'analcime (ANA) possèdent des formes de pores différentes. La première a une forme plutôt cylindrique de 4,1 Å de diamètre alors que la deuxième a une forme plutôt elliptique de 1,6 Å. Cela provoque une différence importante de la diffusion interne. En effet, malgré la même taille de pores, du point de vue de l'adsorption, la LTA possède un potentiel d'adsorption et donc de séparation tandis que la ANA n'en a pas.

1.1.2.3. La dimension du réseau poreux

Le dernier critère de classification souvent utilisé est celui qui prend en compte la direction des canaux. Dans les zéolites, tous les cas existent. Comme exemples, la TON, la MFI et la ITH sont trois zéolites de taille de pores moyenne respectivement, unidimensionnelle, bidimensionnelle et tridimensionnelle. La direction des canaux est un critère très important pour la diffusion des molécules dans la structure. En effet, une zéolite unidirectionnelle possède par définition une limitation de la diffusion due à la progression des molécules le long d'une seule direction de canaux. Comme exemple, le volume microporeux d'une zéolite de petite taille de pores unidirectionnels, comme la MTF est de 0.07 $cm^3.g^{-1}$ tandis que la CHA, petits pores tridimensionnels, possède un volume de 0.3 $cm^3.g^{-1}$.

1.1.2.4. Conclusion

En vue de leurs différentes propriétés de polarité et d'acidité, ainsi que de leurs résistances mécaniques et thermiques, les zéolites sont des catalyseurs et des adsorbants incontournables. Cependant ces composés possèdent 2 limitations. La première vient de leurs relatives faibles tailles de pores, autour de 10Å, qui limite l'utilisation de ces matériaux pour toutes réactions comprenant de plus grosses molécules comme les dérivés de la biomasse (acides gras, lignocellulose). La deuxième limitation vient de leur faible volume poreux qui restreint leurs utilisations pour tout ce qui est stockage de composés. Même si les découvertes de zéolites à taille de pores extra large se font de plus en plus fréquentes, elles restent néanmoins rares et leurs stabilités restent à démontrer.

1.2. Metal Organic Frameworks, (MOFs)

Depuis la fin des années 1990, un nouveau type de matériaux microporeux cristallins a vu le jour, les MOFs. Ces composés ont été particulièrement étudiés dans le domaine de la séparation, du stockage de gaz[14-17] et plus particulièrement dans l'adsorption de l'H_2 et du CO_2, ainsi que dans la catalyse hétérogène[18-25]. Cette explosion de résultats provient de l'exceptionnelle capacité des MOFs à pouvoir être modulée.

Même si les hypothèses posées par la méthode BET ne sont pas adaptées pour mesurer des surfaces spécifiques, d'exceptionnelles valeurs sont reportées comme le Cu(bdc)teda[26], MOF-177[27] et le MOF-101[28] avec des surfaces spécifiques, respectivement de : 4000, 4500 et 5300 $m^2.g^{-1}$. Des valeurs autour de 1300 m^2/g sont très fréquentes.

1.2.1. MOFs : des matériaux hybrides

Les zéolites ne sont construites que par des assemblages tétravalents de Si, O et Al, et ne peuvent être dopées que par quelques cations spécifiques. Ce problème, qui induit une limitation dans les différentes applications, et justement l'un des avantages que confèrent les MOFs. En effet, la kyrielle de MOF existants vient des différents constituants [29, 30].

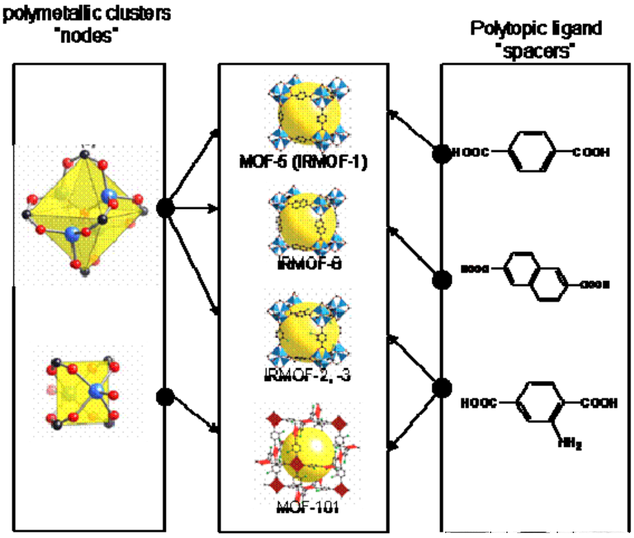

Figure 3 : Auto assemblage de clusters et ligands organiques [31, 32].

La Figure 3 montre comment les MOFs possèdent une impressionnante diversité. En effet, pour un même cluster métallique, il suffit de changer le ligand pour obtenir autant de nouveaux composés. Inversement, un même ligand peut se coordonner avec différents clusters pour obtenir d'autre MOFs. Si en plus, une même géométrie de cluster peut être obtenue par différents métaux [33], le nombre de MOFs possibles devient très vite important. Les 2 paramètres majeurs responsables de la diversité de MOFs sont donc le cation et le ligand.

- Le cation

Les MOFs peuvent être obtenus avec de nombreux cations métalliques. Comme la réactivité en catalyse ou adsorption dépend du métal utilisé, la possibilité d'obtenir des composés avec différents métaux augmente leurs nombres d'application et leurs intérêts. Plusieurs groupes de chercheurs ont réussi à obtenir les mêmes structures cristallines comme le MIL-53[33], MIL-68[34, 35] avec des métaux différents (Al, Ga, In, Fe, Cr) et donc des propriétés différentes. En revanche, pour un même cation et un même ligand, il peut exister différents arrangements cationiques. Il en résulte une nouvelle structure cristalline. La possibilité d'obtenir préférentiellement une structure cristalline ou une autre peut provenir généralement, soit du protocole opératoire (température), soit du solvant utilisé. Trois exemples connus sont i) le IRMOF-1, aussi appelé IRMOF-1 et le MOF-69C [36] et ii) les structures MIL-53 et MIL-68 peuvent s'obtenir par simple variation de la température de réaction et iii) le MIL-53(Cr) et le MIL-101 (Cr) par la variation de la concentration initiale.

- Le ligand

Ces molécules sont des composés poly-chélatants rigides. Les fonctions de coordination sont généralement des carboxylates, des imidazolates ou des amines, mais théoriquement toutes fonctions coordonnantes peuvent être employées. La rigidité de la molécule est elle aussi importante en vue de faciliter l'organisation du polymère de coordination, c'est pour cette raison que les ligands aromatiques ou du moins cycliques sont principalement utilisés. La grande diversité des composés organiques donne un énorme choix de ligands à utiliser. En effet, comme le montre la Figure 3, pour un même cluster, Zn_4O, le groupe de Yaghi[37] a découvert une importante classe de matériaux appelée IsoReticular Metal Organic Frameworks (IRMOF). Cet exemple illustre très bien la diversité induite par les ligands. En effet la différence de volume poreux, ici représenté par la sphère jaune, provient directement de la distance entre les 2 fonctions chélatantes. Selon l'utilisation de l'acide téréphtalique ou de l'acide 4-4' biphényledicarboxylique, les diamètres des pores varient de 0.38 à 2.88nm. Les plus grands pores reportés jusqu'ici étant ceux des MIL-100 et MIL-101 avec 3.4nm [28].

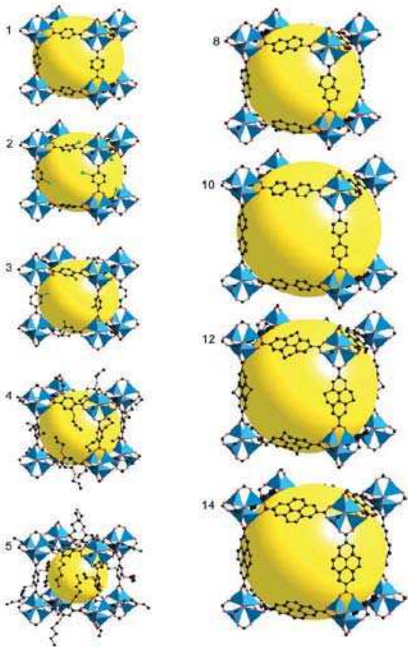

Figure 4 : Famille d'IRMOFs, montrant la capacité à modifier le volume poreux (sphère jaune) et la taille de pores en utilisant différents ligands.

L'une des applications possible de ce genre d'approche pourrait être l'augmentation de la capacité d'adsorption sans modification de l'interaction entre le gaz et l'adsorbant comme dans le cas de l'IRMOF-1, IRMOF-8 et IRMOF-10.

En plus de pouvoir modifier la cavité, il est aussi possible de fonctionnaliser les ligands afin de modifier une caractéristique du composé selon un besoin précis. Deux stratégies sont généralement retenues pour atteindre cet objectif.

La 1ère technique consiste à utiliser lors de la réaction un ligand déjà fonctionnalisé et d'effectuer la synthèse, comme dans le cas de l'IRMOF-1 et l'IRMOF-3. Dans cet exemple les 2 structures sont équivalentes, Cf structure 1 et 2 de la Figure 4, la seule différence réside dans le choix du ligand, l'IRMOF-1 est obtenu avec l'acide téréphtalique, l'IRMOF-3 avec l'acide 2-amino-téréphtalique. Mais cette méthode peut connaître des difficultés car le groupe ajouté, ici $–NH_2$, peut interagir avec le cation et ne pas donner la structure attendue. C'est pour cela qu'une deuxième technique a été développée : la post-fonctionnalisation. Ici un MOF possédant un site 'fonctionnalisable' est synthétisé, une fois obtenu un traitement du composé est effectué en vu d'obtenir un composé possédant différentes caractéristiques. En 2008 Morris et al [38] ont montré le potentiel de cette stratégie en obtenant 2 composés aux caractéristiques différentes, en partant pourtant du même composé de départ : le ZIF-90.

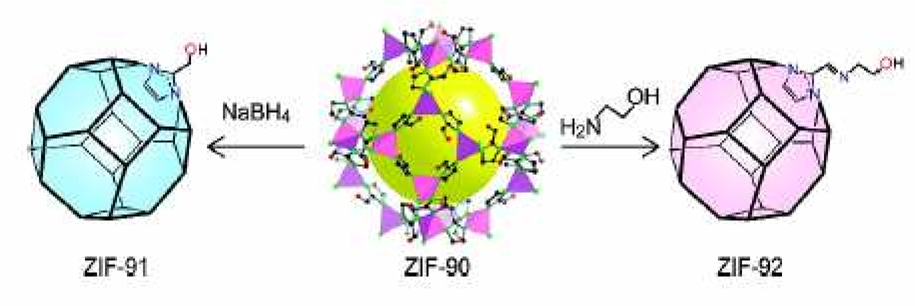

Figure 5 : Obtention de 2 composés aux caractéristiques différentes, ZIF-91 et ZIF-92, à partir d'un même composé de départ.

Cette capacité à modifier la polarité du matériau est particulièrement intéressante pour le traitement des gaz ou la catalyse. Si le matériau est fonctionnalisable, il est possible d'adapter son affinité aux besoins de l'application [32, 39-42].

1.2.2. Approche SBU appliqué aux MOFs

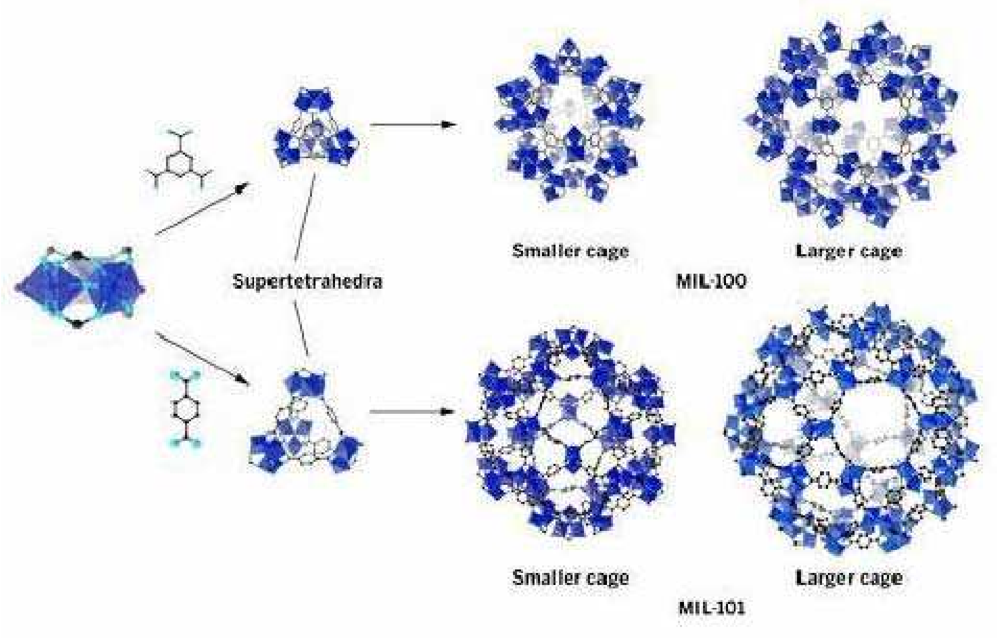

Figure 6 : Agencement d'un cluster trimère en SBU puis en cages pour des composés MIL-100 et MIL-101.

Si dans le cas des zéolithes le SBU représente les différentes combinaisons possibles des différents blocks de tétraèdres, dans le cas des MOFs, le SBU est un motif constitué d'un assemblage de clusters qui se retrouvent de façon ordonnée dans le solide. Cette approche a été systématisée par Yaghi [43]et Ferey [28].

1.2.3. La flexibilité des MOFs

L'une des propriétés les plus surprenantes de certains MOFs provient de leur flexibilité, appelée breathing effect ou encore gate opening.

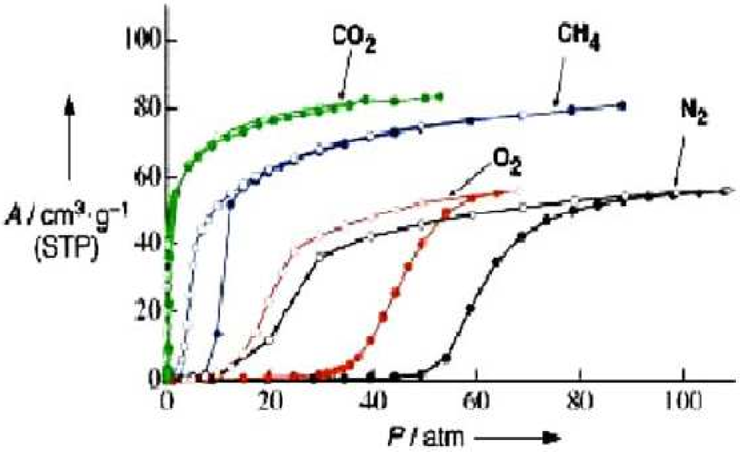

Figure 7 : Effet de la flexibilité du [Cu(4, 4'-bipy)(dhbc)$_2$]·2H_2O à 298K sur différents gaz, adsorption (cercle plein) et désorption (cercle vide).

En outre, ce phénomène se produit lorsque une certaine pression d'un gaz spécifique est appliquée. Ceci produit une déformation des paramètres de mailles et donc des propriétés d'adsorption. Plusieurs exemples de cette capacité a été mise en évidence par Kitaura et al[44] en 2003. Dans ce travail, des isothermes d'adsorption à 298K de plusieurs gaz sont effectuées sur le [Cu(4, 4'-bipy)(dhbc)$_2$]·2H_2O. L'expérience réalisée avec l'O_2 et l'N_2, et le méthane montre une hystérésis qu'on attribue au phénomène de gate opening (Figure 7).

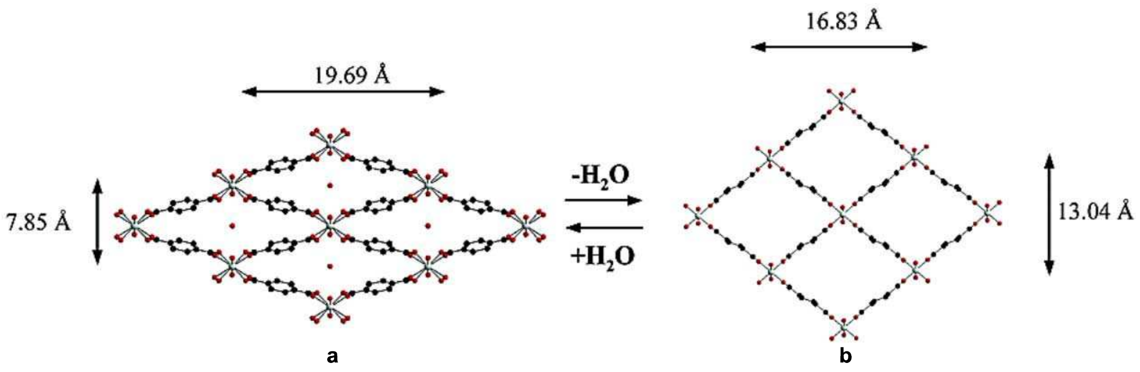

Figure 8 : Représentation cristalline des 2 formes de la structure MIL-53 (Al), forme (a), fermée ou hydratée (gauche), et forme (b) ouverte (droite).

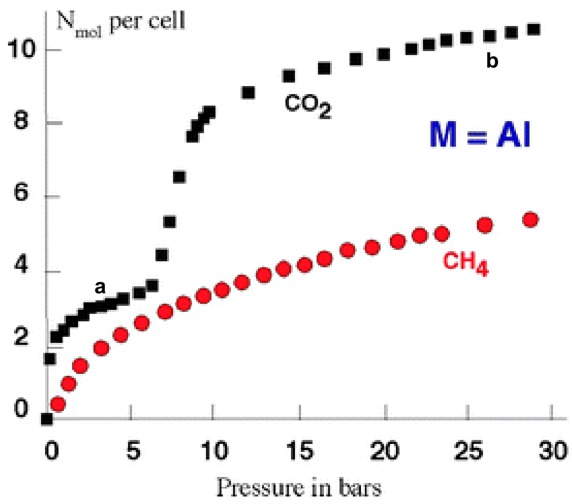

Figure 9 : Adsorption du CO_2 et du CH_4 à 304K sur le MIL-53 (Al) [45] selon la forme fermée (a) ou ouverte (b).

La « respiration » du MIL-53 est un second exemple [45] Figure 8 & Figure 9. Ici, le MIL-53 (Al) hydraté est fermé tandis que lorsque le composé est sec, il est dans sa forme ouverte. Ce phénomène se produit de façon spécifique pour différents gaz. A basse pression de CO2, la structure est sous la forme fermée, puis s'ouvre à partir de 6 bars. [45] [46].

1.2.4. Synthèse de MOFs

D'après Robin et al, le procédé de synthèse des MOFs s'effectue par auto-assemblage selon un mode de polymérisation qui est régie par des liaisons de coordination [47]. Ce qui correspond à la mise en commun d'une paire d'électrons donnée par le ligand, considéré comme base de Lewis, au cation métallique, considéré comme acide de Lewis. A cela vient s'ajouter d'autres interactions comme les liaisons hydrogènes provenant du solvant qui peut fortement influencer le polymère obtenu. Différents protocoles de synthèse ont été développés. Ils possèdent tous leurs avantages et leurs inconvénients. Actuellement cinq grandes méthodes ont été élaborées [28, 34, 48-52].

1.2.4.1. Les méthodes de synthèses pour obtenir des monocristaux

Dans ce cas, le but est d'obtenir un monocristal de taille suffisante (>100µm) pour permettre sa résolution structurale par Diffraction des RX. Il convient de jouer sur les vitesses de nucléations et grossissements.

i) La diffusion de liquide, ici des couches sont formées par des solvants non miscibles possédant chacun un réactif distinct. La réaction prend place à l'interstice des couches.
ii) Une diffusion dans l'air. Dans ce cas, l'approche est similaire à la première technique si ce n'est qu'il y a une barrière physique. Deux béchers possédant un réactif sont placés dans une enceinte fermée, la diffusion dans l'air d'un des réactifs finit par entrer en contact avec les réactifs de l'autre bécher et donne le MOF.

- La méthode solvothermal

Ici tous les réactifs sont mis dans un autoclave, la température de réaction est comprise entre 100 et 200°C sous pression auto-générée. Un des avantages à utiliser cette technique est la diminution de la viscosité du solvant, ce qui provoque une augmentation de la diffusion et de la solubilité des réactifs.

1.2.4.2. Méthodes pour accélérer la synthèse

- La méthode par micro-ondes

Cette méthode permet d'obtenir rapidement un MOF [53-55], Elle est basée sur l'interaction existant entre les différentes couches conductrices et les radiations des micro-ondes. Il résulte de ce traitement une rapide augmentation de la température du substrat. Ce phénomène incrémente le nombre de nucléations ainsi que leurs croissances.

- Synthèse par électrode

Mueller et al[56], ont reporté un moyen assez exotique pour synthétiser un MOF très connue, l'HKUST-1 ou $Cu_3(BTC)_2$. En effet, des plaques de cuivre sont utilisées comme électrode et sont mises dans une solution contenant le ligand organique. Un courant de 1,3A à 12-19V est appliqué. Cette méthode permet une très bonne cristallisation avec des tailles de cristaux de l'ordre de 3µm.

1.2.5. Conclusion

Pour les procédés de séparations et de catalyses, les matériaux microporeux représentent de bons candidats. Leurs tailles de pores, de l'ordre de grandeur des molécules à séparer ou des réactifs, permettent une forte interaction avec les adsorbats et/ou une activation par effet de confinement. C'est pour cette raison que dans cette étude nous nous sommes limités à l'obtention de composé microporeux. Ces sont générallement des zéolithes ou des structures apparentées de types silicoaluminates ou aluminophosphates.

Au niveau diversité, ces composés possèdent 2 limitations. i) Ils sont constitués très majoritairement de Si, Al et P et le nombre et la quantité d'autre cations dans la charpente sont limitées (Ti4+, Ga3+, Sn4+ pour les zéolites) ;. ii) La taille de pore de ces composés se limite à la gamme ultra-microporeuse c'est-à-dire inférieure ou égale à 1nm (sauf cas exceptionnel)

Ces 2 points font justement partis des atouts des MOFs. En effet, l'hétérogénéité de ces composés, que se soit du point de vue des cations utilisables ou des ligands organiques, rendent ces matériaux très attractifs. Cependant, il y a 3 ans (au début de nos travaux), les connaissances sur la synthèse et les caractéristiques de ces composés étaient encore limitées. Au vu des analyses réalisées, les caractéristiques du composé recherché sont de posséder un compromis entre un grand volume poreux et une taille de pores de l'ordre de plus grande que le diamètre cinétique du CO_2 (Ø=3.3Å).

1.3. Le gaz naturel

1.3.1. Ressources et spécification

Tableau 1 : Réserve mondial de GN en 2007 ($1.82 \cdot 10^{14}$ m^3), Production en 2005 ($2.84 \cdot 10^{12}$ m^3) et Consommation en 2005 ($2.82 \cdot 10^{12}$ m^3) [58].

Zone géographique	Réserves [%]	Production [%]	Consommation [%]
Europe de l'ouest	3.0	10.4	17.6
Asie & pacifique (indus)	1.6	1.8	6.0
Amérique du nord	4.2	24.4	24.7
Europe centrale	0.3	0.8	2.7
Europe de l'est	27.0	22.4	18.5
Asie centrale	4.6	5.3	3.6
Moyen orient	40.3	10.3	8.9
Afrique	7.9	6.5	3.0
Asie & pacifique (développé)	7.2	11.7	8.9
Amérique latine	4.0	6.4	6.2

Les demandes mondiales d'énergie sont et seront en constante augmentation, +/-1,7% par an, dans la période 2005-2020. Sachant que cette augmentation ne pourra pas diminuer dans les 50 prochaines années, de nouvelles ressources sont à exploiter en vu de pouvoir pallier à ce besoin. Les énergies fossiles sont, est de loin, les plus utilisées dans notre monde. Les nouvelles normes sur le rejet gazeux et plus particulièrement sur le CO_2, font du gaz naturel (GN) la ressource fossile la plus attractive et elle connaîtra un essor très important dans les années à venir [57] [58].

Dans la majorité des cas, le GN doit être traité dans un endroit différent du site de production. Le transport du gaz peut être effectué principalement par 2 moyens : via des pipelines avec une pureté en CH_4 de 75% ou via des tankers après avoir été liquéfié, avec une pureté de 85%[59]. La différence entre ces 2 modes de transport dépend principalement de la distance et du volume à transporter. Par exemple, le groupe ENI préfère liquéfier le gaz lorsque la nappe est relativement petite (moins de 1 $Tcf.y^{-1} = 2.83\cdot10^{11} m^3.y^{-1}$) et lorsqu'il faut le transporter sur une grande distance (>4800km).

Afin de mieux rentabiliser la production, le GN est classifié en plusieurs parties et sous parties. Premièrement par son origine et sa composition chimique, donnant ainsi 3 catégories : (i) non-associated gas, lorsque le gaz n'est pas en contact avec le pétrole, (ii) gas-cap associated gas, lorsque le gaz est au-dessus de la couche de pétrole dans le réservoir et (iii) associated gas, lorsque le gaz est dissous dans le pétrole. Deuxièmement par sa composition en sortie de réservoir, le GN possède de nombreux polluants comme l'eau, les hydrocarbones C_{3+}, le CO_2, N_2, les composés soufrés et même parfois des traces d'H_2 et Hg. Enfin troisièmement par les moyens mis en œuvre pour extraire le GN, à savoir l'injection de N_2 et/ou de CO_2.

Tableau 2 : Composition général des impuretés pour le transport liquéfié (LNG) ou par pipeline. Total Sulfur comprend du H_2S + COS + des composés

Impurity	Feed to LNG Plant	Pipeline Gas
H_2O	< 0.1 ppmv	150 ppmv
H_2S	< 4 ppmv	5.7 – 22.9 mg·Sm^{-3}
CO_2	< 50 ppmv	3 – 4 vol.%
Total Sulfur	< 20 ppmv	115 – 419 mg·Sm^{-3}
N_2	< 1 vol.%	3 vol.%
Hg	< 0.01 mg/Nm^3	-
C_4	< 2 vol.%	-
C_{5+}	< 0.1 vol.%	-
Aromatics	< 2 ppmv	-

En effet ces derniers peuvent aussi modifier la composition du mélange provoquant des différences de traitement à effectuer. Il en résulte 2 x 2 catégories : le sec et l'humide, qui dépend de la concentration en C_{2+} (>10%vol) ; doux et acide, selon la concentration en gaz acide comme le H_2S (>1%vol) ou le CO_2 (>2%vol). La caractérisation complète du mélange gazeux est donc primordiale pour déterminer les procédés à utiliser afin de pouvoir le transporter ou le raffiner [60] [61] [62].

Les technologies de traitement de gaz peuvent être séparées en 2 catégories[63] [64], i) la séparation, lorsque la concentration des polluants de la réserve de gaz est supérieure à 10 %m, et ii) la purification quand la concentration des polluant est inférieure à 3 %m. S'agissant de la composition du GN qui va imposer le choix de l'adsorbant ainsi que le procédé, une technique de traitement qui fonctionnerait dans de nombreux cas serait considérablement plus rentable.

1.3.2. Les différents traitements

- Déshydratation

Avant de livrer le GN aux usines de raffinage, le mélange doit tout d'abord être séché. Encore aujourd'hui, le moyen de déshydratation le plus utilisé consiste à mélanger le GN avec une solution de TriEthyleneGlycol (TEG) puis de re-adsorbé le TEG hydraté avec un adsorbent spécifique comme une zeolite, une silice ou aluminosilicate [65]. Après la déshydratation du mélange, le TEG est régénéré par chauffage (473K) puis réinjecté dans un autre cycle. En effet, l'eau contenue dans le mélange doit être diminuée à un niveau qui prévient : la corrosion, la formation d'hydrate ainsi que la glace qui peut se former si la quantité est trop importante lors du procédé de cryogénie [66]. Car la formation d'hydrate provenant de l'eau et des hydrocarbones est considérée comme étant la première cause d'incident dans les pipelines. Le même problème peut se rencontrer si la concentration en composé sulfuré ou en CO_2 est trop importante [62].

- Purification des gaz

La désorption des gaz inertes comme le N_2 ou le He ainsi que les gaz acides, principalement le CO_2 et le H_2S, est une étape cruciale de la séparation. Il est à noter que le H_2S est un composé que l'on trouve très rarement dans des proportions supérieurs à 10% vol, mais généralement la proportion est bien plus faible. En revanche le CO_2, 0.5-10 %vol avec un maximum de 70%vol, et le N_2, 0.5 -5 %vol avec un maximum de 25%vol sont les principaux polluants du GN. De plus ces 2 composés peuvent être considérés comme des gaz inertes du point de vue énergie et diminue donc le rendement. Leurs concentrations doivent être absolument diminuées avant la distribution.

- N_2 - He

La séparation du N_2 et He du CH_4 est généralement effectuée par distillation cryogénique. Généralement, cette technique est considérée comme économiquement viable lorsque le flux gazeux dépasse les $4.25 \cdot 10^5$ $Sm^3.d^{-1}$. Ce procédé consiste à envoyer le GN dans une chambre refroidit à très basse température afin de condenser les agents contaminants.

- Gaz acide

Deux types de procédé sont utilisés pour séparer le CH_4 des gaz acides. Soit par le procédé amine, soit par l'utilisation d'un solvant organique. Ces 2 techniques sont à peu près équivalentes, elles consistent à faire buller le mélange gazeux dans une solution basique, généralement une amine, afin de faire réagir l'acide, ou bien de comprimer le GN dans un réacteur pour dissoudre le gaz dans le solvant organique. Dans les 2 cas, l'acide réagit et le complexe formé reste en solution alors que le CH_4 reste en état gazeux. La solution basique est ensuite régénérée par simple chauffage tandis que le solvant est régénéré par réduction de la pression. La limitation de ces procédés vient de l'application très douce que nécessitent ces techniques afin de diminuer les risques qui pourraient provenir de la production des déchets gazeux.

Pour résumer, les sources de GN possèdent des compositions très différentes qui doivent être traité selon la manière adéquate. Les puits de GN trop contaminés ne pourront pas être traités car le coût de la purification serait beaucoup trop élevé pour les procédés actuels. Le procède PSA, Pressure Swing Adsorption, pourrait posséder, s'il est utilisé avec un adsorbant adéquat, de nombreux d'avantages économiques pour les petits champs fortement contaminé et/ou dans des localisations très éloignées.

1.3.3. Procédé PSA pour le traitement du GN.

Jusqu'à présent, l'exploitation des champs de GN fortement contaminé, surtout lorsqu'ils sont petits, est évité car peu rentable. Au vu de la forte croissance de la demande énergétique internationale ainsi que des nouvelles normes écologiques, essentiellement basées sur la régulation des gaz à effet de serre, les entreprises énergétiques ont été forcées de développer des procédés de traitement de gaz rendant le maximum de champ de GN économiquement viable. C'est pour ces raisons que le traitement du GN par le procédé PSA l'est devenu.

Le cycle du PSA est composé de 2 étapes, la $1^{ère}$ consiste à compresser le mélange gazeux dans une enceinte enfermant un adsorbant, puis lorsque le matériau est saturé et que le méthane purifié est évacué, le tamis est régénéré en diminuant la pression, ces étapes sont détaillées dans la prochaine partie. Ce procédé fonctionne donc par des cycles d'adsorption-désorption physiques sans que le moindre produit chimique ne soit utilisé. Il en résulte un gain environnemental considérable. De plus dans les puits, le GN est souvent déjà compressé et se trouve généralement au-dessus des différents constituants, la purification du méthane peut alors s'effectuer sans compression préalable du mélange gazeux, ce qui provoque encore un gain économique non négligeable. Enfin, les 3 derniers avantages de ce type d'installation sont : i) la facilité d'installation, ii) la possibilité d'entièrement automatiser le procédé, et iii) l'utilisation de combinaisons d'adsorbants permet de traiter un grand nombre de contaminants sans pour autant demander une modification du procédé.

1.3.3.1. Fonctionnement du PSA

Le procédé PSA est décrit dans deux brevets publiés vers la fin des années 1960, puis amélioré par la suite[67] [68] [69] [70]. De nos jours, près de 600 brevets américains et 800 articles scientifiques sont parus. Ces installations peuvent avoir différentes tailles allant de petites raffineries, 8.5 $Sm^3.d^{-1}$, pour la production d'oxygène médical à de plus grandes installations, 2.83·106 $Sm^3.d^{-1}$, pour la purification du H_2 dans les installations de steam CH_4 reforming (SMR). Comme tous les procédés d'adsorption, le procédé PSA se décompose en 2 parties.

- *L'étape d'adsorption*. Cette opération est généralement effectuée à haute pression, un mélange gazeux M+N est introduit dans un réacteur possédant un tamis moléculaire, cet adsorbant est préalablement choisi de manière à se qu'il adsorbe spécifiquement l'un des 2 composés. Généralement l'étape d'adsorption s'arrête avant d'arriver à saturation en vue de prévenir la contamination du CH_4 par le gaz à séparer

- *L'étape de désorption*. La régénération s'effectue par diminution de la pression dans la colonne. Lors de cette étape, le mélange gazeux obtenu pendant la régénération du matériau possède une forte teneur en composé adsorbé. La fin de l'étape de régénération s'effectue avant que le tamis ne soit complètement régénéré car la cinétique de désorption devient très lente à recouvrement faible. Il en résulte donc que les cycles d'adsorption-désorption oscillent sans jamais atteindre les positions limites de saturation.

En revanche, la limitation de ce procédé vient du fait que pour fonctionner, le gaz à piéger ne doit pas s'adsorber trop fortement pour permettre sa régénération sans trop de pénalité énergétique.

On peut considérer qu'un cycle entier de PSA s'effectue à température constante, définissant de ce fait une caractéristique très importante de l'adsorbant, la capacité de travail. Cette capacité correspond donc à la différence entre la quantité adsorbée à haute pression et celle à faible pression à la même température. Dans une installation industrielle, afin d'augmenter la rentabilité du procédé, plusieurs colonnes sont placées en parallèle pour permettre un traitement continu des différents mélanges gazeux. Aujourd'hui, les unités PSA utilisent entre 4 et 16 colonnes connectées entre elles par un complexe réseau de tuyaux et de vannes. Selon la manière dont sont effectuées les étapes d'adsorption-désorption, ce procédé porte différent nom, PSA, VSA et TSA.

- Vacuum Swing Adsorption (VSA)

Le VSA correspond à un procédé PSA 'classique' dans lequel l'étape d'adsorption s'effectue à la pression atmosphérique tandis que la désorption s'effectue sous vide. Le problème est que l'utilisation du vide augmente considérablement la complexité de la mise en œuvre du procédé industrie. C'est pour cette raison que cette méthode n'est utilisée qu'en dernier recours.

- Thermal Swing Adsorption (TSA)

Ici, l'étape de régénération s'effectue par chauffage du lit fixe. Généralement, cela est plus facile à mettre en œuvre, car elle ne comporte que les étapes d'adsorptions – désorptions. Mais ce procédé possède 2 problèmes majeurs par rapport au PSA, i) l'utilisation de la température donne un coup énergétique supplémentaire tel, que le coût du chauffage peut se révéler supérieur au prix du gaz purifié. ii) La variation de pression dans le PSA, de l'ordre de la seconde, peut s'exercer beaucoup plus rapidement que la variation de la température, de l'ordre de l'heure. La possibilité d'opérer des cycles très rapidement augmente, bien évidement, le rendement du PSA. Le TSA est donc utilisé lorsqu'une faible variation de la température engendre un considérable shift de la quantité adsorbé.

1.3.3.2. Propriété de l'adsorbant recherché

Afin de pouvoir séparer un mélange gazeux, un adsorbent doit pouvoir interagir avec un composé ou une famille de composés sans avoir d'interaction avec les autres constituants du milieu. Les différences d'adsorption peuvent provenir soit de la différence des capacités d'adsorption, appelée sélectivité thermodynamique, des différents composés à l'équilibre, soit de la vitesse d'adsorption des différents composés, appelé sélectivité cinétique. Cette dernière forme de séparation n'est possible que lorsque la différence des vitesses d'adsorption entre les différents composés est très importante. Généralement, ces différences de vitesse proviennent de la différence de diffusion des composés due aux gènes stériques à l'intérieur des pores lorsque les diamètres poreux et les tailles des molécules sont du même ordre de grandeur. Dans certain cas, les différences de vitesse peuvent être tellement différentes que le composé possédant la plus petite diffusion n'est pas adsorbé. Aujourd'hui, la séparation de l'azote de l'air par l'utilisation de tamis moléculaire de petits pores comme les zeolites est le seul procédé commercial utilisant la méthode de séparation cinétique.

- Interaction gaz-solide

L’adsorption, est plus spécifiquement la physisorption, est basée sur les faibles attractions entre les molécules et le solide qui sont dues aux faibles chaleurs d’adsorption. Les forces d’adsorption peuvent être catégorisées en 2 groupes, les forces de Van Der Waals et les forces électrostatiques. Parfois l’adsorption provient de la synergie entre ces 2 forces d’interaction. Quelques paramètres physico-chimiques des différents composés présents dans le GN sont représentés dans le tableau suivant :

Molécule	**σ [Å]**	**α [Å^3]**	**μ [D]**	**Θ [D·Å]**	**T_c [K]**
CH_4	3.80	2.448	0.000	0.02	190
N_2	3.64	1.710	0.000	1.54	126
CO_2	3.30	2.507	0.000	4.30	304
H_2O	2.65	1.501	1.850	2.30	647
H_2S	3.60	3.630	0.970	3.74	373
He	2.60	0.208	0.000	0.00	5
H_2	2.89	0.787	0.000	0.43	39
CO	3.76	1.953	0.112	2.04	133
Reference	[5]	[71]	[71]	[71]	[72]

Les adsorbants capables d’améliorer les interactions électrostatiques, comme les liaisons hydrogènes, sont généralement des molécules hydrophiles. La plupart du temps elles peuvent adsorber de petites molécules polaires, comme l’ H_2O, bien plus fortement que ne laisse prévoir une simple force adsorption de type van der waals. Les adsorbent hydrophiles les plus courants sont les zéolites, les oxydes de silices et d’alumines. Les liaisons hydrogènes sont des liaisons particulières qui nécessitent des groupes hydroxyles à la surface de l’adsorbant et des molécules possédant des groupes HX- avec X= O, S ou N. A l’opposé, les composés hydrophobiques sont exclusivement régit par les interactions de type van der Waals, comme les charbons actifs.

En accord avec les descriptions des différentes interactions décrites ci-dessus, la sélectivité thermodynamique d’un matériau peut être améliorée. Dans le cas d'une zéolite, sa polarité peut être augmentée lors de la synthèse en augmentant, par exemple, le ratio Si : Al et /ou en modifiant le contre ion. D'un autre coté, les groupes polaires comme les espèces carboxyliques peuvent être introduites dans les charbons actifs par des traitements d'oxydation.

- La structure poreuse des adsorbants.

L'interaction entre les molécules adsorbées et l'adsorbant dépend de la composition chimique des 2 composés. Cette interaction joue un rôle important au début de l'adsorption lorsque la surface est encore 'vierge' d'adsorbant. Cependant, les mécanismes d'adsorption et par conséquence les performances de séparation sont principalement gouvernées par la structure poreuse des adsorbants. La classification IUPAC a classifié en 3 catégories la taille de pore, les micro, meso et macro pores en fonction de leurs tailles de pore. Cette classification correspond à différents mécanismes d'adsorption.

Dans le cas de micropore, taille de pore < 20Å, l'adsorption s'effectue par remplissage des pores[73] [74]. L'interaction gaz - solide est considérablement augmentée lorsque la molécule de gaz et la taille des pores sont de la même dimension. De plus, la séparation d'un mélange gazeux peut s'effectuer si le composé que l'on veut obtenir pur est le seul à posséder un diamètre moléculaire supérieur à la taille de pore du tamis.

Dans le cas ou l'adsorbant possède des mésopores, 20 Å < taille de pore < 500 Å, ou des macropores, taille de pore > 500 Å, l'adsorption s'effectue par multicouche en accord avec le model BET[75]. Dans ce type d'adsorption, les molécules ne possèdent pas la même interaction lorsqu'elles se situent sur la surface de l'adsorbant ou au centre du pore. Si l'interaction entre la surface - molécule est supérieure à l'interaction entre molécule - molécule, les molécules s'adsorbent et se propagent dans la structure. Ce phénomène est appelé condensation capillaire. C'est ce phénomène qui contrôle l'adsorption dans les pores de grande taille, et c'est pour cette raison que les silices mésoporeuses et les alumines ont été très utilisées dans la déshydratation du GN et dans la séparation CH_4 - C_{3+}.

- Equilibre d'adsorption et ΔH

L'équilibre d'adsorption est directement relié à l'évaluation de la capacité d'adsorption, de la sélectivité ainsi que de la régénération de l'adsorbant. La quantité n_i d'un composant i adsorbé à une température T dépend de la concentration de P_i dans le fluide. La modélisation de l'équilibre d'adsorption, dans des conditions d'isothermes, permettra, entre autres, de déterminer les pressions de travail ainsi que les temps d'adsorption et de régénération essentielle à la conception de pilote PSA. Généralement, à faible pression partielle du gaz adsorbé, la loi d'Henry décrit très bien les systèmes obtenus.

Équation 1 : $n_i(p_i,T) = H_i(T)p_i$

Avec H_i, la constante d'Henry.

Cette loi provient d'une dérivation de la loi de Langmuir.

Équation 2 : $n_i(P_i,T) = \dfrac{n_{i,\max}K_i(T)p_i}{1+K_i(T)p_i}$

Avec $n_{i,max}$= Saturation en composé i de l'adsorbant dans ces conditions.
$K_i(T)$= constante d'adsorption

Lorsque la pression partielle de i est très faible, $p_i \rightarrow 0$, Équation 2 peut se réécrire en :

Équation 3 : $n_i(P_i,T) = n_{i,\max}K_i(T)p_i$

Parce que l'expérience est effectuée à température constante, $n_{i,max}$ et $K_i(T)$ sont constants et permettent de retrouver l' Équation 1.

Au vu de ces équations, une grande valeur de la constante d'Henry correspond donc soit une forte constante d'adsorption, résultant d'une forte interaction entre l'adsorbant et l'adsorbat, soit une forte capacité d'adsorption résultant d'un grand volume poreux et/ou une combinaison des deux.

Le modèle de Langmuir est basé sur 2 hypothèses : i) tout les sites d'adsorption du matériau sont équivalent et ii) il n'y a pas d'interaction entre les molécules adsorbées. De part ces hypothèses, la force d'adsorption n'est pas censée se modifier selon le taux de recouvrement du matériau, ce qui est bien évidement faux. Malgré cela, si l'expérience est effectuée à faible pression partielle, ces hypothèses sont valides et le modèle décrit assez bien le comportement d'un adsorbant microporeux.

Tableau 3 : Chaleur d'adsorption à recouvrement nul pour quelques adsorbants sur les principaux constituants du GN à 303 K.

	q_{st} [kJ·mol^{-1}]			
Adsorbant	**CH_4**	**CO_2**	**N_2**	**Référence**
Norit Extra	20.60	22.00	-	76
Calgon BPL	16.10	25.70	-	76
Kensai Maxsorb	16.60	16.20	-	76
A'dall A10	16.20	21.60	-	76
Osaka Gas A	18.30	17.80	-	76
Silicalite	20.90	27.20	17.60	77
NaZSM-5	26.50	50.00	24.10	77
NaX	19.20	49.00	19.90	77

L'adsorption est un phénomène exothermique. La chaleur d'adsorption est une mesure de la force d'interaction des espèces adsorbées. Le ΔH_{ads} calculé est généralement plus important à faible recouvrement qu'à fort. Ce phénomène est dû à la non homogénéité de l'adsorbant et à l'adsorption spécifique des molécules sur les sites les plus 'forts'. C'est pour cette raison que les taux de recouvrement sont indiqués lorsque les différentes chaleurs d'adsorption sont calculées. Généralement le ΔH_{ads} est donné à recouvrement « nul ». D'un point de vu du procédé, le ΔH_{ads} renseigne sur : i) l'énergie nécessaire pour désorber, régénérer l'adsorbant, et ii) sur l'augmentation de la température du réacteur lorsque le procédé sera dans une phase d'adsorption dans des conditions adiabatiques.

Tableau 4 : Chaleur d'adsorption moyenne, pour quelques adsorbants sur les principaux constituant du GN à 303K.

	q [kJ·mol^{-1}]					
Adsorbant	**CH_4**	**CO_2**	**N_2**	**H_2O**	**C_2H_6**	**Référence**
NaX	13.81	34.31	16.74	51.46	31.38	78
Kclinoptilolite	25.10	39.75	25.10	-	29.29	78
CaClinoptilolite	15.06	25.10	20.08	-	10.46	78
MgClinoptilolite	29.98	-	19.99	-	-	79
SrETS-4	14.67	-	21.20	-	-	79
γ-Al_20_3	10.46	33.47	8.37	48.53	17.57	78

Les fortes chaleurs d'adsorption mise en jeu entre le CO_2 et les zéolites provoquent d'importantes variations de la température lors de l'application du procédé qui gène le bon fonctionnement de la séparation par adsorption. En effet, vu que l'adsorption est exothermique et la désorption est endothermique, une forte chaleur d'adsorption provoquera l'effet inverse recherché lors des cycles, c'est-à-dire une augmentation de la température lors de l'adsorption ainsi qu'une baisse de la température lors de la régénération. La détermination des chaleurs d'adsorption est donc un paramètre très important pour une séparation par PSA. Généralement elles sont déterminées par microcalorimétrie ou par adsorption à T=cst.

- Sélectivité et régénération (= capacité de travail)

Ces 2 paramètres, essentiels à déterminer pour l'utilisation d'un adsorbant dans le PSA, dépendent directement de la chaleur d'adsorption. La sélectivité est basée sur la différence d'affinité qu'il existe entre le tamis et les différentes molécules présentes. Si N est le composé le plus adsorbé et M le moins, la sélectivité, α, à pour définition :

Équation 4 : $$\alpha_{N,M} = \frac{n_N . P_M}{n_M . P_N}$$

Avec n_i= nombre de mole adsorbé du constituant i et P_i pression partielle du composé i.

Lorsque α est comprise entre 2 et 100, l'adsorbant est considéré comme acceptable [80]. Généralement si un adsorbant est très sélectif, la régénération nécessitera de l'énergie. En effet si l'interaction entre gaz-adsorbant est forte il faudra utiliser beaucoup d'énergie pour la désorber. Un compromis entre les deux paramètres est donc nécessaire pour trouver un adsorbant efficace et rentable.

1.3.4. Capacité d'adsorption des différents adsorbants

Comme le montre la Figure 10, la plus part des adsorbants utilisés pour le captage du CO_2 sont des composés relativement très polaire. De se fait l'interaction entre le gaz et l'adsorbant et tellement grande que la saturation s'atteint dès que P_{CO2}=0,2 comme c'est la cas pour la 13X. Cette forte interaction est justement un problème pour le procédé PSA car il demandera beaucoup trop d'énergie pour être régénéré. Dans le cas de composé moins polaire, l'interaction avec les CO_2 est beaucoup moins importante. Il en résulte que l'adsorption à faible pression partielle est moins élevée et que le coup énergétique de la régénération sera moins élevé aussi. De part cette expérience, le composé à rechercher doit avoir un caractère plutôt apolaire avec un volume poreux le plus important possible.

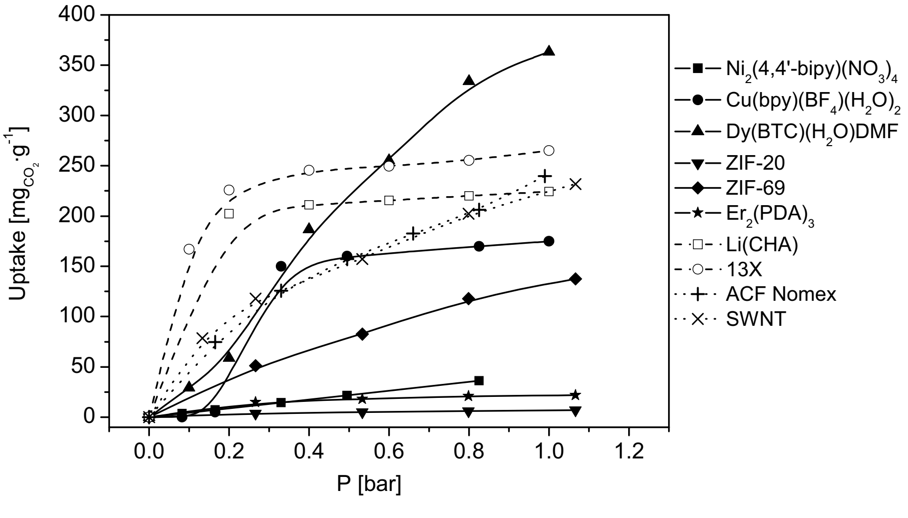

Figure 10 : Isotherme d'adsorption de CO_2 à 273K sur quelques adsorbants de références et des MOFs. Symbole ouvert, Zéolites, symbole fermé, MOFs, croix, Carbons.

$Ni_2(4,4'\text{-bipy})(NO_3)_4$[81], $Cu(bpy)(BF_4)(H_2O)_2$[82], Dy(BTC)(H$_2$O)DMF[83], ZIF-20[84], ZIF-69[85], $Er_2(PDA)_3$[86], Li(CHA)[87], 13X[83], ACF Nomex[88], SWNT[89].

1.3.5. Conclusion

Au vu de l'augmentation de la demande énergétique mondiale et des restrictions environnementales, l'exploitation de nombreux puits de GN considéré jusque là comme trop pollués commence à être rentable. Néanmoins, 2 problèmes résultent de la purification de ces puits : i) les techniques de séparation de gaz utilisées demandent trop d'énergie lorsqu' ils sont fortement contaminés, ii) Les différentes techniques de séparation doivent être adaptées à un certain type de GN, ce qui provoque plusieurs installations d'usine de purification. C'est dans ce contexte que le procédé PSA devient rentable. En effet, cette technique possède plusieurs avantages, i) il suffit de rajouter des couches d'adsorbant dans le réacteur pour pouvoir adsorber différents composés et ainsi adapter le tamis moléculaire aux mélanges gazeux, ii) l'instalation d'un procédé PSA est relativement facile et peu couteuse, surtout pour des petits champs, iii) il peut être entièrement automatisé et enfin iv) le fait de ne pas utiliser de solution donne un gain écologique non négligeable par rapport à d'autres procédés. Le principal problème de cette méthode est de trouver un adsorbant adéquat. Les principales caractéristiques de ce tamis sont : i) une importante capacité de travail, ii) un ratio sélectivité – régénération adapté, iii) une faible chaleur d'adsorption, iv) une bonne stabilité thermique et mécanique, v) qu'il ne doit pas gêner la diffusion du gaz entre les particules du tamis, et enfin vi) il doit avoir une densité 'raisonnable'.

1.4. Etat de l'art de l'alkylation

1.4.1. Contexte socio-économique

De nos jours, les réactions catalytiques des composés organiques représentent, aux USA, 1 Trillions de $US par an. Le seul domaine de la catalyse hétérogène acide génère dans le monde quelques milliards de $US annuel[90]. Vu l'énorme intérêt économique, de nombreux groupes de chercheurs ont essayé d'optimiser ces réactions. Comme dans la grande majorité des cas, les améliorations à effectuer sont principalement basées sur le rendement, le gain d'énergie et depuis quelques années sur l'impact écologique. Dans ce sens, l'une des premières améliorations à effectuer est de passer d'une catalyse homogène à hétérogène. En effet, l'utilisation d'un matériau comme catalyseur possède plusieurs avantages, une simple filtration est généralement suffisante pour les séparer, ils sont réutilisables et ils peuvent permettre des catalyses stéréo-sélectives. En revanche, seules les molécules possédant un diamètre cinétique plus petit que leurs tailles de pores peuvent être utilisées. L'une des réactions catalytiques les plus importantes est la réaction d'alkylation de type Friedel-crafts sur les aromatiques et plus particulièrement sur le benzène. On retrouve ces réactions dans i) l'industrie plastique où l'addition de l'éthylène au benzène est la première étape de l'obtention du styrène et des caoutchoucs, ii) dans l'industrie chimique pour la production du cumène pour l'obtention du phénol et de l'acétone et enfin iii) dans l'industrie des détergents pour l'obtention de composé aux propriétés tensioactives. A titre indicatif, en 1994, 72% du benzène consommé dans le monde, environ 17Mt/an, a été transformé par une alkylation. Dans cette étude nous nous limiterons à la catalyse d'aromatiques à l'aide de catalyseur hétérogène.

1.4.2. Réaction chimique

Une réaction d'alkylation consiste à greffer un composé aliphatique (=saturé) sur une molécule. Ce genre de réaction à besoin de catalyseur pour fonctionner, les procédés industriels se font par catalyse acide, de Brønsted ou Lewis, homogène comme : $AlCl_3$, HF, H_3PO_4, BF_3 et H_2SO_4, mais aussi par catalyse hétérogène [91, 92], principalement des zéolites acides à pores larges comme la H-BEA[93] ou moyen comme la MFI[94]. Enfin, les dernière recherches ont mis en évidences des activités par voie basique [95, 96], ou radicalaire [97, 98].

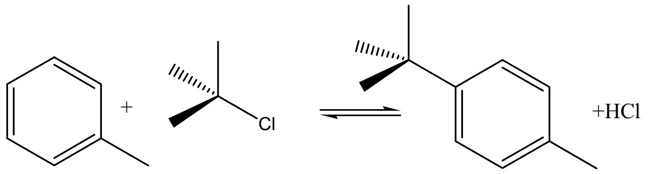

Figure 11 : Exemple d'alkylation du $Cl\text{-}C(CH_3)_3$ sur le toluène.

Selon les conditions de réaction, divers résultats de produits peuvent être obtenus. Il peut y avoir des mélanges de stéréoisomères, des polyalkylations ou des isomérisations.

- Stéréoisomère

Lorsque l'alkylation est effectuée sur un aromatique substitué, l'agent alkylant peut être greffé dans les différentes positions ortho-, méta- ou para-. De plus, selon l'encombrement des réactifs utilisés, certains composés sont plus ou moins favorisés, mais la sélectivité de la réaction peut surtout être contrôlée par l'utilisation d'un catalyseur hétérogène avec une taille de pore défini.

- Polyalkylation

Selon le mécanisme de la réaction, le produit obtenu peut être plus réactif que le produit initial, ce qui provoque une polyalkylation. En effet, un intermédiaire de réaction peut être stabilisé par l'effet inductif du substituant greffé[99]. Encore une fois, l'utilisation d'un catalyseur hétérogène avec une taille de pore particulière devrait limiter ce phénomène.

- Isomérisation.

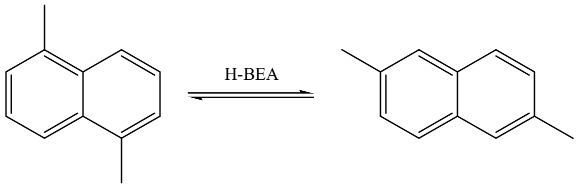

Figure 12 : Exemple d'isomérisation du

1-5 diméthylnaphtalène en 2-6 diméthylnaphtalène

Si la réaction est effectuée avec un catalyseur acide, selon la force, le type d'acidité ou la taille de pore du catalyseur, le produit obtenu peut s'isomériser[100, 101]. Une isomérisation est un réarrangement spatial des substituants. Dans le cas des polyalkylations de composé, les groupements vont se greffer dans les positions les plus thermodynamiquement favorables.

Pour résumer, ces trois phénomènes sont régit principalement par la forme du catalyseur et plus précisément par leurs tailles de pore. Il en résulte qu'un grand contrôle de la cristallinité est donc requis pour accentuer ou diminuer un phénomène. Néanmoins, une limitation aux zéolites apparaît clairement. En effet, la faible diversité des zéolites empêche l'utilisation de ces dernières lorsque les molécules possèdent des diamètres cinétiques plus grands que la taille des pores des matériaux. Cette limitation peut être dépassée si les composés possèdent de grandes tailles de pores, comme c'est le cas pour les MOFs.

1.4.3. Mécanisme

La réaction d'alkylation à la particularité de fonctionner selon différents processus. Par réaction acide, que se soit de Brønsted ou Lewis, par réaction basique, radicalaire ou par réaction d'oxydation. Il est à noter que les 3 dernières n'ont jamais dépassé le stade du laboratoire et que tous les procédés industriels passent par une catalyse acide homogène ou non.

- Acide

Ce type de réaction est une substitution électrophile et l'intermédiaire de réaction passe par un carbocation. De ce fait, toutes les règles qui régissent cet intermédiaire s'appliquent, comme la stabilisation d'un ion carbonium lorsqu'il est substitué. La seule différence dans le mécanisme, quelque soit le type de catalyseur utilisé, provient de l'étape d'activation. Le 1er modèle de la réaction a été proposé par Friedel-Crafts en 1877 sur la base d'un acide de Lewis[102].

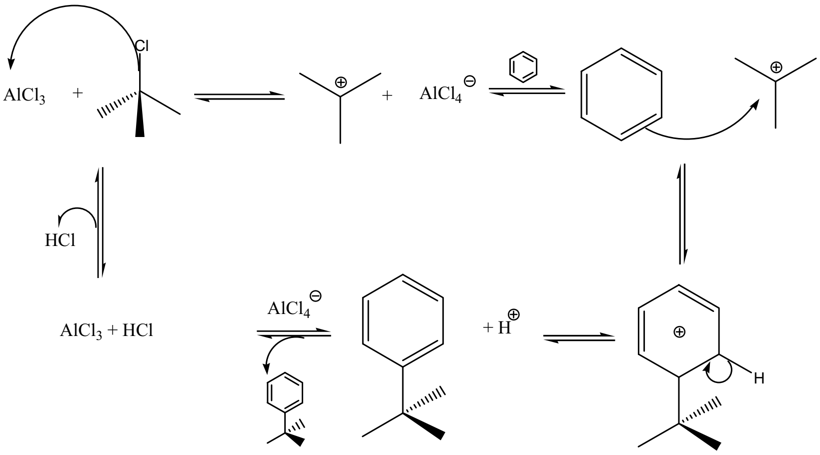

Figure 13 : Mécanisme acide de Friedel-Crafts sur l'alkylation du benzène avec terBuCl.

Dans cet exemple, l'activation du terBuCl est effectuée par un acide de Lewis homogène, $AlCl_3$. Ce processus est favorisé lorsque le réactif est halogéné, dans le cas d'un alcool, un acide de Brønsted sera plus efficace car il protonera la fonction alcool pour donner de l'eau. Bien entendu afin de pouvoir activer la fonction alcool, l'acide doit être très fort pour passer le gap d'énergie de l'alcool à l'eau. Généralement les procédés industriels sont basés sur l'utilisation d'une catalyse homogène, bien que très efficace, la sélectivité de ce type de réaction n'est pas très élevée.

- Basique

Dans ce processus, l'intermédiaire de réaction est un carbanion. Les catalyseurs utilisés sont généralement des alcalins ou des donneurs d'hydrure. Un mécanisme à été proposé par Pines et al en 1955[103]

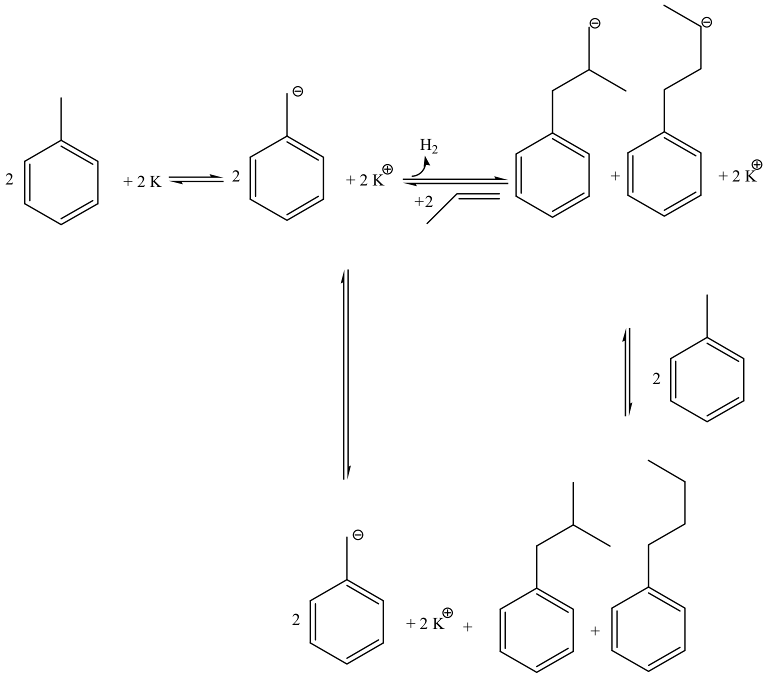

Figure 14 : Mécanisme d'alkylation basique du toluène avec le propylène.

Dans ce mécanisme, la fixation du groupement carboné s'effectue préférentiellement au bout de la chaîne alkyl contrairement à la catalyse acide où le réactif se greffe sur le noyau. De ce fait, lorsque la réaction s'effectue par un mécanisme basique, le site d'alkylation s'effectue dans la zone la moins encombrée. Malgré le fait que cette approche ouvre de nouvelle perspective d'alkylation elle n'est toujours pas industrialisée.

- Oxydation

Les alkylations utilisant la voie redox ont vu le jour suite à des études effectuées pour changer les catalyseurs homogènes en hétérogènes. Comme exemple on peut donner les travaux effectués par Figueras et al[104, 105]. Ils ont mis en évidence l'activité oxydante d'argile mésoporeux à base de différents cations métallique sur l'alkylation du benzène sur le chlorobenzène. Après avoir effectué une série de tests avec différents substituants, ces derniers ont pu proposer le mécanisme suivant :

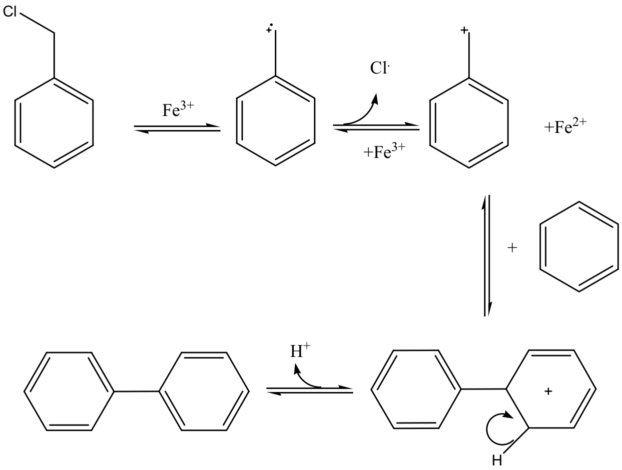

Figure 15 : Mécanisme d'oxydoréduction

Du C_7H_7Cl avec C_6H_6 à l'aide d'une argile à base de Fe.

Avec :

$$Fe^{2+} + Cl^{\bullet} \longrightarrow Fe^{3+} + Cl^{-}$$
$$Cl^{-} + H^{+} \longrightarrow HCl$$

Équation 5 : Equations terminales

Plusieurs cations ont été testés, Fe, Zn, Cu, Ce, Zr, Ti, Cr. Toutes ces glaises ont montré des activités catalytiques à 293K avec des conversions de 100% au bout de 5min pour les composés à base de Fe et Zn. En revanche si la sélectivité est proche de 100% pour des ratios Benzène : agent alkylant important, elle diminue lorsque la concentration d'agent alkylant augmente.

- Radicalaire

La réaction d'alkylation par cette technique est la plus récente. Elle voit son intérêt augmenter avec celui de l'écologie. En effet, le principal intérêt de ce mécanisme est sa tolérance pour l'eau[98]. De ce fait, 3 avantages ressortent de cette application, i) la réaction fonctionne sans solvant ou composé néfaste pour l'environnement, ii) la mise en œuvre du procédé en est d'autant plus simplifiée et iii) l'utilisation d'aucune molécule néfaste pour l'homme lors du procédé permet à celui-ci d'être utilisé dans la synthèse de médicament. Un exemple de mécanisme a été proposé sur une oléfine par le groupe de Dondi et al.

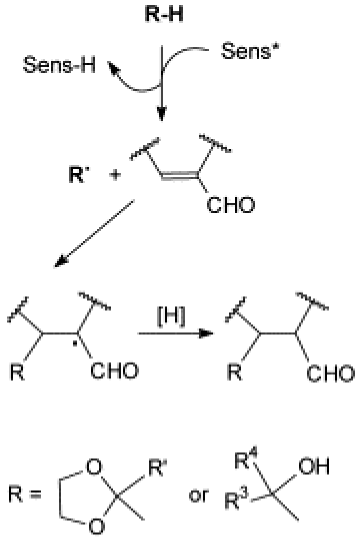

Figure 16 : Mécanisme radicalaire sur une oléfine

Généralement le précurseur radicalaire est obtenu par 'photo-activation' sur une oléfine, cette technique possède de bon rendement sur les réactions de crotonisation quels que soient les subsistants des réactifs utilisés.

1.4.4. Conclusion

L'alkylation est une réaction catalytique excessivement utilisée dans les différentes applications industrielles par des procédés de type catalyse homogène.. L'utilisation de ce type de catalyseur engendre 3 problèmes : i) une faible sélectivité, due à l'intermédiaire de réaction se trouvant en solution, ii) un surcoût énergétique pour distiller le catalyseur du produit et iii) un impact écologique supplémentaire provenant du retraitement des déchets. Ce sont pour ces raisons que de nombreux efforts ont été effectués pour remplacer les catalyseurs par des matériaux. Si le remplacement de ces catalyseurs a engendré une baisse dans la conversion, plusieurs groupes de chercheurs ont mis en évidence différents types de mécanisme d'alkylation permettant des additions sur de nouveaux sites, comme c'est la cas pour la catalyse basique, ou dans des conditions qui restaient encore difficiles comme l'alkylation dans l'eau par un procédé radicalaire. Mais la principale avancée vient de la mise en évidence de l'effet de la porosité sur la réaction. Ainsi une molécule ayant un diamètre du même ordre de grandeur verra son interaction, donc sa réactivité, avec le matériau augmentée. Les zéolites ont été largement utilisées comme catalyseur hétérogène avec de très bonnes réactivités pour la MFI et la BEA acide. Paradoxalement le phénomène de confinement qui provient de la porosité des zéolites engendre une limitation aux molécules plus petites que la taille de pore de ces dernières. Ce problème peut être dépassé en utilisant des composés cristallins avec des tailles de pores plus grandes. C'est pour cette dernière raison que l'utilisation des MOFs pourrait être une bonne alternative en vue d'utiliser des molécules de dimension plus importante.

1.5. Positionnement de ce travail

Au vu de la constante croissance de la demande internationale énergétique ainsi que des restrictions écologiques, notamment sur les gaz à effet de serre, de nombreux effort en recherche et développement ont été déployé afin de pallier à ces demandes. Les énergies fossiles sont, et de loin, les sources d'énergie les plus utilisées. De ces ressources, le gaz naturel est le moins polluant. En revanche la composition des différents champs rend très compliqué le traitement du GN. En effet, selon la composition du champ, les méthodes de traitement sont différentes. Il en résulte que les champs trop petits ou trop pollués étaient abandonnés car pas rentable. C'est dans ce contexte que le procédé PSA s'est développé afin d'homogénéiser les méthodes de traitement du GN et de rendre rentable les plus petits champs. La limitation de ce procédé réside dans le l'obtention d'un adsorbant adapté qui permettrait d'adsorber préférentiellement un gaz spécifique dans un mélange gazeux sans avoir besoin d'ajouter une énergie. Une partie du travail effectuée sera donc de trouver un adsorbant qui permettra d'adsorber spécifiquement le CO_2 dans le GN. Des spécifications minimales sur les performances d'adsorbants potentiels ont été identifiées dans le cadre de TopCombi Ces spécifications sont récapitulées dans le tableau suivant.

Tableau 5 : Objective, donné par ENI, de CA, Sélectivité et de désorption à T=30°C sur le CO_2 pour qu'un adsorbant soit économiquement viable.

T=30°C	Objectif
Capacité d'adsorption (5bar) [cm^3(STP).g^{-1}]	50
Sélectivité (ratio molaire CO_2/CH_4) (5 bar)	3
Désorption 5 →1 bar [w%]	50

En plus de ces critères le composé doit avoir un coût faible et une stabilité thermique et mécanique suffisante. Pour atteindre ces objectifs, le matériau doit posséder une taille de pore du même ordre de grandeur que le CO_2 avec un grand volume poreux. Actuellement, il existe plusieurs familles de matériaux possédant ces caractéristiques. Néanmoins, si certaines familles, comme les zéolites, possèdent des caractéristiques très proches de celles cherchées leurs limitations résident dans leurs faibles volumes poreux. Depuis une dizaine d'année, une nouvelle famille de composé cristalline a vue le jour, les MOFs. Ces composés semblent être d'excellent candidat pour la séparation des gaz par le procédé PSA. En effet, due à leurs grands volumes poreux, certains MOFs possèdent une capacité d'adsorption bien supérieure à celle des autres adsorbants. C'est pour ces raisons que nous avons choisie de se focaliser sur l'obtention d'un MOF comme adsorbant.

En parallèle de ces travaux et au vu de la diversité des MOFs obtenues, une étude sur le potentiel catalytique des MOFs a été effectuée sur l'alkylation de composé aromatique. Cette réaction a été choisie car, en plus d'être fortement utilisé dans l'industrie, elle a la particularité de pouvoir fonctionner selon différents mécanismes, que se soit acide, basique, radicalaire ou par oxydation. Dans cette partie, nous nous sommes limités à l'étude du caractère acide des MOFs que se soit d'un point de vu de Lewis ou Brønsted et du potentiel d'encapsulation de site actif dans les MOFs.

2. Chapter II: Development and validation of a combinatorial screening method

2.1. Introduction

At the start of the TOPCOMBI project (2005), very little was known about synthesis mechanisms and protocols for industrial production of MOFs. At that time, most MOF protocols were developed to obtain single crystals in order to determine the new MOF structures. The synthesis kinetics therefore has to be very slow for large crystals to be obtained. The syntheses are carried out in a batch reactor with diluted reactants under soft conditions; this allows the single crystal form to be promoted. When single crystals larger than 100x100x100 microns are obtained, it is quite easy to determine the full structure by using state of the art X-ray diffraction techniques. On the other hand, this approach possesses several limitations. First of all, homogeneity is a concern, since for a given set of batch reaction conditions, a number of single crystals are obtained, but only one of them is characterized and it cannot be certain that the entire crystal is equivalent. Also, with the reaction taking place under diluted conditions, the very small amount of MOF obtained (a few milligrams) greatly complicates the study of the MOF's potential for reaction or adsorption. Finally, the reaction time and poor yields present challenges, with most syntheses needing several hours, and sometimes several days, to be completed. These limitations complicate the use of MOFs for any application.

For these reasons, new approaches to the synthesis of MOFs have to be developed. The main objective of this work is to develop synthesis protocols that can produce homogeneous batches of MOF on the gram scale and that can easily be upscaled to the industrial level for mass production. Moreover, the majority of MOFs are synthesized by using toxic solvents, which can pose a problem given the increasingly strict safety regulations involved. The ultimate point of this study is to determine if it is possible to substitute a toxic solvent like DMF with one that is less toxic.

To the best of our knowledge, in 2003, Huang was the first to report the synthesis of IRMOF-1 by the precipitation method using Et_3N in an organic media. More recently, detailed characterizations of precipitated IRMOF-1 were carried out, revealing non-homogeneity of phases and crystalline defects. In Chapter IV, we report our investigations regarding the characterization of precipitated IRMOF-1 and the consequences on catalysis.

In the precipitation method, the various parameters that have an impact on the crystalline phases were not reported. The setup of a HT screening method which would cover different metals and ligands with different solvents and precipitating agents would be very valuable in the perspective of identifying key parameters. In this way, we should be able to conclude whether new synthesis conditions can lead to new unknown phases and whether well-known MOFs can be obtained in various conditions that are very different from state of the art methods and conditions. An outcome of the synthesis parameter screening will be to identify possible solvent and processing operations to allow the substitution of DMF. The proof of concept for the high throughput screening methodology was carried out on two systems, namely the Cu/trimesic acid and Zn/terephthalic acid systems, which can potentially lead to the well-known HKUST-1 and IRMOF-1 phases, respectively.

2.2. Screening Parameters

2.2.1. Solvent Selection

Regardless of the preparation method, the nature of the solvent is a key parameter in the synthesis of MOFs. This is even more important for precipitation methods. An appropriate solvent has to render soluble the different reactants. The difficulty comes from the very different polarity of the reactants. Indeed, the metal precursor is generally an inorganic salt, while the ligand is an organic compound. Today, the most frequently used solvent is DMF. There are several reasons for this: i) thanks to its high dielectric characteristics, DMF dissolves the vast majority of reactants, ranging from inorganic salts to polar organic molecules; ii) its high boiling point (426 K) makes it possible to increase the solubility of reactants when solvothermal techniques are used; and iii) at high temperature, it degrades by reacting with water and nitric acid as shown in Figure 17, with the formation of diethylamide, which can act as a base.

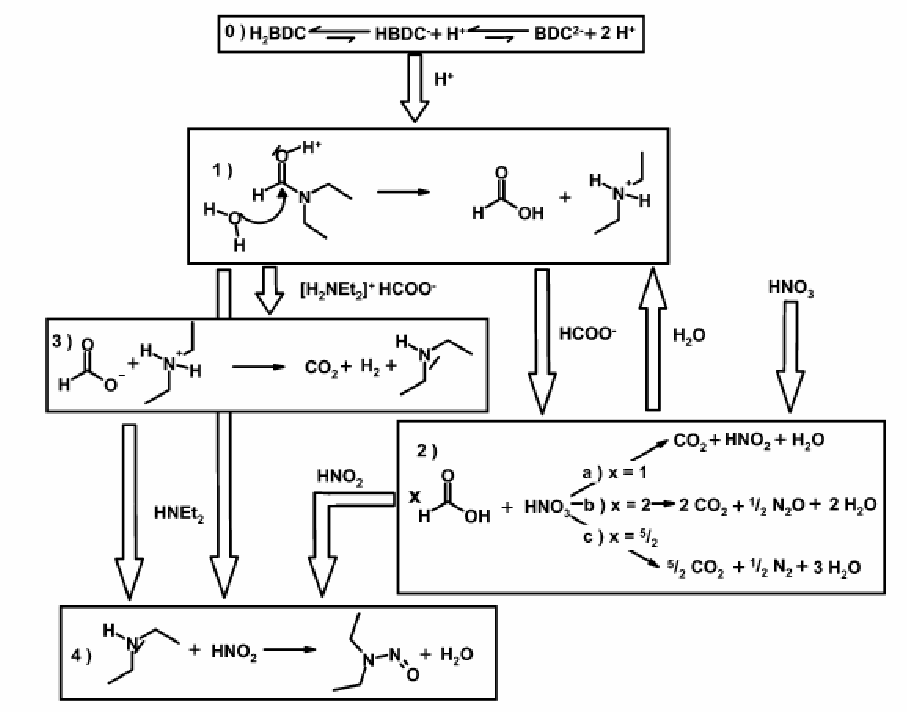

Figure 17: Postulated reaction pathways for the degradation of DMF in solvothermal conditions of IRMOF-1/MOF-69c synthesis [106].

Many different solvents could have been investigated for a screening study. Obviously, a selection of the solvent had to be carried out. From the recent work of Prof. G. Rothenberg, we can pinpoint two main criteria for classifying solvents: the properties associated with the polarity (e.g., dielectric constant) and the properties associated with the donor effect (i.e., basicity). The first will dictate to which extent the precursors can be solubilized. For solvents exhibiting high dielectric constants such as DMF or DMSO, it is expected that appropriate solubility will be observed. On the other hand, for solvents exhibiting low polarity, such as THF or ether, the solubility of salts would be too low. In this case, we have decided to perform mixtures with water in order to enable the solubilization of salts [33 34, 35].

The selected solvents are ranked with respect to their dielectric constant. Their basicity is also an important parameter, which may lead to the formation of different phases. Indeed, the more a solvent is a donor, the more it will interact with the cation in solution, thereby generating different SBUs, which in turn lead to different structures. In our case study, however, the selection of solvents according to their basicity is made difficult, since a basic agent will be added to carry out the precipitation. The solvents showing the most important donor characteristic are amine-based liquids such as Et_3N, pyridine and formamides.

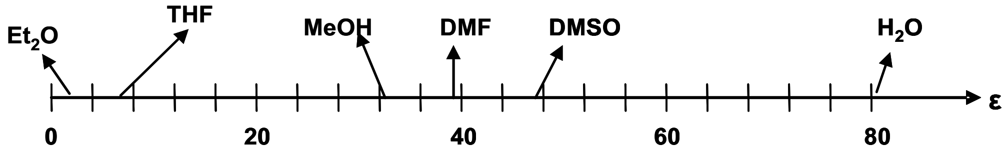

Figure 18: Dielectric constant of selected solvents.

2.2.2. Base Selection

The thermodynamics and the species involved in the reaction synthesis of IRMOF-1 (as an example) are depicted in Figure 19. The solvated cations and anions, neutral metal-organic clusters and the formed solid coexist in the reaction medium. Without the addition of a base, the kinetics is usually slow, which is a key advantage for obtaining monocrystals. By adding concentrated aqueous acid solution onto IRMOF-1, the solid is completely dissolved. This method is commonly used in the context of liquid NMR to characterize organic molecules that can be entrapped or grafted into MOF networks [107]. In contrast, the equilibrium of the reaction is, in principle, shifted to the formation of the solid when a base is added to the reaction mixture. As said above, when DMF is used in solvothermal conditions, basic agents are generated *in situ* over the course of the reaction, which should therefore lead to higher yield and faster kinetics.

Figure 19: Shift of the reaction equilibrium by addition of a base to trap the formation of liberated acid.

At low temperature and regardless of the solvent, a precipitated agent can be added to the reaction mixture to drive the synthesis to the solid in yield and kinetics. Many basic agents can be used in theory. How can we proceed to select a diverse set of basic agents that would cover most of the possibilities? According to the diagram in Figure 19, the stronger the base is, the more shifted the equilibrium shall be.

Therefore, we have chosen as our main selection criterion the pKa of the corresponding bases. The selected bases are shown, in Figure 20, on the pKa scale. Another parameter which can be important is the “donor” (i.e., complexing) character of the bases. Indeed, pyridine and histidine are known to form organometallic complexes and therefore can compete with the carboxylate ligand to chelate the cations. Finally, we have chosen 2,6-di-tert-butylpyridine because of the steric hindrance provided by the bulky groups.

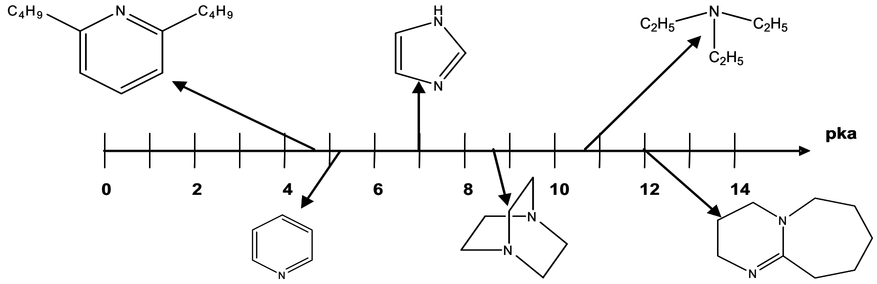

Figure 20: pKa of bases employed.

2.3. Protocol for Combinatorial Screening

By varying the strength, i.e., the kinetics, of the reaction, and the possible competition of amines with the cations, novel phases can be expected. Obviously, the solvent will also play a different role depending on the bases, and interactions that are difficult to anticipate can be expected. The combination of various solvents and amines should therefore lead to a greater diversity of synthesis conditions that may accelerate the discovery of new solids or new conditions to prepare known MOFs.

To answer this question, two screenings were made on already known and characterized MOFs: HKUST-1 and IRMOF-1. We chose these materials because they are state of the art MOFs that are very well described in the literature.

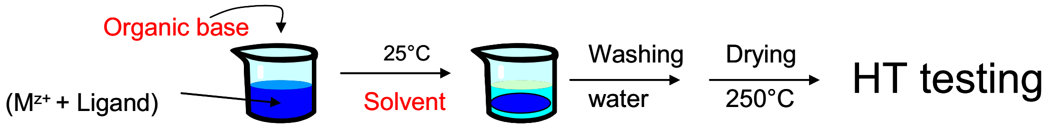

Figure 21: Screening protocol used on different systems.

The screening involves a systematic variation of the solvent and base. For example, the typical procedure for the Cu-BTC system is to mix 0.52 mmol of $Cu(NO_3)_2{\cdot}5H_20$ (Riedel-de Haën, pure) with 0.48 mmol of H_3BTC (benzene 1,3,5-tricarboxylic acid, Aldrich, 95%) in the same solvent at room temperature. Next, 1.4 mmol of base are added dropwise. The powder obtained is separated by centrifugation. Then, the MOF is washed with water and dried for 12 h at 170°C. The water is used to be sure that the MOF is not water-soluble and is therefore appropriate for use in an industrial process. A different washing protocol was used for the Zn-TT system, for which DMF was used. Indeed, we found that IRMOF-1 is very moisture-sensitive (see Chapter IV). More recently, this was reported in several studies[108].

In practice, mother solutions of the nitrates and ligands dissolved in the different solvents are prepared, as are mother solutions of the bases. Then, the combinatorial synthesis can proceed by adding the base to the solution under stirring. Six bases and four solvents were selected for the Cu-BTC system, while four bases and seven solvents were selected for the Zn-TT system. The entire screening represents 24 experiments for Cu-BTC and 28 for Zn-TT.

Cu-BTC

	DMF	DMSO	MeOH	THF - H_2O
dibutylpyridine				
Pyridine				
Imidazol				
DABCO				
Et_3N				
DBU				

Zn-TT

	DMF	DMF - H_2O	DMF - EtOH	DMSO	DMSO - H_2O	DMSO - EtOH	THF - H_2O
DBU							
Et_3N							
DABCO							
Pyridine							

Figure 22: Matrices of the two screening systems.

2.4. Results

2.4.1. Characterization Setup

X-ray diffraction (XRD) patterns were recorded on a Bruker D5005 apparatus. The N_2 adsorption/desorption isotherms were measured on an ASAP 2010M machine from Micromeritics. The specific surface area was determined by the BET method, the pore volume by t-plot analysis, and the pore diameter by DFT. The samples were further characterized by TG/TD analysis with a Setaram - Type Setsys Evolution 12 setup. Inductively Coupled Plasma (ICP) emission spectrometry was used for the analysis of the bulk chemical composition of the samples. DRIFT analysis was carried out on a Nicolet Magna 550 equipped with an MCT detector. The samples were loaded in a DRIFT Spectratech cell equipped with ZnSe windows.

- Adsorption Study at High Pressure

The determination of the adsorption capacity of the different initial MOFs has to be carried out at high pressure in order to study the capacity of the material in conditions resembling those of the process. With this in mind, we used the BELSORP-HP^{TM}. This setup permits an accurate determination of the adsorbed gas on around 100 mg of sample, at high pressure, up to 30 bars for the temperature range 50 - 400°C.

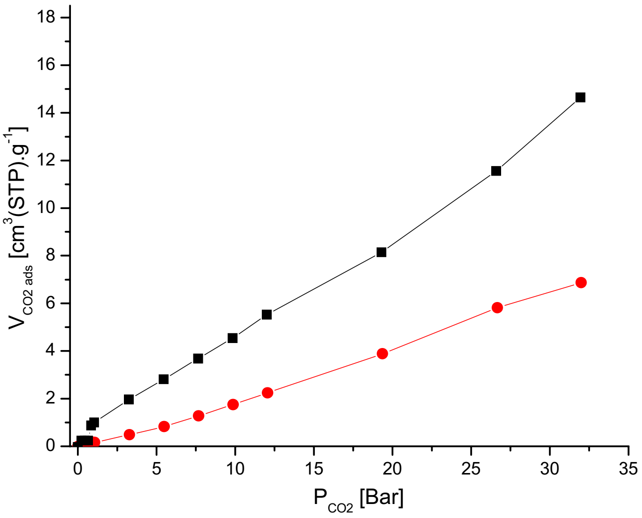

Figure 23: CO_2 adsorption on Ce(BTC) at 303 K for different equilibrium times: 7200 s (black squares) and 1800 s (red circles).

The main advantage of this setup is the possibility of modifying the equilibrium time of each adsorption point. Figure 23 shows two experiments of CO_2 adsorption on Ce(BTC) with different equilibrium times. Thanks to this figure, we can see the importance of this parameter and determine the real adsorption capacity of a material, without disturbances linked to diffusion.

2.4.2. Cu-BTC System

2.4.2.1. XRD Study

Two different phases are obtained by the screening carried out on the Cu-BTC system. The imidazole-THF/H_2O system leads to an intense blue powder with an XRD pattern which has not been reported so far, to the best of our knowledge. The second phase is obtained for eleven different conditions and has been shown through characterization to be HKUST-1, as discovered by Chui et al. [109].

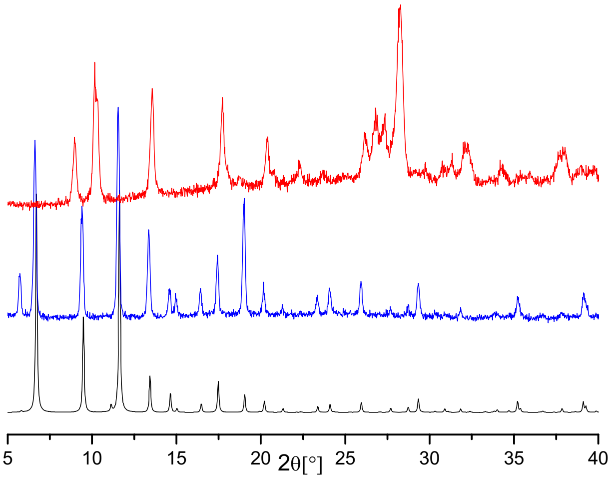

Figure 24: XRD patterns from the imidazole-THF/H_2O system (top), HKUST-1 XRD patterns obtained with the pyridine – DMF system (middle), theoretical pattern for HKUST-1 [109] (bottom).

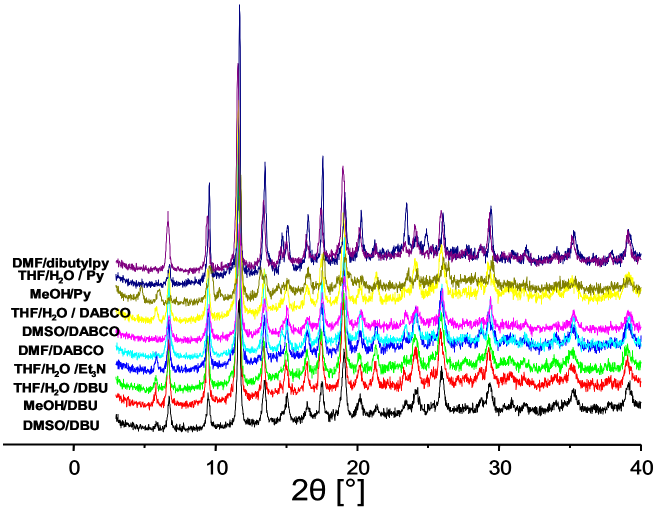

Figure 25: The entire set of HKUST-1 XRD patterns obtained from the screening.

These results make it possible to compare the diffractograms obtained with those in the literature and show the importance of the solvent and base used. As shown in Figure 24, even if the solution is homogenous and possesses the same concentration, the phase obtained depends on the solvent and the base. Figure 25 confirms the importance of the parameters. According to the XRD patterns, several phases possess amorphous parts, but in the case of the DMF-pyridine system, HKUST-1 is obtained with no amorphous part.

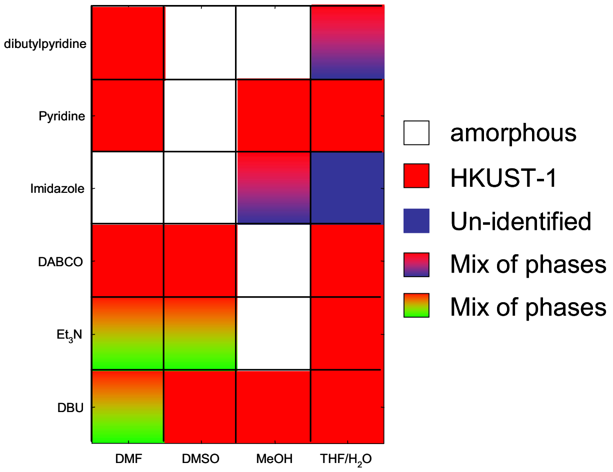

Figure 26: Screening results for the Cu-BTC system.

To resume the situation, we obtain HKUST-1 eleven times. One unidentified phase appears with the imidazole-THF/H_2O system, and seven materials are amorphous. Five times we obtain a mix of phases: twice there is a mix of HKUST-1 and the previously mentioned unidentified phase, and three times there is a mix of HKUST-1 and another unidentified phase. The HKUST-1 can be obtained in all solvents but DMF, and THF/H_2O appears to be the best choice. DBU, DABCO and pyridine appear to be the most efficient bases.

2.4.2.2. Characterization of the porous structure

The porosity analysis was carried out with the ASAP 2010 apparatus with N_2 adsorption at 77 K. Four samples were tested, namely the unknown phase and three different HKUST-1. Two HKUST-1 originated from the screening (pyridine-DMF and Et_3N-H_2O/THF systems) and the last one was obtained via the Max Planck Institute (MPI) protocol [110]. The unknown phase is not porous.

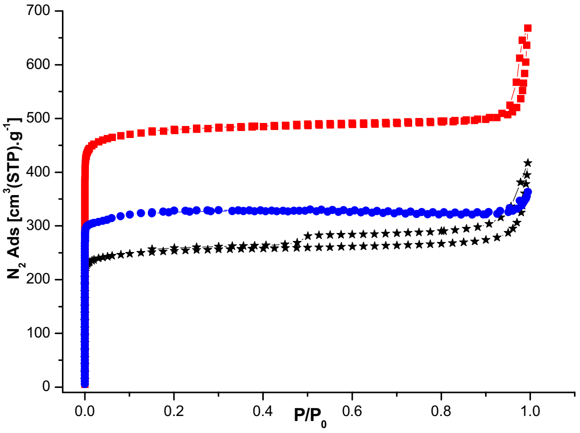

Figure 27: N_2 isotherms at 77 K on HKUST-1: pyridine-DMF (red, square), Et_3N-H_2O/THF (blue, circle) and MPI (black, star).

The materials were activated at 200°C during 10 h. Type I isotherms are obtained for all samples. The specific surface area is comprised between 1506 and 900 m².g^{-1} and the porous volume between 0.8 and 0.3 cm^3.g^{-1}. These results are in good agreement with those found by Huang et al. [48]. The variation in the porosity can be correlated with the XRD analysis. Indeed, the high specific surface area corresponds to the material obtained with no amorphous part. The determination of the pore size is carried out on the Et_3N-H_2O/THF HKUST-1.

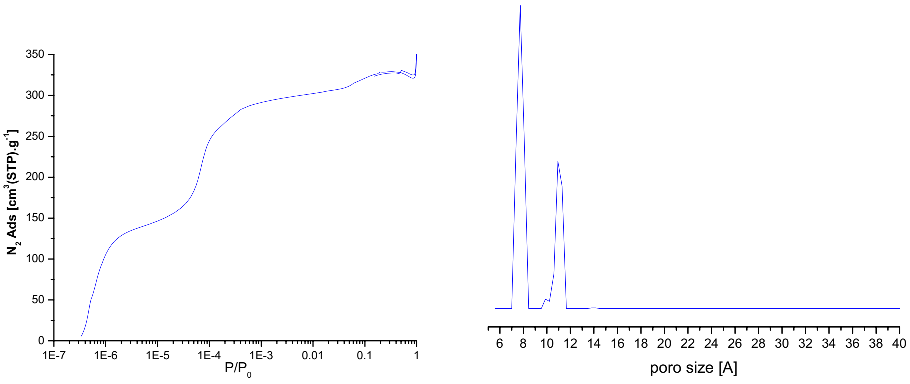

Figure 28: N_2 isotherms at 77 K on HKUST-1 (d) (left), pore size distribution for HKUST-1 (d) (right).

As shown in Figure 28, there are only two pore sizes in this structure, around 8 and 11 Å. This result is in good agreement with the works of Chui et al. [109].

2.4.2.3. TDA-TGA

The thermal stability under air was examined using a Setaram setup.

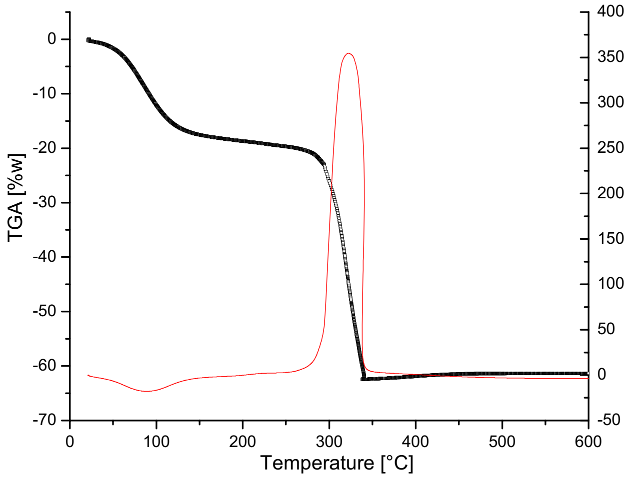

Figure 29: TG/TD analysis on HKUST-1.

The analysis was carried out on the HKUST-1 obtained with the pyridine-DMF system. The material shows dehydration at 100°C, with 17% water loss and thermal stability below 300°C, as reported by P. Chowdhury et al. [111]. This result correlated with the carbon balance makes it possible to confirm the high purity of the crystalline phase.

In conclusion, HKUST-1 has been obtained eleven times with different base-solvent systems using the precipitation method. The reactions take place rapidly even if the purity of the different syntheses varies. In no case can we correlate the parameters chosen with the HKUST-1 phase obtained. The best crystalline phase is obtained with the pyridine-DMF system. In this case, the porosity analysis gives S_{BET}=1506m².g^{-1} and V_{porous}=0.8 cm^3.g^{-1}. According to the evidence of the characterization results, this HKUST-1 is chosen for the CO_2 adsorption test.

2.4.3. Zn-TT System

2.4.3.1. XRD Study

In order to continue to validate the precipitation method, we extended the Cu-BTC system to another reference MOF: IRMOF-1, also called IRMOF-1. After a rapid overview of the state of the art on the Zn-TT system, it appears that several different phases exist for this system. Nevertheless, the majority of these syntheses are carried out by autoclave and there are only a few precipitation studies. As described above, 28 experiments are carried out. We found that: i) no reaction proceeds with pyridine and $THF-H_2O$ regardless of the parameters used; and ii) in agreement with the work of Huang et al. [48], IRMOF-1 is obtained when DMF is used with DABCO or Et_3N. We cannot correlate the other phases with those already known [48, 108, 112, 113].

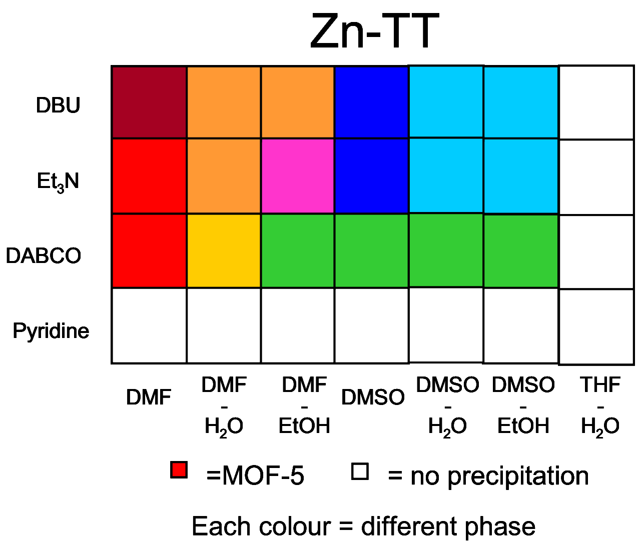

Figure 30: Screening results for the Zn-TT system.

As expected, the majority of the experiments lead to a crystalline phase. When DMF and Et_3N are used, the precipitate can be correlated with the IRMOF-1 phase as pointed out by Huang et al. [48].

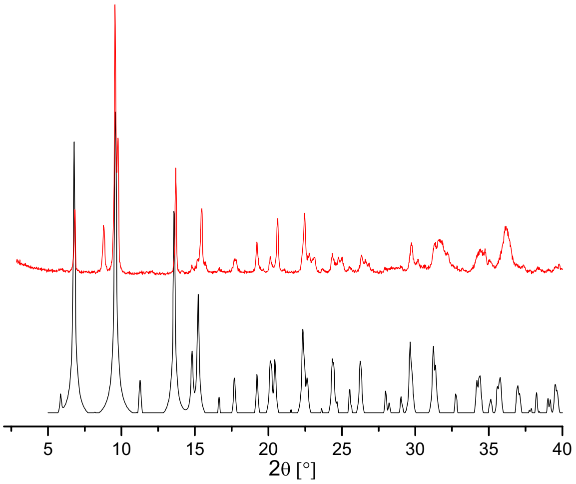

Figure 31: XRD pattern of the IRMOF-1 obtained by the screening (red, top) compared with literature data (black, bottom) for IRMOF-1 [48].

As can be seen, there is a good correlation between the simulation and the experiment. This synthesis is reproducible and the characterization, described later, possesses a high correlation with the literature.

For the other materials, the characterization is a little bit more complicated. Indeed, the syntheses give several phases that cannot be correlated with the literature despite the presence of several peaks in common with the work of Wright [108]. For these syntheses, the materials are formed by different coordinations of Zn^{2+}, TT^{2-}, H_2O and the solvent used, for example: $[Zn_3(TT)_3(H_2O)_3]\cdot 4DMF$, $[Zn(TT)(H_2O)]\cdot DMF$, $[Zn(TT)]\cdot DMF$, $Zn(TT)(H_2O)$, $Zn(TT)(H_2O)_2$ and $[Zn_3(TT)_3]\cdot 6CH_3OH$. These kinds of materials are very sensitive to the hydrogen bond, mainly with water and solvent, and after several months the structure can change. It follows that the determination of unknown structures is considerably complicated by this phenomenon. The strong changeability of these kinds of materials could be attributed to the form of the cluster, $Zn_4O(TT)$ or $Zn(TT)$ and the solvent used. Nevertheless, we already know that the precipitation approach makes it possible to find different new structures even if we cannot determine what they are because we obtain the MOF in the form of powder. Moreover, these kinds of materials are very sensitive to humidity and cannot be used for any application with the GN. Consequently, this system is abandoned even if it permits the discovery of new MOF phases.

2.5. Conclusion

We have shown that it is possible to prepare known MOFs by precipitation at room temperature. We have also demonstrated that combinatorial screening by varying the nature of the solvent and base is very efficient for discovering novel synthesis conditions. This HT screening can be a very valuable method for finding conditions allowing the replacement of toxic solvents such as DMF. We have shown that HKUST-1 can be prepared at room temperature in a mixture of green solvents with quantitative yield. This novel synthesis procedure can certainly be developed in a continuous process to produce large amounts of HKUST-1 with high homogeneity. We have also seen that the diversity of the experimental conditions is a driving force to discover new phases. The precipitation methods, however, yield microcrystalline powders which are difficult to investigate for structural resolution when XRD patterns are not trivial.

3. Chapter III: $\Delta H_{\theta \to 0}$ determination of different MOFs

3.1. Introduction

Today, there are only a few articles dealing with the determination of the heat of adsorption and the diffusivity of several gases for MOFs. This situation may find its origin in two reasons: i) lack of knowledge of the new materials and ii) lack of reference allowing comparison of results. This kind of information is, however, very important to acquire in view of using the materials for any application. With this in mind, this section deals with the validation of the screening determination of heat of adsorption of seven gases on three MOFs by three methods: TAP, gravimetric analysis and simulation. All of these results are then systematically compared.

3.2. Selection of Adsorbents

3.2.1. HKUST-1

HKUST-1, or $Cu_3(BTC)_2.3H_2O$, is a binuclear Cu_2 paddlewheel [109]. Three types of bond come from the cluster. The cations are interconnected. Two water molecules are coordinated on the cluster and can be removed very easily by heating. The Lewis centres created are accessible. The clusters are interconnected by a BTC^{3+} ligand.

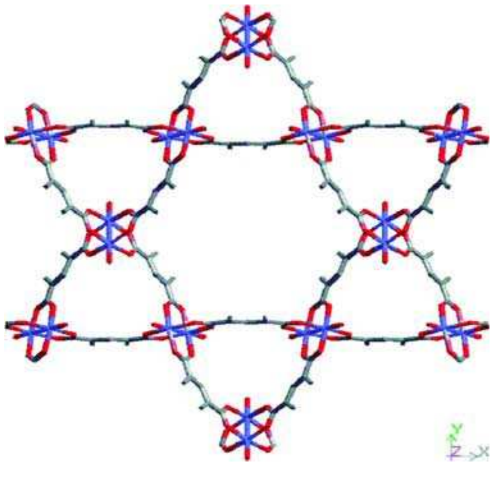

Figure 32: Crystalline structure of HKUST-1 [111].

As shown in Figure 32, there are two types of cavities and pore sizes. The large cages (13.2 and 11.1 Å in diameter) are interconnected by 9 Å windows of square cross-section. They are also connected to tetrahedral-shaped side pockets of roughly 6 Å through triangular-shaped windows of about 4.6 Å (3.5 Å in the hydrated form).

3.2.2. IRMOFs

IRMOF-1, also called IRMOF-1, is composed of Zn_4O tetranuclear clusters connected by benzene-1,4-dicarboxylate ligands (TT), to generate a cubic framework (Figure 33).

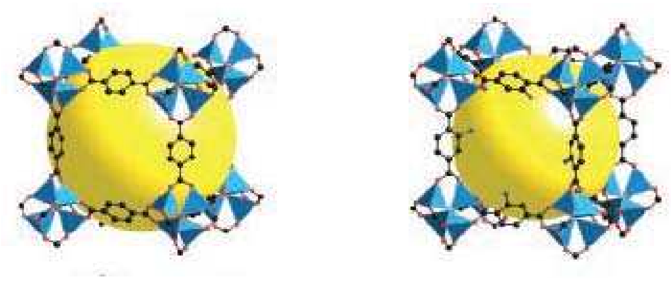

Figure 33: Representation of IRMOF-1(left) and IRMOF-3 (right).

The cage size is around 15 Å and the pore opening equal to 7.5 Å. The only difference between IRMOF-1 and IRMOF-3 comes from the ligand. Indeed, as shown in Figure 33, an amino group is added to the terephthalic acid in the case of IRMOF-3. The reason why we chose these materials is the “functionalization” capacity of IRMOFs. As a matter of fact, one way to theoretically increase the adsorption capacity of the MOF is to add a polar group like $–NH_2$ onto the structure, as here on the ligand. The aims of this part of the study are to determine the real influence of the polarity enhancement and to prove that is possible to find an accurate way to evaluate the heat of adsorption of unknown materials.

In this study, heats of adsorption at very low coverage of Kr, Xe, N_2, CH_4, CO_2, n-C_4H_{10} and i-C_4H_{10} are reported for HKUST-1, IRMOF-1 and IRMOF-3.

3.2.3. Synthesis and Characterization

The protocol used for HKUST-1 is the same as for the screening method, with DMF as solvent and pyridine as base. The specific surface area is around 1500 $m^2.g^{-1}$ for 0.8 $cm^3.g^{-1}$ of pore volume. The IRMOFs are obtained by the solvothermal method described by Mueller [56]. In brief, benzene-1,4-dicarboxylic acid (H_2BDC, Aldrich, 2.5 g, 15 mmol) and $Zn(NO_3)_2 \bullet 4H_2O$ (Merck, Pro Analysis, 5.8 g, 20 mmol) are dissolved in 500 ml of DMF (Aldrich, anhydrous). The solution is heated at reflux for 18 h. The resulting white precipitate is filtered under inert atmosphere at room temperature and washed three times with DMF. The samples were kept under inert atmosphere. Samples were characterized by XRD, ^1H and ^{13}C NMR, IR, and N_2 physisorption at 77 K. The BET specific surface areas are 1100 and 630 m^2g^{-1}, for IRMOF-1 and IRMOF-3, respectively.

3.3. Kinetic Setup

3.3.1. TAP Reactor

The Temporal Analysis of Products (TAP) reactor is a kinetic setup that makes it possible to determine the thermodynamic constant of various materials onto different gases. The calculation of these data is possible following the measurements of the mean residence times of gas phase species. The accuracy of the thermodynamic constant depends on the sensitivity of this measurement.

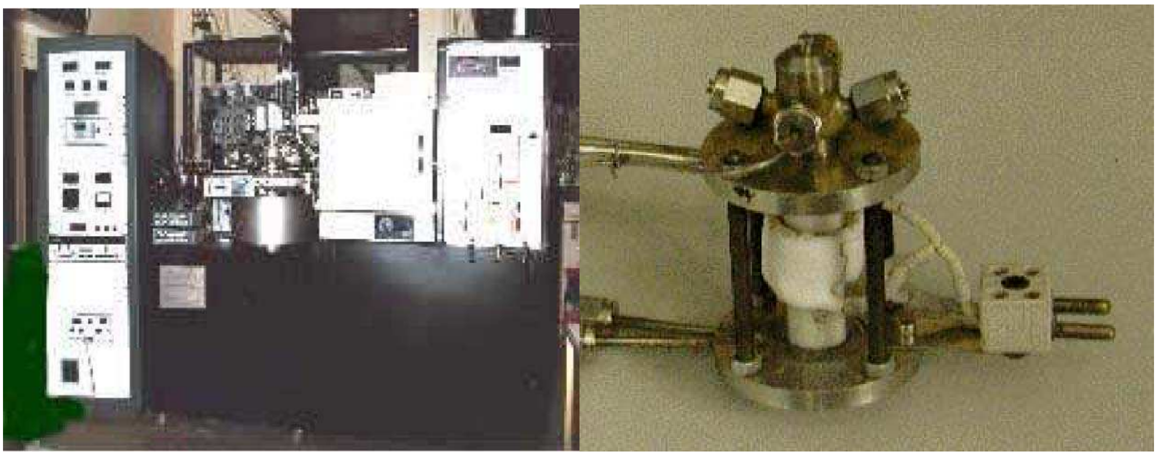

Figure 34: Picture of the TAP-2 reactor (left) and the microreactor (right).

The TAP system, as shown in Figure 34, is composed of a valve-manifold assembly, an ultra-high vacuum system, a quadrupole mass spectrometer (QMS), a microreactor and a gas blending station. The valve-manifold assembly allows the injection onto the catalyst of a perfectly known pulse of a gas mixture (a few nanomoles) at high frequency, typically between 250 and 500 µs. The vacuum system decreases the pressure down to the range of 10^{-8} Torr. Since this setup has to allow the determination of the heat of adsorption at low coverage, the experiment is carried out in the Knudsen regime. Here, the detector is a QMS. To permit the study of the transition state, the detector is positioned at around 1 cm from the microreactor. The microreactor is a stainless steel fixed-bed reactor. It can be heated to around 700°C +/- 1°C. Typically, the catalyst loading is between 100 and 300 mg. Meanwhile, the gas blending station is used for preparing accurate gas mixtures and producing constant gas flows. The principal difference between the TAP reactor and other kinetic setups comes from the pulse response experiment, with a narrow, perfectly characterized pulse injected into the microreactor. This experiment takes place in the Knudsen regime. An important characteristic of this regime is the independence between the diffusivity of the individual components of a mix and the gas composition. In order to attain this regime, it is necessary to work under high vacuum. Moreover, since the disturbance created by the injection of a small number of molecules onto the fixed-bed reactor is negligible, the kinetics corresponds to the constant kinetic state of the catalyst. In view of validating the results obtained by this method, all of the results are compared with those obtained by gravimetric analysis and by grand canonical Monte Carlo simulation.

3.3.2. Gravimetric Setup

The gravimetric analysis results are obtained by a Rupprecht & Patashnick TEOM 1500 pulse mass analyzer. The data are obtained from the variation of the catalyst mass during the adsorption under gas flow. Since this process is carried out in an attempt to validate the results of the TAP screening, only the adsorption of CO_2 is studied. The TEOM analysis presents several advantages: a well-defined flow profile, eliminating possible diffusion and buoyancy phenomena; a very fast response time resolution (0.1 s); and a high mass resolution across the entire range of pressure and temperature. That said, the mechanical fragility of the setup makes this method of analysis incompatible with a screening approach. Typically, 70 mg of adsorbent sieved between 0.2 – 0.3 mm is pretreated at 550 K under He for each adsorption isotherm. During the experiment, the P_{CO2} varies from 0.2 to 133 kPa. In view of determining the heat of adsorption at low recovery, the data points obtained are fitted with the Langmuir-Hinshelwood equation. The entire set of results is also correlated with the grand canonical Monte Carlo simulation in collaboration with Northwestern University. In this study, only the simulation results, and not an explanation of the technique, are presented.

3.3.3. Modeling

The MOF particles are modeled as squared slabs with a characteristic length L_z located in the macropores of the silica-alumina matrix. These particles are considered to be symmetrical. Reversible sorption takes place at the exterior of MOF particles and is described by an equation analogous to Henry's law:

$$C_{A,z}\Big|_{z=l/2} = H'C_A \tag{1}$$

where H' is the analogous Henry coefficient (m_g^3/m_s^3), C_A is the reactant concentration (mol/m^3) and z the MOF coordinate (m). Only the adsorbed molecules diffuse into the micropores. During TAP experiments, the concentration in the reactor remains very low and therefore the diffusion in the MOF pores is assumed to be independent of the concentration and is therefore described by Fick's law. Inside the pores, first order irreversible reaction takes place on the acid sites.

The reactor is divided into three zones: two inert zones of quartz beads between which the catalyst is placed. The diffusion in all three zones is described by Knudsen diffusion. In the catalyst zone, the flux into the catalyst particles is included in the model. Actually, the MOF particles are located within a macroporous matrix. However, the diffusion into the macropores is relatively fast and can therefore be lumped into the Knudsen diffusion coefficient according to the following equation[114]:

$$D_{K,p} = \frac{D_K}{(1+(\varepsilon_p(1-\varepsilon_b))/\varepsilon_b)} \tag{2}$$

where $D_{K,}$ is the Knudsen diffusivity in the bed (m^2/s), $D_{K,p}$ the Knudsen diffusivity in the pores of the particle (m^2/s), ε_p the particle porosity (m_g^3/m_s^3) and ε_b the bed porosity (m_g^3/m_r^3). This leads to the following continuity equation for the catalyst zone:

$$\varepsilon_b \frac{\partial\, C_A}{\partial\, t} = D_{K,p} \frac{\partial^2 C_A}{\delta\, x^2} - (1-\varepsilon_b) a_z J_{A,z} \tag{3}$$

where t is the time (s), x the reactor coordinate (m), a_z is the MOF surface area per volume (m^2/m^3) and $J_{A,z}$ (mol/m^2 s) is the molar flux into the MOF as given by equation 3:

$$J_{A,z} = D_{z,eff} \frac{\partial^2 C_{A,z}}{\partial\, z^2} \tag{4}$$

where $D_{z,eff}$ is the effective Knudsen diffusivity (m^2/s) in the MOF.

Parameter estimation was performed by fitting the entire simulated response curve to the experimental one in the time domain. For each curve, the sum of the squared deviations over 400 data points was used as the objective function which was minimized using an algorithm based on Marquardt's method[115]. Diffusion and sorption parameters were determined simultaneously by matching the simulated response curves of the hydrocarbons to the experimentally obtained ones at low temperatures between 523 and 673 K where no reaction takes place. The kinetic parameters were estimated from the response curves at temperatures from 773 to 923 K, fixing the diffusion and sorption parameters at the values determined at low temperatures. For the regression analysis, a reparameterized form of the Arrhenius and Van 't Hoff equations was used. A full statistical analysis, which included the calculation of the 95% confidence intervals on the estimated parameters, was performed after regression.

3.4. Results

Figure 35 shows a TAP example of Xe adsorption on IRMOF-1.

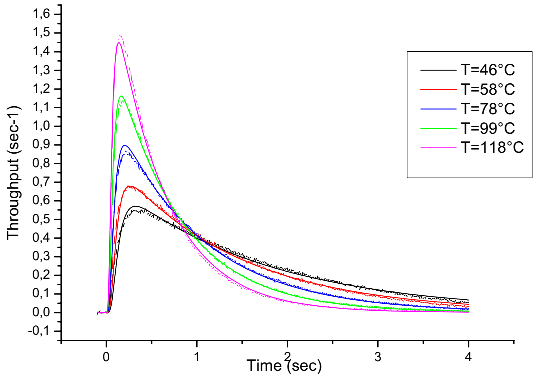

Figure 35 : TAP-2 experimental data (solid) and modelling (dashes) for Xe pulses on IRMOF-1 at various temperatures.

After normalization, there is clearly a strong correlation between experimental data (solid line) and modelling (dashed line) at different temperatures. As expected, molecular diffusion increases with temperature. The different heats of adsorption are determined by modelling the transient signals. The heats of adsorption measured experimentally for various gases on IRMOF-1, IRMOF-3 and HKUST-1 are reported in Figure 5.

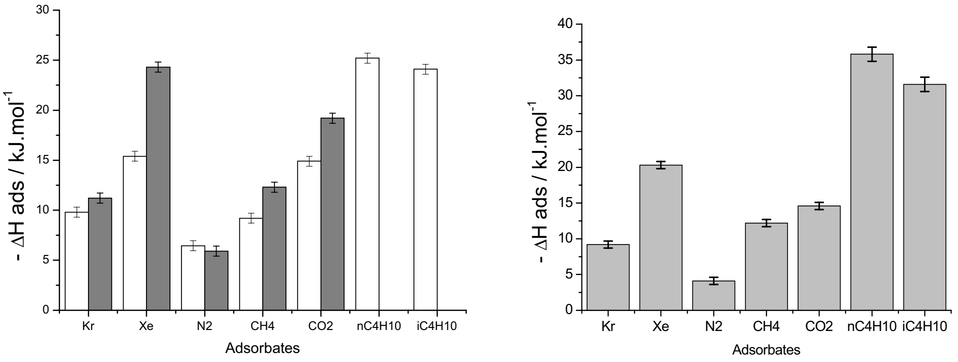

Figure 36: Heats of adsorption at very low coverage measured by TAP-2 experiments (left) on IRMOF-1 (white) and IRMOF-3 (gray). Polarizability (Å^3) values of the gases are: N_2 (1.47), Kr (2.8), CH_4 (2.6), CO_2 (2.91) and Xe (4.04) from Lide D. R. [116]. Heats of adsorption at very low coverage measured by TAP-2 experiments on HKUST-1(right).

Heats of adsorption have rarely been reported in the literature for MOFs. Two studies reported different values for ^{129}Xe adsorption on IRMOFs. Ooms et al. [117] found the heat of adsorption of ^{129}Xe on IRMOF-1 to be - ΔH=12 kj.mol^{-1}, which is in good agreement with the results obtained by the three techniques used here (gravimetric analysis, TAP and simulation). On the other hand, Pawsey et al. [118] reported values around 5-6 kJ.mol^{-1}. The difference between these ΔH could come from the state of the IRMOFs, as these structures are very sensitive to humidity. IRMOF-1 can be hydrated into MOF-69c. In the study carried out by Pawsey et al., IRMOF-1 is kept in a glove box. Even though Ooms et al. used the same protocol in other aspects, their sample was not kept in a glove box, which could have led to its having a higher degree of hydration, and therefore increased framework polarity and higher ΔH. Moreover, the heat of adsorption of the classic nonpolar adsorbents, such as carbon-based materials, is in the range of 15-20 kJ.mol^{-1}. Figure 35 shows the heat of adsorption of ^{129}Xe on IRMOFs. This experiment clearly shows the influence of the addition of amino groups onto the MOF. As indicated by Millward et al. [119], the presence of amino groups usually increases the heat of adsorption. This increase can be correlated with the polarizability of the molecule. Indeed, the interaction with a polar group increases the affinity. The ΔH of different gases on HKUST-1 is represented in Figure 36. One of the main results obtained is the enhancement of the difference in heat of adsorption between CO_2 and CH_4 with IRMOF-1 and IRMOF-3 (the latter structure has added amino groups that favour this enhancement) by this way, it is possible to enhance the separation factor of the CO_2/CH_4 mix. In the case of HKUST-1, for Krungleviciute et al. [120] and Wang et al. [48], isosteric sorption enthalpies decrease sharply with loading. Values of 14.0 and 35 kJ.mol^{-1} are measured at the lowest coverage for Ar and CO_2, respectively. Our measurements for CO_2 differ significantly for HKUST-1. Finsy et al. have reported 50 kJ.mol^{-1} for n-butane [121].

Figure 37 represents CO_2 adsorption on HKUST-1 and IRMOF-3 using TEOMS analysis.

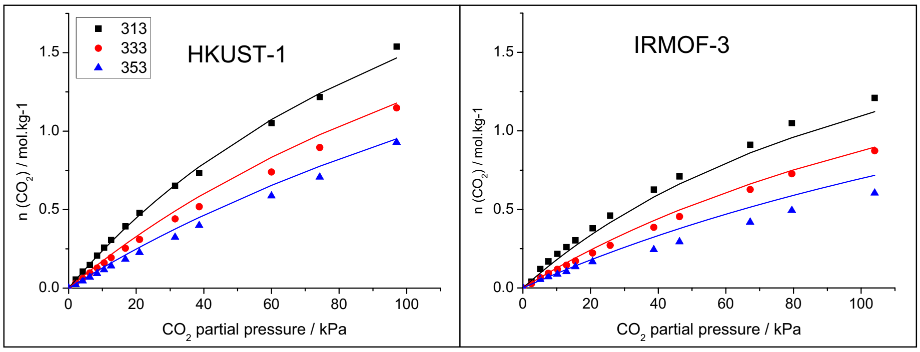

Figure 37: CO_2 adsorption isotherms obtained by gravimetric measurements (dots) and simulated data (line) of HKUST-1 and IRMOF-3. IRMOF-1 data are not shown.

The gravimetric experiments are performed at three temperatures: 313 K, 333 K and 353 K. Here, the equilibrium state is attained for each point, which makes it possible to use the Langmuir model for the fitting. The results obtained are lower than those obtained with TAP. This is due to the measurement conditions. Indeed, the TAP data are obtained only at very low coverage without any interaction between the adsorbed molecules. This condition is not attained with the TEOMS experiment. When we correlate the ΔH obtained by the TAP method and by simulation, Figure 7 is obtained.

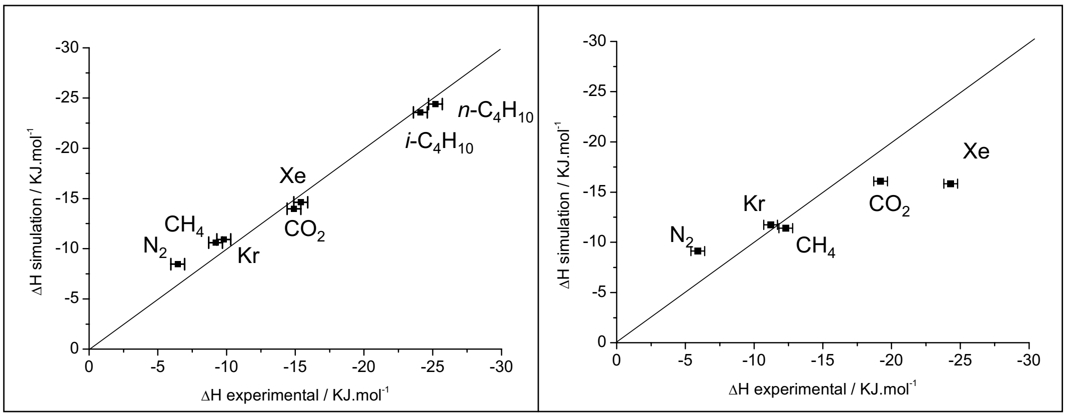

Figure 38: Comparison between low-loading adsorption enthalpies measured by TAP and calculated by Monte Carlo simulation for IRMOF-1 (left) and IRMOF-3 (right).

In Figure 38, excellent correlation is shown for all the ΔH obtained on IRMOF-1 with different gases. In the case of IRMOF-3, there is a high correlation between the experiment and the simulation for CH_4 and Kr. For the other gases, the differences in heat of adsorption are more important. In the case of HKUST-1, the lack of accessibility - or the inaccessibility - of the small pores leads to different results.

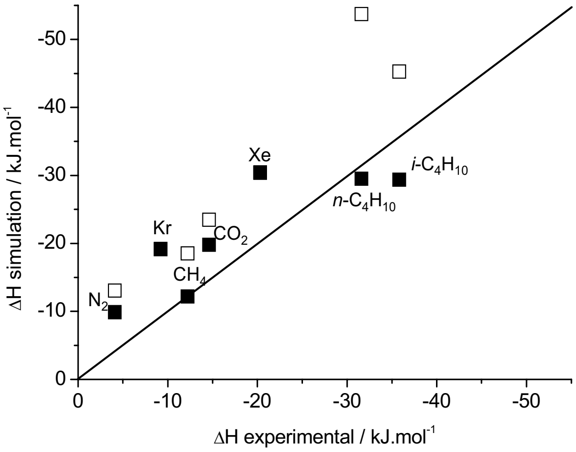

Figure 39: Comparison between ΔH measured by TAP-2 and calculated by Monte Carlo simulation for HKUST-1, with access to small pores that is limited (empty square) or nonexistent (full square).

For HKUST-1, the correlation is not as good as for the IRMOFs. One reason can be the lack of accessibility (or the inaccessibility) of the small pores. As a matter of fact, the simulation carried out when the small pores are blocked gives a better result than that conducted when the pores are free. It can be concluded from this situation that the small pores are not accessible during this experiment. The reason for this phenomenon is not yet known.

3.5. Conclusion

Heats of adsorption have been measured for a systematic set of gases for three common MOFs (IRMOF-1, IRMOF-3, and HKUST-1). In addition, molecular simulations have been performed for the same systems. Agreement between simulation and experiment is excellent for IRMOF-1 and good for IRMOF-3. Simulations predict a strong temperature dependence of the heat of adsorption in HKUST-1, which is reduced significantly when the small pockets are blocked. The combined experimental and simulation study sheds light on discrepancies found in the literature for adsorption in HKUST-1. These results can lead us to two important conclusions. First of all, it can possible to rapidly determine the heat of adsorption of different gases on different MOFs. Second, the difference of heat of adsorption of different gases can be enhanced when the adsorbent is functionalized with an appropriate molecule.

4. Chapter IV: Application of HT precipitation for the discovery of MOFs for CO_2/CH_4 separation

4.1. Introduction

The second chapter has shown that MOFs can be obtained by precipitation in various conditions of solvent and bases. From the two systems investigated, Cu-Terephthalic acid and Zn- Terephthalic acid, different conclusions can be drawn. First, the diversity of the synthesis conditions, by varying solvent and bases, is large enough to fall on known MOF structures (HKUST-1, IRMOF-1). Second, it also allows to generate new compounds. However, the structural characterisation of the latter are make difficult due to the very small crystallite sizes which are not appropriate for single crystal studies and to the very low amount (<100mg) which do not allow proper XRD records for structural refinement.

The objective of this chapter is the application HT synthesis for the development of new MOFs for the CO_2/CH_4 separation in the frame of natural gas treatment. The objectives for a first screening is to discover adsorbents with a CO_2 capacity larger than 50 cm^3.(NTP).g^{-1}, a selectivity at 5bar of CO_2/CH_4 molar ratio larger than 3 and a CO_2 regenerability from 5 to 1 bar larger than 50%.

The first step of this work deal with the criteria for MOF design for CO_2/CH_4 separation in order to select cationic and ligand building blocks. As mention earlier, the main issue using HT methods are solid characterisations. Another related open question is: can miniaturised synthesis (<100mg) be scale-up to grams quantity in order to allow structural characterisation by powder XRD and measurements of CO_2/CH_4 isotherms. Finally, preliminary adsorption kinetic studies were performed on best samples in order to qualify diffusion phenomena.

4.2. MOFs design for CO_2/CH_4 separation

For example, the polarity of the structure is affected by the ligand and the metallic precursor, while the pore size depends only on the ligand.

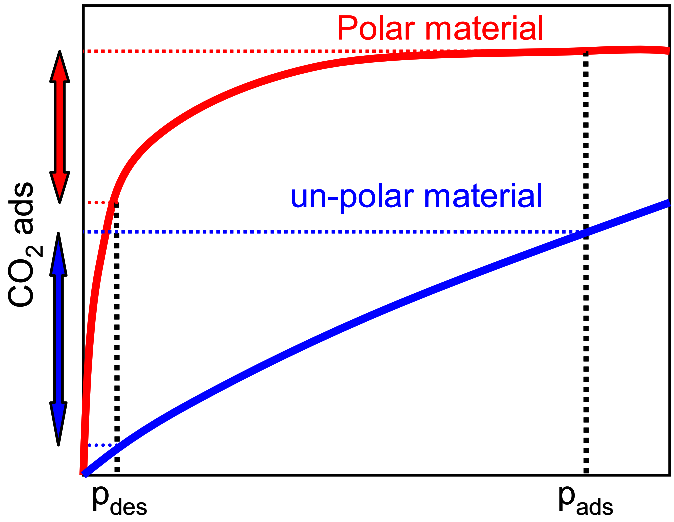

Figure 40 : Polarity effect on CO_2 adsorption; the arrows correspond to the WC adsorption of the different materials.

Contrary to the characteristic requirement for gas separation by the membrane process, a high affinity with a specific gas of the mixture is not needed. Indeed, as shown in Figure 40, a polar material with a high specific surface area adsorbs a large amount of CO_2. On the other hand, the interaction between the materials and the gas is too strong, making the adsorption take place at low pressure. To regenerate the material, high vacuum and/or increasing temperature are necessary. This step requires energy, increasing the process cost. The material therefore has to possess a weak interaction with the species. A very interesting advantage of MOF materials comes from the possibility of tuning the framework. Of course, the possibility of adding a specific molecule onto the framework allows the modification of several MOF characteristics such as polarity, acidity or number of active sites, which is helpful for gas separation. For example, Corma et al. [122] have shown the effect of the polarity on CO_2 adsorption. Here, the CO_2 adsorption was carried out on several zeolites with a different Si/Al ratio.

As expected, there are strong adsorptions of CO_2 at low partial pressure when the material is polar (low Si/Al ratio) Figure 41. The adsorption curve becomes more linear when the compound becomes less polar. According to these observations, the possibility of tuning the MOF structure can be an important advantage in view of increasing the difference in CO_2/CH_4 adsorption.

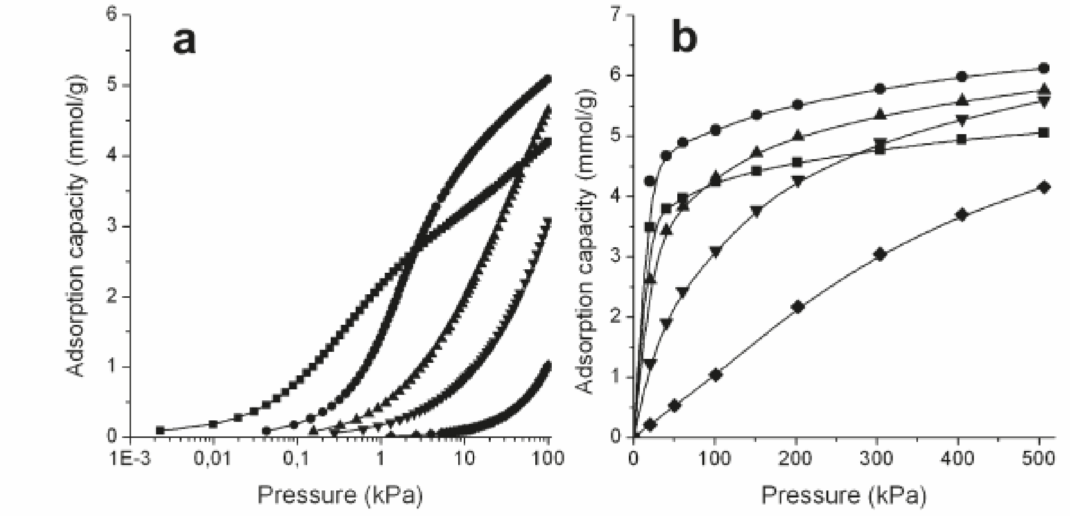

Figure 41 : CO_2 adsorption isotherms measured at 303 K in the (a) low- and (b) high- pressure ranges of LTA zeolites having Si/Al ratios of 1 (■), 2 (●), 3.5 (▲), 5(▼) and ∞ (♦).

Another important requirement deal with an appropriate size of the pores of the adsorbents MOF with very large micropores and/or small mesoporous adsorbents such as MIL-101 or MOF-177 have in principle very large CO_2 capacity at saturation. However, they show little CO_2 adsorption at moderate pressure due to the weak wall-wall interactions. On the contrary, ultra-microporous adsorbents may exhibit favourable CO_2 adsorption strength at moderate pressure; as the expense however of a small capacity. Therefore, total CO_2 capacity and CO_2 heat of adsorption are inversely linked and an optimum has to be found in terms of pore sizes of the adsorbent.

With respect to the analysis made in order to find a good CO_2 adsorbent for the PSA process, the chosen criteria to design appropriate MOF adsorbents are:

- nonpolar framework in order to avoid too strong interaction with CO_2 as in the case of Al-rich zeolites
- Micropores ranging from 0.5 to 1 nm in order to generate physisorption properties of moderate strength
- Eventually uncoordinated metal centres to enhance CO_2 interactions with the framework

These parameters can be controlled through the choice of ligands and/or the cation.

At the level of the ligand selection, the use a carboxylic acid with

- a short length between the two chelating functions
- and/or a smaller angles (less than 180°) made from the carboxylate species

Shall allow to synthesize MOFs with smaller pore size.

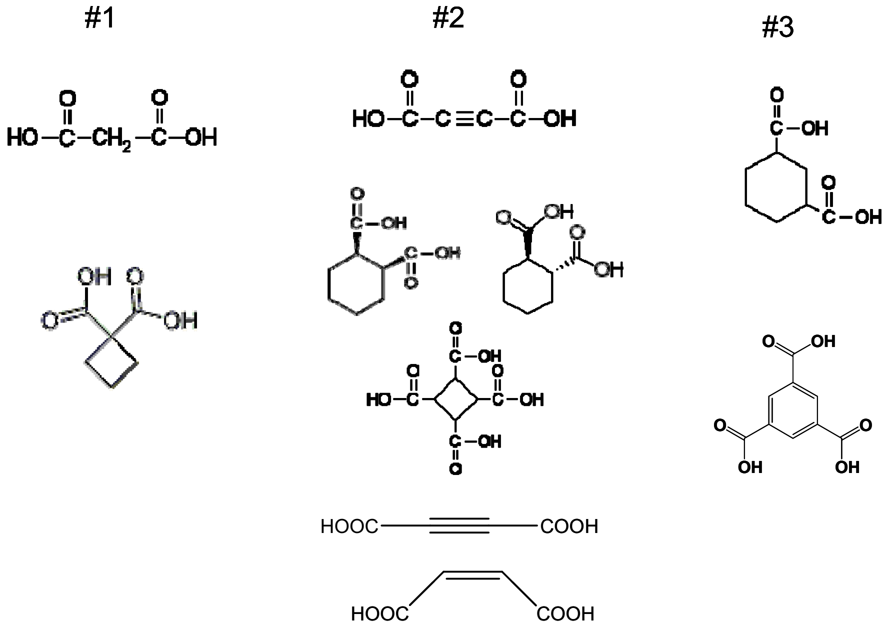

Figure 42 : Package of the ligand used. The packaging is made on the carbon number between the acidic function, 1, 2 or 3 carbons.

This approach is intuitive because the ligand and the cluster can be organized in different ways like the MIL-53 and MIL-68 structures or, in a specific case, the structure can be interpenetrated, like IRMOF-1 [112], but in the case of a long and straight ligand (such as biphenyldicarboxylic acid), the odds of obtaining a small pore size are decreased.

Another parameter that is important for gas separation is the choice of metal precursor in the aim of obtaining an uncoordinated centre. We know from the state of the art that transition metals, specifically copper, Ni, Co, Zn and Lanthanides, may provide uncoordinated centres. Moreover, due to the f subshell of the lanthanide, the number of uncoordinated centres could be increased if an MOF is obtained with this kind of metal. For these reasons, we chose for the first screening the H_3BTC ligand, 12 metallic nitrate precursors, five transition metals (Co, Ni, Cu, Zn and Ru) and seven lanthanides (La, Ce, Pr, Nd, Sm, Gd and Tb). The solvents chosen have to render soluble the entire metal-ligand system; we therefore selected five solvents (DMF, DMSO, THF, Et_2O/H_2O and THF/H_2O). Three bases were selected: pyridine, Et_3N and dabco.

All of the combinations were made, involving 180 syntheses, for which 53 samples were crystalline. No MOFs were obtained with Ru, Ni and Co. DMSO and DMF appeared to be the most efficient solvents used. The characterization of the various samples was carried out as for the validation of HKUST-1 and IRMOF-1. For the sake of clarity, only the results with the H_3BTC ligand are given, but several ligands were tested, such as muconic acid, cis/trans 1,2 cyclohexanedicarboxylic acid, acetylenedicarboxylic acid and maleic acid. Nevertheless, due to the various problems encountered, as the solubilization in water, low porosity or non reproductivity, all MOFs obtained with these ligands cannot be considered an efficient adsorbent.

4.2.1. Characterization of the Ln – H_3BTC system

- XRD Patterns and Classification

When the screening synthesis is used, several problems appear. One of them is the classification of the phases. For example, the screening made on the Lanthanide-BTC system involves 90 powders with around 40 crystalline phases. Due to the difficulty of manually grouping the patterns into families, classification by statistical analysis was performed. The method of Principal Component Analysis (PCA) was used [123]. This method is implemented in all statistical packages; is commonly used for the High Throughput screening of drugs

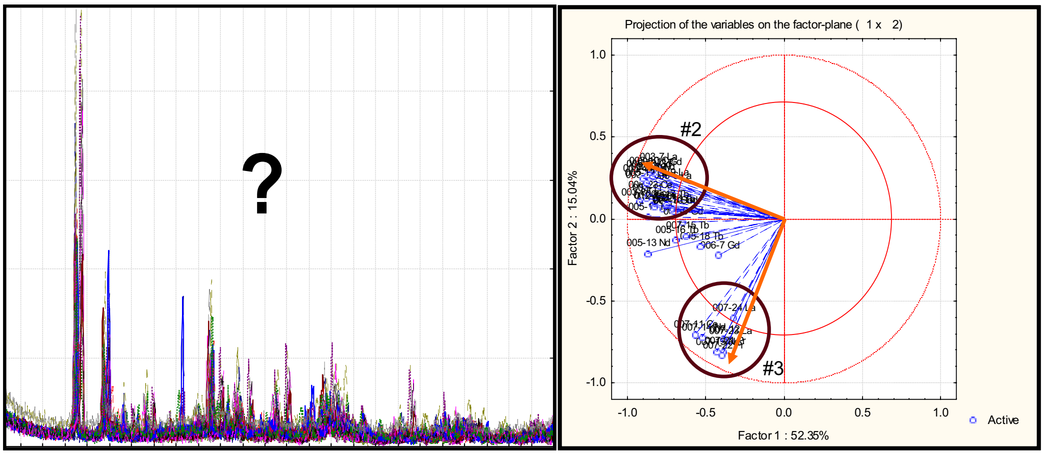

Figure 43: The entire XRD patterns from the screening of Ln-(BTC) (left) and XRD pattern classification from clustering analysis (right).

In short, the XRD patterns are converted to normalized vectors and then projected onto a plane. All of the projections in the same region near the norm come from the same diffractogram. In this way, a rapid classification of the different phases can be obtained. In the H_3BTC - Lanthanide case, two families of crystalline phases, called 2 and 3, are brought to light. The solvents used were DMF and DMSO, respectively. These materials were obtained with different lanthanides (La, Ce, Nd, Gd, Tb and Pr).

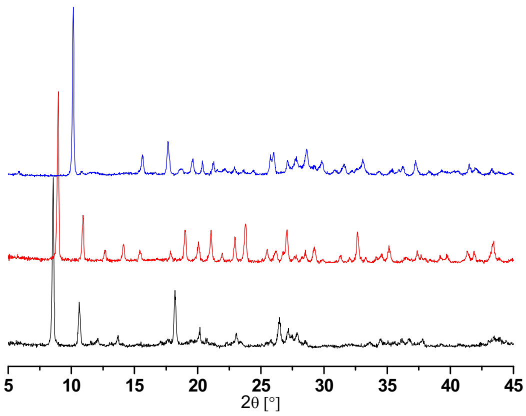

Figure 44: XRD patterns of met-BTC system screening. Zn-(BTC) (top), $La_x(BTC)_y(DMSO)_z$ f3 (middle) and La(BTC)(DMF) f2 (bottom).

As shown in Figure 44, three different patterns with high crystalline phases are obtained. The reactions take place rapidly. All of these materials are reproducible with no amorphous part. The Zn-(BTC) system is obtained with three types of solvent: DMF, H_2O/THF and H_2O/Et_2O. Only Et_3N leads to this phase with DMF and H_2O/THF, but the three bases give the phase with H_2O/Et_2O. In the case of the Ln-BTC system, two families are discovered. Figure 44 shows the XRD patterns obtained with several metals. When these kinds of results are obtained by the screening method, we know that these phases are reproducible and can be obtained with different metals. If the first result is necessary for any application, the second makes it possible to study the influence of the metal on CO_2 adsorption without any diffusion influence. When the precipitation method is chosen, the MOF form obtained is a powder. One of the difficulties of this approach lies in determining the structure of unknown materials, such as family 3. Even if these materials are crystalline, we cannot rapidly determine the structure; but if the structure is not determined, it cannot be optimized for the application. This is not the case for family 2.

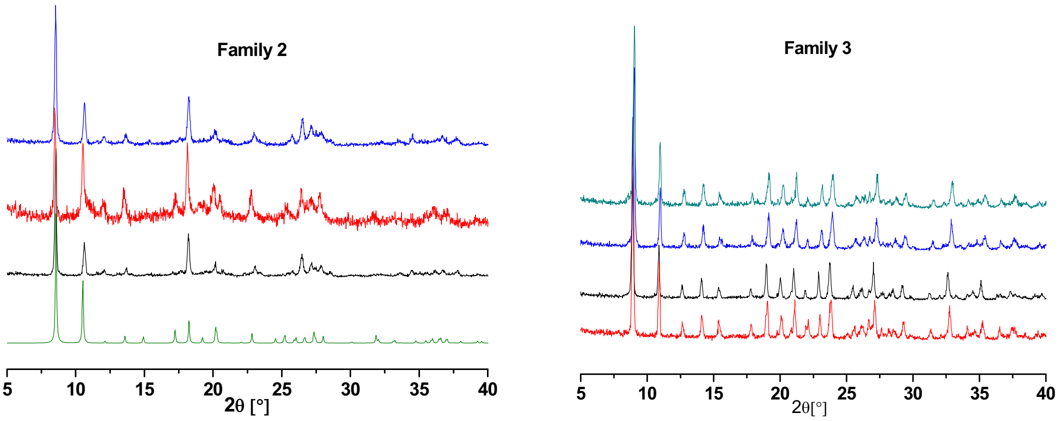

Figure 45: From top to bottom, XRD patterns of family 2: Ce(BTC)(DMF), Pr(BTC)(DMF), La(BTC)(DMF) and theoretical data from Guo et al. [83] (left). From top to bottom, XRD patterns of family 3: $Nd_x(BTC)_y(DMSO)_z$, $Pr_x(BTC)_y(DMSO)_z$, $Ce_x(BTC)_y(DMSO)_z$ and $La_x(BTC)_y(DMSO)_z$ (right).

In view to determine the corresponding structure of the XRD patterns that we obtained, Dr JL. Paillaud, from MPC, IS2M, ENSCMu, France, helped us to make the indexation of our XRD and the data obtained from the Dy(BTC)(H_2O) of Guo et al. For Dr Paillaud, the diffractogramme indexation shows a high correlation with the similar lattice parameters and also an identical space group ($P4_322$). Prior to the Rietveld refinement, he tried to complete the structural resolution. Despite the limited information on the diffractogramme, he could still locate the atoms of lanthanum and this is very similar to the Dy(BTC) quoted above. The SBU are composed of one lanthanide cation, one BTC ligand and one water molecule. The guest DMF does not occupy a specific place in the framework. Each lanthanide cation is coordinated with six oxygen atoms of six carboxylate groups of BTC and with the oxygen of the water molecules. The syntheses of these phases were obtained early 2006. At the same time Guo published structural resolution of very similar compounds based on Dy^{3+} cation[83]. Latter Guo et al are extended their study to the determination of several isoreticular compounds based on Tb, Ho, Er, Tm and Yb and the BTC ligand[124]. In their study, X-ray diffraction reveals a three-dimensional framework crystallized in a chiral space group, $P4_322$

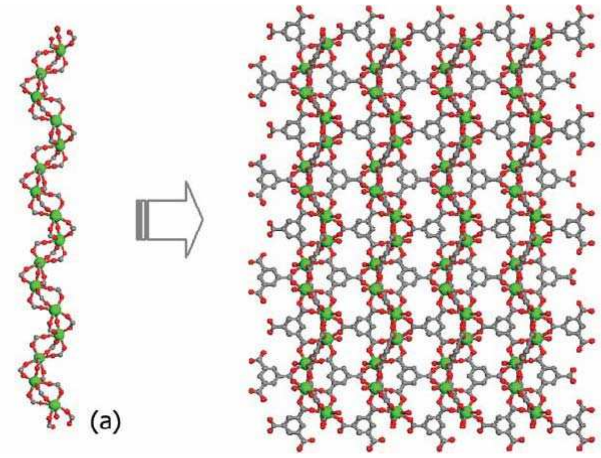

Figure 46: The one-dimensional chiral inorganic chain along the [001] direction (a) are connected to impenetrable organic walls along the [100] and [010] direction. (Metal, green; O, red; C, grey).

- Thermogravimetric analysis

Figure 47 shows the results of thermogravimetric (TG) analysis carried out on La(BTC)(DMF)(H_2O). This experiment was performed under air.

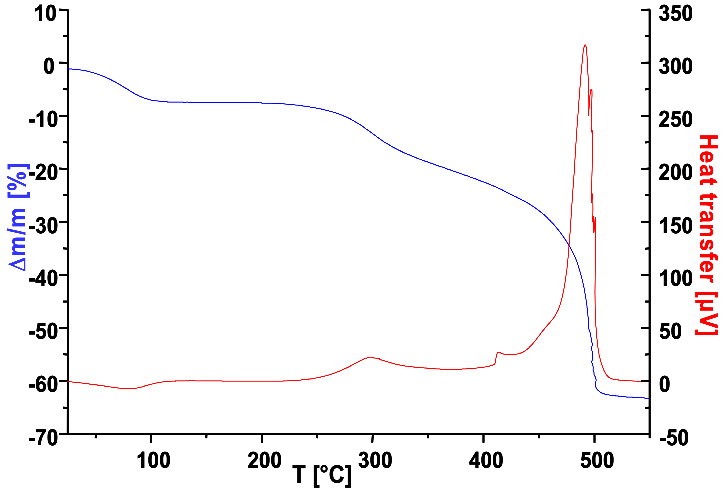

Figure 47 : TG-TD analysis of La(BTC)(DMF)(H_2O) under air.

Around 86°C, a weight loss of 7.9% correlates with an endothermic peak that can be attributed to dehydration. The thermal stability is around 400°C. At 327°C, a weight loss of 8.8% correlates with an exothermic peak that may be attributed to a rearrangement. For Guo et al. [83], there is a rearrangement due to the loss of guest DMF and coordinated water (Figure 47).

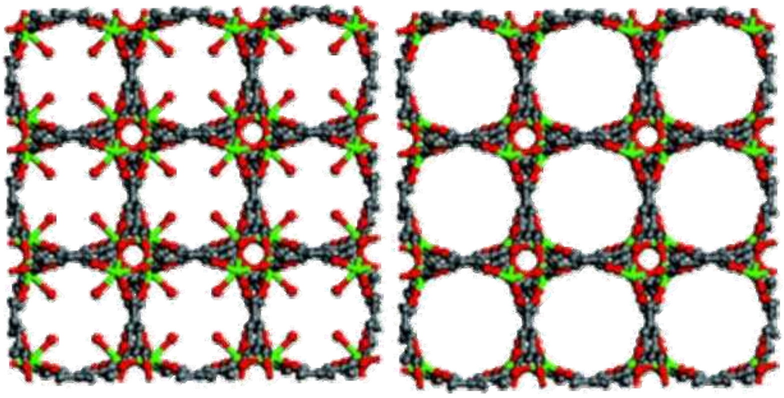

Figure 48: Hydrated form of La(BTC)(H_2O) (left); dehydrated form of La(BTC) (right).

The water molecule is coordinated on the metal cluster in the [001] direction. The pore size of the circular channel is around 7 x 7 Å².

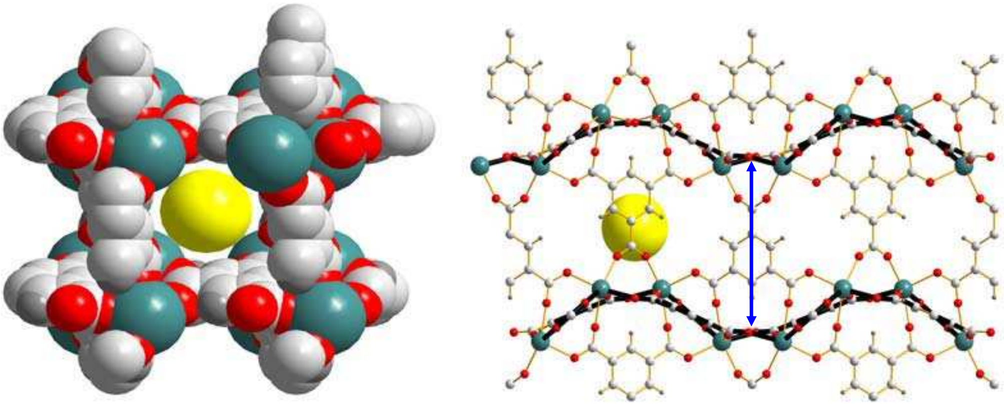

Figure 49 : La(BTC) structure representation with van der Waals radius (left) in plan [001] and in plan [010] (right). Yellow sphere diameter =5.3Å, blue arrow length= 7 Å. C=grey, La =green and O=red.

As shown in this figure, the material contains channels forming a zig-zag array parallel to the [010] axis. Despite that, the pore windows are circular. The empty diameter of the pore entries amounts to approximately 5.3Å.

- XRD Thermal Analysis

Taking into account the TG analysis result, an XRD analysis was performed on these materials at different temperatures under N_2.

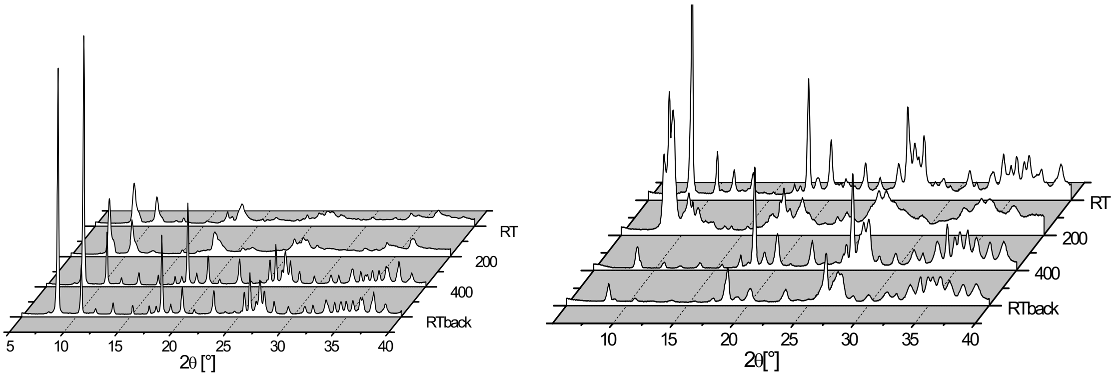

Figure 50: Controlled temperature XRD patterns of family 2 (left) and family 3 (right).

The results obtained in Figure 50 are in good agreement with the TG analysis. Indeed, the data at 350°C show a rearrangement, with this phase kept upon return to room temperature. The same study was carried out on family 3. The first analysis made at 200°C shows a modification of the phases. Then, the crystalline phase is lost. These experiments are another proof of the influence of the solvent. Indeed, even if two phases are obtained with the same reactant, the thermal effect of these materials is completely different.

- Porosity

The BET analysis carried out on the Zn-(BTC) system (f3) led to a result of around 20m².g^{-1} following a pre-treatment for 4 h at 200°C under vacuum. This specific surface area is not sufficient for any separation application, so this phase was abandoned. In order to study the effect of a thermal treatment on the morphology of La(BTC), three different samples from the same synthesis lot were tested by using ASAP 2010^{TM}, respectively at 150°C, 250°C and 350°C under vacuum, for 16 h. Then each sample was characterized by N_2 adsorption at 77 K.

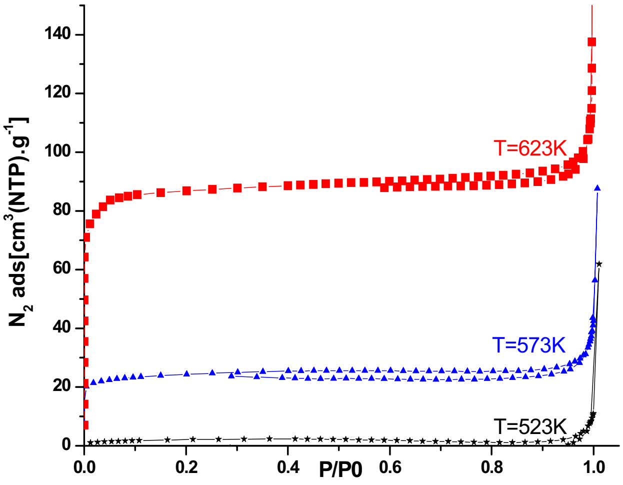

Figure 51: Thermal pretreatment effect for La(BTC)(DMF) on N_2 isotherm at 77 K: 523 K (black stars), 573 K (blue triangle), 623 K (red square).

Table 6: Apparent Specific Surface Area (SSA) and pore volume (V_P) of La(BTC)(DMF) samples whose N_2 adsorption isotherms at 77 K are reported in Figure 1. SSA and V_P are evaluated, respectively, by the BET method and the Gurvitsch rule.Treatment

	SSA	**V_P**
[K]	**[m^2/g]**	**[ml/g]**
423	**8**	**0.012**
523	**87**	**0.058**
623	**340**	**0.17**

The La(BTC)(DMF) sample treated at 423 K is virtually nonporous, while those treated at 523 K and 623 K are characterized by type I isotherms. This experiment provides two pieces of information. First of all, an extremely slow adsorption of N_2 at 77 K on porous samples is observed - up to 20 h for one isotherm point - probably due to the slow kinetic diffusion of N_2 molecules (d_{N2} = 3.64 Å) into narrow micropores (8 – 10 Å) from estimated by DFT method from isotherm data. Second, the isotherm of these materials can hardly be interpreted. Indeed, the desorption branch lies below the adsorption branch. This could be explained by the flexibility of the structure, but another experiment must be carried out to confirm this hypothesis. Based on these results, the La(BTC) samples to be employed for adsorption tests were treated at 623 K.

4.2.2. CO_2 Adsorption on Ln(BTC)

- Pre-treatment Effect

In order to understand these phenomena, CO_2 adsorption at 303 K was carried out over Ce(BTC) after pre-treatment at three temperatures: 523 K, 673 K and 623 K. Due to the previously observed slow adsorption kinetics, 4800s equilibration time was adopted.

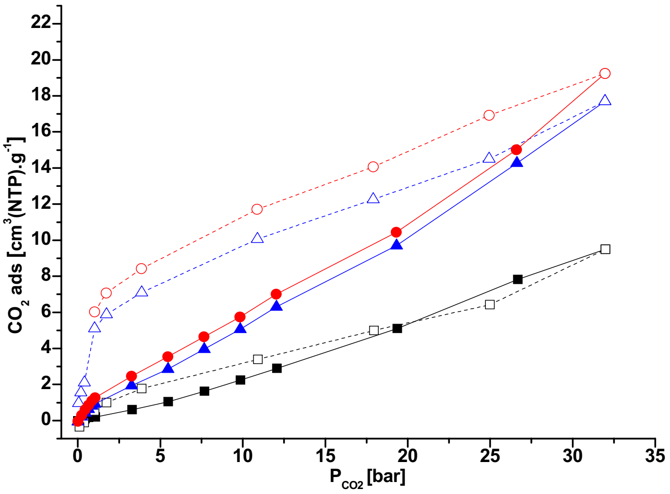

Figure 52 : Pretreatment effect on CO_2 adsorption at 303 K on Ce(BTC)(DMF)$(H_2O)_x$. 532 K (black square), 573 K (blue triangle), 623 K (red circle).

Figure 52 shows the effect of pre-treatment on CO_2 adsorption. As expected, CO_2 adsorption increases with the pre-treatment temperature. Indeed, for the material pre-treated at 523 K, there is a weak adsorption. This result is probably due to the non-dehydration of the material. When the water is removed, the adsorption increases from 10 to 18 cm^3(NTP).g^{-1} without modification of the structure. Furthermore, the materials with high pre-treatment temperature show hysterias that could be attributed to a breathing effect. But for conclude we have to make an XRD experiment *in situ* and we have not access to this kind of set up in IRCELyon. Anyway, this phenomenon is not required for the PSA process. Indeed, with this kind of property, the regeneration step can function at pressure below atmospheric and require too much energy. These experiments show the importance of the pre-treatment step. According to this result, all the materials are pre-treated for 2 h at 623 K under vacuum.

- Metal Effect

In order to study the influence of the metal on CO_2 adsorption in the absence of diffusion effect, the adsorption test at high pressure is carried out on the different Ln(BTC) using HP belsorp. Based on the results of the pre-treatment and porosity studies, it was decided to pre-treat about 50 mg of adsorbent for 2 h at 623 K under vacuum.

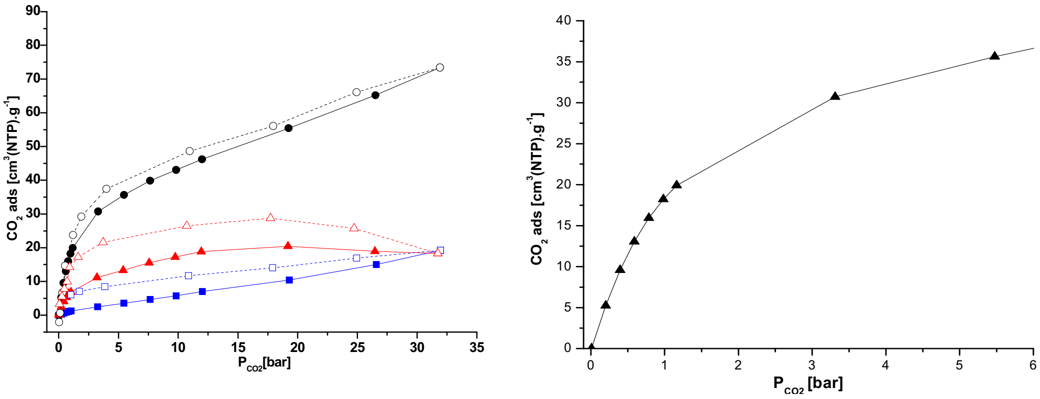

Figure 53: CO_2 ads (solid) / des (dash) at 303 K of La(BTC) (circle), Pr(BTC) (triangle), Ce(BTC) (square) (left), CO_2 ads at 303 K at low pressure on La(BTC) (right)

Figure 53 shows the adsorption capacity of the different materials. According to these results, La(BTC) should be the best candidate for the gas separation. Indeed, its adsorption capacity is higher than that of the other materials, and the adsorption takes place with no breathing property. Moreover, this figure shows the La(BTC) adsorption at low pressure. The linear shape of the isotherms is consistent with weak interaction among adsorbed molecules and La(BTC). This phenomenon is most likely due to the nonpolar state of La(BTC).

Table 7 : Summary of objectives and results of the La(BTC) at T=303 K

T=303 K	Objectives	La(BTC)
Ads Capacity (5bar) [$cm^3(NTP).g^{-1}$]	50	35
Selectivity (molar ratio CO_2/CH_4)(5 bar)	3	N.A.
Desorption 5 →1 bar [w% $cm^3(NTP).g^{-1}$]	50	43

The adsorption capacity at 5 bar is 35 $cm^3(NTP).g^{-1}$ and the desorption from 5 to 1 bar is around 43%. These results are close to the screening target, but the adsorption kinetics of La(BTC) are too slow to permit this adsorbent to be used in the PSA process. It is reason why we did not carried out the CH_4 adsorption.

4.3. Conclusion

This screening represents more than 600 experiments. Around 10% of the materials obtained are crystalline and 3% are microporous. The classification of a crystalline material obtained with a given ligand is carried out by an appropriate tool, Statistica, which permits a rapid classification of the crystalline phases. These experiments have led to two types of materials based on different lanthanide and BTC ligands. Moreover, Guo et al. have determined one structure to be Ln(BTC), while the other structure is still unknown. The porosity of the Ln(BTC) compound is greater than 300 $m^2.g^{-1}$, which is enough for CO_2 adsorption testing. After testing the effect of the metal, it appears that the material based on the lanthanide metal is the most efficient and that the target point for obtaining a good adsorbent should be the pre-treatment step. In fact, when it was adapted, the material almost reached the target. Nevertheless, its kinetics of adsorption is too slow for any application.

5. Chapter V: Engineering of coordination polymers for shape selective alkylation of large aromatics and the role of defects

5.1. Introduction

The catalytic potential of Metal-Organic Frameworks (MOFs) is the most recent and exciting aspect of these materials. The extremely high diversity of MOFs obtained could permit an important catalytic effect. There are nevertheless few published studies dealing with this domain. This apparent paradox can be explained by the weakness of the MOF structure database, which is due to the appearance of many new materials in a very short time. Today, zeolites are generally used for heterogeneous catalysis, but their uses are limited due to several weaknesses emanating from the relatively small pore size of this kind of material. One application that poses a problem for zeolites is the alkylation of very large molecules. Due to their larger pore size, MOFs make it possible to alkylate very large polyaromatic compounds. For example, Horcajada et al. [125] reported the catalytic activity of two different MIL-101s (Fe, Cr) for Friedel-Crafts benzylation. We have recently shown in a short account that microporous zinc carboxylate frameworks show outstanding shape-selectivity properties for similar alkylation-type reactions [91].

5.2. Catalytic Strategy

In this study, two approaches are developed. The first approach involves the development of M-OH Brønsted sites on the MOF structure for catalytic alkylation. One of the two methods employed in this aim is a mimetic approach, which consists in reproducing within MOFs the already-known active sites of solids such as H-zeolite. Two compounds were selected in this context: MIL-53 (Al)[45]; and MOF-69c, with Al(OH)(bdc) and $Zn_3(OH)_2(bdc)$ structures, respectively. These perfectly characterized materials possess structures containing free hydroxide groups.

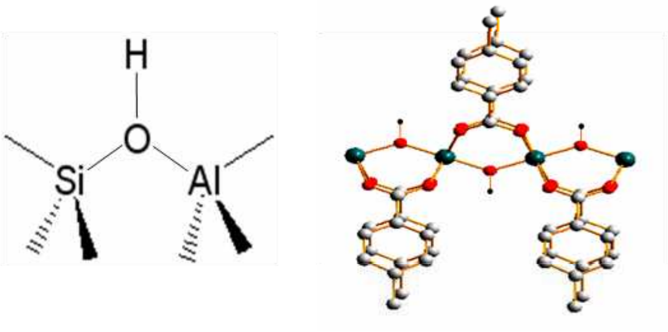

Figure 54: MOF selection by a zeolite mimetic approach. Diagram of Brønsted centres in zeolites showing μ_2 - bridging hydroxyl (left); and inorganic chain of MIL-53 showing μ_2 hydroxyl groups as potential acid centres (right).

The second method is to create defects in the MOF structure cluster in order to increase the number of Lewis acid sites. The two strategies used to this end were: i) increasing the reaction kinetics; and ii) using a mixture of poly- and monodentate ligands during the MOF synthesis. The structure of the MOF selected does not possess an –OH function. For this reason, we selected the IRMOF family.

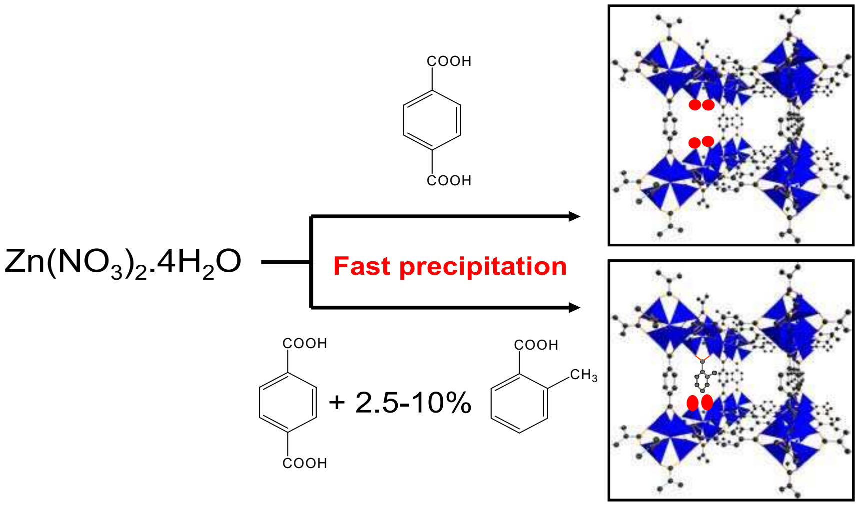

Figure 55: Diagram of the two synthesis routes used to generate structural defects: missing ligand method (top), isomorphous substitution by a monocarboxylic acid (bottom).

The second approach employed in this study involves using MOFs for catalytic shape selectivity. In keeping with their high diversity of pore sizes and volumes, some MOFs exhibit larger cavities than do zeolites such as BEA or MOR. It is reasonable to suppose that analogous shape-selectivity effects could be also observed for MOF materials[7]. In this work, we have studied the alkylation of various aromatic compounds of different sizes in order to highlight the pore shape selectivity. For that, we selected toluene and biphenyl to be alkylated by *tert*-butyl chloride. The different catalysts used are IRMOFs[126] and hydrated IRMOFs called MOF-69s [127] by Yaghi et al. The possibility of using different carboxylic ligands to tune the pore size of the structure presents a strong advantage for studying shape selectivity.

5.3. Synthesis

As mentioned at the beginning of the Catalytic Strategy section, the first step of this work is to obtain MOFs with –OH groups. While the mimetic approach consists in reproducing already-known materials, the second method, which consists in creating defects, can be employed by testing the different synthesis routes. Indeed, it is known that the purity of the crystal depends on the reaction kinetics. If the kinetics is increased, the number of crystal defects is increased as well. With this in mind, different synthesis routes were tested.

- Solvothermal Synthesis (IRMOF-1 solvo)

Here the synthesis is performed according to the process reported by Sabo et al. [128]. DEF is used as solvent. In view of obtaining a product of high purity, the metallic nitrate precursor is tetrahydrated and there is no base. The synthesis is carried out in a Teflon-lined stainless-steel autoclave at 373 K for 20 h. The solid is filtered off, washed and finally exchanged with $CHCl_3$. Finally, the material is evacuated and handled in a glove box for transfer into a Schlenk-type vessel.

- Slow Precipitation Synthesis (IRMOF-1 basf)

The preparation of this IRMOF-1 follows the procedure reported by Mueller et al. [56]. DMF is used as solvent. Here the reaction is carried out in a glass reactor equipped with a reflux condenser and a Teflon-lined stirrer. After 7 h of stirring at 403 K, the solid is filtered off, washed three times with DMF and dried at 403 K under vacuum for 3 h. Here the precursor is $Zn(NO_3)_2.6H_2O$ and the reaction takes place without a base.

- Fast Precipitation Synthesis (IRMOF-1 pre)

IRMOFs can also be obtained by the precipitation procedure designed by Huang et al. [48]. Here the reaction takes place instantaneously at room temperature after the dropwise addition of Et_3N. After 90 min. of stirring, the powder is filtered and washed three times with DMF and heated at 403 K overnight under dry air flow. This procedure is extended to the synthesis of the isoreticular compounds IRMOF-3, Zn-MOF-8 and Zn-MOF-10 by using 2-aminoterephthalic acid, naphthalene-2,6-dicarboxylic acid and biphenyl-4,4'-dicarboxylic acid, respectively [126].

This procedure is also used for the creation of defects by uncoordinated ligands. The precipitation takes place in a mixture of *o*-toluic acid and benzenedicarboxylic acid (bdc). Three samples are prepared with toluic acid : bdc ratios equal to 2.5, 5, and 10 wt.% in order to yield ZnIRMOF-1 (2.5), ZnIRMOF-1 (5) and ZnIRMOF-1 (10), respectively.

- Synthesis of MOF-69 Family

MOF-69s are the hydrated forms of IRMOF structures. They are obtained by the protocol reported by Loiseau et al. [50]. The difference between an IRMOF and an MOF-69 comes from the addition of deionized water during the reaction. In this case, the structure of MOF-69c is $Zn_3(OH)_2(bdc)_2•2DEF$. This experimental procedure is extended to the synthesis of MOF-69a and b with biphenyl-4,4'-dicarboxylic acid and naphthalene-2,6-dicarboxylic acid, respectively.

- Reference Materials and Catalysts

MIL-53(Al) was purchased from Aldrich (Basolite A100). The acid forms of beta (H-BEA, Si/Al=13.75) and mordenite (H-MOR, Si/Al=10) zeolites are obtained from the commercial Na forms (Fluka) by ammonium exchange followed by calcination treatment. The ion exchange is carried out with a 10 wt.% solution of NH_4COOCH_3 in water at 80ºC during 4-5 h followed by calcination treatment at 823 K during 3 h. This procedure is repeated twice. Both $AlCl_3$ (Aldrich 99.9 %), and $ZnCl_2$ (Alfa Aesar, anhydrous, 98+ %) are used as received, as reference Lewis acids.

Table 8: Summary of MOF samples synthesized and used as catalysts in this study.

Sample Name	Basic Structure	Linker	Synthesis Method	Reference
IRMOF-1 solvo	IRMOF-1	H_2bdc	Solvothermal	[128]
IRMOF-1 basf	IRMOF-1	H_2bdc	Basf procedure	[56]
IRMOF-1 pre	IRMOF-1	H_2bdc	Fast precipitation	[48]
ZnIRMOF-1 (2.5)	IRMOF-1	H_2dbc + 2-methyl toluic acid (2.5%)	Fast precipitation	this study
ZnIRMOF-1 (5)	IRMOF-1	H_2dbc + 2-methyl toluic acid (5%)	Fast precipitation	this study
ZnIRMOF-1 (10)	IRMOF-1	H_2dbc + 2-methyl toluic acid (10%)	Fast precipitation	this study
MOF-69A	MOF-69	biphenyl-4,4'-dicarboxylic acid	Solvothermal	this study
MOF-69B	MOF-69	naphthalene-2,6-dicarboxylic acid	Solvothermal	this study
MOF-69C	MOF-69	H_2bdc	Solvothermal	[50]
IRMOF-3 pre	IRMOF-3	2-aminoterephthahlic acid	Fast precipitation	this study
Zn-MOF-8	MOF-69	naphthalene-2,6-dicarboxylic acid	Fast precipitation	this study
Zn-MOF-10	MOF-69	biphenyl-4,4'-dicarboxylic acid	Fast precipitation	this study

- Alkylation

The alkylation reactions take place in an autoclave with autogenous pressure. They are carried out in n-decane with an aromatic : *t*-BuCl molar ratio of 2:1. The catalytic sample (30 mg) is activated at 403 K under vacuum. After 2 h, the solid is recovered by filtration at room temperature. The reaction mixtures are analyzed by gas chromatography with an HP 6890N equipped with an HP-5 capillary column (30 m length). The toluene conversion is calculated by taking into account the initial concentration (100% excess). Identification of the different isomer configurations is performed by GC-MS (HP 6890 equipped with HP-5/HP-1 capillary columns, an HP 5973 quadrupole detector - ionic impact at 70 eV, and NIST02 library).

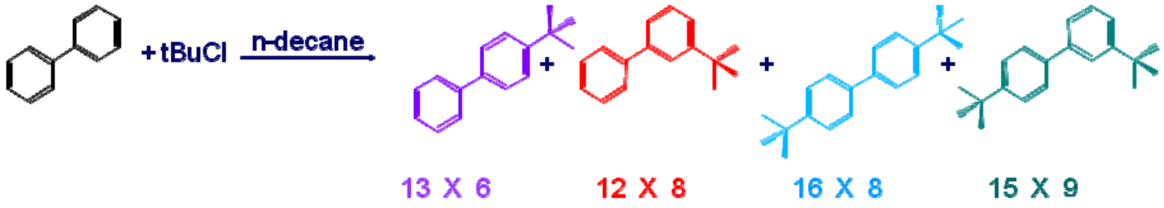

Figure 56: Example of alkylation reaction and different products obtained at 100°C after two hours with their kinetic diameters [Å].

Two experiments are necessary to confirm that the reactions take place heterogeneously with no leaching. First of all, the reaction is carried out at room temperature. Then, fresh reactants are added to the liquids recovered from the reaction mixture and a new reaction run is performed.

5.4. RESULTS

The characterization of the catalysts was begun as with the validation method. In view of determining the effect of structural modification due to the different strategies used, DRIFT analysis and liquid ^{1}H-RMN were carried out. DRIFT analysis was carried out on a Nicolet Magna 550 equipped with an MCT detector. The samples were loaded in a DRIFT Spectratech cell equipped with ZnSe windows. A thin layer of SiC sieved at 200-400 µm was first loaded to improve thermal exchange. Then, SiC was covered with the samples. Water desorption was then performed by heating the cell to 220°C under 50 $ml.min^{-1}$ of He. The cell was then cooled down to room temperature and scans were performed in He flow. Solid state ^{1}H NMR analysis was carried out with a DX-400 Bruker in static conditions in order to allow quantification. Liquid ^{1}H NMR (Bruker Avance 250) was used to quantify the substitution of di- to monocarboxylate for the Zn-IRMOF-1 (2.5), (5) and (10) samples. After the synthesis, the samples were digested in a $DCl/D_2O/DMSO\text{-}d_6$ mixture, thus liberating the linkers in solution on the acid forms. The choice of *o*-toluic acid as the monocarboxylic acid was made because its methyl groups make it possible to distinguish chemical shifts between the two linkers. The integration of the characteristic signals of the two linkers allowed the quantification of the respective amount of mono- and dicarboxylate linkers for the three samples.

5.4.1. Study of crystallinity

5.4.1.1. MOF-69 Structure

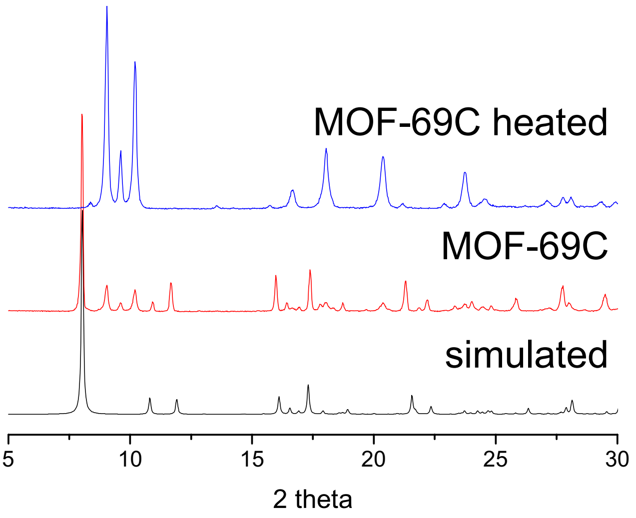

Figure 57: Powder X-ray diffraction patterns of simulated MOF-69C (bottom), $Zn_3(OH)_2(bdc)_2$•2DEF (MOF-69C) (centre), and $Zn_3(OH)_2(bdc)_2$•DEF (top).

The XRD analysis carried out on MOF-69c reveals a mixture of two phases, $Zn_3(OH)_2(bdc)_2$•2DEF (MOF-69c) and $Zn_3(OH)_2(bdc)_2$•DEF. The different MOF-69c coordinations can be obtained by heating at 170°C in air. These results are in good agreement with the work of Rosi et al. [31].

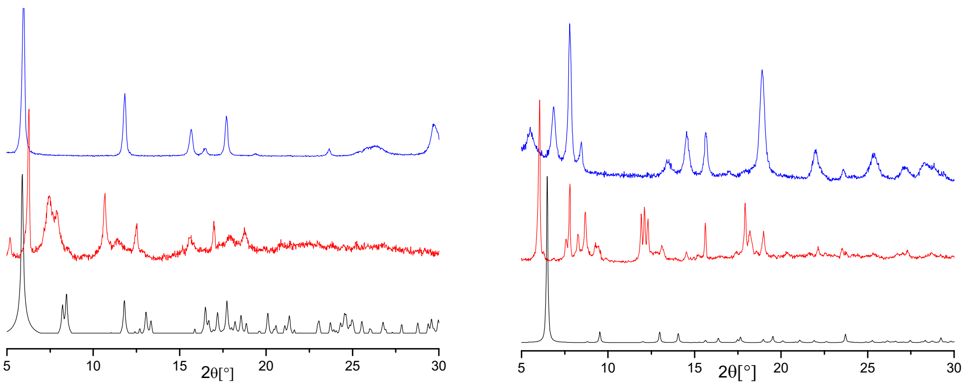

Figure 58: XRD patterns of MOF-69a simulated (bottom), experimental (centre) and Zn-MOF-10 (top) (left); and MOF-69b simulated (bottom), experimental (centre) and Zn-MOF-8 (top) (right).

In this case, the expected results are not seen. Indeed, the simulated XRD patterns of the different MOF-69s and their corresponding experimental data cannot be correlated, and there is also no correlation between IRMOF-8 and -10 and between Zn-MOF-8 and -10. Nevertheless, the indexation of the XRD data of the Zn-MOF-8 and -10 samples reveals the presence of MOF-69 type phases instead of the IRMOF structures. The cell parameters of Zn-MOF-8 are 21.59(2), 20.88(4), 11.94(2), and 90 96.10(2), 90 with C2/c as a space group. For Zn-MOF-10, the cell parameters are 20.180(1), 18.562(1), 12.164(1), 90 95.34(5), 90 with the same space group. These results are in good agreement with the data of MOF-69b and MOF-69a, respectively.

5.4.1.2. IRMOF Structures

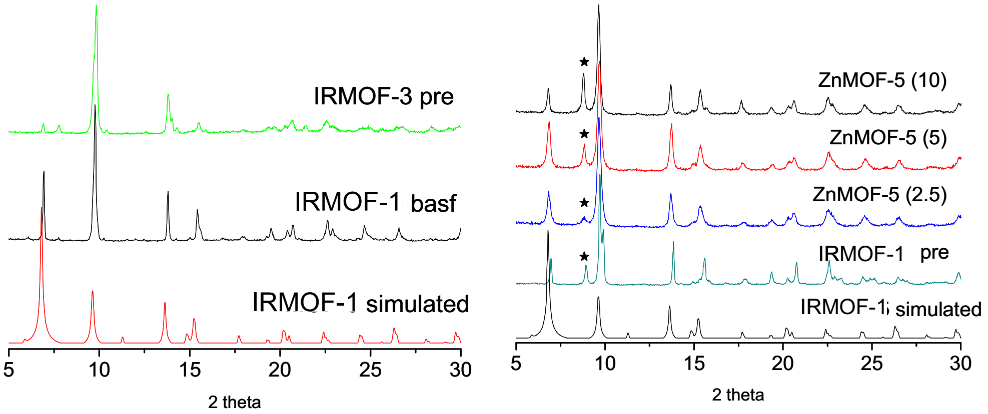

Figure 59: Powder X-ray diffraction patterns of IRMOF-1 basf (centre) and IRMOF-3 pre (top) samples compared with the simulated pattern (bottom) (left). Powder X-ray diffraction patterns of IRMOF-1 based samples prepared by precipitation (IRMOF-1 pre) and with increasing monocarboxylic acid content: ZnIRMOF-1 (2.5), (5), and (10), respectively. The symbol * indicates Zn(bdc)•xH_2O (N phase) (right).

Despite the high sensitivity of the IRMOF-1 structure, in particular with respect to humidity, IRMOF-1 is obtained regardless of the protocol followed. In the case of the terephthalic : *o*-toluic system, the XRD patterns show the presence of hydrated IRMOF phases, Zn(bdc).xH_2O. According to the data obtained for ZnMOF-8 and -10 as well as for ZnIRMOF-1, the synthesis conditions applied lead to the MOF-69 family instead of to the IRMOF family.

5.4.1.3. MIL-53 Structure

The MIL-53 structure, Al(OH)bdc, was discovered by Loiseau et al. [129], with two carboxylate functions linked to two distinct Al in an octahedral setting. These connections generate 1D channels with different pore sizes depending on the nature of the inserted molecules; these channels are responsible for the breathing effects observed. In open form, the MIL-53 structure has an orthorhombic system with the following parameters: a= 6.608(1), b= 16.675(3), c= 12.813(2) Å² and 8.5 x 8.5 Å² as channel dimensions.

5.4.2. Structural Study

In order to characterize hydroxyl groups, DRIFT and ^{1}H-NMR studies were carried out.

- DRIFT

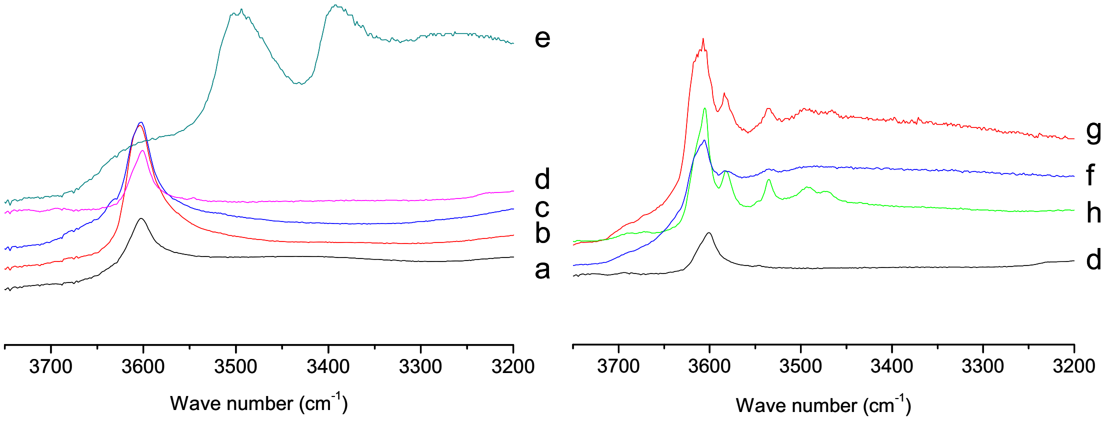

Figure 60: DRIFT spectra recorded after drying at 220°C under N_2 flow. Key: Zn-MOF-8 (a), IRMOF-1 basf (b), MOF-69C (c), IRMOF-1 pre (d), IRMOF-3 (e), ZnIRMOF-1 (2.5) (f), ZnIRMOF-1 (5) (g), and ZnIRMOF-1 (10) (h).

After drying, the data obtained by DRIFT analysis show a common intense signal around 3600 cm^{-1} for the entire sample. This band can be attributed to the Zn-OH bond. While this band is expected in the case of MOF-69, due to the μ_3-OH species, the pure IRMOF structure should not appear. For IRMOF-3, two intense signals around 3500 and 3390 cm^{-1} can be seen. These signals correspond to the stretching and bending vibration bond of –NH_2 species, respectively. For the ZnIRMOF-1 samples, the presence of mono-acid is accompanied by a cluster defect. This phenomenon increases the number of hydroxide sites created and it is accompanied by an increase of the signal at 3580 cm^{-1} and by an additional signal at 3530 cm^{-1}. It can be noted that the signal intensity can be correlated with the wt.% of the mono acid added during the synthesis.

- ^{1}H-NMR

The presence of hydroxyl groups shown by the DRIFT analysis is confirmed by ^{1}H-NMR.

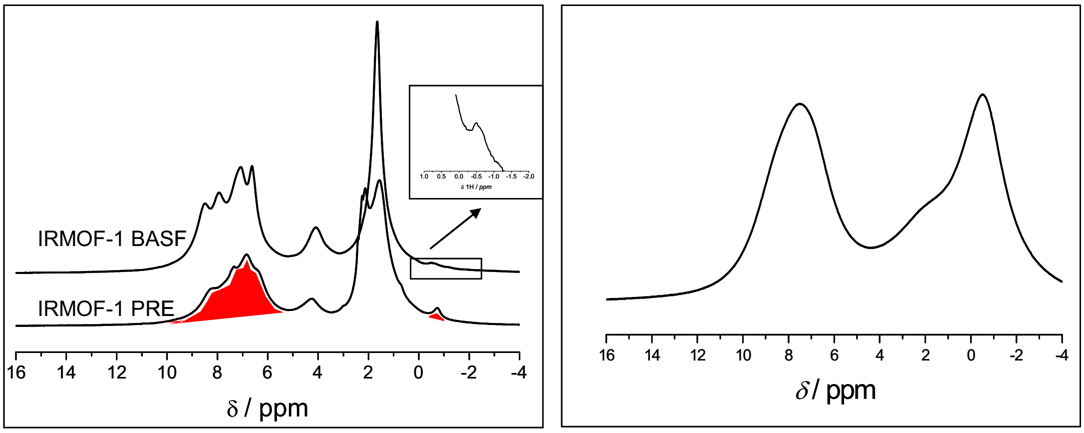

Figure 61: Solid ^{1}H NMR of IRMOF-1 samples prepared by BASF and precipitation methods (left). Solid ^{1}H NMR of MOF-69C (right).

For the different IRMOF-1s, the presence of Zn-OH species is revealed by ^{1}H-NMR analysis. Nevertheless, the peak intensity at δ= -0.4 ppm depends on the sample preparation. The μ_3-OH : bdc peak integration ratio is 10 and 25 for the IRMOF-1 BASF and IRMOF-1 PRE structures, respectively. In the case of the MOF-69 structure, the high intensity peak at δ= -1 ppm can be assigned to Zn-(μ_3-OH)-Zn chains, as reported by Loiseau et al. [50].

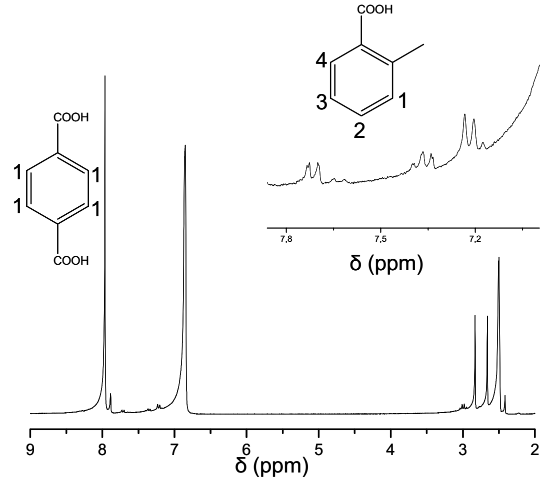

Figure 62: Liquid ^{1}H NMR of digested ZnIRMOF-1 (2.5).

In the case of the different ZnIRMOF-1s obtained, the partial substitution of the terephthalic ligand by the *o*-toluic compound is determined by the ^{1}H NMR of the –CH_3 group of the *o*-toluic acid (Figure 62). The presence of the distinctive aromatic resonances at δ(ppm) = 7.21 (m, 2 H, $H_{1\text{-}1}$, $H_{1\text{-}3}$), 7.44 (t, 1 H, $^1J_{HH}$ = 6.5Hz, $H_{1\text{-}2}$) and 7.72 (d, 1 H $^1J_{CH}$ = 6.5 Hz, $H_{1\text{-}4}$) indicates the presence of liquid phase *o*-toluic acid, which finds its origin in the porous framework. Depending on the percentage of monocarboxylic acid used in the synthesis, the peak integration reveals dicarboxylate : monocarboxylate ratios between 1:17 and 1:53 for IRMOF-1 pre and IRMOF-1 BASF, respectively. There are good correlations between the ^{1}H-NMR and DRIFT analyses. In conclusion, the presence of the Zn-OH function is confirmed in the different materials, even if this function is not present in the structure of the IRMOFs. In view of determining the nature and the strength of the acidity function, pyridine adsorption was carried out from room temperature to 200°C followed by FTIR. In no case was significant adsorption determined for IRMOF-1 or MIL-53 (Al). The adsorption of pyridine in low amounts cannot, however, be ruled out, since the signals could be masked by the intense carboxylate bands. Although further investigation is required to further characterize the acid centres, we can conclude that the acidity of the Zn-OH identified is much weaker than that of the surface hydroxides of reference oxides such as silica-alumina. For the same reason, the presence of a certain number of Lewis acid sites could not be ruled out.

5.4.3. Porosity

The N_2 isotherms at 77 K (Figure 63) show a microporous structure and a specific pore size for the materials studied. Surface areas, micropore volumes and pore sizes are also reported in **Erreur ! Source du renvoi introuvable.**.

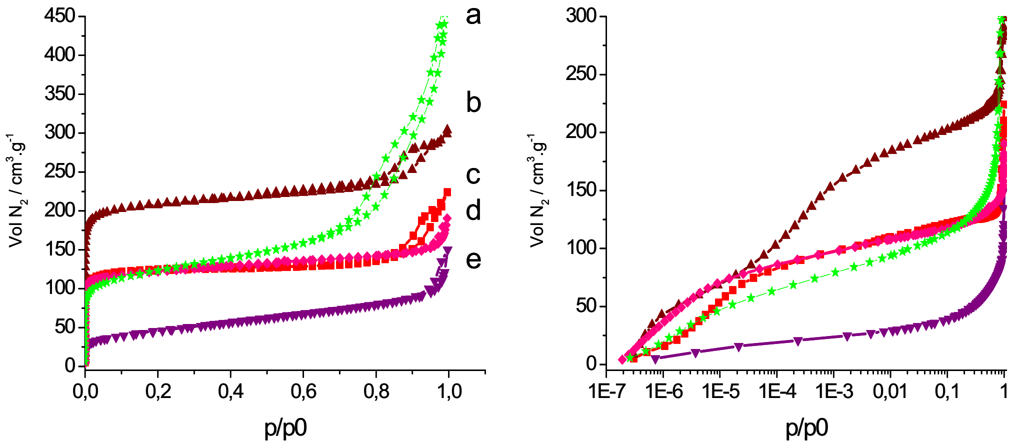

Figure 63: N_2 adsorption/desorption isotherms at 77 K in log scale (left) and linear scale (right) for: H-BEA (a), Zn-MOF-8 (b), IRMOF-1 (c), IRMOF-3 (d) and Zn-MOF-10 (e).

Table 9: N_2 physisorption results: [a] from BET analysis, [b] from t-plot analysis, [c] from DFT analysis.

Sample	Surface Area ($m^2 \cdot g^{-1}$)[a]	Pore volume / ($cm^3 \cdot g^{-1}$)	Micropore volume / ($cm^3 \cdot g^{-1}$)[b]	Pore diameter / (Å)[c]
IRMOF-1 solv	2600	0.3	1.31	-
IRMOF-1 basf	400	-	-	-
IRMOF-1 pre	450	0.32	0.18	8.8
MOF-69a	270	-	-	-
MOF-69b	970	-	-	-
MOF-69c	45	-	-	-
IRMOF-3	426	0.25	0.16	7.3
ZnMOF-8	730	0.46	0.29	7.3 / 11.6
ZnMOF-10	160	0.17	0.02	8.7
H-BEA	430	0.62	0.10	7.7

As expected, the porosity of the IRMOF-1 obtained by the solvothermal method is in good agreement with the values already reported [119]. The high surface area correlated with the XRD pattern proves the high purity of the crystalline phases. As expected, the results of the other synthesis methods are less crystalline, resulting in a decrease in the specific surface area and pore volume. Nevertheless, these results are in good agreement with those reported in the literature [48, 112]. For ZnMOF-8, despite the low resolution of the XRD patterns, the logarithmic plot shows two steps corresponding to two different pore sizes. For the MOF-69 series, the porosity of MOF-69c is very low, while MOF-69a and MOF-69b possess high specific surface areas.

5.4.4. Catalytic Tests

In order to determine the acidic potential of the MOFs studied, the Friedel-Crafts reaction was carried out. Two reasons led us to choose this reaction type: i) the catalyst can achieve the reaction with Brønsted and/or Lewis acids; and ii) the composition and the structure of the alkylating agent can modify the reactivity. Indeed, the alkyl-halides are more reactive than are alkenes or alcohols. Furthermore, if the reaction takes place with carbocation species, the most substituted agents are promoted.

One problem inherent to the Friedel-Crafts reaction comes from the reactivity of the substituted product. It is higher than that of the less-substituted aromatics regardless of the kind of acidity [99]. Consequently, several undesired polyalkylations are performed. In order to limit this issue, several research groups have worked with a high excess of aromatic reagent with respect to the alkylating agent. In our work, the reaction takes place in an autoclave under autogenous pressure. The molar ratio of aromatic to alkylating agent is 2:1. As mentioned in the Catalytic Strategy section, toluene and biphenyl are used as aromatic reagents and *tert*-BuCl as the alkylating agent. Despite the high activity of *tert*-BuCl for this reaction, HCl is a resulting subproduct and this product can be modify or destroy the catalyst. In this study, two series of experiments are carried out. The first screening is performed at high temperature (170°C) during 2 h in order to differentiate the inactive phase from the active formulation (**Erreur ! Source du renvoi introuvable.**).

Table 10: Catalytic results for the *tert*-butylation of toluene and biphenyl at 170°C after 2 h. Selectivity [a] 4-*tert*-butyltoluene, [b] 4-*tert*-butylbiphenyl, [c] sum of di-alkylated products. MIL-53 (Al) samples [d] are tested as made or after being activated either at 220°C under N_2 flow or at 170°C under vacuum (10^{-5} mbar). In all cases, meta-isomers are not detected. However, the presence of a minor quantity of meta-isomers cannot be ruled out. Key: n.a., not analyzed.

	Toluene	Selectivity			Biphenyl	Selectivity		
Catalyst	conversion	para[a]	ortho	di[c]	conversion	para[b]	ortho	di[c]
IRMOF-1 solvo	n.a.	-	-	-	n.a.	-	-	-
IRMOF-1 basf	73	84	16	0	n.a.	-	-	-
IRMOF-1 pre	73	82	18	0	37	90	6	4
IRMOF-3 [d]	0	-	-	-	0	-	-	-
Zn-MOF-8	86	84	16	0	38	97	3	0
Zn-MOF-10	86	82	18	0	39	99	1	0
MOF-69C	81	81	19	0	33	89	7	4
MIL-53(Al) [d]	0	-	-	-	0	-	-	-
H-BEA	90	72	28	0	70	66	18	16
H-MOR	n.a.	-	-	-	15	75	0	25
$AlCl_3$	64	46	54	0	64	50	35	15
$ZnCl_2$	8	77	23	0	n.a.	-	-	-

For toluene alkylation, IRMOF-3, MIL-53(Al) and $ZnCl_2$ do not work. For the other catalysts, the conversion is in the range of 70 to 80% and the selectivity is higher than 80%. Even if the conversions are lower than the H-BEA conversion, the MOFs show higher selectivity than do the reference catalysts. For biphenyl alkylation, the results confirm the same trend. Even if the conversion is lower than for zeolite and $AlCl_3$, the selectivity toward 4-*tert*-butyl-biphenyl is in the range of 90%.

In order to discriminate between the different activities of the MOFs, alkylation was carried out at 100°C (Table 4). Obviously, IRMOF-3 and MIL-53(Al) do not work at this temperature, regardless of the activation procedure applied. The conversions of the other catalysts are lower - between 8 and 62% - than for the first experiment. In these conditions, equilibrium is not achieved and it can be possible to interpret the differences in the conversion in light of the variations in IRMOF preparation protocol. As expected, the most crystalline and porous IRMOF shows the lowest conversion, around 13%.

Table 11: Catalytic results for the *tert*-butylation of toluene and biphenyl at 100°C after 2 h.

Catalyst	Toluene conversion	Selectivity para	Selectivity ortho	Selectivity di	Biphenyl conversion	Selectivity para	Selectivity ortho	Selectivity di
IRMOF-1 solvo	13	90	10	0	n.a.	-	-	-
IRMOF-1 basf	47	89	11	0	n.a.	-	-	-
IRMOF-1 pre	40	88	12	0	28	100	0	0
ZnIRMOF-1 (2.5)	30	85	15	0	n.a.	-	-	-
ZnIRMOF-1 (5)	46	86	14	0	n.a.	-	-	-
ZnIRMOF-1 (10)	36	86	14	0	n.a.	-	-	-
MOF-69C	8	90	10	0	n.a.	-	-	-
MOF-69A	15	89	11	0	n.a.	-	-	-
MOF-69B	23	90	10	0	n.a.	-	-	-
Zn-MOF-8	47	90	10	0	13	100	0	0
Zn-MOF-10	62	92	8	0	10	100	0	0
MIL-53 (Al)	0	-	-	-	n.a.	-	-	-
H-BEA	67	72	28	0	30	55	25	20
H-MOR	5	85	15	0	5	81	0	19
$AlCl_3$	n.a.	-	-	-	55	47	34	19

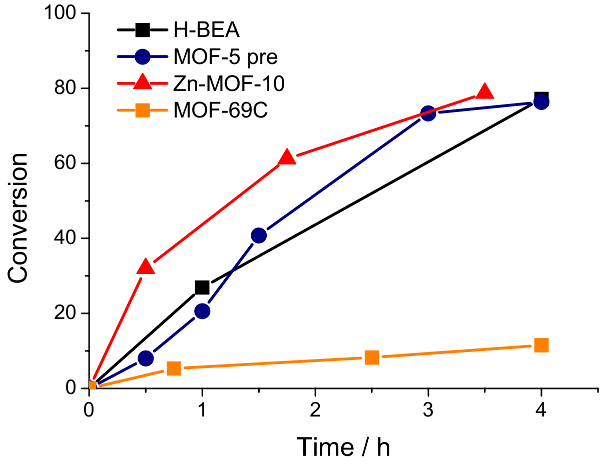

Figure 64: Kinetic curves for different catalytic samples in the *tert*-butylation of toluene at 100°C.

For all of the other IRMOFs, the conversion is around 40%, even if *o*-toluic acid is used as the ligand. We also observe significantly lower activities for MOF-69 type samples, the lowest activity being for MOF-69C which also has the lowest specific surface area. Surprisingly, Zn-MOF-8 and -10 show the highest catalytic activities, although they have similar structures to MOF-69B and MOF-69A, respectively. Kinetic studies confirm the ranking of MOF activities with Zn-MOF-10 > IRMOF-1 pre > MOF-69C (Figure 64).

It can be concluded that the conversion of H-BEA at 100°C is higher than that of the IRMOF materials, but the IRMOFs are more selective than are zeolites, irrespective of the Zn-carboxylate system or the protocol. The difference of selectivity between BEA and the IRMOFs can be explained by isomerization. Several isomerization test reactions have been performed to investigate product reactivity in MOFs. In the absence of an alkylation agent, 4-*tert*-butyltoluene does not isomerize on MOF compounds at 100°C, in contrast to acidic zeolites. This means that para-alkylation is performed during the reaction and the product does not react further, probably due to the weak acidity of the MOFs investigated. This result may explain the superior selectivity of the MOF materials.

5.4.5. Catalyst Post Characterization and Leaching Tests

Following alkylation, IRMOF-1 pre was recovered and washed with n-decane under inert atmosphere. It can be reused without any loss of conversion or selectivity. Two post characterizations, solid ^{1}H-NMR and XRD analysis, were carried out on the recovered catalyst. The first method reveals an intense peak at δ = 3.4 ppm that can be assigned to the H_3O^+ Cl^- species. The same spectrum is obtained when HCl (36%) is added to fresh IRMOF-1 pre. This means that the HCl produced during the reaction is trapped in the framework. In this case, the hydration of the acid could be a reason for the partial hydrolysis of the framework, as shown by the peak at δ = 14 ppm and the altered form of the diffractogram (Figure 65).

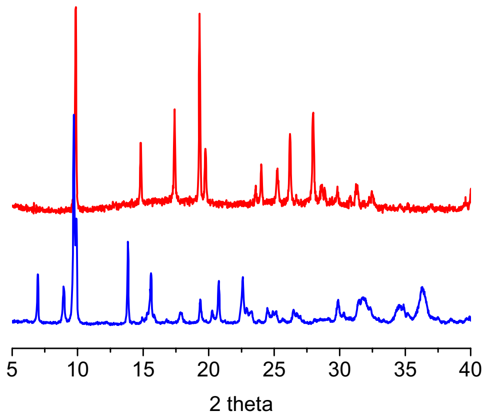

Figure 65: Powder XRD patterns of IRMOF-1 pre before (bottom) and after reaction (top).

Because the linkers from the solid framework are also made from aromatic species, one can question whether the alkylation could take place on the terephthalate linkers as well. In order to be sure that the catalyst works in heterogeneous phase and that it can be reused with no leaching effect, several analyses have to be made. After verification that the reaction does not work without the catalyst, leaching trials are carried out. After reaction, the catalyst is separated from the solution and a new reaction is started after addition of fresh reactant. No additional conversion is detected; this result confirms the hypothesis of the HCl trapped within the framework. The last experiment consists in carrying out the reaction at low temperature (50°C) in an attempt to ascertain that the catalysts are not soluble at high pressure. In these conditions, the reaction works, indicating that the IRMOFs are not soluble in n-decane and that the reaction takes place under heterogeneous conditions.

5.4.6. H-D Exchange During the Reaction

In order to determine the role of $Zn(OH)_2$, alkylation with toluene-d_8 was carried out at 100°C during 2 h. The catalyst was then recovered and characterized by solid ^{1}H-NMR.

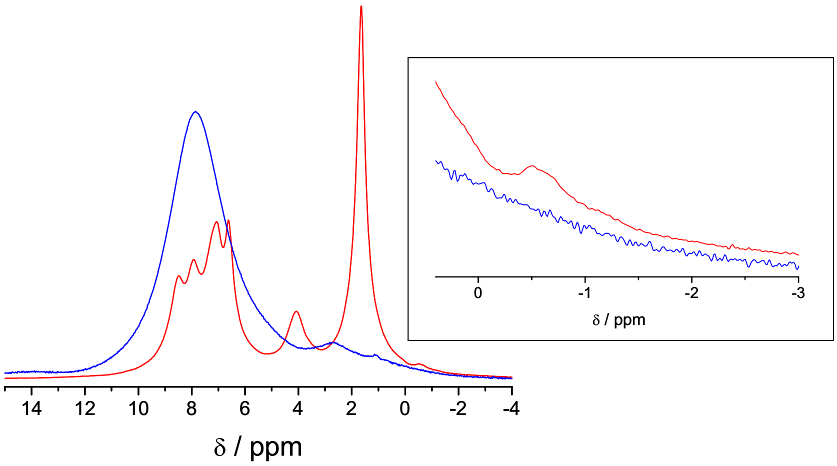

Figure 66: Solid ^1H NMR post characterization after running the alkylation with toluene-d_8.

As shown in Figure 13, the peak at -0.4 ppm, corresponding to the proton of Zn-OH species, has disappeared. This is an indication of proton exchange, which is characteristic of acidic reactions.

5.5. Discussion

The presence of Zn and Cl ions in the structure can lead to the formation of active sites for the alkylation reaction. Nevertheless, we can rule out the possibility of Zn-Cl as a catalytic species arising from structural modifications, since kinetic studies show that MOF catalysts are active as of the first minutes of operation, in contrast to MIL-101(Cr) [125]. Also, the poor activity of $ZnCl_2$ tested as a powder at 170°C (only 8% conversion) confirms that $ZnCl_2$ is not the catalytic species. In the case of IRMOFs, even if a sharp IR band at 3600 cm^{-1} is exhibited for the entire set of IRMOFs, the inactivity of IRMOF-3 is probably due to the presence of amino groups inside its structure, which could cancel the proton exchange. Another interesting result is the low activity of IRMOF-1 solvo, probably due to the high purity of the crystal. Indeed, the IRMOF structure $ZnO_4(bdc)_3$ does not possess $Zn(OH)_2$. In this case, the presence of 0.02% water in the *tert*-BuCl solution could be responsible for the partial hydrolysis of the structure. The last proof comes from the evidence of the ZnOH-ZnOD exchange during the reaction with toluene-d_8. All of these results confirm the importance of the Zn-OH species for the catalytic properties. The inactivity of MIL-53(Al) could be explained by the weakness of the acidity of bridging μ_2-OH. Even if pyridine adsorption did not allow the determination of the strength of acid sites, preliminary molecular modelling results (DFT) indicate a very low acidity of MIL-53 (Al).

All of the characterizations of IRMOF-1 (pre) are in very good agreement with the results obtained by Huang et al. [48] and Hafizovic et al. [112]. According to their results, TG analysis shows an excess of 10 wt.% Zn with respect to the IRMOF-1 structure. For Hafizovic, this excess comes from the presence of zinc hydroxide in the pores and is confirmed by the splitting of the diffraction peak at 9.7°. The authors point out, however, that other structural changes could result in the same distortion. The ^{1}H-NMR analyses carried out on the different IRMOFs confirm the presence of Zn-OH-Zn species. Recently, Hausdorf et al. [106] highlighted the transformation of IRMOF-1 into MOF-69c under moist conditions. The MOF phase is promoted under humid conditions, as is the case in our protocol. According to these results, it is possible that the IRMOF-1 also contains minor amounts of Zn-(μ_3OH)-Zn or of MOF-69c microcrystallites that are not detectable by XRD. Finally, it was recently demonstrated that pure IRMOF-1 undergoes a rapid phase transformation to MOF-69c under moist conditions that is accompanied by a drastic decrease in porous volume [128].

In the case of the MOF-69 structure, the presence of Zn-OH-Zn species is more important than the IRMOF structure, as confirmed by the ^{1}H-NMR analysis. In contrast to the specific surface area of MOF-69c, MOF-69a and b show a specific surface area that is comparable to or higher than that of IRMOF-1. A necessary result of this increase has to be an increase of the number of accessible sites in the structure. Nevertheless, the IRMOFs are more active than the MOF-69 samples, despite having far fewer sites. This indicates that Zn-μ_3OH-Zn species have a moderate activity and/or that another much more active kind of Zn-OH exists in precipitated IRMOF-1. Obviously, exposure to water at the synthesis stage and/or to humidity upon handling the IRMOF-1 samples is responsible for the generation of structural defects such as Zn-OH species. In addition, the isomorphous substitution of dicarboxylate by monocarboxylate linkers creates other types of Zn-OH species. Unfortunately, the characterization, quantification and examination of the catalytic role of these samples are made difficult by the high sensitivity of IRMOF-1 with respect to moisture.

The pore size distribution is calculated in two ways: the Horvath-Kawazoe and Density Function Theory (DFT) methods. Even if the values found are not very accurate, because the pore structure geometry of the IRMOFs and the adsorption sites are unknown, these determinations make it possible to compare classes of similar materials.

Table 12: Theoretical cage and window sizes from structural data. [a] "Free-space" diameter refers to the diameter of the largest sphere that can fit in the cage or through the window when van der Waals radii are assumed for all framework atoms from [126], [b] from [130]

	Cage free space diameter / Å	Window free space diameter / Å
IRMOF-1[a]	15.1	7.8
IRMOF-8 [a]	18.0	9.2
H-BEA [b]	6.6	6.1

According to experimental and theoretical data, the diffusion of the polyalkylated product is not disturbed by the steric hindrance of the porous solids even if there is polyalkylation. As a result, the shape selectivity observed for the IRMOFs cannot come from the steric hindrance. We suggest that the biphenyl is adsorbed onto a specific site that allows the formation of a specific product. Once alkylated, it cannot be activated in the same manner because of steric hindrance, and double alkylation cannot proceed.

5.6. Conclusion

The zeolite mimetic approach has permitted the selection and testing of several MOFs which possess hydroxide groups in their structure, such as MOF-69 and MIL-53. The ^{1}H-NMR and IR characterizations carried out have made it possible to conclude that Zn-OH species play a role in the catalytic reaction. Nevertheless, the possibility of increasing the crystal defects by using monocarboxylate linkers is very hard to interpret. Indeed, IRMOF-1 pre has the same activity as the different Zn-IRMOF-1s obtained. These results come from the presence of Zn-OH species inside the pores of the IRMOF-1 pre when, during the synthesis, no precautions against humidity are taken. Even if the creation of defects performed in this work does not make it possible to draw conclusions about their real effect on the alkylation, we believe that this method may lead to the generation of a new class of catalysts whose acidity and hydrophobic properties differ from those encountered in zeolites. We have also demonstrated that MOFs can perform 100% shape-selective catalytic alkylations of large aromatic molecules. This discovery has led us to generate a new class of Brønsted acid MOFs which are more acidic and can perform alkylation and isomerization at room temperature.

6. Chapter VI: Investigation of MIL-53 (Al, Ga) for acid Brønsted-type catalysis: Experimental and Molecular Modelling

6.1. Introduction

In order to complete the mimetic approach developed in the last section, a number of experiments have to be performed. Indeed, the low activity of the catalysts used can be explained by the weak acidity of MIL-53(Al) and by the low porosity of MOF-69c. This analysis leads us toward new objectives: porous MOFs with strong acidity must be found in order to identify an efficient alkylation catalyst, and the mechanism of the catalytic aromatic alkylation must be investigated. This is why we have chosen the MIL-53 structure for further study. This material is built from infinite chains of corner-sharing $MO_4(\mu_2\text{-}OH)_2$ (M = Al, Cr, Fe, Ga)[33, 35, 131, 132] and possesses a high specific surface area. We have limited this investigation to MIL-53 (Al) and MIL-53 (Ga), also called IM-19. The acid strength of these MOFs was tested by CO and H_3CCN adsorption, while the catalytic testing focused on the Friedel-Crafts alkylation at 100°C over different substituted aromatic compounds, in an aim to propose a reaction mechanism by using the Hammett equation.

6.2. Experimental

6.2.1. Catalysts

In this study, three MOFs and one zeolite are used as alkylation catalysts. The reference materials are MOF-69c, obtained via the protocol described in the last part, as well as H-BEA (Si/Al=13.75). The catalysts tested are MIL-53 (Al) (Aldrich, Basolite^{TM} A100) and MIL-53 (Ga), patented by Chaplais et al.[133] This protocol consists in dissolving gallium nitrate and terephthalic acid in an HF mixture. The guest molecules are removed by heating at 220°C for one day under air.

6.2.2. Catalytic Tests

In order to evaluate the activity of MIL-53 (Ga), the kinetics of toluene alkylation by *tert*-BuCl was examined under the same conditions (100°C) as for the previous study. Then, the most promising catalysts were tested for toluene alkylation with several less reactive alkyl agents such as phenol, *tert*-butanol, Cl-benzene, n-BuCl and 1-hexene. These reactions were also carried out in an autoclave with 30 mg of catalyst at 170°C for 2 h. In order to make it possible to use the Hammett equation, five alkylations with *tert*-BuCl were made on different substituted aromatic compounds: toluene, benzene, Cl-benzene, Br-benzene and NC-benzene. For the first two compounds, the conditions were identical to those employed before. On the other hand, the alkylations with the last three compounds were more difficult, so the reaction was carried out 100 mg of catalyst for 2 h for the X-Benzene and for 7 h for NC-Benzene.

6.2.3. CO and H_3CCN Adsorption

The Brønsted and Lewis acidities of MIL-53 (Al) and MIL-53(Ga) were evaluated by IR spectroscopy by following the modifications in the spectroscopic features of CO (Figure 2) and CD_3CN (Figure 3). Before the measurements, the samples were heated at 280°C in air for 24 h and then activated at 250°C under high vacuum. The IR spectra, collected at 100 K and at 303 K for CO and CD_3CN respectively, were recorded upon decreasing the partial pressures of probe molecules. Band positions and shifts were simulated by DFT in order to propose respective assignments.

6.3. Results and Discussion

6.3.1. Kinetic Results

Figure 67 shows the results of the kinetic study carried out over different catalysts. After 30 minutes, MIL-53 (Ga) leads to total conversion with 40% selectivity toward 4-*tert*-Bu-toluene. In order to ensure that the experiment takes place in heterogeneous phase, an experiment at room temperature is carried out. This experiment shows total conversion after one day. This result confirms not only the high activity of MIL-53 (Ga), but also that the catalyst is not soluble during the reaction.

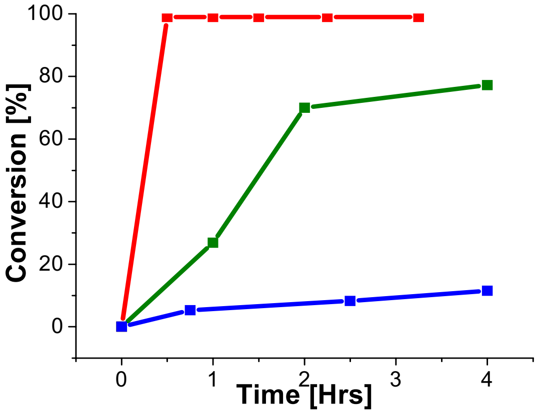

Figure 67: Conversion of toluene alkylation with *tert*-BuCl at 100°C: MIL-53 (Ga) (red), H-BEA (green) and MOF-69c (blue).

Moreover, the chemical analysis carried out after filtration does not reveal the presence of Ga cation inside the solution. This test confirms that MIL-53 (Ga) is not destroyed during the reaction. In view of the high activity of this material, other reactions were attempted using various alkyl agents: chlorobenzene, phenol, n-BuCl, 1-hexene and *tert*-BuOH. None of these reactions proceeded. One reason could be the combination of the setup and the organic framework of the MOF. Indeed, since these molecules are more difficult to alkylate, the temperature and/or pressure generally have to be increased. Unfortunately, one of the weaknesses of MOFs is that their organic framework causes a low thermal stability. The experiments performed at higher temperature simply destroy the catalyst. An alternative could be to increase the pressure, but our setup does not permit this. Under these conditions, we cannot draw conclusions regarding the activity of MIL-53 (Ga) toward these compounds.

6.3.2. IR Study

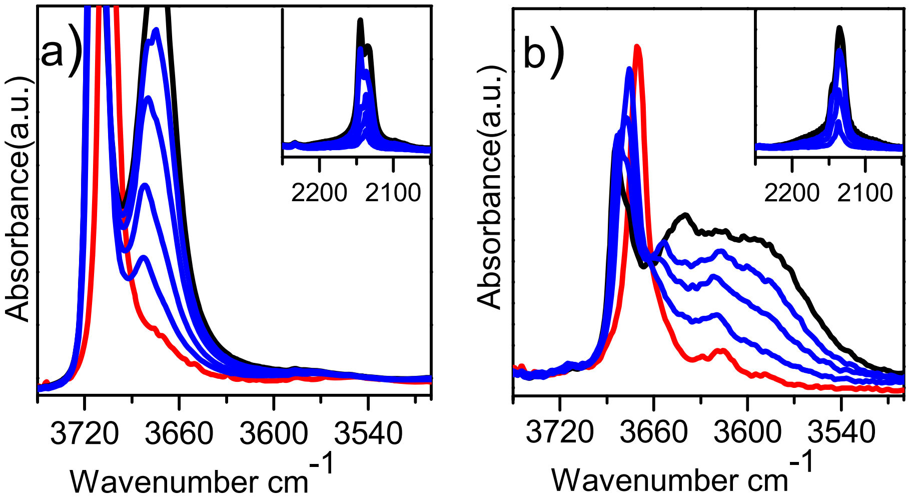

Figure 68: FTIR spectra of CO adsorbed at 100 K: spectra collected at RT under vacuum (red); spectra collected at 100 K in the presence of 40 mbar of CO (black); and spectra collected at decreasing coverage and increasing temperatures (blue). Part a) represents MIL-53(Al); part b), MIL-53(Ga).

Theoretical calculations are in very good agreement with experimental data for ν(OH) bands: 3709 (th) and 3704 cm^{-1} (exp) for MIL-53(Al); and 3663 (th) and 3669 cm^{-1} (exp) for MIL-53(Ga). The cooling of the samples induces small blue hydroxyl shifts of Δν = +10 and +15 cm^{-1} for Al and Ga samples, respectively. This phenomenon is probably due to a response of the flexible structure of the framework to a change in temperature. Upon CO adsorption[134], rather small red shifts appear in the –OH vibration regions, together with very small blue and red shifts in the C≡O region.

In particular, for MIL-53(Al), Δν(OH) = - 30/-50 cm^{-1} while for MIL-53(Ga), Δν = -50/-100 cm^{-1} are observed. Surprisingly, a parallel perturbation in the CO stretching region is not present. In fact, in both cases, the main absorptions are detected around the CO liquid-like frequency (*ca.* 2140 cm^{-1}): namely doublets at 2145-2137 cm^{-1} and 2147-2137 cm^{-1}, respectively. These bands are reversible only upon prolonged outgassing, which indicates that they are associated with some stable adduct.

Theoretical calculations indicate four main adsorption modes for CO:

1 - The traditional "C adduct" -OH···CO

2 - A reverse "O adduct" -OH···OC

3 - A bridging adduct -OH···OC···OH- at the centre of the cavity

4 - A benzene adduct, B···CO is near the benzene ring (B) of the linker. Several orientations have been studied (see Supporting Information). Contrary to the results obtained by Camarota et al.[135] on phenylene periodic mesoporous organo-silica with crystalline walls, it is not possible to stabilize any M-OH···CO···B or M-OH···OC···B adducts due to excessive distances between M-OH and B.

Adsorption energy and frequency calculations show that these four kinds of adducts exhibit quite similar stabilities. The C adduct, however, remains the most stable, and leads to the highest □□(OH), but to very small expected blue shifts in the CO region (2145 cm^{-1}), in agreement with experiments. The three other modes induce very small calculated □□(OH) and slightly negative CO shifts (from 2142 to 2131 cm^{-1}), which may explain the lower frequency component of the experimental doublet. As a synopsis, the experiments in combination with theory show that the CO region is very poorly discriminating with respect to the relative acidities of these materials, but the OH region allows us to conclude that the Brønsted acidity follows the order: MIL-53(Al) < MIL-53(Ga). Note that only the MIL-53(Al) sample shows a small presence of Lewis sites (band at 2230 cm^{-1}), likely due to the external surface of the material. The higher Brønsted acidity shown by MIL-53(Ga) is further confirmed upon CD_3CN adsorption (Figure 3)[136].

In both samples, however, both OH and CN shifts are very modest, lower than those observed for silicalite[136]. Also, for both samples, a very small fraction of Lewis sites is revealed (weak bands at around 2320 cm^{-1})[137]. Calculations predict -OH···NC-CH_3 adducts, with a higher red / blue shift in the OH / CN region for MIL-53(Ga) (for example, Δv_{CN} = +17 and +23 cm^{-1} for MIL-53(Al) and MIL-53(Ga), respectively).

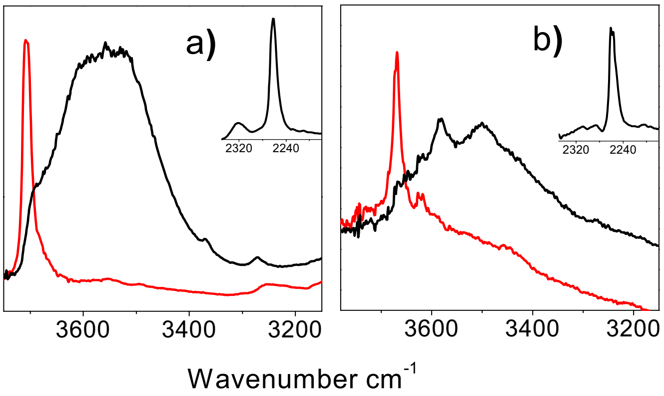

Erreur ! Source du renvoi introuvable.: FTIR spectra of adsorbed CD_3CN: spectra collected at RT under vacuum after activation (red); spectra collected in presence of vapour pressure of CD_3CN (black). Part a) represents MIL-53(Al); part b), MIL-53(Ga).

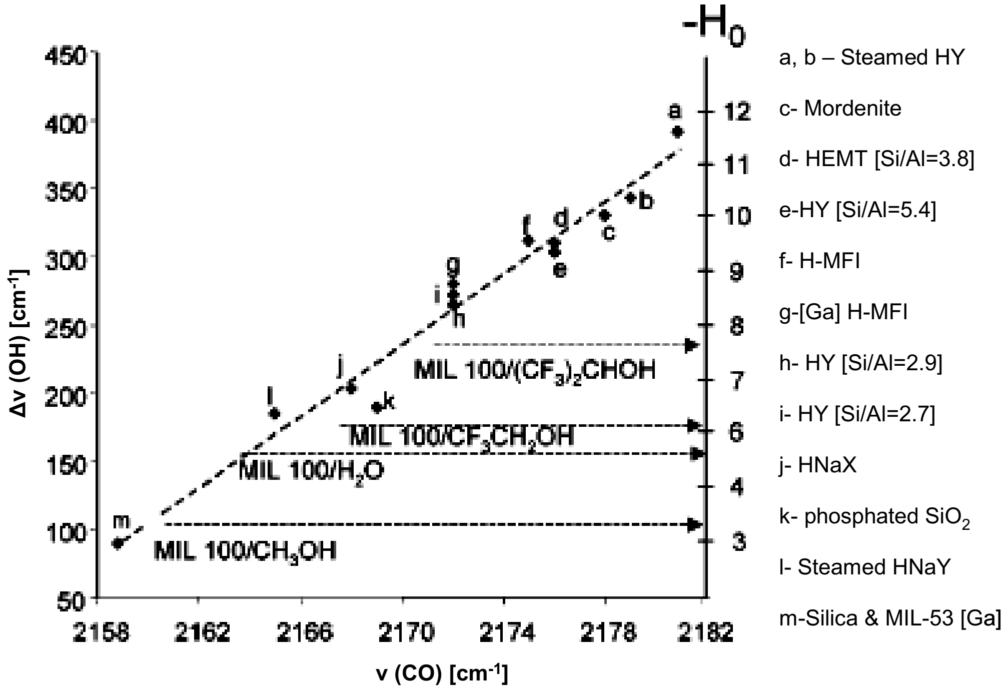

Figure 69: Brønsted acid strength of OH groups from various grafted species on MIL-100(Cr) measured by CO adsorption, figure from [138].

From adsorption measurements and molecular modelling, it can be concluded that MIL-53 presents a very mild Brønsted-type acidity even weaker than that found in silica[139], the Ga form being more strongly acidic than the Al form.

6.4. Reaction Mechanism

The Hammett equation[140] is an appropriate tool for identifying the type of reaction mechanism. Indeed, this equation is a linear free energy relationship correlating the activity of a reaction with different substituted reactants.

Equation 6: $$-RT\ln\left(K^{X}\right)+RT\ln\left(K^{0}\right)=\Delta G=\frac{A}{d^{2}}\left(\frac{B_1}{D}+B_2\right)$$

Here, K^X is the rate constant for a substituted reactant, K^0 is the rate constant for an unsubstituted reactant, R is the perfect gas constant, T is the temperature, ΔG is the free energy, d is the distance from the substituent to the reacting group, D is the dielectric constant of the reaction medium, and A, B1 and B2 are constants that are independent of the temperature and solvent. If the reactions are carried out using the same solvent, concentration and temperature, the equation can be rewritten as:

Equation 7 : $$\log\left(\frac{k^{X}}{k^{0}}\right)=\sigma\rho$$

Here, k_0 is the equilibrium constant for X = H, k is the equilibrium constant for the group X, ρ is a constant for a given reaction under a given set of conditions and σ is a constant characteristic of the group X.

Table 13: σ value for several substituents.

benzene-x	benzene-CH_3	benzene-H	benzene-Cl	benzene-Br	benzene-CN
σ	-0.14	0	0.24	0.26	0.7

According to Equation 7, if we plot $\log\left(\frac{k^{X}}{k^{0}}\right)=f(\sigma)$ for these five alkylations with *tert*-BuCl, we have to obtain a straight line if there is only one kind of reaction. The slope of the line gives two pieces of data: i) the charge of the intermediate and ii) an estimation of the heat of reaction[141]. In summary, if the slope is negative, then the intermediate is destabilized by the -i substituent effect, and consequently, the charge of the intermediate is positive. If the slope is positive, the charge is negative. Since the acidic intermediate possesses a positive charge, the form of the curve allows us to propose a reaction mechanism.

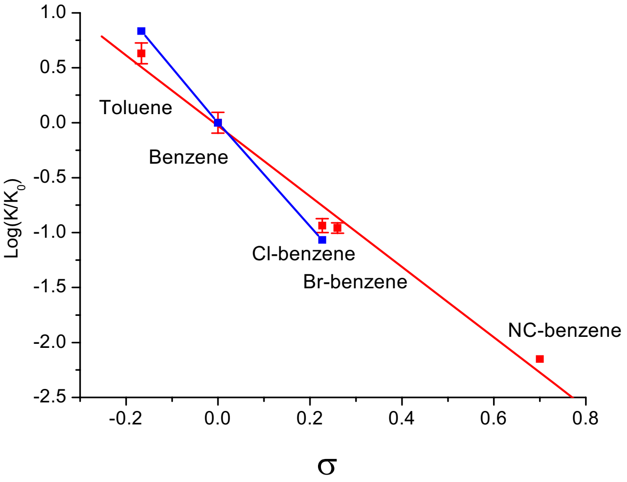

Figure 70 : Effect of the substituent on the alkylation rate over MIL-53(Ga) (red) and HY20[99].

The results obtained for the alkylation with the various aromatic molecules gives a straight line with negative slope. This experiment has therefore made it possible to determine that there is only one reaction and that the charge of the intermediate is positive, which corresponds to an acidic reaction. According to the two slopes of this figure, the acidity of MIL-53 (Ga) is weaker than the acidity of HY20. This result is in good agreement with the IR study. Nevertheless, it is very surprising that we obtain an acidic reaction with a very low acidity strength determination. According to these results, we can propose a reaction mechanism for the alkylation of toluene by *tert*-Butyl-Cl with MIL-53(Ga) (Figure 75).

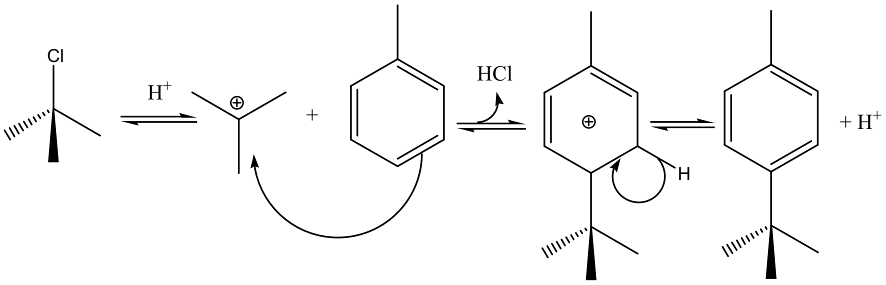

Figure 75: Proposed reaction mechanism for the alkylation of toluene by *tert*-Butyl-Cl with MIL-53(Ga).

6.5. Conclusion

The IR study has revealed that the principal kind of acidity in the MIL-53 structure is of the Brønsted type, even if the acid strength observed is lower than that of silica. On the other hand, the straight line obtained by the plotting of the Hammett equation corresponds to an acidic reaction. The combination of these two results suggests that the bridging hydroxides are responsible for the catalytic effect. Given these results, one could expect the mimetic approach to be a good strategy for finding a catalytically active MOF. We can anticipate that other rod-like structures exhibiting bridging –OH, such as MIL-68, could also lead to new catalysts. A French patent, n° 08/05.536, has been issued following this study.

7. Conclusion Générale

Ce travail a été effectué dans le cadre d'un programme intégré européen TopCombi qui avait pour objectifs généraux de développer des méthodes « haut –débit »HD pour accélérer les découvertes de nouveaux catalyseurs et adsorbants. Le sous-projet dans lequel j'ai initié la thèse consistait à découvrir de nouveaux adsorbants pour la purification du gaz naturel par des méthodes HD avec un cahier des charges fourni par Eni. J'ai débuté ce travail en Fév 2006 lors de mon stage de Master. A cette période, les publications sur les MOFs comme adsorbants étaient encore relativement limitées. Elles étaient surtout orientées vers la synthèse de MOF à volume poreux très élevé pour le stockage de H_2, CH_4 et CO_2. Il y avait alors encore très peu d'études sur la séparation et sur la capture du CO_2 dans le gaz naturel, en vu d'une application industrielle.

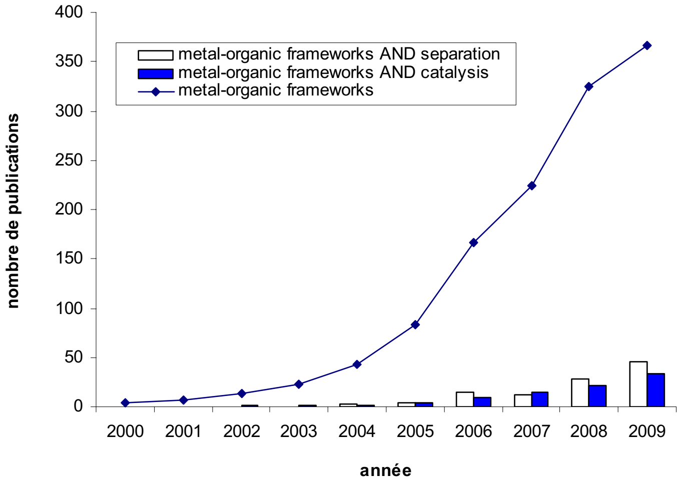

Figure 71 : Nombre de publication traitant des MOFs en fonction de l'année.

Sur les MOFs, les questions posées étaient alors :

- Existe-t-il des MOFs avec des structures poreuses et des propriétés de polarités adéquates ?
- Les MOFs sont-ils suffisamment stables ?
- Peut-on en produire de grosses quantités avec des méthodes compatibles avec les installations courantes ?

Ainsi que des questions d'un point de vue méthodologique comme :

- Quelles méthodes de synthèses peuvent être utilisées ?
- Quelles méthodes de mesures d'adsorption (équilibre / transitoire ; volumétrique / gravimétrique) ?
- Quels critères de classement, sélections ?

TopCombi avait pour contexte, entre autre, d'accélérer les découvertes par les outils et méthodes combinatoires. Vers la mi-thèse, nous disposions de bibliothèques de MOFs et de plusieurs plateformes de tests en catalyse. Ainsi, nous avons entrepris dans une démarche exploratrice, l'évaluation des MOFs en diverses catalyses acides et d'oxydations. Parmi elles, deux « hits » ont été obtenus. Le premier était inattendu. l'IRMOF-1 pour l'alkylation. Aussi, nous nous sommes concentrés sur son étude en l'ouvrant à d'autres catalyseurs en fin de thèse. Le second système est en cours d'étude au laboratoire.

Au niveau synthèse, nous avons montré qu'il est possible d'obtenir de nombreux solides de types MOFs. Par la technique de précipitation à température ambiante. Les études de faisabilité ont porté sur les systèmes Cu/trimesic acid et Zn/terephthalic acid. Pour le premier, le composé HKUST-1 est obtenu avec une très haute surface BET (>1500$m^2.g^{-1}$) après 1h d'agitations. Ce composé est obtenu de façon reproductible avec un rendement autour de 70%.

En se basant sur la méthode de précipitation, nous avons développé un protocole de criblage combinatoire. Le principe de cette méthode est de solubiliser les précurseurs métalliques et l'acide carboxylique dans différents solvants organiques polaires (DMF, DMSO, MeOH) et des mélanges (THF/H_2O), puis d'ajouter une base organique avec différents pKa (DBU, ET_3N, Dabco, imidazole, pyridine, di-tert-butylpyridine) en vu d'accélérer la formation des carboxylates. En partant d'un couple précurseur métallique/ligand, un plan d'expériences de 24 synthèses est généré. Dans la majorité des systèmes, nous avons observé que la diversité engendrée par la combinaison des paramètres est suffisante pour obtenir des phases pures et/ou des mélanges. Au total, 50 systèmes Metal/Ligand ont été criblés avec un total supérieur à 600 synthèses d'échantillons. Dans cette thèse, les phases Ln(btc) ont été découvertes par cette méthode. Dans le même temps, Guo publiait la même famille cristalline $Dy(BTC)(H_2O)\cdot(DMF)$[83]. D'autre part, de nombreuses phases dans d'autres systèmes ont été mises à jour. Cependant, nous n'avons pas poursuivi les travaux de caractérisations car ces phases étaient peu poreuses (S_{BET}<50m^2.g^{-1}). De plus, cette méthode de synthèse qui favorise la vitesse de nucléation, n'est pas adaptée à l'obtention de monocristaux de tailles compatibles pour une résolution structurale par des moyens classiques. Ceci constitue le principal frein de cette méthode pour la découverte de nouveaux MOFs. Une autre limitation de cette méthode est la difficulté de solubiliser les différents réactifs à température ambiante Ce qui amène à utiliser des solutions peu concentrées ($2.6*10^{-2}$ mol.L^{-1}) dans certains systèmes.

En marge de cette thèse, cette technique de criblage a été utilisée par d'autres collaborateurs dans divers programmes sur les MOFs. Plusieurs nouveaux matériaux ont été découverts, notamment IHM-2 et SIM-1.

Les déterminations des chaleurs d'adsorption de six gaz sur le HKUST-1, IRMOF-1 et IRMOF-3 ont pu être effectuées à l'aide de 3 techniques différentes, le TAP, la simulation GCMC (collaboration Prof. R. Snuur) et par méthode gravimétrique. Dans le cas des IRMOFs, la corrélation existant entre ces trois techniques est bonne. En revanche, pour l'HKUST-1, la divergence entre les résultats obtenus par l'expérience et la simulation est plus prononcée. Ce phénomène pourrait s'expliquer par la présence de molécules dans la porosité de la structure qui gênent l'accessibilité des sites actifs du MOF lors de l'utilisation des méthodes expérimentales qui n'existent pas dans la simulation. D'autre part, ce travail a permis de montrer le faible effet de la fonctionnalisation des MOFs par des fonctions -NH_2, pour l'adsorption du CO_2. Ainsi, nous avons privilégié la conception de nouveaux MOFs vers des solides dont les tailles de pores sont plus petites (par rapport à l'IRMOF et l'HKUST-1) plutôt que la fonctionnalisation du réseau par des groupes basiques.

Parmi les ligands sélectionnés pouvant éventuellement conduire à des MOFs de « petites » tailles de pores, le trimisate a le double avantage de posséder trois groupes chélatants (donc une plus forte densité) et un angle entre les fonctions carboxylates pouvant conduire à la formation de cavités circulaires. Le criblage a été orienté vers des éléments Ln pour deux raisons. i) ils sont connus pour la richesse de leurs modes de coordinations et ii) les oxydes de Ln sont connues pour leurs fortes aptitudes à adsorber le CO_2. Cette stratégie a permis de trouver plusieurs solides de type Ln(BTC) avec Ln = La, Ce, Sm, Gd, Nd et Tb ainsi qu'une autre phase avec Ln= La, Ce, Nd, Pr et Tb. Pour La(BTC), une étude structurale a été réalisée en collaboration avec JL Paillaud (Mulhouse) concluant à une structure de groupe d'espace $P4_322$ similaire aux résultats de Guo et al pour la phase $Dy(BTC)H_2O$. Ces matériaux possèdent des pores unidimensionnels cylindriques tortueux de petites tailles, 7*7 Å avec des passages plus petits à 5.3Å, ainsi qu'une bonne stabilité thermique. Par contre notre étude de la porosité nous a donnée une surface spécifique de $300m^2.g^{-1}$, V_{por}=0.17 $mL.g^{-1}$, contre $600m^2.g^{-1}$. La forme de l'isotherme (type I) et les valeurs montrent clairement, que le solide est microporeux avec des petits pores, plus proches des valeurs des zéolithes. Les capacités d'adsorption du CO_2 pour La(BTC) sont assez proches de l'objectif des 50 $cm^3.NTP.g^{-1}$ à 5 bars (première étape du cahier des charges). Malheureusement, la cinétique d'adsorption du CO_2 est extrêmement lente. Plusieurs jours (>2) sont nécessaires pour réaliser une isotherme. La structure poreuse tubulaire unidimensionnelle et tortueuse et de petite dimension (passage à 7x5Å) est probablement à l'origine de cette diffusion particulièrement lente. Même si nous n'avons pas observé des phénomènes de « respiration », il est possible qu'un certain degré de flexibilité existe dans la structure pouvant engendrer des phénomènes dynamiques hôtes-invités. En conséquence, ces matériaux ne peuvent pas être utilisés comme adsorbants dans un procédé PSA.

Les résultats obtenus sur l'effet catalytique des MOFs semblent être les plus prometteurs. Le désigne de MOF par approche mimétique des zéolithes nous a conduit à sélectionner des structures microporeuses présentant des ponts hydroxyles (structure MOF-69, MIL-53). Grâce aux résultats obtenus par les analyses RMN et IR nous avons pu mettre en évidence que les fonctions Zn-OH possèdent un rôle clé sur l'activité catalytique des composés sans pour autant pouvoir déterminer un mécanisme réactionnel. Même si nous avons pu créer des défauts dans la structure cristalline en substituant un diacide par un monoacide, nous n'avons pas pu noter un impact sur la conversion. Une raison à ce phénomène pourrait être la formation de particules de type $Zn(OH)_2$ dans la structure lorsque le composé n'est pas conservé dans un endroit sec. Enfin, nous avons pu montrer que les IRMOFs possèdent une très bonne sélectivité lors des alkylations de composés polyaromatiques. Cette information nous a permis de tester une nouvelle classe de MOFs possédant des sites d'acide de Brønsted qui donnent lieu à de nouveaux effets catalytiques.

Nous avons ensuite étudié les propriétés de la structure MIL-53 à base de Ga et Al. Nous avons pu montrer que le MIL-53(Ga) est très actif avec une conversion totale à température ambiante. En revanche, la sélectivité de la réaction avec ce type de catalyseur ne dépasse pas 35%. Pour déterminer le mécanisme réactionnel de cette réaction, deux études sont effectuées parallèlement. i) La détermination de la charge de l'intermédiaire réactionnelle a été déterminée en utilisant l'équation de Hammett. Cette dernière a révélé la présence d'un intermédiaire à charge positive caractéristique d'un mécanisme acide. ii) La détermination de la force acide de ces composés a été effectuée par étude IRTF par adsorption de molécules sondes (CO et CH_3CN) en collaboration avec Prof S. Bordiga (Turin). Cette étude a montré que les forces acides Ga-OH de ces composés sont faibles, similaires à des silanols acides et qu'il existe très peu de sites de Lewis. Au premier abord, la force de l'acidité telle que mesurée n'est pas en adéquation avec les activités catalytiques. Cependant, on peut émettre l'hypothèse d'un mécanisme concerté impliquant deux sites diamétralement opposés grâce à la flexibilité du réseau.

Au vu des résultats de ces travaux sur la capacité d'adsorption ou de catalyse des MOFs, ces composés semblent posséder un réel potentiel. La diversité des cations et des ligands utilisés ainsi que de la possibilité de fonctionnaliser la structure selon les besoins de la réaction donnent un atout indéniable à l'utilisation de ces matériaux pour des réactions où les matériaux connus sont inefficaces. En revanche les problèmes de stabilité thermique limitent leurs utilisations pour des applications orientées vers le raffinage.

Au niveau séparation les perspectives de ces travaux seraient de continuer les recherches en vu d'obtenir des composés possédant des réseaux poreux tridimensionnel de nature microporeuse.

Appendix

Summary structure table

Nom	Famille	structure	metal	Ligand
MIL-53	MOF	1D	Al, Ga	A.Terephtalique
MIL-68	MOF	1D	Al, Ga, In	A.Terephtalique
HKUST-1	MOF	3D	Cu	A.1,3,5 tribenzoïque
IRMOF-1 (MOF-5)	MOF	3D	Zn	A.Terephtalique
IRMOF-8	MOF	3D	Zn	A.Naphtalenedicarboxylique
IRMOF-10	MOF	3D	Zn	A.Biphenyldicarboxylique
MOF-69c	MOF	1D	Zn	A.Terephtalique
H-BEA	Zéolithe	3D	-	-
H-MOR	Zéolithe	1D	-	-

Some XRD patterns from the screening

Terephthalic acid

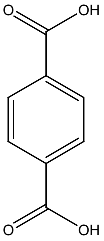

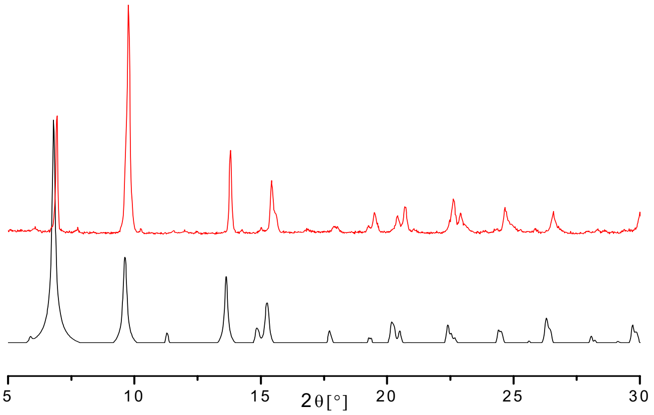

Figure 72 : XRD patterns of IRMOF-1 by precipitation way (top) and Huang[48] result (bottom).

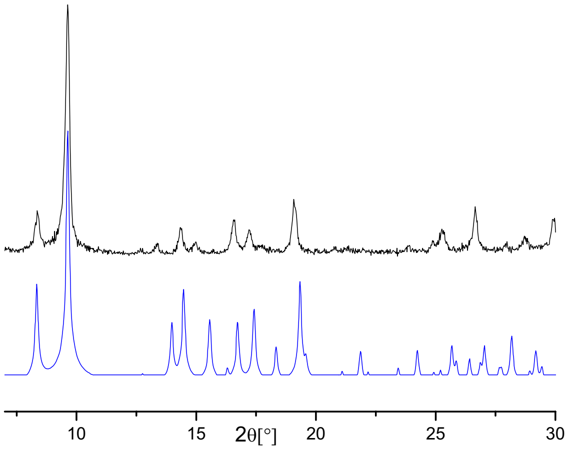

Figure 73 : XRD patterns of MOF-68(In) by precipitation way (top) and Férey[142] result (bottom).

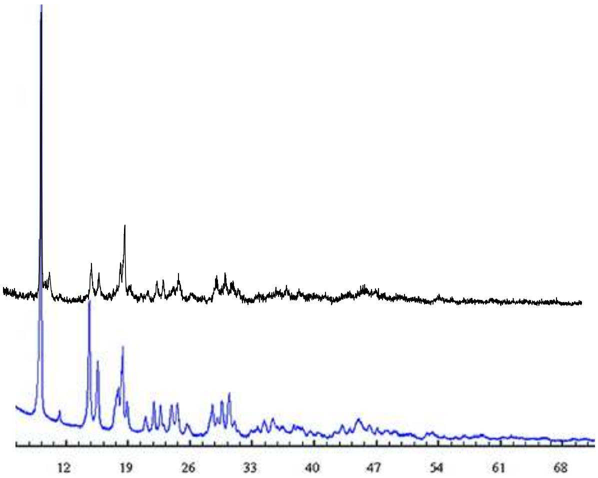

Figure 74 : XRD patterns of $Ln_2(TT)_3(H_2O)_4$ by precipitation way (top) with Ln= La, Ce and Nd, and Kerbellec[143] result (bottom).

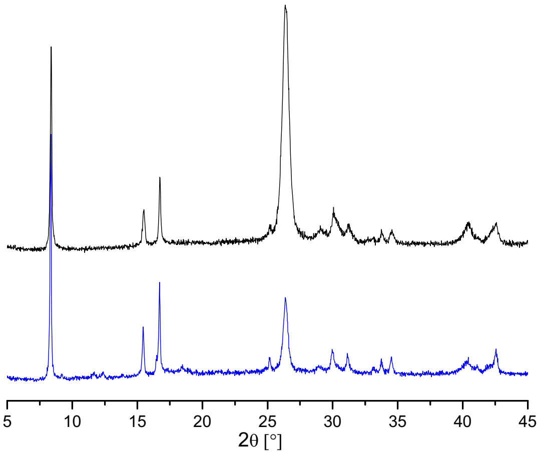

Figure 75 : XRD patterns of Cu-TT parameters with Et_3N (top) and dabco(bottom).

Muconic acid

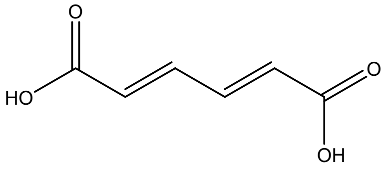

- With Cu

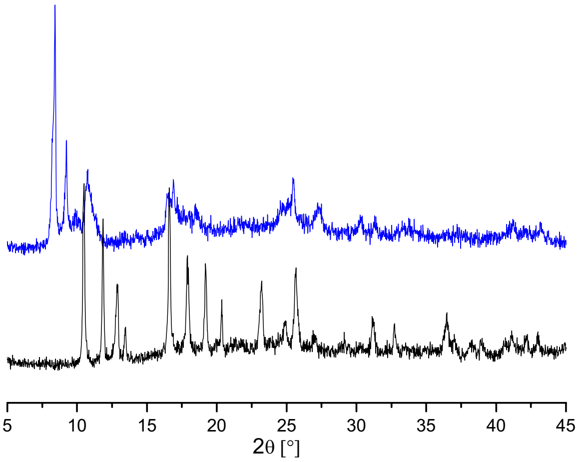

Figure 76 : XRD patterns of Cu-muco parameters with DMF (top) and DMSO (bottom).

- With Zn

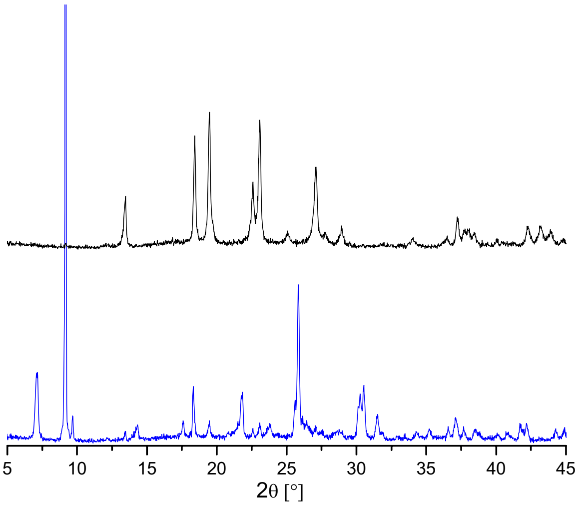

Figure 77 : XRD patterns of Zn-muco parameters with DMF (top) and DMSO (bottom).

- With Ln

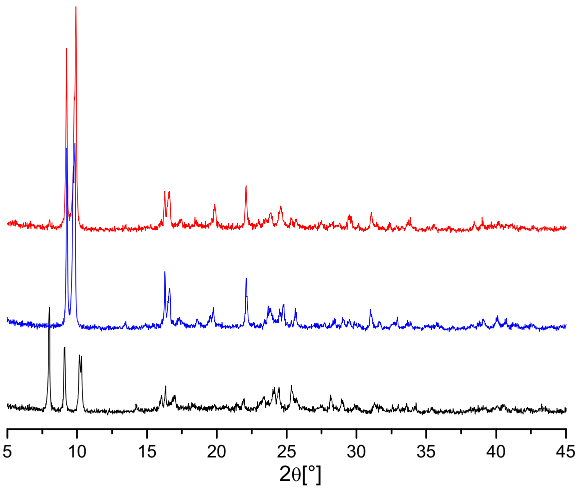

Figure 78 : XRD patterns of Nd-muco (Top), Ce-muco (middle) and La-muco (bottom) in DMF

Malonic acid

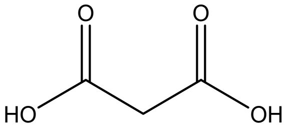

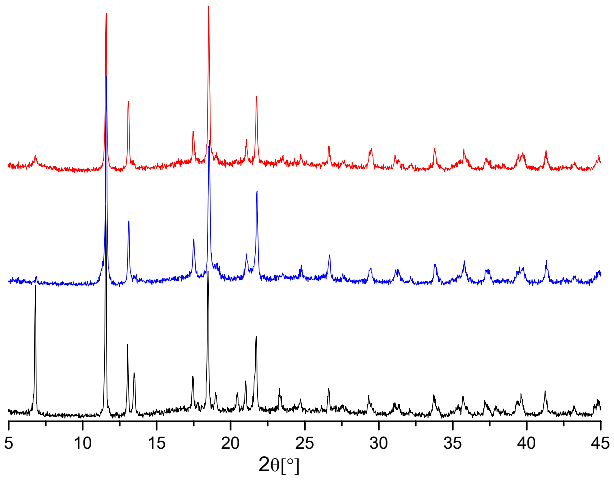

Figure 79 : XRD patterns of Zn-malo parameters with DMF (top), EtOH (middle) and DMSO (bottom).

Maleic acid

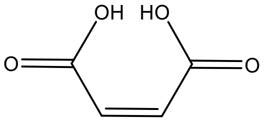

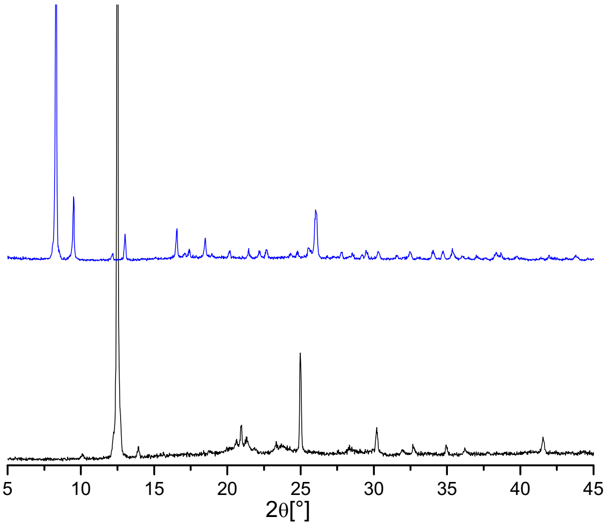

Figure 80 : XRD patterns of Zn-maleic parameters with Zn (top) and Cu (bottom).

Trans-CHD

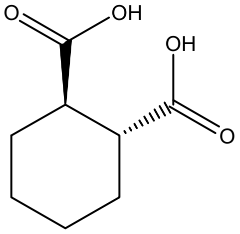

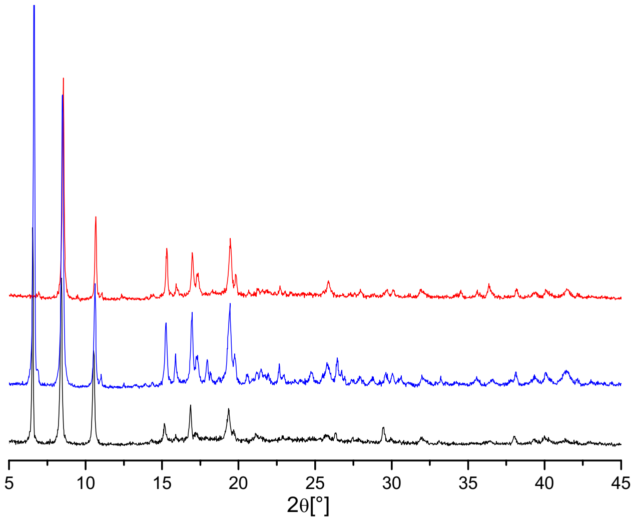

Figure 81 : XRD patterns of Zn trans-CHD with dabco, THF (top), EtOH (middle) and DMF (bottom).

Cis-CHD

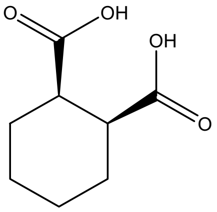

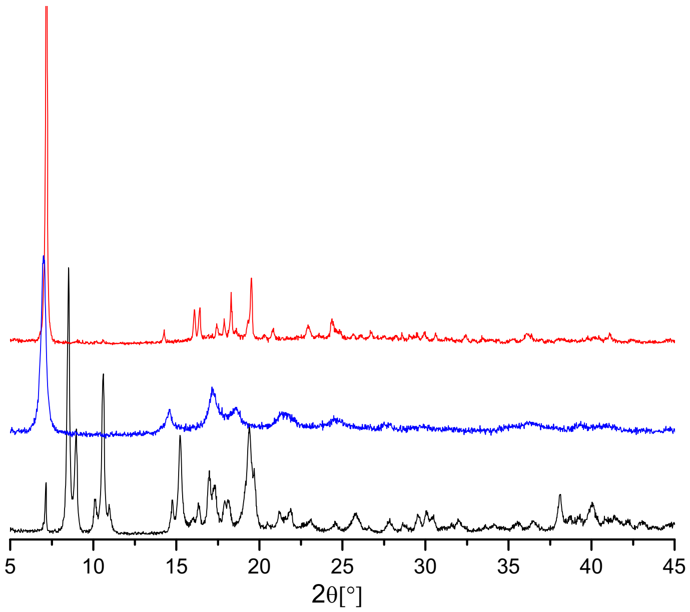

Figure 82 : XRD patterns of Cis-CHD with dabco, Zn, EtOH (top), Cu EtOH (middle) and Zn THF (bottom).

Moreover these few ligands used, we also work with the 2,5 pyridinedicarboxylic acid, acetylenedicarboxylic acid, *p*-phenylenediacetic acid and the Nitrilotri-methylphosphonic acid. But we have not obtained any interesting phases.

1. D. H. Everett and J. C. Powl, *J. Chem. Soc., Faraday Trans. 1*, 1976, **72**, 619-636.
2. Derouane, *chemical Physics Letters*, 1987, **142**, 200-2004.
3. A. J.-M. Derouane. E. G, Lucas.A A, *journal of catalysis*, 1988, **110**, 58-73.
4. A. Corma, *Nature*, 2009, **461**, 182.
5. D. W. Breck, *Zeolite molecular sieves*, 1974, John Willey & Sons, New York.
6. R. Babarao, Z. Q. Hu, J. W. Jiang, S. Chempath and S. I. Sandler, *Langmuir*, 2007, **23**, 659.
7. C. A. Armengol. E, Garcia. H and Primo. J, *Applied catalysis A-general*, 1997, **149**, 411.
8. R. M. Barrer, *Zeolites and clay materials as sorbents and molecular sieves*, Academic Press, London, 1978.
9. J. Weitkamp, *Solid State Ionics*, 2000, **131**, 175-188.
10. R. L. Nargin. G, Rajic. N, *zeolites*, 1991, **11**, 192-194.
11. K. V. Rajic. N, Stojakovic. D, *zeolites*, 1990, **10**, 169-173.
12. J. L. Paillaud, B. Harbuzaru, J. Patarin and N. Bats, *Science*, 2004, **304**, 990-992.
13. L. Kang, W. Deng, T. Zhang, Z. Liu and K.-L. Han, *Microporous and Mesoporous Materials*, 2008, **115**, 261-266.
14. H. Park, J. F. Britten, U. Mueller, J. Lee, J. Li and J. B. Parise, *Chemistry of Materials*, 2007, **19**, 1302-1308.
15. B. Panella and M. Hirscher, *Adv. Mater.*, 2005, **17**, 538-+.
16. J. Lee, J. Li and J. Jagiello, *Journal of Solid State Chemistry*, 2005, **178**, 2527-2532.
17. L. Bastin, P. S. Barcia, E. J. Hurtado, J. A. C. Silva, A. E. Rodrigues and B. Chen, *The Journal of Physical Chemistry C*, 2008, **112**, 1575.
18. F. Xamena, A. Abad, A. Corma and H. Garcia, *Journal of Catalysis*, 2007, **250**, 294-298.
19. D. Mravec, P. Zavadan, A. Kaszonyi, J. Joffre and P. Moreau, *Applied Catalysis a-General*, 2004, **257**, 49-55.
20. J. H. Clark and D. J. Macquarrie, *Organic Process Research & Development*, 1997, **1**, 149-162.
21. M. T. B. B. D. V. J. H. G. L. Ying Lu, 2008, pp. 2411-2417.
22. S. Opelt, S. Türk, E. Dietzsch, A. Henschel, S. Kaskel and E. Klemm, *Catalysis Communications*, 2008, **9**, 1286-1290.
23. N. V. Maksimchuk, M. N. Timofeeva, M. S. Melgunov, A. N. Shmakov, Y. A. Chesalov, D. N. Dybtsev, V. P. Fedin and O. A. Kholdeeva, *Journal of Catalysis*, 2008, **257**, 315-323.
24. J. Gascon, U. Aktay, M. D. Hernandez-Alonso, G. P. M. van Klink and F. Kapteijn, *Journal of Catalysis*, 2009, **261**, 75-87.
25. R. Banerjee, H. Furukawa, D. Britt, C. Knobler, M. O. Keeffe and O. M. Yaghi, *Journal of the American Chemical Society*, 2009, **131**, 3875-3877.
26. K. Seki, *Langmuir*, 2002, **18**, 2441-2443.
27. A. G. Wong-Foy, A. J. Matzger and O. M. Yaghi, *Journal of the American Chemical Society*, 2006, **128**, 3494-3495.
28. G. Ferey, C. Mellot-Draznieks, C. Serre, F. Millange, J. Dutour, S. Surble and I. Margiolaki, *Science*, 2005, **309**, 2040-2042.
29. G. Férey, *Journal of Solid State Chemistry*, 2000, **152**, 37-48.
30. M. O'Keeffe, M. Eddaoudi, H. Li, T. Reineke and O. M. Yaghi, *Journal of Solid State Chemistry*, 2000, **152**, 3-20.

31. N. L. Rosi, M. Eddaoudi, J. Kim, M. O'Keeffe and O. M. Yaghi, 2002, pp. 401-404.
32. J. L. C. Rowsell and O. M. Yaghi, *Microporous Mesoporous Mater.*, 2004, **73**, 3.
33. L. Hamon, C. Serre, T. Devic, T. Loiseau, F. Millange, G. r. FeÌ□rey and G. D. Weireld, *Journal of the American Chemical Society*, 2009, **131**, 8775-8777.
34. K. M. Barthelet, J. Ferey, G. Riou, D, *Chem. Commun.*, 2004, **5**, 520-521.
35. T. L. Volkringer, N. Guillou, G. Ferey, S. Bourrely, *Studies in surface science and catalysis* 2008, **174 a**, 447-450.
36. H. F. Clausen, R. D. Poulsen, A. D. Bond, M.-A. S. Chevallier and B. B. Iversen, *Journal of Solid State Chemistry*, 2005, **178**, 3342-3351.
37. O. M. Yaghi, M. O'Keeffe, N. W. Ockwig, H. K. Chae, M. Eddaoudi and J. Kim, *Nature*, 2003, **423**, 705-714.
38. R. Morris and P. Wheatley, *Angew. Chem., Int. Ed.*, 2008, **47**, 4966-4981.
39. A. K. Cheetham, G. Ferey and T. Loiseau, *Angewandte Chemie-International Edition*, 1999, **38**, 3268-3292.
40. S. Kitagawa, R. Kitaura and S. Noro, *Angewandte Chemie-International Edition*, 2004, **43**, 2334-2375.
41. C. N. R. Rao, N. Srinivasan and R. Vaidhyanathan, 2004, pp. 1466-1496.
42. M. J. Rosseinsky, *Microporous and Mesoporous Materials*, 2004, **73**, 15-30.
43. J. R. Long and O. M. Yaghi, *Chemical Society Reviews*, 2009, **38**, 1213-1214.
44. R. Kitaura, K. Seki, G. Akiyama and S. Kitagawa, *Angew. Chem., Int. Ed.*, 2003, **42**, 428.
45. S. Bourrelly, P. L. Llewellyn, C. Serre, F. Millange, T. Loiseau and G. Ferey, *Journal of the American Chemical Society*, 2005, **127**, 13519-13521.
46. G. Ferey and C. Serre, 2009, pp. 1380-1399.
47. F. K. M. Robin A.Y, *coordination chemistry reviews*, 2006, **250**, 2127.
48. L. M. Huang, H. T. Wang, J. X. Chen, Z. B. Wang, J. Y. Sun, D. Y. Zhao and Y. S. Yan, *Microporous and Mesoporous Materials*, 2003, **58**, 105-114.
49. S. Kitagawa, S. Noro, J. A. McCleverty and T. J. Meyer, in *Comprehensive Coordination Chemistry II*, Pergamon, Oxford, 2003, pp. 231-261.
50. T. Loiseau, H. Muguerra, G. Ferey, M. Haouas and F. Taulelle, *Journal of Solid State Chemistry*, 2005, **178**, 621-628.
51. S. Surble, F. Millange, C. Serre, T. Duren, M. Latroche, S. Bourrelly, P. L. Llewellyn and G. Ferey, *Journal of the American Chemical Society*, 2006, **128**, 14889-14896.
52. O. M. Yaghi, H. L. Li, C. Davis, D. Richardson and T. L. Groy, *Acc. Chem. Res.*, 1998, **31**, 474-484.
53. J.-S. Choi, W.-J. Son, J. Kim and W.-S. Ahn, *Microporous and Mesoporous Materials*, 2008, **116**, 727-731.
54. W. Mori, S. Takamizawa, C. N. Kato, T. Ohmura and T. Sato, *Microporous and Mesoporous Materials*, 2004, **73**, 31-46.
55. Y. Yoo, Z. Lai and H.-K. Jeong, *Microporous and Mesoporous Materials*, 2009, **123**, 100-106.
56. U. Mueller, M. Schubert, F. Teich, H. Puetter, K. Schierle-Arndt and J. Pastre, *Journal of Materials Chemistry*, 2006, **16**, 626-636.
57. www.eni.it.
58. eni, *ENI World oil & gas reviews*, 2007, **www.eni.it**.
59. A. J. Kidnay and W. R. Parrish, *Fundamentals of natural gas processing*, Taylor & Francis, London, 2006.

60. A. Rojey, C. Jaffret, S. Cornot-Gandolphe, B. Durand, S. Jullian and M. Valais, *Natural gas : production processing transport*, Editions Technip, Paris, 1997.
61. A. Kohl and R. Nielsen, *Gas purification*, Gulf Publishing, Houston, 1997.
62. U. Daiminger and W. Lind, Engelhard, 2004.
63. G. E. Keller, *Industrial gas separations*, ACS, Washington, 1983.
64. www.ias.vub.ac.be.
65. M. A. Huffmaster, in *54th Laurance Reid Gas Conditioning Conference*, Oklahoma, USA, 2004.
66. P. Hale and K. Lokhandwala, in *54th Laurance Reid Gas Conditioning Conference* Oklahoma, USA, 2004.
67. C. W. Skarstrom, US patent 2,944,627, 1960.
68. P. Guerin de Motgareuil and D. Domine, french Patent 1,223,261, 1960.
69. D. M. Ruthven, *wiley, New York*, 1984.
70. S. Sircar, *Ind. Eng. Chem. Res*, 2002, **41**, 1389-1392.
71. www.srdata.nist.gov/cccbdb/, *NIST Computational chemistry comparison and benchmark database*, 2006.
72. R. H. Perry and D. W. Green, *Perry's Chemical Engineers' Handbook*, McGraw-Hill, New York, 1999.
73. K. Kaneko, in *Studies in Surface and Catalysis*, eds. A. Dabrowski and V. A. Tertykh, Elsevier, Amsterdam, 1996, pp. 573-598.
74. M. M. Dubinin, 1960, **60**, 235-241.
75. S. Brunauer, P. H. Emmett and E. Teller, *Journal of the American Chemical Society*, 1938, **60**, 309-319.
76. S. Himeno, T. Komatsu and S. Fujita, *J. Chem. Eng. Data*, 2005, **50**, 369-376.
77. J. A. Dunne, R. Mariwala, M. Rao, S. Sircar, R. J. Gorte and A. L. Myers, *Langmuir*, 1996, **12**, 5888-5895.
78. U. Mueller, L. Lobree, M. Hesse, O. M. Yaghi and M. Eddaoudi, in *U.S.*, (BASF Aktiengesellschaft, Germany; The Regents of the University of Michigan). Us, 2003, p. 13 pp.
79. A. Jayaraman, A. J. Hernandez-Maldonado, R. T. Yang, D. Chinn, C. L. Munson and D. H. Mohr, *Chem. Eng. Sci.*, 2004, **59**, 2407-2417.
80. K. S. Knaebel, D. M. Ruthven, J. L. Humphrey and R. Carr, in *Emerging separation and separative reaction technologies for process waste reduction*, eds. P. Radecki, J. C. Crittenden, D. R. Shonnard and J. L. Bulloch, AIChE, New York, 1999, pp. 33-129.
81. A. J. Fletcher, E. J. Cussen, T. J. Prior, M. J. Rosseinsky, C. J. Kepert and K. M. Thomas, *Journal of the American Chemical Society*, 2001, **123**, 10001-10011.
82. D. Li and K. Kaneko, *Chemical Physics Letters*, 2001, **335**, 50-56.
83. X. D. Guo, G. S. Zhu, Z. Y. Li, F. X. Sun, Z. H. Yang and S. L. Qiu, *Chem. Commun.*, 2006, 3172-3174.
84. H. Hayashi, A. P. Cote, H. Furukawa, M. O/'Keeffe and O. M. Yaghi, *Nat Mater*, 2007, **6**, 501-506.
85. R. Banerjee, A. Phan, B. Wang, C. Knobler, H. Furukawa, M. O'Keeffe and O. M. Yaghi, 2008, pp. 939-943.
86. L. Pan, K. M. Adams, H. E. Hernandez, X. Wang, C. Zheng, Y. Hattori and K. Kaneko, *J. Am. Chem. Soc.*, 2003, **125**, 3062.
87. J. Zhang, R. Singh and P. A. Webley, *Microporous and Mesoporous Materials*, 2008, **111**, 478-487.
88. A. M.-a. M. C. Blanco Lopez, J. M. D. Tascon, *carbon*, 2000, **38**.

89. M. Cinke, J. Li, C. W. Bauschlicher, A. Ricca and M. Meyyappan, *Chemical Physics Letters*, 2003, **376**, 761-766.
90. N. A. C. S. i. f. a. <http://www.nacatsoc.org/who.asp/>.
91. U. Ravon, M. E. Domine, C. Gaudillere, A. Desmartin-Chomel and D. Farrusseng, *New journal of chemistry*, 2008, **32**, 937-940.
92. D. Farrusseng, S. Aguado and C. Pinel, 2009, pp. 7502-7513.
93. G. S. Nivarthy, A. Feller, K. Seshan and J. A. Lercher, *Microporous and Mesoporous Materials*, 2000, **35-36**, 75-87.
94. K. H. Chandawar, S. B. Kulkarni and P. Ratnasamy, *Applied Catalysis*, 1982, **4**, 287-295.
95. S. C. Lee, S. W. Lee, K. S. Kim, T. J. Lee, D. H. Kim and J. C. Kim, *Catalysis Today*, 1998, **44**, 253-258.
96. S. Ostrowski and J. C. Dobrowolski, *Journal of Molecular Catalysis A: Chemical*, 2008, **293**, 86-96.
97. D. H. R. Barton, A. Gateau-Olesker, S. D. Géro, B. Lacher, C. Tachdjian and S. Z. Zard, *Tetrahedron*, 1993, **49**, 4589-4602.
98. D. Dondi, I. Caprioli, M. Fagnoni, M. Mella and A. Albini, *Tetrahedron*, 2003, **59**, 947-957.
99. B. Coq, V. Gourves and F. Figuéras, *Applied Catalysis A: General*, 1993, **100**, 69-75.
100. A. Corma, V. I. Costa-Vaya, M. J. Díaz-Cabañas and F. J. Llopis, *Journal of Catalysis*, 2002, **207**, 46-56.
101. F. J. Llopis, G. Sastre and A. Corma, *Journal of Catalysis*, 2004, **227**, 227-241.
102. C. J. Friedel. C, *Compt, Rend, Hebd, Seances, Acad, Sci*, 1877, **84**, 1392.
103. H. Pines, J. A. Vesely and V. N. Ipatieff, *Journal of the American Chemical Society*, 1955, **77**, 554-559.
104. K. Bachari, J. M. M. Millet, B. Benaïchouba, O. Cherifi and F. Figueras, *Journal of Catalysis*, 2004, **221**, 55-61.
105. T. Cseri, S. Békássy, F. Figueras and S. Rizner, *Journal of Molecular Catalysis A: Chemical*, 1995, **98**, 101-107.
106. S. Hausdorf, F. Baitalow, J. Seidel and F. Mertens, *Journal of Physical Chemistry A*, 2007, **111**, 4259-4266.
107. M. R. Savonnet, U. Agaudo, S. Bazer-Bachi, D. Lecocq, V. Bats, Pinel, C. Farrusseng, D, *Green Chem.*, 2009, **11**, 1729.
108. E. Mark, M. Robert, M. Z. S. Alexandra, L. Philip and A. W. Paul, 2001, pp. 5168-5175.
109. S. S. Y. Chui, S. M. F. Lo, J. P. H. Charmant, A. G. Orpen and I. D. Williams, *Science*, 1999, **283**, 1148-1150.
110. K. Schlichte, T. Kratzke and S. Kaskel, *Microporous and Mesoporous Materials*, 2004, **73**, 81-88.
111. C. B. P.Chowdhury, D Meister, F Dreisbach, S Gumma, *Microporous and Mesoporous Materials*, 2009, **117**, 406-413.
112. J. Hafizovic, M. Bjorgen, U. Olsbye, P. D. C. Dietzel, S. Bordiga, C. Prestipino, C. Lamberti and K. P. Lillerud, *Journal of the American Chemical Society*, 2007, **129**, 3612-3620.
113. H. Li, C. E. Davis, T. L. Groy, D. G. Kelley and O. M. Yaghi, *Journal of the American Chemical Society*, 1998, **120**, 2186-2187.
114. J. H. B. J. H. J.P. Huinink, G.B. Marin, *Can. J. Chem. Engng*, 1996, **74**, 580.
115. D. W. Marquardt, *J. Soc. Indust. Appl. Math.*, 1963, **11**, 431.

116. D. Lide, R, *Hanbook of chemistry and Physics (84th ed)*, 2004.
117. K. J. Ooms and R. E. Wasylishen, *Microporous and Mesoporous Materials*, 2007, **103**, 341-351.
118. S. Pawsey, I. Moudrakovski, J. Ripmeester, L.-Q. Wang, G. J. Exarhos, J. L. C. Rowsell and O. M. Yaghi, *The Journal of Physical Chemistry C*, 2007, **111**, 6060-6067.
119. A. R. Millward and O. M. Yaghi, *J. Am. Chem. Soc.*, 2005, **127**, 17998.
120. V. Krungleviciute, K. Lask, L. Heroux, A. D. Migone, J. Y. Lee, J. Li and A. Skoulidas, *Langmuir*, 2007, **23**, 3106-3109.
121. L. Alaerts, C. E. A. Kirshhock, M. Maes, M. A. van der Veen, V. Finsy, A. Depla, J. A. Martens, G. V. Baron, P. A. Jacobs, J. F. M. Denayer and D. E. De Vos, *Angew. Chem., Int. Ed.*, 2007, **46**, 4293.
122. M. Palomino, A. Corma, F. Rey and S. Valencia, *Langmuir*, 2009.
123. D. Farrusseng, *Surface Science Reports*, 2008, **63**, 487-513.
124. Z. Li, G. Zhu, X. Guo, X. Zhao, Z. Jin and S. Qiu, *Inorg. Chem.*, 2007, **46**, 5174-5178.
125. P. Horcajada, S. Surble, C. Serre, D. Y. Hong, Y. K. Seo, J. S. Chang, J. M. Greneche, I. Margiolaki and G. Ferey, *Chem. Commun.*, 2007, 2820-2822.
126. M. Eddaoudi, J. Kim, N. Rosi, D. Vodak, J. Wachter, M. O'Keefe and O. M. Yaghi, *Science*, 2002, **295**, 469-472.
127. N. L. Rosi, M. Eddaoudi, J. Kim, M. O'Keeffe and O. M. Yaghi, *Angewandte Chemie-International Edition*, 2001, **41**, 284-+.
128. M. Sabo, A. Henschel, H. Froede, E. Klemm and S. Kaskel, *Journal of Materials Chemistry*, 2007, **17**, 3827-3832.
129. S. C. Loiseau. T, Ferey. G., *Chem. Eur. J.*, 2004, **10**, 1373.
130. M. D. Foster, I. Rivin, M. M. J. Treacy and O. D. Friedrichs, *Microporous and Mesoporous Materials*, 2006, **90**, 32-38.
131. C. Serre, F. Millange, C. Thouvenot, M. Nogues, G. Marsolier, D. Louer and G. Ferey, *Journal of the American Chemical Society*, 2002, **124**, 13519-13526.
132. G. Chaplais, A. Simon-Masseron, F. Porcher, C. Lecomte, D. Bazer-Bachi, N. Bats and J. Patarin, 2009, pp. 5241-5245.
133. G. Chaplais, A. Simon-Masseron, F. Porcher, C. Lecomte, D. Bazer-Bachi, N. Bats and J. Patarin, *Phys. Chem. Chem. Phys.*, 2009, **11**, 5241-5245.
134. A. Zecchina, G. Spoto and S. Bordiga, *PCCP*, 2005, **7**, 1627-1642.
135. U. P. Camarota. B, *J. Phys. Chem. C*, 2008, **112**, 19560-19567.
136. F. Bonino, A. Damin, S. Bordiga, C. Lamberti and A. Zecchina, *Langmuir*, 2003, **19**, 2155-2161.
137. H. Knoezinger and H. Krietenbrink, *J. Chem. Soc., Faraday Trans. 1*, 1975, **71**, 2421-2430.
138. A. Vimont, H. Leclerc, F. Mauge, M. Daturi, J. C. Lavalley, S. Surble, C. Serre and G. Ferey, *Journal of Physical Chemistry C*, 2007, **111**, 383-388.
139. A. Vimont, H. Leclerc, F. Mauge, M. Daturi, J.-C. Lavalley, S. Surble, C. Serre and G. Ferey, *The Journal of Physical Chemistry C*, 2006, **111**, 383-388.
140. Hammett, 1937, **59**, 96-103.
141. S. J. Wiley ed., *Advanced Organic Chemistry : Reactions, Mechanisms, and Structure* 1992.
142. C. Volkringer, M. Meddouri, T. Loiseau, N. Guillou, J. Marrot, G. Ferey, M. Haouas, F. Taulelle, N. Audebrand and M. Latroche, *Inorg. Chem.*, 2008, **47**, 11892-11901

143. N. K. Kerbellec, D.; Haquin, V.; Etienne, M.; Daiguebonne, C.; Guillou, O., *Inorg. Chem.*, 2009, **48**, 2837.

Chemical Engineering Journal 155 (2009) 553–566

Contents lists available at ScienceDirect

Chemical Engineering Journal

journal homepage: www.elsevier.com/locate/cej

Review

Natural gas treating by selective adsorption: Material science and chemical engineering interplay

Marco Tagliabue[a], David Farrusseng[b,*], Susana Valencia[c], Sonia Aguado[b], Ugo Ravon[b], Caterina Rizzo[a], Avelino Corma[c], Claude Mirodatos[a]

[a] *Eni S.p.A, Refining & Marketing Division, via Felice Maritano 26, 20097, San Donato Milanese, Italy*
[b] *Université Lyon 1, IRCELYON, Institut de Recherches sur la Catalyse et l'Environnement de Lyon, UMR CNRS 5256, avenue Albert Einstein 2, 69626 Villeurbanne, France*
[c] *Instituto de Tecnología Química, UPV-CSIC, Universidad Politécnica de Valencia, Avenida de los Naranjos s/n, 46022, Valencia, Spain*

ARTICLE INFO

Article history:
Received 22 January 2009
Received in revised form 3 September 2009
Accepted 7 September 2009

Keywords:
Natural Gas
Methane
Carbon dioxide rejection
Nitrogen rejection
Pressure swing adsorption
Zeolite
Carbons
Metal open framework
MOF

ABSTRACT

The paper addresses current needs in Natural Gas (NG) treating. Basic principles of Pressure Swing Adsorption (PSA) separation processes are described. A state of the art of microporous adsorbents in the frame of NG treating is given. It includes reference and advanced zeolites, carbon based materials and Metal-Organic Frameworks (MOFs). The pros and cons of each material category are discussed. Guidelines to develop on-purpose materials are given from thermodynamics and material state of the art. Finally, PSA applicability to inert (nitrogen and carbon dioxide) rejection from NG is discussed.

© 2009 Elsevier B.V. All rights reserved.

1. Scope of the review

Gas treating technologies can be roughly divided into two main categories [1,2]: (i) *separation*, with contaminant concentration of about 10 wt.% or higher in feed; (ii) *purification*, with contaminant concentration less than about 3 wt.% in feed. Pressure Swing Adsorption (PSA) represents a state of the art technology both in separation and purification of gaseous mixtures [3–9]. As in all adsorption technologies, the nature of feed and products drives the choice of the most adequate adsorbing material and process design. For this reason, a strong integration between process engineering and material science is requested in PSA development and optimisation.

The paper addresses current needs in *Natural Gas* (NG) treating. Basic principles of adsorption processes including adsorbent–adsorbate interactions and current PSA technologies are described. A state of the art of microporous adsorbents in the frame of NG treating is given. It includes reference and advanced *zeolites*, *carbon-based materials* and *Metal-Organic Frameworks* (MOFs). Finally, PSA applicability to inert (nitrogen and carbon dioxide) rejection from NG is discussed.

2. Natural gas: from the reservoir to the marketplace

2.1. Resources and specifications

The progress of the international energy demand shows a 1.7% average annual growth in the 2005–2020 period. This growth concerns all energy sources, although fossil fuels will still rule the energy scene for the next fifteen years.

NG demand will account for the highest growth rate and in 2020 it will exceed that of coal, that will be penalised by the increasing restrictions in pollutant emissions (especially in Europe).

Novel transport technologies, the remarkable reserves found, the lower overall costs and the environmental sustainability all point to NG (less polluting than oil and coal and now used in more efficient plants) as the primary energy source in the near future [10,11].

Reservoirs are frequently far from final markets (Table 1): as a consequence, NG has to be transported either by pipelines as gaseous mixture containing at least 75 vol.% of methane or by tankers as *Liquified Natural Gas* (LNG), containing at least 85 vol.%

---

[*] Corresponding author.
E-mail address: david.farrusseng@ircelyon.univ-lyon1.fr (D. Farrusseng).

1385-8947/$ – see front matter © 2009 Elsevier B.V. All rights reserved.
doi:10.1016/j.cej.2009.09.010

Table 1
2007 world gas reserves (referred to world gas reserves = 1.82×10^{14} m^3) compared to 2005 world gas production (referred to world gas production = 2.84×10^{12} m^3) and 2005 world gas consumption (referred to world consumption = 2.82×10^{12} m^3) [11].

Area	Reserves [%]	Production [%]	Consumption [%]
Western Europe	3.0	10.4	17.6
Industrialised Asia and Pacific	1.6	1.8	6.0
North America	4.2	24.4	24.7
Central Europe	0.3	0.8	2.7
Eastern Europe	27.0	22.4	18.5
Central Asia	4.6	5.3	3.6
Middle East	40.3	10.3	8.9
Africa	7.9	6.5	3.0
Developing Asia and Pacific	7.2	11.7	8.9
Latin America	4.0	6.4	6.2

of methane [12]. The choice between the two transportation technologies depends mainly on the distance and on the volume of gas to be transported. According to an Eni on-shore case-study, LNG could be considered the preferred choice in case of relatively small fields (less than 1 Tcf y^{-1} = 2.83×10^{11} m^3 y^{-1}) and long distance (more than 3000 miles = 4800 km). NG is frequently identified according with its origin and/or chemical composition. Classification by origin provides three main categories: (i) *non-associated gas* which is not in contact with oil; (ii) *gas-cap associated gas* overlying the oil phase in the reservoir; (iii) *associated gas* dissolved in the oil at the reservoir conditions (*solution gas*).

As produced from gas fields, NG generally contains variable amounts of several contaminants such as water, light paraffins, aromatics, carbon dioxide, nitrogen and sulphur compounds. Minor amounts of helium (less than 1 vol.%) and mercury (generally 5–300 μg Nm^{-3}, in few cases more than 1000 μg Nm^{-3}) can be also present. Furthermore, enhanced hydrocarbon recovery operations by nitrogen and/or carbon dioxide injection into reservoirs modify the chemical composition of produced gas. NG can be also classified into *dry* or *wet* depending on the amount of C_{2+} hydrocarbons (wet gas for C_{2+} content higher than 10 vol.%) and into *sweet* or *sour* depending on the amount of acid gas (sour gas for hydrogen sulphide content higher than 1 vol.% and/or carbon dioxide content higher than 2 vol.%). Chemical composition determines the operations requested to meet specifications requested for NG transportation and final processing (Table 2).

Unconventional hydrocarbon sources such as *CoalBed Methane* (CBM) and *LandFill Gas* (LFG) have recently drawn energy companies' attention. The gaseous mixtures entrapped in coal beds are mainly composed by methane (up to 80–99 vol.%) and minor amounts of carbon dioxide, nitrogen, hydrogen sulphide and sulphur dioxide [14]. The gas produced by waste decomposition in landfills is a complex gaseous mixture containing carbon dioxide as the main contaminant [15]. In general, before supplying to processing plants and downstream customers *gas conditioning* operations are requested [12,13,16–18]. Water content has to be reduced to levels that prevent corrosion, hydrate formation and freezing in cryogenic equipments. Indeed, the formation of hydrates from water and hydrocarbons is considered the primary cause of plugging of transmission lines. Until today, the most applied water separation technology remains scrubbing with TriEthyleneGlycol (TEG), followed by scavenging on solid adsorbents (zeolite, silica, silica–alumina, alumina pure or mixed together, activated carbons) [19]. After dehydration, TEG is regenerated at high temperature (about 473 K) and recycled to scrubbers. Hydrocarbons heavier than methane contribute to NG heating value. On the other hand, C_{3+} hydrocarbons can cause problems: either pressure or temperature variations can cause their fall out of the gas phase. C_{3+} hydrocarbons can also cause plugging of downstream valves and pipes or fouling of other equipments (*i.e.* gas separation membranes). Their content is generally adjusted by gas chilling and/or scrubbing with liquid hydrocarbons and successive scavenging on the same solid adsorbents used for dehydration.

Table 2
Typical compositional specifications on feed to LNG plant and on pipeline gas (Total Sulfur refers to H_2S + carbonyl sulphide, COS + organic sulphur) [12,13].

Impurity	Feed to LNG Plant	Pipeline Gas
H_2O	<0.1 ppmv	150 ppmv
H_2S	<4 ppmv	5.7–22.9 mg Sm^{-3}
CO_2	<50 ppmv	3–4 vol.%
Total Sulfur	<20 ppmv	115–419 mg·Sm^{-3}
N_2	<1 vol.%	3 vol.%
Hg	<0.01 mg/Nm^3	–
C_4	<2 vol.%	–
C_{5+}	<0.1 vol.%	–
Aromatics	<2 ppmv	–

The removal of inert gases (mainly nitrogen but also helium) and acid gases (such as carbon dioxide and hydrogen sulphide) is of considerable importance inasmuch as they can be present to a significant extent. NG containing hydrogen sulphide in proportions higher than 10 vol.% are not very common and many gases contain practically no hydrogen sulphide. Conversely, nitrogen and carbon dioxide are common NG contaminants, with average proportions in the range 0.5–5.0 vol.% for nitrogen (with peaks of over 25 vol.%) and 0.5–10 vol.% for carbon dioxide (with peaks up to 70 vol.%). When sulphur compounds and carbon dioxide levels are too high, they need to be reduced in order to avoid formation of solids in cryogenic units and steel pipes corrosion. Furthermore, both nitrogen and carbon dioxide can be considered *inert gases* with no heating value: for this reason, they must be removed to low levels (Table 2) before distribution to final users. Nitrogen and helium rejection from NG are usually operated by cryogenic fractional distillation. Cryogenic *Nitrogen Rejection Units* (NRUs) are considered economically acceptable for gas flows exceeding 15 MMscf d^{-1} = 4.25×10^5 Sm^3 d^{-1} [20], although higher flow ranges are recommended (50 MMscf d^{-1} = 1.42×10^6 Sm^3 d^{-1}) [18]. Acid gas bulk removal (*gas sweetening*) is mainly performed either by aqueous amine or organic solvent scrubbing. The acid gas saturated (*rich*) fluid is regenerated by high temperature stripping (less than about 400 K, in case of amine) or by pressure reduction (in case of solvents) and then recycled to scrubbers. These treatments have to be run carefully, in order to reduce risks deriving from dangerous chemical handling and toxic waste production.

2.2. Opportunities from PSA technologies for natural gas treating

So far, the exploitation of highly contaminated gas streams (*poor gases* or *low-Btu gases*) has not been considered economically attractive because of high capital and operative costs of current gas treating technologies. As a consequence, these gaseous mixtures are frequently not converted into energy [21]. In this context, among the emerging gas treating technologies, PSA processes have drawn market attention because of their intrinsic eco-compatibility and flexibility:

- PSA technology is based on the use of regenerable solid adsorbents. According to that, it does not require the management of chemicals (*e.g.* amine, solvents), thus providing considerable environmental benefits;
- adsorbent regeneration does not require heating. Consequently, PSA process energy intensity is low;
- PSA units can be easily downsized to skid-mounted modules suitable for the exploitation of small gas reservoirs.

3. PSA general features

PSA basic concepts are described in two patents granted in the late 1950s [22,23] and since then, R&D effort in this field has been continuous [4,7]. Sizes of commercial PSA units range from small devices (about 300 scf d^{-1} = 8.50 $Sm^3\,d^{-1}$) for the production of 90 vol.% oxygen from air for medical use, to large refinery plants (about 100 MMscf d^{-1} = 2.83×10^6 $Sm^3\,d^{-1}$) for the production of high purity hydrogen from *Steam Methane Reforming* (SMR).

Like all adsorption separation processes, PSA involve two basic steps:

- during *adsorption step*, certain components of a gaseous mixture are selectively adsorbed on a porous solid. This operation, performed at relatively high pressure by contacting the gaseous mixture with the adsorbent in a packed column, produces a gas stream enriched in the less strongly adsorbed component of the feed mixture (the *raffinate*). After a given time of operation, the adsorbing bed approach saturation and regeneration is requested;
- during *regeneration* or *desorption* step the adsorbed components are released from the solid by lowering their gas phase partial pressures inside the column. After this operation, the adsorbent is ready to be employed in a further cycle. The gaseous mixture obtained from regeneration (the *extract*) is enriched in the more strongly adsorbed components of the feed.

In practice, several columns are operated in a swing-mode to make the process continuous and additional steps are added to the basic cycle, in order to maximise productivity and energy saving.

It is common practice to include a low pressure purge step in the cycle in order to promote adsorbent regeneration. Purge is generally operated by recycling part of raffinate (*purge gas* or *sweep gas*). According to that, raffinate is obtained at about the same pressure of feed, in a pure form while the extract is discharged as secondary product, in impure form and at pressure lower than feed. The whole cycle last minutes or even seconds and is operated under approximately isothermal conditions. The *working capacity* is the difference in loading between the points corresponding to adsorption and regeneration pressures on the same adsorption isotherm. It has to be noticed that in cases of strongly adsorbed species heating at high temperature (*e.g.* around 573 K for release of water from zeolites in NG dehydration processes) is the only regeneration option. This strategy is referred as *Temperature Swing Adsorption* (TSA).

NG is often available at wellhead at high pressure. At least in principle, by using adsorbents able to capture contaminants, PSA processes can produce pure methane at high pressure as raffinate, thus reducing further compression work before transmission to downstream customers.

4. Adsorption fundamentals

The essential requirement of adsorption separation processes is an adsorbent that preferentially adsorbs a family of related components from a mixed feed. Adsorbent selectivity may depend on difference in adsorption at equilibrium (*equilibrium selectivity* or *thermodynamic selectivity*) or on a difference in adsorption rates (*kinetic selectivity*). Kinetic selectivity is possible when a great difference among adsorption/desorption rates of different components exists. This is due to sterically hindered diffusion through pores characterised by pore mouth diameter comparable with molecular size of fed species. Difference in rates may be so great that the slower diffusing species are almost excluded from the adsorbent (*size-selective sieving*). Currently, nitrogen separation from air by using small pore zeolites or carbon molecular sieves is the only commercial PSA process based on kinetic selectivity. Therefore, both solid–fluid phase interactions and diffusion through adsorbent pores must be considered during material selection and tailoring [3,6,24,25].

Table 3

Physico-chemical properties of some molecular species present in NG (hydrogen and carbon monoxide are reported for comparison): σ: *kinetic diameter*, α: *polarisability*, μ: *dipole moment*, Θ: *quadrupole moment*, T_c: *critical temperature*. Quadrupole moment indicative values have been computed by *Density Functional Theory* (DFT) method.

Molecule	σ [Å]	α [Å^3]	μ [D]	Θ [D·Å]	T_c [K]
CH_4	3.80	2.448	0.000	0.02	190
N_2	3.64	1.710	0.000	1.54	126
CO_2	3.30	2.507	0.000	4.30	304
H_2O	2.65	1.501	1.850	2.30	647
H_2S	3.60	3.630	0.970	3.74	373
He	2.60	0.208	0.000	0.00	5
H_2	2.89	0.787	0.000	0.43	39
CO	3.76	1.953	0.112	2.04	133
Reference	[26]	[27]	[27]	[27]	[28]

4.1. Gas–solid interactions

Adsorption (*physisorption*) is based on attraction forces among the solid phase and the species constituting the gas phase, with relatively low adsorption heat. Usually, $q_{ads} < 2q_{vap}$, where q_{ads} and q_{vap} represent, respectively, adsorbate heat of adsorption and vaporisation. Adsorption forces can be categorised into two main groups: (i) *van der Waals forces*, directly correlated with adsorbate molecular polarisability and (ii) *electrostatic forces* such as polarisation forces, surface field–molecular dipole interactions and surface field gradient–molecular quadrupole interactions. Adsorption is usually promoted by synergies among these different kinds of interactions. Key physico-chemical properties of common NG components are reported in Table 3. Carbon dioxide and nitrogen adsorption on polar surfaces (*e.g.* zeolites) is mainly promoted by surface field gradient–molecular quadrupole interactions. Conversely, adsorption of large non-polar molecules (*e.g.* hydrocarbons) is essentially due to their molecular polarisability.

Adsorbents able to promote electrostatic interactions (as well as hydrogen bonding) are generally referred as *hydrophilic*. In general, they are able to adsorb small polar molecules (like water) much more strongly than would be expected simply from van der Waals forces alone. Common hydrophilic adsorbents are zeolites, silica and alumina. Conversely, adsorbents operating exclusively by van der Waals forces (*e.g.* most activated carbons) are referred as *hydrophobic*. According with the gas–solid interactions described above, thermodynamic selectivity can be optimised by tailoring adsorbent physico-chemical characteristics. Zeolite polarity can be tuned at the synthesis step (*e.g.* by choosing the Si/Al molar ratio and counter cations) or by post-synthesis treatments [29]. Besides, polar groups such as carboxylic species can be introduced on activated carbons by oxidation treatments [30].

4.2. Adsorbent porous texture

Adsorbent–adsorbate interactions play an important role for the very first adsorption layers. However, adsorption mechanism and hence separation performances are essentially determined by the porous texture of adsorbent. IUPAC classification categorises pores into micro-, meso- and macropores according to their *pore size* (*d*, *i.e.* diameters of cylindrical pores or distance between the sides of slit-shaped pores). This classification corresponds to different adsorption mechanisms, although the ratio adsorbate molecule size *vs.* pore size is the effective discriminating factor. Adsorption in *micropores* ($d \leq 20$ Å) takes place by *micropore filling* [31,32]. In this

Table 4
Isosteric heat of adsorption extrapolated at zero coverage (q_{st}) of some NG components on commercial activated carbons and zeolites at about 303 K.

Adsorbent	q_{st} [kJ mol^{-1}]			Reference
	CH_4	CO_2	N_2	
Norit Extra	20.60	22.00	–	[37]
Calgon BPL	16.10	25.70	–	[37]
Kensai Maxsorb	16.60	16.20	–	[37]
A'dall A10	16.20	21.60	–	[37]
Osaka Gas A	18.30	17.80	–	[37]
Silicalite	20.90	27.20	17.60	[38]
NaZSM-5	26.50	50.00	24.10	[39]
NaX	19.20	49.00	19.90	[39]

Table 5
Average heat of adsorption (q) of some NG components on various adsorbents at about 303 K.

Adsorbent	q [kJ mol^{-1}]					Reference
	CH_4	CO_2	N_2	H_2O	C_2H_6	
NaX	13.81	34.31	16.74	51.46	31.38	[40]
KClinoptilolite	25.10	39.75	25.10	–	29.29	[40]
CaClinoptilolite	15.06	25.10	20.08	–	10.46	[40]
MgClinoptilolite	29.98	–	19.99	–	–	[41]
SrETS-4	14.67	–	21.20	–	–	[41]
γ-Al_20_3	10.46	33.47	8.37	48.53	17.57	[40]

case, adsorbent–adsorbate interactions are greatly enhanced since gas molecules and pore sizes are comparable and each gas molecule experience the force field generated by pore walls. In addition, molecular sieving can take place if one component is larger than pore opening. Microporous zeolites and carbons commonly used adsorbents as described in Sections 4.1 and 4.2.

Regarding adsorption both in *mesopores* (20 Å < $d \leq$ 500 Å) and in *macropores* (d > 500 Å), adsorbate molecules are organised by multiple layers according to the proposed mechanistic models (*e.g.* the Brunauer–Emmett–Teller one [33]). Molecules belonging to the layer contacting the solid surface are strongly attracted while molecules in the central region of the pore are essentially free from the force field. Adsorbate partial pressure inside mesopores is higher than outside. As partial pressure exceeds critical value (if adsorption temperature is below the critical value), bulk adsorbate condensation takes place inside the pore. This phenomenon is referred as *capillary condensation*.

Together with surface interactions, capillary condensation causes water and C_{3+} hydrocarbon adsorption on mesoporous absorbents. For this reason, mesoporous silica, alumina and silica–alumina are extensively used in NG dehydration and C_{3+} hydrocarbon removal (Section 1). Besides, M41S materials have been recently proposed for gas treating [34].

Macropores (d > 500 Å) behave in gas adsorption as open surfaces. Thus, their contribution to adsorption capacity is generally negligible and their main role is to facilitate transport within adsorbent particles. According to that, most commercial adsorbents consist of aggregated microporous grains, usually with a binder, to form macroporous hyper-structures. The binder also provides mechanical resistance (*e.g.* to pressure shocks) to adsorbent particles.

4.3. Adsorption equilibrium and heat of adsorption

The concept of adsorption equilibrium is deeply involved in the evaluation of adsorbent specific capacity, selectivity and regenerability (working capacity). Equilibrium *adsorption isotherms* $n_i = f(p_i,T)$ (where n_i is the amount of component i adsorbed at temperature T and at partial pressure p_i) and *heat of adsorption* represent essential input data for PSA process modelling [35].

Heat of adsorption is a measure of the strength of interactions between adsorbate and adsorbent (adsorption is an exothermal phenomenon). For adsorbents characterised by energetically heterogeneous surfaces (*e.g.* most zeolites) heat of adsorption is higher at low loadings, describing interactions on strongest sites. Thus, it is properly referred as *isosteric* (*i.e.* at a definite loading) heat of adsorption, q_{st}. From process engineering point of view, heat of adsorption is a measure of the energy required for adsorbent regeneration and provides an indication of temperature variations that can be expected on the bed during adsorption (and desorption) under adiabatic conditions. Tables 4 and 5 provide representative heat of adsorption values for some NG components referred to common adsorbents. Due to high adsorption heat, variations of about 30 °C are reported on zeolitic materials for carbon dioxide capture from NG [36]. These temperature variations are detrimental for PSA efficiency since temperature rising during adsorption step decreases adsorbate uptake and bed temperature decrease during desorption step reduces adsorbate release.

4.4. Selectivity

Equilibrium selectivity is the key parameter to evaluate adsorbent separation ability. It is based on differences in affinities of the adsorbent for the different species constituting the fluid phase. Given an adsorbent and a gaseous mixture in which N is the more strongly adsorbed component and M the predominant but less strongly adsorbed one, equilibrium selectivity is generally expressed by using the *separation factor* $\alpha_{N,M}$:

$$\alpha_{N,M} = \frac{n_N}{n_M}\frac{p_M}{p_N} \approx \frac{K_N}{K_M} \tag{1}$$

where n_N, p_N, n_M, p_M are values obtained from pure component isotherms. It may be shown that in many cases $\alpha_{N,M}$ can be computed as the ratio among N and M Henry's constants (K_i) thus often referred as *Henry's selectivity*. For PSA applications, $\alpha_{N,M}$ values comprised between 2 and 104 may be considered acceptable [9]. For the same adsorbent, adsorbed and desorbed amounts can differ significantly from different conditions of pressures and temperatures. Furthermore, kinetic effects have to be considered when relevant. According to that, additional selectivity criteria have been suggested [42–44].

4.5. Selectivity vs. regenerability

An energy intensive regeneration step is the price you have to pay in case of very selective adsorbents. For this reason, adsorbent design main objective should be to find out an optimal trade-off between selectivity and regenerability. Table 6 contains a collection of separation factors referred to different couples of gases on Calgon BPL^{TM} activated carbon and CaNaA zeolite (commercial 5 A molecular sieve) [8].

Table 6
Separation factors $\alpha_{N,M}$ on Calgon BPL^{TM} activated carbon and CaNaA zeolite (commercial 5 A molecular sieve) at 303 K [8].

Mixture N–M	$\alpha_{N,M}$	
	BPL^{TM} Activated Carbon	CaNaA Zeolite
CO_2–CH_4	2.5	195.6
CO_2–CO	7.5	59.1
CO_2–N_2	11.1	330.7
CO_2–H_2	90.8	7400.0
CO–CH_4	0.33	3.3
CO–N_2	1.48	5.6
CO–H_2	12.11	125.0
CH_4–N_2	4.5	1.7
CH_4–H_2	36.6	37.8
N_2–H_2	8.2	22.3

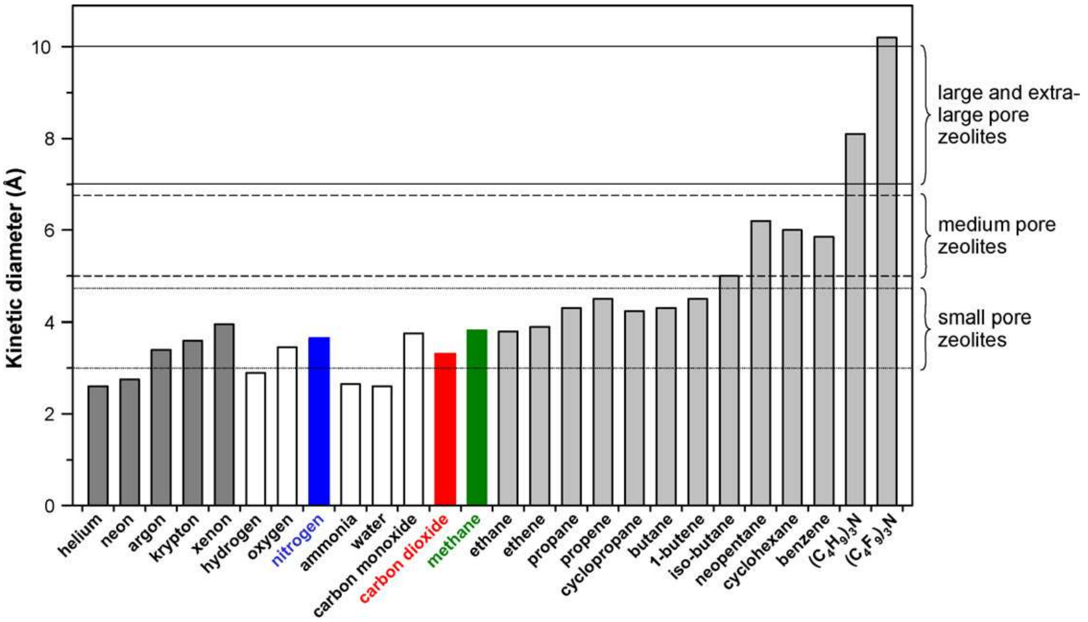

Fig. 1. Kinetic diameter of several molecules (taken from ref. [26]) compared with the pore diameter of different types of zeolites.

Zeolite CaNaA is much more selective than activated carbon in carbon dioxide separation from other gases. On the other hand, the great affinity of CaNaA zeolite for carbon dioxide make extremely difficult carbon dioxide displacement by sweeping with other gases (*e.g.* methane, hydrogen), as requested in typical PSA processes (Section 2). Effective carbon dioxide desorption from CaNaA zeolite can only be obtained by applying more complex or energy intensive strategies like vacuum or high temperature heating (TSA). Regarding nitrogen rejection from NG, it is evident that both Calgon BPL^{TM} activated carbon and CaNaA zeolite show poor selectivities. Although this is merely a case study, it depicts a general behaviour: both methane and nitrogen are able to interact weakly with most adsorbents. Furthermore, their molecules show similar kinetic diameters (σ_{N2} = 3.64 Å, σ_{CH4} = 3.80 Å), making molecular sieving extremely difficult. Thus, very few adsorbents are able to selectively adsorb nitrogen from NG (Section 4.1).

5. Adsorbent design and state of the art

Adsorbent development is an essential step in PSA process design, as outlined in previous Sections. Adsorbents suitable to PSA processes have to satisfy several requisites: (i) selectivity; (ii) regenerability by pressure reduction; (iii) specific capacity; (iv) fast interparticle diffusion; (v) chemical and physical stability; (vi) low cost per unit volume; (vii) reasonable packing density to avoid oversized vessels. It is important to stress that adsorbent cost is a key parameter to be considered for industrial application. Common A, X and Y zeolites are extensively employed in gas industry, although the use of more sophisticated structures is frequently proposed in literature as a way to improve separation performances. Zeolite and carbon adsorbents have been successfully used for inert rejection from raw NG streams whereas MOFs are emerging adsorbents that are gathering great attention because of their outstanding pore volumes. These three categories of adsorbents are described in Sections 4.1–4.3.

5.1. Microporous zeolites and aluminophosphates

Zeolites found in nature and synthesised ones are obtained under hydrothermal conditions and can be divided in those having low Si/Al molar ratio (from 1 to 5) and those of high Si/Al molar ratio (from 5 to ∞), being the formers much more hydrophilic materials [26]. Zeolites are tridimensional aluminosilicate frameworks constituted by Si and Al tetrahedra linked through bridging oxygen atoms giving rise to a regular distribution of pores and cavities of molecular dimensions (Fig. 1). In low Si/Al molar ratio zeolites, the negative charge generated by aluminium in the framework is compensated by small cations such as alkali and alkaline-earth metal cations, whereas the use of large organic molecules allows obtaining higher Si/Al molar ratio zeolites. By means of a great variety of organic molecules based on quaternary ammonium cations as *Structure Directing Agents* (SDAs), several existing zeolites have been obtained with higher Si/Al molar ratios and interestingly, a large number of new zeolitic materials have been synthesised. Up to now, 191 different zeolitic materials with known structure exist [45] and this number is even larger since zeolites in which the structure has not been solved are reported in the open and patent literature. Aluminophosphates (AlPOs) are related materials with similar structures than zeolites constituted by Al and P tetrahedra.

Discovery of zeolitic microporous adsorbents has represented one of the major breakthroughs in the field of adsorption and separation of gas mixtures. The great availability of zeolite structures with different pore size and topology, together with the possibility of preparing them in a wide range of chemical compositions make zeolites very useful adsorbents for gas separations, getting chances for the selection of the most appropriated material for a given separation process. As a consequence of their well defined crystalline structures, these materials have uniform pore sizes in the range of molecular dimensions (3–10 Å) achieving microporosity volumes up to 0.35 cm^3 g^{-1}. Furthermore, the benefit of the high thermal, hydrothermal and chemical stability, allows their use as adsorbents and catalysts in many processes [46,47].

Zeolites can be classified according to different criteria. The most commonly used is the one referring to the *dimensions of the pore apertures*. According to that, zeolites can be divided in the following groups:

- *small pore zeolites*: constituted by channels delimited by 8 *Member Rings* (8 MR) with pore diameters around 4 Å. In this group, zeolitic materials such as zeolite A (LTA) and chabasite (CHA) are the most common;

- *medium pore zeolites*: constituted by channels delimited by 10 MR and pore apertures around 5–6 Å. Zeolites ZSM-5 (MFI) and ferrierite (FER) belong to this group;
- *large pore zeolites*: constituted by channels delimited by 12 MR with pore diameters around 7 Å. Faujasite (FAU) type of zeotites (X and Y) and beta (BEA) are large pore ones;
- *extra-large pore zeolites*: constituted by channels delimited by rings of more than 12 MR and pore apertures larger than 7 Å. These zeolitic materials have been obtained in the latest years and examples of them are CIT-5 (CFI) and ITQ-33 zeolites.

The *shape of the pores* is another important factor, since there are zeolites with pore apertures delimited by the same number of tetrahedra but with different shapes, making them to behave quite differently when adsorbing molecules. For instance, zeolite A (LTA) and analcime (ANA) are both small pore zeolites, being the former comprised by circular pores of 4.1 Å and the latter consisting of elliptical pores with a smaller dimension of 1.6 Å that makes it useless for adsorption of molecules.

Other criterion for classifying zeolitic materials is the *dimensionality of their channels*. Thus, zeolite structures comprised by one-dimensional, two-dimensional and three-dimensional pore systems exist, depending on the arrangement of the channels in one, two or the three directions of the space. Examples can be found in the medium pore size zeolitic materials theta-1 (TON), ZSM-5 (MFI) and ITQ-13 (ITH) consisting of one-, two- and three-dimensional pore systems, respectively. Dimensionality of the channels is a quite important parameter for separation processes in terms of diffusion of the molecules along the porous structure. Indeed, a one-dimensional zeolite usually results a less open structure with lower micropore volume and limitations by diffusion may take place since the molecules must diffuse along one straight channel. As an example, the micropore volume of the small pore one-dimensional zeolite MCM-35 (MTF) is $0.07\,\mathrm{cm^3\,g^{-1}}$ whereas that of the small pore three-dimensional chabasite (CHA) is $0.30\,\mathrm{cm^3\,g^{-1}}$.

Finally, the *channel connection* is another way of differentiating these materials and zeolites with interconnected pores, independent ones and those forming cages can be found. Examples of zeolites with interconnected pores are beta (BEA) and ZSM-5 (MFI), zeolite MCM-22 (MWW) contains independent channels and examples of zeolitic structures with cages are zeolite A (LTA) and faujasite (FAU). The presence of interconnected pores is relevant in adsorption processes since diffusion of the molecules along the channels is favoured in this type of materials. Also the presence of large cages in the structure is an important point for adsorption as these zeolites usually are characterized by very large micropore volume available for adsorption of the molecules.

The earliest reports on the use of zeolitic materials as gas adsorbents are dated on the 1950s and 1960s. Use of zeolites as adsorbents for gas chromatography able to separate gases such as hydrogen, oxygen, carbon dioxide, nitrogen, methane and carbon monoxide was reported [48]. Later, different zeolites have been described as useful adsorbents in gas mixtures containing carbon dioxide, nitrogen and methane, such as ion exchanged mordenite [49], where it is stated that the separation ability increases with increasing electrostatic field in the zeolite cavities. Also, faujasite-type zeolites (X and Y) while ion exchanged with alkali or alkaline-earth ions, NaA, CaA, silicalite, ZSM-5 and other microporous molecular sieves (*e.g.* the silicoaluminophosphate SAPO-5 and SAPO-11) have been described as adsorbents. On the other hand, natural occurring zeolites have been also used in different gas separation processes. Indeed, zeolites such as erionite, mordenite, chabasite and clinoptilolite have been widely employed as adsorbents in air separation and purification, NG purification, hydrocarbon separation, oxygen/argon and hydrogen purifications, among others [50]. A comparison on the use of three different natural zeolites (erionite, mordenite and clinoptilolite) as adsorbents for purification of methane mixed with carbon dioxide shows that clinoptilolite is the best adsorbent for purifying NG [51]. Several reports on the use of clinoptilolite exchanged with different cations as adsorbents for removing carbon dioxide and in separation of methane/nitrogen mixtures have been also reported [52,53]. It has been described that when using clinoptilolite for the separation of methane/nitrogen mixtures, separation efficiency can be controlled by the cationic surface population [54].

The low cost of natural zeolites is often cited as a major incentive for their use. It has been demonstrated that although the raw material cost is relatively low, processing and shipping operations could make these adsorbents even more expensive than the synthetic ones. According to that, also in the case of natural zeolites a wise evaluation of adsorbent separation performances and cost is recommended [50].

Regarding to the use of zeolites in PSA, several processes have been reported in where adsorbents such as zeolites A, X, silicalite or mordenite are employed [55–57] and comparison with other adsorbents such as activated carbon can be also found [58]. The Petlyuk$^{\mathrm{TM}}$ PSA process has been proposed for the separation of ternary gas mixtures, such as carbon dioxide/methane/nitrogen. It consists of two pairs of adsorption columns employing three kinds of adsorbents: activated carbon, zeolite 13X and carbon molecular sieves [59].

Recently, zeolite and other molecular sieve membranes have also shown potential for application in separation processes. Small-, medium-, and large-pore zeolites have been used to prepare membranes able to separate carbon dioxide from methane, as is the case of SAPO-34 [60], silicalite-1 [61] and zeolite Y [62], respectively. Because both carbon dioxide ($\sigma_{\mathrm{CO_2}} = 3.3\,\text{Å}$) and methane ($\sigma_{\mathrm{CO_2}} = 3.80\,\text{Å}$) molecules are much smaller than the pores of large pore and medium pore zeolites, separation with these membranes was mainly based on competitive adsorption. In contrast, it is reported that membranes based on small pore zeolites and molecular sieves such as zeolite DDR [63] and SAPO-34 [64], having pores similar in size to methane but larger than carbon dioxide, allow the separation of these molecules by differences in size. A recent review on carbon dioxide separation by zeolite membranes can be found elsewhere [65]. However, it is worth to mention that the up-scaling of high quality zeolite membranes is still a major issue for commercialisation purposes. Finally, it shall be pointed out that the very recent great availability of different zeolitic materials in their pure silica composition has opened a new application field for hydrocarbon separation processes involving olefins separations. Indeed, the use of pure silica microporous materials instead of charged silicoaluminate zeolites is preferred, since the former will not suffer any pore blocking due to the oligomerization of the adsorbed olefins. In this line, non-charged zeolites with pore openings formed by 8MR, such as chabasite [66], ITQ-32 [67] and AlPO materials [68], among others, have shown excellent olefin/paraffin separation properties, suggesting separation procedures alternative to energy intensive cryogenic distillations, currently used for that purpose.

Separation of molecules by using zeolites as adsorbents can be taken place by molecular sieve effect or by selective adsorption. Regarding separation by molecular sieving and, taking into account the kinetic diameter of the molecules involved ($\sigma_{\mathrm{CO_2}} = 3.30\,\text{Å}$, $\sigma_{\mathrm{N_2}} = 3.64\,\text{Å}$, $\sigma_{\mathrm{CH_4}} = 3.80\,\text{Å}$), zeolites with pore diameters smaller than 3.80 Å would be required. In the database of the *International Zeolite Association* (IZA) [45], 62 small pore (8MR) zeolites appear, but only four of them have pore sizes smaller than

Table 7
Small pore (8 MR) zeolites with pore size smaller than 3.8 Å.

IZA Code	Name	Dimensionality	Pore Size [Å^2]
ACO	ACP-1	3	2.8 × 3.5 3.5 × 3.5
AFX	SAPO-56 SSZ-16	3	3.4 × 3.6
PAU	Paulingite ECR-18	3	3.6 × 3.6
RHO	Rho	3	3.6 × 3.6

3.80 Å (Table 7) that would be adequate for separation of carbon dioxide and nitrogen from methane.

On the other side, the interaction of the adsorbent with the adsorbate molecules is a key factor for separation processes. Indeed, as the interaction is stronger the desorption step becomes harder and the regenerability of the adsorbent decreases. Taking into account the differences in polarity of the molecules ($CO_2 \gg N_2 \approx CH_4$), it is expected a very strong interaction of carbon dioxide with polar zeolite adsorbents making more difficult their regenerability as, indeed, has been observed in some zeolites such as CaNaA (Section 3.5). For this reason, high silica and pure silica zeolites being much less polar materials would be more desirable for this separation process provided that these adsorbents exhibit a satisfactory adsorption capacity. Among the existing small pore zeolites, those that can be synthesized in pure silica form are listed in Table 8 and could be in principle the most adequate adsorbents for this purpose.

Regarding to the availability for preparing and using these materials, in the case of those selected for the separation based on molecular sieve effects (Table 7), ACP-1 is a cobalt-phosphate that is unstable, paulingite is a mineral and the possible candidates would be SAPO-56, SSZ-16, ECR-18 and zeolite rho. In the case of the small pore pure silica zeolites (Table 8), most of them can be prepared and among them, it is expected that good adsorbents could be found for their use in these separation processes.

The titanosilicate ETS-4 is a small pore member of the *Engelhard TitanoSilicate* (ETS) family [69,70]. The ETS-4 structure consists of an interconnected octahedral–tetrahedral framework with narrow 8 MR pore openings. The ETS-4 structure involves corner sharing SiO_4 tetahedra and TiO_6 octahedra units as well as TiO_5 units. Although larger openings are present in its structure, faulting ensures that access to the crystal interior of ETS-4 occurs through the relatively narrow 8 MR, analogous to what is seen in small-pore zeolites. The size of the 8 MR pore can be tuned by exchanging cations from sodium to strontium and by dehydration using a controlled thermal treatment (between 373 K–573 K). The progressive contraction of the effective pore size of the 8 MR pore openings profoundly affects the adsorption properties. When the material is calcined at 463 K, methane is readily adsorbed while larger molecules are essentially excluded. Methane adsorption declines with further pore contraction and once the material has been dehydrated at 543 K, substantial methane exclusion occurs whereas smaller molecules (like nitrogen or carbon dioxide) are readily adsorbed. Due to these peculiar properties, an adsorbent based on ETS-4, referred as *Contracted TitanoSilicate-1* (CTS-1), has been implemented in the Molecular Gate^{TM} technology for nitrogen rejection from NG (Section 5.1) [71,72].

Table 8
Small pore (8 MR) pure silica zeolites.

IZA Code	Name	Dimensionality	Pore Size [Å]
CHA	Chabasite	3	3.8 × 3.8
DDR	Deca-dodecasil 3R	2	3.6 × 4.4
IHW	ITQ-32	2	3.5 × 4.3
ITE	ITQ-3	2	3.8 × 4.3 2.7 × 5.8
ITW	ITQ-12	2	2.4 × 5.4 3.9 × 4.2
LTA	ITQ-29	3	4.1 × 4.1
MTF	MCM-35	1	3.6 × 3.9
NSI	Nu-6(2)	2	4.5 × 2.6 4.8 × 2.4
RTE	RUB-3	1	3.7 × 4.4
RTH	RUB-13	2	3.8 × 4.1 2.5 × 5.6
RWR	RUB-24	1	5.0 × 2.8

5.2. Carbon adsorbents

Carbon adsorbents are widely employed because of their peculiar properties, mainly due to their low polarity [73]: (i) they are able to perform separation and purification without requiring prior stringent moisture removal (in contrast to most zeolites); (ii) they adsorb more non-polar and weakly polar organic molecules than other adsorbents do; (iii) they exhibit low heat of adsorption, resulting in low energy intensive regeneration operations. Carbon adsorbents can be roughly divided into four categories:

- Activated Carbons (ACs);
- Carbon Molecular Sieves (CMS);
- Activated Carbon Fibers (ACFs);
- carbon-based nanomaterials (e.g. Single Wall Carbon Nanotubes, SWNTs).

Among them, ACs and CMS are the most employed materials in industrial gas separations.

AC source raw materials are carbonaceous matters such as wood, peat, coals, petroleum coke, bone, coconut shell, fruit nuts. AC preparative route is largely empirical although a general understanding of the related phenomena has been reported [74]. It essentially involves a low temperature (about 773 K) carbonisation followed by activation at high temperature (about 1273 K). During carbonisation, condensation of polynuclear aromatic compounds, breakage of sidechain groups together with cross-linking reactions occur. In particular, cross-linking avoids the development of graphitic structures that are virtually nonporous, thus not suitable for adsorption applications. Starting with the initial pores present in the raw material, additional pores with the desired pore size distribution can be created by activation processes. Flushing with mild oxidising gases (*e.g.* carbon dioxide, steam) or treatments with inorganic chemicals (*e.g.* potassium hydroxide, zinc chloride, phosphoric acid) are usual procedures. Both oxygenate groups and inorganic cations introduced during the activation step determine the polarity of the final product. By proper choice of precursor, carbonisation and activation steps it is possible to obtain ACs characterised by the desired pore size distribution and polarity. *Iodine number* is the most common empirical descriptor for AC adsorption capacity. It is defined as the milligrams of iodine adsorbed by one gram of carbon. Iodine number values are directly correlated with specific surface area ones.

Presently, main AC applications in the NG industry are [75]: (i) purification of recycled amines and glycols in gas sweetening and dehydration facilities; (ii) NG contaminants (*e.g.* sulfur, mercury) scavenging; (iii) equipment and catalyst protection. ACs impregnated with chemicals are frequently used. In this case, due to absorption phenomena, regeneration can be laborious and often promoted by high temperature heating (*e.g.* gas sweeping at till

723 K for alkali-impregnated ACs for sulphur scavenging from Claus reactor tail gas). Additional *ex situ* treatments can be requested.

The preparation of CMS is broadly similar but often includes additional treatments with organic species that are cracked or polymerised on the carbonised matter [76]. CMS for large scale applications are obtained from coals. A very narrow pore size distribution, in general centered on 5 Å, is obtained by accurate control of synthesis conditions. Due to precise pore size tuning, CMS are discriminated from ACs on the basis of the separation mechanism exploited. ACs separate molecules exploiting differences in their adsorption equilibrium constants. Conversely, CMS provide molecular separation on the basis of rates of adsorption. Currently, CMS are mainly employed in PSA processes for hydrogen and helium purification (which can also be done by ACs) and nitrogen production from air [77,78]. Carbon dioxide separation from natural gas by CMS-based PSA systems has been extensively studied [79,80,81,82,83] and commercial units (suitable also for nitrogen rejection) are available (Sections 5.1 and 5.2).

ACFs are produced from polymeric and pitch fibers [84]. Besides their fibrous form, they have the following peculiar properties with respect to ACs: (i) narrow and uniform pore size distribution (8–10 Å) which enhance interaction with adsorbates; (ii) small and uniform fiber diameter (hence fast adsorption–desorption diffusion); (iii) electrically conductive and heat resistant allowing desorption by electrical heating; (iv) high strength and elasticity.

Despite of these favourable properties, their high cost limits the use to small units, mainly in environmental applications (*e.g.* air or water treatment). On the other hand, manufacture of ACF thin membranes appear promising for high purity hydrogen production from refinery gases [8,85].

Finally, SWNTs consist in seamless cylinders wrapped by a graphite sheet (or graphene sheet). The hexagonal honeycomb lattice of the graphene sheet can be oriented in many possible directions relative to the axis of the tube, determining the metallic or semiconducting nature of these materials. They are prepared mainly by hydrocarbon or carbon monoxide decomposition at high temperature. SWNT main characteristics are: (i) high thermal and electrical conductivities; (ii) high strengths; (iii) high stiffness. According to that, they hold potential application in high technology fields (*e.g.* microelectronics). As adsorbent, they have provided promising results for hydrogen storage, although careful validation of published data is recommended [86,87]. Presently, neither industrial production processes nor commercial applications of these materials are reported.

5.3. Metal-organic frameworks

In contrast to zeolites, for which a relatively limited number of structures exists (Section 4.1), the versatility of coordination and organic chemistry allow to design an almost infinite variety of MOF structures [88–91].

MOF materials actually bridge the pore size gap between zeolite and mesostructured silica such as M41S materials, as shown in the arbitrary selection in Fig. 2. Aside from pore size and when pore topology is considered, one can find analogies between zeolites and MOFs. For instance, the pore structure can be one-dimensional with straight channels such as found for rod-like materials (MIL-53, MIL-68 and MOF-69), while IRMOF structures show three-dimensional cubic channel arrangements. In addition, as for zeolites, complex porous architecture with large cavities, reduced pore aperture and side pockets can be observed. A striking example is the HKUST-1 structure consisting of two types of “cages” and two types of “windows” separating these cages [92,93]. Large cages (13.2 and 11.1 Å in diameter) are interconnected by 9 Å windows of square cross-section. The large cages are also connected to tetrahedral-shaped side pockets of roughly 6 Å through triangular-shaped windows of about 4.6 Å. Typical zeolite topologies are also found in imidazolate based MOFs (also called ZIFs) such as SOD, LTA, RHO [94]. As a consequence, beta (9.6 Å) and alpha (16.4 Å) cages can be found in *sod*- and *rho*-ZMOF, respectively [95]. In terms of adsorption properties, MOF materials exhibit two major differences with respect to classical adsorbents:

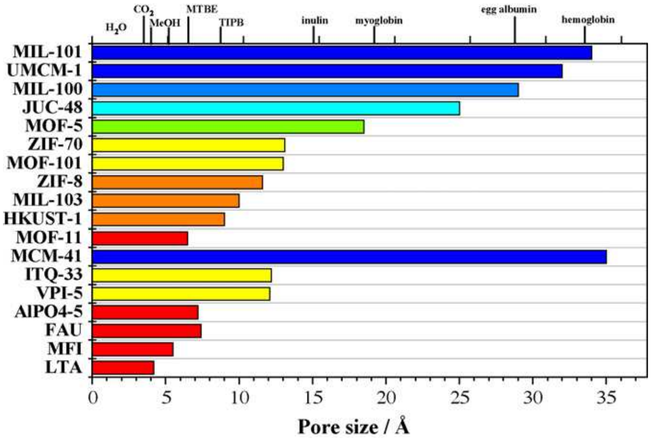

Fig. 2. Cavity size of porous MOFs (Å) compared with standard aluminosilicates and aluminophosphates. Porous materials are selected arbitrarily; pore sizes are approximate due to the variety of pore shapes involved.

- Framework flexibility upon adsorption–desorption [96,97]. In contrast with the permanent porosity typical of classical “rigid” adsorbents (carbons, zeolites), adsorption on MOF may evolve dynamically depending on the nature and quantity of host molecules [98–100]. In many examples, it is observed that the adsorption process can take place stepwise at different pressures depending on the adsorbed gas leading to adsorption–desorption isotherms with hysteresis phenomena. This phenomenon, usually named *gate opening* arises mainly from the flexibility of the networks. For instance, carbon dioxide and methane adsorptions on MIL-53 are strongly affected by the presence of water which causes drastic changes in the pore shapes [101,102].
- Very high adsorption capacities per mass unit due to very large micro-, mesoporous volumes. This is specially the case when considering high pressure domains ($P > 25$ bar). For example, CO_2 adsorption capacities at 50 bar are twice and three time larger for MOF-177 and MIL-101 with respect to NaX [103]. These outstanding capacities can be advantageous for gas storage applications [104–106,88].

For comparison purposes, carbon dioxide adsorption isotherms of various carboxylate based MOFs and reference carbon materials and zeolites are plotted in Fig. 3. The stability of carboxylate based MOFs upon water adsorption is usually pointed out as a major drawback for their applications [116,117]. In contrast, imidazolate based MOFs (also called ZIFs) are much more chemically stable and have been recently proposed as candidates for carbon dioxide capture [94,118,119]. Similarly to high silica zeolites and carbon adsorbents, the observed linear trend of carbon dioxide isotherms on MOFs (at low pressure) is a general feature. The adsorption mainly proceeds by van der Walls and quadrupole interactions. As a result, MOF exhibits lower heats of carbon dioxide adsorption which can be taken as a decisive advantage for PSA process (Table 9). Indeed, it shall allow desorbing much more carbon dioxide at the regeneration step, thus increasing the working capacity. However, it is at the expenses of lower selectivity values which directly penalize the rate of methane recovery and which may not be sufficient to fulfil raffinate specifications (Table 2).

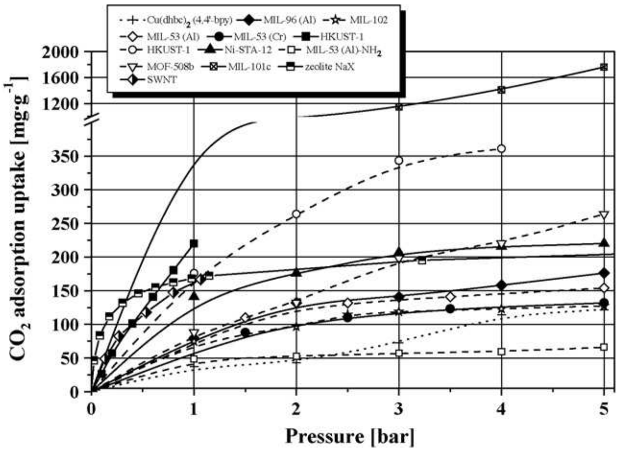

Fig. 3. Carbon dioxide adsorption isotherms measured at about 300 K for various MOFs and reference materials: Cu(dhbc)$_2$(4,4′-bpy) [107], MIL-96 (Al) [108], MIL-102 [109], MIL-53 (Al) [98], MIL-53 (Cr) [101], HKUST-1 [110], HKUST-1 [111], Ni-STA-12 [99], MIL-53 (Al)-NH$_2$ [112], MOF-508b [113], MIL-101c [114] and SWNTs [115].

Therefore new generation of MOF adsorbents shall be designed to selectively enhance carbon dioxide interactions with the framework while still limiting methane uptake. Two different strategies can be envisaged: (i) a *structural* route aiming at synthesizing MOF adsorbents with micropore size in the range of medium pore zeolites in order to benefit from stronger wall-molecules interactions. This can be achieved by networks interpenetration strategy [120]; (ii) a *functionalisation* route dealing with the enhancement of framework polarity. Simulations were performed on virtual compounds corresponding to the IRMOF topology with virtual organic linkers. It has been concluded that the use of short linkers or linkers highly functionalised with halogen moieties (*e.g.* bromine) would result in an increase of adsorption heats [121]. At IRCELYON, we have investigated the effect of functionalisation with basic amino groups on various carbolylate based MOFs (Fig. 4) [122,123]. Similarly, other authors have investigated ZIF functionalisation (ZIF-68, 78, 69, 82, 90) with polar groups such as -NO$_2$, -Cl, -CN and carboxyl [118,124]. Clearly, higher heats of CO$_2$ adsorption are found for functionalised adsorbents with respects to unpolar ZIF-8 (Table 10). However, it is worth to mention that the enhancement of the framework polarity is usually accompanied with a stronger adsorption of water as revealed by lager uptake at low pressure (Fig. 4).

Although MOF materials are intensely investigated for capture applications, much more insights is required before envisioning any industrial application for gas separation such as the effects of mixture of various gases and vapours (including water), adsorption-desorption kinetics, shaping and poisoning issues.

Table 9
MOFs CO$_2$/CH$_4$ separation performaces (zeolite 13X is reported for comparison): α_{CO_2,CH_4}: Henry's selectivity, S_{CO_2,CH_4}: selectivity estimated as the molar ratio of adsorbed carbon dioxide and methane at 5 bar, Δn: working capacity estimated as the difference between the adsorbed carbon dioxide at 5 bar and the adsorbed carbon dioxide at 1 bar, n_{CO_2}: amount of adsorbed carbon dioxide at 5 bar; q_{st}: carbon dioxide isosteric heat of adsorption, N.A.: not available.

Adsorbent	α_{CO_2,CH_4}	S_{CO_2,CH_4}	Δn [%]	n_{CO_2} [mg g^{-1}]	q_{st} [kJ mol^{-1}]
Cu(dhbc)$_2$(4,4′-bpy)	N.A.	∞	64	122	N.A.
MIL-96 (Al)	N.A.	9.4	56	180	33
MIL-102	N.A.	6.5	41	128	N.A.
MIL-53 (Al)	N.A.	4.4	42	154	40
MIL-53 (Cr)	N.A.	∞	54	132	N.A.
HKUST-1	5.5	11.3	51	361	26
Ni-STA-12	N.A.	12.5	36	220	34
MOF-508b	2.9	8.2	67	264	16
MIL-101c	31	9.2	65	1760	24
NaX	93	1.8	17	208	49

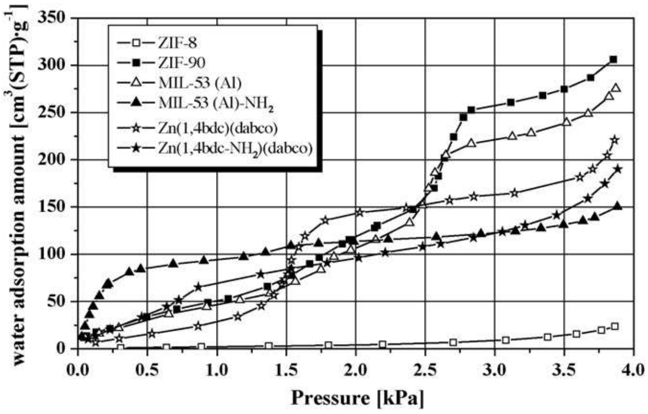

Fig. 4. Effect of MOF functionalisation on water adsorption measured at 313 K.

6. PSA applications

6.1. PSA applications to nitrogen removal from natural gas

The use of CMS as hydrocarbon–selective adsorbents suitable for PSA units for CBM enrichment has been suggested by Bergwerksverband (former Bergbau–Forschung) in a patent assigned in the 1980s [125]. This approach has been implemented by Nitrotec [126–128] for nitrogen rejection. Three gas treating plants (15 MMscf d^{-1} = 4.25 × 10^5 m^3 d^{-1} each) were installed in Texas in the 1990s. Nitrotec process utilises CMS to remove hydrocarbons from the stream containing nitrogen and operates at an optimum pressure of between 2 and 4 bar. The stream flows through the CMS bed with the hydrocarbon being trapped and the nitrogen being vented. Hydrocarbons are recovered by vacuum desorption (recovery of about 95%) and thus, have to be compressed to pipeline delivery pressure.

The Nitrex^{TM} [129,130] process developed by UOP by using the proprietary Polybed^{TM} PSA platform (mainly employed for high purity hydrogen production [8]) appears to be founded on the same principles of Nitrotec one. Hydrocarbon recovery up to 95% is claimed also in this case. One nitrogen rejection unit based on this technology was commissioned in Texas in the early 1990s, with a feed flow rate of about 2.3 MMscf d^{-1} = 6.51 × 10^4 Sm^3 d^{-1}.

On the other hand, very few PSA processes for nitrogen rejection from natural gas based on nitrogen preferential adsorption have been developed. The primary issue is in finding an adsorbent that has selectivity for nitrogen over methane suitable to provide a commercial viable process. In fact, large part of known adsorbents are characterised by equilibrium adsorption selectivity that favour methane over nitrogen (Section 3.5). According to that, processes based on kinetic separation have been suggested. A TSA moving bed process for nitrogen rejection from natural gas, based on fast adsorption/desorption cycles on zeolite 4A, was patented in the 1950s [131]. The apparatus disclosed in this patent

Table 10
ZIFs CO$_2$/CH$_4$ separation performances [118] (see Table 9 for comparison).

Adsorbent	α_{CO_2,CH_4}	S_{CO_2,CH_4}	n_{CO_2} [mg g^{-1}]	q_{st} [kJ mol^{-1}]
ZIF-68	5	3.8	72	20.8
ZIF-78	10	3.7	99	31
ZIF-82	9	4.7	101	23.9
ZIF-8	N.A.	2.8	28	N.A.

Fig. 5. Molecular Gate^{TM} adsorption system for nitrogen and/or carbon dioxide removal (courtesy of Guild Associates, www.moleculargate.com).

appears to be not practical and it does not provide a cost efficient separation method in view of high equipment and maintenance costs and adsorbent degradation by attrition. As a consequence, no plants based on this technology have ever been realised. On the other hand, clinoptilolite (a natural zeolite) is frequently cited in literature as rate selective adsorbent for the separation of nitrogen and methane. In particular, the use of magnesium exchanged clinoptilites has been patented by UOP [132]. Although, UOP patent indicates PSA as the preferred adsorption technology, no technical details are specified.

The Molecular Gate^{TM} PSA process has been developed by Engelhard (now BASF Catalysts) and presently licensed by Guild Associates [18,133–135]. It employs a proprietary adsorbent based on the synthetic titanosilicate ETS-4 (Section 4.1). This adsorbent is referred as Contracted TitanoSilicate 1 (CTS-1). Differently to essentially all known adsorbents, CTS-1 equilibrium adsorption selectivity favours nitrogen over methane. The unique behaviour of CTS-1 adsorbent makes this process suitable for nitrogen rejection from NG by nitrogen selective adsorption. As water adsorption can hydrate and thus change the pore size of CTS-1, it is good practice to remove the water beforehand (*i.e.* by adsorption on silica gel) if present in large amount (Fig. 5).

Feed is introduced into Molecular Gate^{TM} at high pressure. In most cases, optimum operating pressure is around 8 bar. Methane, ethane and about half the propane pass through the bed of adsorbent as raffinate stream, with less than 1 bar pressure drop. The system adsorbs also the residual water, all of the carbon dioxide and all of the C_{3+}. These hydrocarbons do not fit within the pore of the adsorbent. However, they are attracted to the binder used to hold the molecular sieve crystals together and are removed with the other adsorbed components into the tail gas. Adsorbent is regenerated by applying vacuum together with a minimal methane purge. The methane depleted stream (obtained as extract, at atmospheric pressure) is partially recycled to feed. Methane recovery higher than 90% has been declared.

It is interesting to point out that Molecular Gate^{TM} technology has been proposed also for carbon dioxide rejection and successfully tested for the upgrading of biogas (containing 3000 ppmv of H_2S) to pipeline quality NG [136]. Upgrading of landfill gas contaminated by siloxanes has been also claimed [137].

Molecular Gate^{TM} units able to treat $10\,\mathrm{MMscf\,d^{-1}} = 2.83 \times 10^5\,\mathrm{Sm^3\,d^{-1}}$ of NG, downsizeable till $0.5\,\mathrm{MMscf\,d^{-1}} = 1.41\ 10^4\,\mathrm{Sm^3\,d^{-1}}$ are commercially available.

6.2. Applications to carbon dioxide removal from natural gas

Differently to nitrogen, carbon dioxide shows great affinity for several commercial adsorbents. As a consequence, the patent literature on carbon dioxide rejection from NG by PSA is extremely rich and mainly focused on processes rather than on adsorbents.

One of the earlier patents in this field (assigned to Union Carbide, now UOP) describes a PSA system based on a zeolite able to selectively adsorb carbon dioxide from low quality NG [138]. This system exploits displacement with carbon dioxide (*rinse*) to remove adsorbed methane from zeolite bed and to purge methane from column void space. The high purity of the obtained carbon dioxide is a benefit derived by the addition of this additional step.

A similar strategy is described in a group of patents assigned to Air Products & Chemical [139–141] in which PSA processes for carbon dioxide separation from methane (and/or hydrogen) are described. Carbon-based porous materials (ACs, CMS) are in this case the preferred adsorbents.

After desorption step, high pressure purge with carbon dioxide is followed by rinse at an intermediate pressure with an extraneous gas such as air or carbon dioxide itself. The column is then subjected to vacuum to remove the extraneous gas or any remaining carbon dioxide.

A process for methane recovery from LFG, combining a TSA and PSA units is described in a further patent assigned to Air Products & Chemicals. Specifically, the TSA unit removes water and minor impurities from the gas, which then goes to a PSA system devoted to carbon dioxide rejection [142]. The addition of a further PSA unit aimed to nitrogen rejection has been suggested to improve obtained methane quality [9].

The use of clinoptilolites for carbon dioxide rejection from poor gases is disclosed in a patent assigned to Gas Separation Technology [143]. The adsorbent has such a strong attraction to carbon dioxide that little desorption occurs even at very low pressure. According to that, regeneration by exposure to dry air is suggested.

Engelhard has successfully applied the Molecular Gate^{TM} technology to carbon dioxide rejection from NG (Section 5.1).

Nitrotec commercialises PSA units suitable for carbon dioxide rejection from natural gas. These units operate adsorption at a pressure between 3 and 17 bar. Carbon dioxide is desorbed from the

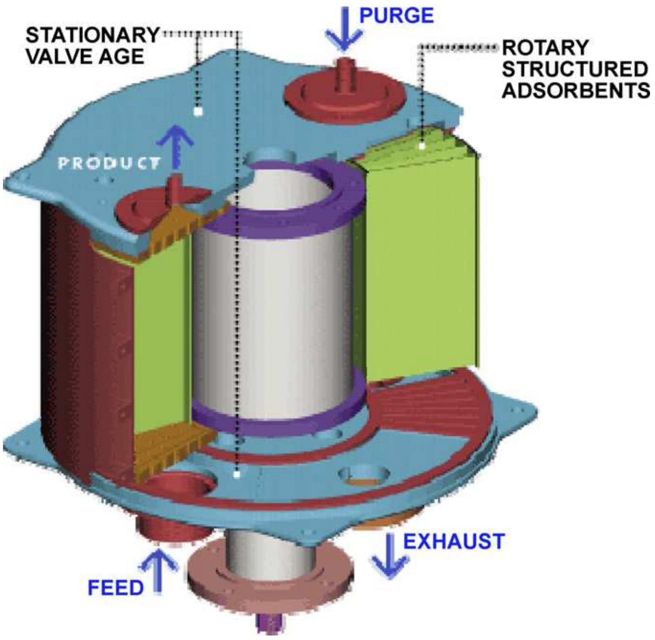

Fig. 6. RCPSA^{TM} module scheme (courtesy of Xebec, www.xebecinc.com).

Fig. 7. Refinery application of RCPSA™ technology (courtesy of Xebec, www.xebecinc.com).

bed by vacuum [144]. In this case, the nature of the adsorbent is not specified.

BOC (now part of Linde) has presented a PSA process (based on an unspecified zeolite) for the production of fuel and carbon dioxide from LFG. According with the proposed scheme, the methane rich stream is partially used as fuel and partially converted into electricity. The carbon dioxide rich stream can be commercialised, due to its high purity. Also in this case, LFG pretreatment is suggested in order to maximise efficiency and avoid damages to the PSA unit.

The effectiveness of the BOC process is discussed as case study based on a 5 MMscf $d^{-1} = 1.41 \times 10^5$ Sm^3 d^{-1}, feed flow [145].

Bergwerksverband (former Bergbau–Forschung) has demonstrated the effectiveness of CMS in carbon dioxide rejection from pretreated LFG. Operations have been performed during the 1980s on two pilot plants located, respectively, in Germany (850 scf $d^{-1} = 2.41 \cdot 10$ Sm^3 d^{-1}, feed flow) and Holland (25 Mscf $d^{-1} = 7.08 \times 10^2$ Sm^3 d^{-1}, feed flow). Unlike the process developed by the same company for nitrogen rejection by CMS (see Section 5.1), the inert rich stream is recovered as extract and the methane rich stream (up to 97 vol. %) as raffinate stream [146].

Osaka Gas has presented an integrated system for the exploitation of biogas: it comprises a PSA unit (for the separation of carbon dioxide from methane) and a methane adsorptive storage system. The technology (based on ACs) has been validated through a pilot plant able to treat 425 scf $d^{-1} = 1.21 \times 10$ Sm^3 d^{-1} of biogas. Methane with the purity of 98 vol. % or higher was produced with a recovery of 90–95%. The PSA process was stable over one year [147].

7. Conclusions and perspectives

Although many adsorbents are commercially available, there are still demand for robust (high chemical stability against other contaminants, high mechanical stability against attrition), cheap (low synthesis cost since adsorbent cost represents a significant part of the investment cost) and *energy efficient* materials (*e.g.* with appropriate selectivity in order to limit the number of separation steps, large working capacity to reduce the cycle frequency, high regenerability to avoid use of external heat). Nevertheless, breakthrough processes can be anticipated if new materials can be design. Among others, a challenge in the materials development is the design of adsorbents which are less moisture sensitive due to the high cost of intensive drying. On the other hand, all kind of adsorbents which could process nitrogen rejection by molecular sieving shall lead to very valuable alternative processes.

Considering process engineering, *Rapid Cycle PSA* approach (RCPSA™) is a significant improvement. Xebec (former QuestAir Technologies) offers compact PSA units (0.01–9 MMscf $d^{-1} = 2.83 \times 10^2$ to 2.54×10^5 Sm^3 d^{-1} of purified NG), based on proprietary rotary valves [148,149] and state of the art adsorbents (mainly for carbon dioxide and water removal). Xebec plans to build larger capacity PSA systems for NG processing based on the rapid cycle RCPSA™ system jointly developed with ExxonMobil Research and Engineering [150,151]. RCPSA exploits both proprietary valves and structured adsorbents. Structured adsorbents overcome fluidisation limitations of beaded adsorbents, allowing higher cycle speeds (up to 50 cycles per minute) than conventional systems. The result is a significant size reduction of separation units (till 1/20 of state of the art PSA plants of the same productivity). Furthermore, the rotary valve technology replaces the bulky network of piping and valves used in conventional PSA systems with two compact, integrated valves. Structured adsorbent and rotary valve are packaged into modules as depicted in Fig. 6. Modular designs are being developed with total capacities up to 80 MMScf $d^{-1} = 2.27 \times 10^6$ Sm^3 d^{-1} [152]. A prototype has been operated at an ExxonMobil refinery for the production of high purity hydrogen (Fig. 7).

Acknowledgements

This work was supported by TopCombi (NMP2-CT2005-515792) funded by the European Union and by MECAFI (ANR-07PCO2-003-05), ACACIA (ANR-08PCO2-001), funded by the *French Research National Agency* (ANR). The authors thank the colleagues Enrico F. Gambarotta, Angelo Carugati, Francesco Frigerio (all of Eni), Michael J. Mitariten (Guild Associates), Daryl Musselman (Xebec), Fernando Rey (Instituto de Tecnología Química, Valencia) for the effective cooperation.

Appendix A.

Although the use of metric units is strongly encouraged by the scientific community, imperial units are currently employed in the gas industry. Thus, gas volume is frequently reported as *standard cubic feets* (scf or frequently SCF) *i.e.* measured at 60 °F = 289 K and 14.70 psi = 1.01 bar. SCFD is another common acronym for daily flows expressed as standard cubic feet.

In metric units, volume is given as either *normal cubic meters*, Nm^3 (where normal conditions are $T = 273$ K, $P = 1$ bar) or *standard cubic meters*, Sm^3 (where standard conditions are $T = 288$ K, $P = 1$ bar.

Prefix M represents 10^3 while MM, B, T represent 10^6, 10^9 and 10^{12}, respectively.

In this review imperial units are reported in order to give a realistic picture of the natural gas world, although conversion into metric units is provided too.

References

[1] G.E. Keller II, Industrial gas separation, in: T.E. Whyte Jr., C.M. Yon, E.H. Wagener (Eds.), ACS Symposia Series, vol. 223, ACS, Washington, USA, 1983.
[2] International Adsorption Society, 2008, http://ias.vub.ac.be.
[3] D.M. Ruthven, S. Farouw, K.S. Knaebel, Pressure Swing Adsorption, Wiley-VCH, New York, USA, 1994.
[4] D.M. Ruthven, Principles of Adsorption and Adsorption Processes, Wiley, New York, USA, 1984.
[5] J.L. Humphrey, G.E. Keller, Separation Process Technology, McGraw-Hill, New York, USA, 1997.
[6] R.T. Yang, Adsorbents: Fundamentals and Applications, Wiley, New York, USA, 2003.
[7] S. Sircar, Pressure swing adsorption, Ind. Eng. Chem. Res. 41 (2002) 1389–1392.
[8] S. Sircar, T.C. Golden, Purification of hydrogen by pressure swing adsorption, Sep. Sci. Technol. 35 (2000) 667–687.
[9] Knaebel, D. Ruthven, J.L. Humphrey, R. Carr, in: P.P. Radecki, J.C. Crittenden, D.R. Shonnard, J.L. Bulloch (Eds.), Emerging Separation and Separative Reaction Technologies for Process Waste Reduction: Adsorption and Membrane Systems, AIChE Center for Waste Reduction Technologies, New York, USA, 1999.
[10] Eni sustainability report, 2006, www.eni.it.
[11] Eni world oil & gas review, 2007, www.eni.it.
[12] A.J. Kidnay, W.R. Parrish, Fundamentals of Natural Gas Processing, Taylor & Francis, Boca Raton, USA, 2006.
[13] Gas Processors Suppliers Association Engineering Data Book, 12th ed., GPSA, Tulsa, USA, 2004.
[14] R.M. Flores, Coalbed methane: from hazard to resource, Int. J. Coal Geol. 35 (1998) 3–26.
[15] G. Nagl, Recover high-Btu gas from new sources, Hydrocarbon Process. 86 (2007) 45–48.
[16] A. Rojey, C. Jaffret, S. Cornot-Gandolphe, B. Durand, S. Jullian, M. Valais, Natural Gas: Production Processing Transport, Editions Technip, Paris, France, 1997.
[17] A. Kohl, R. Nielsen, Gas Purification, 5th ed., Gulf Publishing, Houston, USA, 1997.
[18] U. Daimiger, W. Lind, Adsorption processes for natural gas treatment: a technology update, Engelhard Brochure (2004).
[19] M.A. Huffmaster, Gas dehydration fundamentals: introduction, in: Proceedings of the 54th Laurance Reid Gas Conditioning Conference, Norman, USA, 2004.
[20] K. Pale, K. Lokhandwala, Advances in membrane materials provide new solutions in the gas business, in: Proceedings of the 54th Laurance Reid Gas Conditioning Conference, Norman, USA, 2004.
[21] J. Johnson, Chem. Eng. News 85 (2007) 10–110.
[22] C.W. Skarstrom, Method and apparatus for fractionating gaseous mixtures by adsorption, US Patent 2,944, 627 (1960) assigned to Esso Research & Engineering.
[23] P. Guerin de Motgareuil, D. Domine, Procédé de séparation d'un mélange gazeux binarie par adsorption, French Patent 1,223,261 (1960) assigned to L'Air Liquide.
[24] S.J. Gregg, K.S.W. Sing, Adsorption, Surface Area and Porosity, Academic Press, London, Great Britain, 1982.
[25] F. Roquerol, J. Roquerol, K.S.W. Sing, Adsorption by Powders and Porous Solids: Principles, Methodology and Applications, Academic Press, London, Great Britain, 1999.
[26] D.W. Breck, Zeolite Molecular Sieves, John Willey & Sons, New York, USA, 1974.
[27] NIST Computational chemistry comparison and benchmark database, NIST standard reference database n. 101 rel. 14, September 2006, in: R.D. Johnson III (Ed.), http://srdata.nist.gov/cccbdb.
[28] R.H. Perry, D.W. Green, Perry's Chemical Engineers' Handbook, McGraw-Hill, New York, USA, 1999.
[29] G.H. Kühl, in: J. Weitkamp, L. Puppe (Eds.), Catalysis and Zeolites: Fundamentals and Applications, Springer, New York, USA, 1999.
[30] H.P. Boehm, Surface oxides on carbon and their analysis: a critical assessment, Carbon 40 (2002) 145–149.
[31] K. Kaneko, Micropore filling mechanism in inorganic sorbents, in: A. Dabrowski, V.A. Tertykh (Eds.), Studies in Surface and Catalysis, Elsevier, Amsterdam, 1996, pp. 573–598.
[32] M.M. Dubinin, The potential theory of adsorption of gases and vapors for adsorbents with energetically nonuniform surfaces, Chem. Rev. 60 (1960) 235–241.
[33] S. Brunauer, P.H. Emmett, E. Teller, Adsorption of gases in multimolecular layers, J. Am. Chem. Soc. 60 (1938) 309–319.
[34] A. Macario, A. Katovic, G. Giordano, F. Lucolano, D. Caputo, Synthesis of mesoporous materials for carbon dioxide sequestration, Microporous Mesoporous Mater. 81 (2005) 139–147.
[35] D.P. Valezuela, A.L. Myers, Adsorption Equilibrium Data Handbook, Prentice Hall, Englewood Cliffs, USA, 1989.
[36] S. Sircar, Separation of methane and carbon dioxide gas mixtures by pressure swing adsorption, in: Proceedings of the 78th AIChE Annual Meeting, New York, USA, 1987 (paper 100c).
[37] S. Himeno, T. Komatsu, S. Fujita, High-pressure adsorption equilibria of methane and carbon dioxide on several activated carbons, J. Chem. Eng. Data 50 (2005) 369–376.
[38] J.A. Dunne, R. Mariwala, M. Rao, S. Sircar, R.J. Gorte, A.L. Myers, Calorimetric heats of adsorption and adsorption isotherms. 1. O_2, N_2, Ar, CO_2, CH_4, C_2H_6, and SF_6 on Silicalite, Langmuir 12 (1996) 5888–5895.
[39] J.A. Dunne, M. Rao, S. Sircar, R.J. Gorte, A.L. Myers, Calorimetric heats of adsorption and adsorption isotherms. 2. O_2, N_2, Ar, CO_2, CH_4, C_2H_6, and SF6 on NaX, H-ZSM-5, and Na-ZSM-5 zeolites, Langmuir 12 (1996) 5896–5904.
[40] S.U. Rege, R.T. Yang, M.A. Buzanowski, Sorbents for air prepurification in air separation, Chem. Eng. Sci. 55 (2000) 4827–4838.
[41] A. Jayaraman, A.J. Hernandez-Maldonado, R.T. Yang, D. Chinn, C.L. Munson, D.H. Mohr, Clinoptilolites for nitrogen/methane separation, Chem. Eng. Sci. 59 (2004) 2407–2417.
[42] M.W. Ackley, Multilayer adsorbent for PSA gas separation, US 6,152,991 (2000) assigned to Praxair.
[43] S.U. Rege, R.T. Yang, A simple parameter for selecting an adsorbent for gas separation by pressure swing adsorption, Sep. Sci. Technol. 36 (2001) 3355–3365.
[44] J. Kärger, D.M. Ruthven, Diffusion in Zeolites, Wiley, New York, USA, 1992.
[45] International Zeolite Association database of zeolite structures, http://www.iza-structure.org/databases.
[46] A. Corma, From microporous to mesoporous molecular sieve materials and their use in catalysis, Chem. Rev. 97 (1997) 2373–2419.
[47] R.M. Barrer, Zeolites and Clay Materials as Sorbents and Molecular Sieves, Academic Press, London, Great Britain, 1978.
[48] J. Janak, M. Kejci, H.E. Dubsky, Properties of Ca zeolite as an adsorbent for gas chromatography, Ann. N. Y. Acad. Sci. 72 (1959) 731–738.
[49] E.F. Vansant, R. Voets, Adsorption of binary gas-mixtures in ion-exchanged forms of mordenite, J. Chem. Soc. Faraday Trans. I 77 (1981) 1371–1380.
[50] M.W. Ackley, S.U. Rege, H. Saxena, Application of natural zeolites in the purification and separation of gases, Microporous Mesoporous Mater. 61 (2003) 25–42.
[51] R. Hernandez-Huesca, L. Diaz, G. Aguilar-Armenta, Adsorption equilibria and kinetics of CO_2, CH_4 and N_2 in natural zeolites, Sep. Purif. Technol. 15 (1999) 163–173.
[52] C.C. Chao, H. Rastelli, Process for purification of hydrocarbons using metal exchanged clinoptilolite to remove carbon dioxide, US Patent 4,935,580 (1990) assigned to UOP.
[53] M.W. Ackley, R.T. Yang, Adsorption characteristics of high-exchange clinoptilolites, Ind. Eng. Chem. Res. 30 (1991) 2523–2530.
[54] T.C. Frankiewicz, R.G. Donnelly, in: T.E. White (Ed.), Industrial Gas Separations, vol. 11, ACS, Washington, USA, 1983.
[55] S. Sircar, Regeneration of adsorbents, US Patent 4,784,672 (1988) assigned to Air Products & Chemicals.
[56] E. Richter, Industrial processes for gas separation by pressure swing adsorption, Erdol und Kohle. Erdgas. Petrochemie 40 (1987) 432–438.
[57] H. Rastelli, C.C. Chao, D.R. Garg, Selective adsorption of CO_2 on zeolite, US Patent 4,775,396, (1988) assigned to Union Carbide.
[58] J. Hart, W. Thomas, Gas separation by pulsed pressure swing adsorption, Gas Sep. Purif. 5 (1991) 125–133.
[59] F. Dong, H.M. Lou, A. Kodama, M. Goto, T. Hirose, The Petlyuk PSA process for the separation of ternary gas mixtures: exemplification by separating a mixture of CO_2-CH_4-N_2, Sep. Purif. Technol. 16 (1999) 159–166.
[60] J.C. Poshusta, V.A. Tuan, E.A. Pape, R.D. Noble, J.L. Falconer, Separation of light gas mixtures using SAPO-34 membranes, AIChE J. 46 (2000) 779–789.
[61] L.J.P. van den Broeke, F. Kapteijn, J.A. Moulijn, Transport and separation properties of a silicalite-1 membrane - II. Variable separation factor, Chem. Eng. Sci. 54 (1999) 259–269.
[62] K. Kusakabe, T. Kuroda, A. Murata, S. Morooka, Formation of a Y-type zeolite membrane on a porous alpha-alumina tube for gas separation, Ind. Eng. Chem. Res. 36 (1997) 649–655.
[63] T. Tomita, K. Nakayama, H. Sakai, Gas separation characteristics of DDR type zeolite membrane, Microporous Mesoporous Mater. 68 (2004) 71–75.
[64] S.G. Li, J.G. Martinek, J.L. Falconer, R.D. Noble, T.Q. Gardner, High-pressure CO_2/CH_4 separation using SAPO-34 membranes, Ind. Eng. Chem. Res. 44 (2005) 3220–3228.
[65] M. Pera-Titus, S. Miachon, J. Sublet, S. Aguado, D. Farrusseng, Ceramic membranes for CO_2 capture: present and prospects, submitted for publication.
[66] D. Olson, Light hydrocarbon separation using eight-member ring zeolites, US Patent 6,488,741 (2002) assigned to The Trustess of the University of Pennsylvania.
[67] M. Palomino, A. Cantin, A. Corma, S. Leiva, F. Rey, S. Valencia, Pure silica ITQ-32 zeolite allows separation of linear olefins from paraffins, Chem. Commun. (2007) 1233–1235.
[68] S. Reyes, V. Krishnan, G. De Martin, J. Sinflet, K. Strohmaier J. Santiesteban, Separation of propylene from hydrocarbon mixtures, World Patent 03/080548 (2003) assigned to ExxonMobil Research and Engineering.
[69] S.M. Kuznicki, V.A. Bell, S. Nair, H.W. Hillhouse, R.M. Jacubinas, C.M. Braunbarth, B.H. Toby, M. Tsapatsis, A titanosilicate molecular sieve with adjustable pores for size-selective adsorption of molecules, Nature 412 (2001) 720–724.

[70] R.P. Marathe, K. Mantri, M.P. Srinivasan, S. Farooq, Effect of ion exchange and dehydration temperature on the adsorption and diffusion of gases in ETS-4, Ind. Eng. Chem. Res. 43 (2004) 5281–5290.

[71] S.M. Kuznicki, V.A. Bell, I. Petrovic, P. Blosser, Separation of nitrogen from mixtures thereof with methane utilising barium exchanged ETS-4, US Patent 5,989,316 (2000) assigned to Engelhard.

[72] S.M. Kuznicki, V.A. Bell, I. Petrovic, B.T. Desai, Small pored crystalline titanium molecular sieve zeolites and their use in gas separation processes, US Patent 6,068,682 (2000) assigned to Engelhard.

[73] H. Juntgen, New applications for carbonaceous adsorbents, Carbon 15 (1977) 273–283.

[74] T.J. Barton, L.M. Bull, W.G. Klemperer, D.A. Loy, B. McEnaney, M. Misono, P.A. Monson, G. Pez, G.W. Scherer, J.C. Vartuli, O.M. Yaghi, Tailored porous materials, Chem. Mater. 11 (1999) 2633–2656.

[75] M.J. Bourke, A.F. Mazzoni, The roles of activated carbons in gas conditioning, in: Proceedings of the 39th Laurance Reid Gas Conditioning Conference, Norman, USA, 1989.

[76] H.C. Foley, Carbogenic molecular-sieves—Synthesis, properties and applications, Microporous Mater. 4 (1995) 407–433.

[77] S. Sircar, T.C. Golden, M.B. Rao, Activated carbon for gas separation and storage, Carbon 34 (1996) 1–12.

[78] H. Juntgen, K. Knoblauch, K. Harder, Carbon molecular-sieves—Production from coal and application in gas separation, Fuel 60 (1981) 817–822.

[79] A. Jayaraman, A.S. Chiao, J. Padin, R.T. Yang, C.L. Munson, Kinetic separation of methane/carbon dioxide by molecular sieve carbons, Sep. Sci. Technol. 37 (2002) 2505–2528.

[80] A. Kapoor, R.T. Yang, Kinetic separation of methane carbon dioxide mixture by adsorption on molecular-sieve carbon, Chem. Eng. Sci. 44 (1989) 1723–1733.

[81] A. Kapoor, R.T. Yang, C. Wong, Surface diffusion, Catal. Rev. Sci. Eng. 31 (1989) 129–214.

[82] V.G. Gomes, M.M. Hassan, Coalseam methane recovery by vacuum swing adsorption, Sep. Purif. Technol. 24 (2001) 189–196.

[83] S. Cavenati, C.A. Grande, A.E. Rodrigues, Upgrade of methane from landfill gas by pressure swing adsorption, Energy Fuels 19 (2005) 2545–2555.

[84] M. Suzuki, Activated carbon fiber: fundamentals and applications, Carbon 32 (1994) 577–586.

[85] S. Sircar, W.E. Waldron, M. Anand, M.D. Rao, Hydrogen recovery by pressure swing adsorption integrated with adsorbent membranes, US Patent 5,753,010 (1998) assigned to Air Products and Chemicals.

[86] H.G. Schimmel, G.J. Kearley, M.G. Nijkamp, C.T. Visserl, K.P. de Jong, F.M. Mulder, Hydrogen adsorption in carbon nanostructures: comparison of nanotubes, fibers, and coals, Chem. Eur. J. 9 (2003) 4764–4770.

[87] C. Zandonella, Is it all just a pipe dream? Nature 410 (2001) 734–735.

[88] G. Ferey, Hybrid porous solids: past, present, future, Chem. Soc. Rev. 37 (2008) 191–214.

[89] C. Mellot-Draznieks, G. Ferey, Assembling molecular species into 3D frameworks: computational design and structure solution oh hybrid materials, Prog. Solid State Chem. 33 (2005) 187–197.

[90] S. Natarajan, S. Mandal, Open-framework structures of transition-metal compounds, Angew. Chem. Int. Ed. 47 (2008) 4798–4828.

[91] D.J. Tranchemontagne, J.L. Mendoza-Corteǐs, M. O'Keeffe, O.M. Yaghi, Secondary building units, nets and bonding in the chemistry of metal–organic frameworksw, Chem. Soc. Rev. 38 (2009) 1257–1283.

[92] C. Chmelik, J. Kaerger, M. Wiebcke, J. Caro, J.M. van Baten, R. Krishna, Adsorption and diffusionof alkanes in CuBTC crystals investigated using infra-red microscopy and molecular simulations, Microporous Mesoporous Mater. 117 (2008) 22–32.

[93] J.L.C. Rowsell, O.M. Yaghi, Effects of functionalization, catenation, and variation of the metal oxide and organic linking units on the low-pressure hydrogen adsorption properties of metal-organic frameworks, J. Am. Chem. Soc. 128 (2006) 1304–1315.

[94] R. Banerjee, A. Phan, B. Wang, C. Knobler, H. Furukawa, M. O'Keeffe, O.M. Yaghi, High-throughput synthesis of zeolitic imidazolate frameworks and application to CO_2 capture, Science 319 (2008) 939–943.

[95] Y. Liu, V.C. Kravtsov, R. Larsen, M. Eddaoudi, Molecular building blocks approach to the assembly of zeolite-like metal-organic frameworks (ZMOFs) with extra-large cavities, Chem. Commun. 14 (2006) 1488–1490.

[96] A.J. Fletcher, K.M. Thomas, M.J. Rosseinsky, Flexibility in metal-organic framework materials: impact on sorption properties, J. Solid State Chem. 178 (2005) 2491–2510.

[97] K. Uemura, S. Kitagawa, M. Kondo, K. Fukui, R. Kitaura, H.C. Chang, T. Mizutani, Novel flexible frameworks of porous cobalt(III) coordination polymers that show selective guest adsorption based on the switching of hydrogen-bond pairs of amide groups, Chem. Eur. J. 8 (2002) 3586–3600.

[98] S. Bourrelly, P.L. Llewellyn, C. Serre, F. Millange, T. Loiseau, G. Ferey, Different adsorption behaviors of methane and carbon dioxide in the isotypic nanoporous metal terephthalates MIL-53 and MIL-47, J. Am. Chem. Soc. 127 (2005) 13519–13521.

[99] S.R. Miller, G.M. Pearce, P.A. Wright, F. Bonino, S. Chavan, S. Bordiga, I. Margiolaki, N. Guillou, G. Ferey, S. Bourrelly, P.L. Llewellyn, Structural transformations and adsorption of fuel-related gases of a structurally responsive nickel phosphonate metal-organic framework, Ni-STA-12, J. Am. Chem. Soc. 130 (2008) 15967–15981.

[100] S. Kitagawa, R. Kitaura, S. Noro, Functional porous coordination polymers, Angew. Chem. Int. Ed. 43 (2004) 2334–2375.

[101] P.L. Llewellyn, S. Bourrelly, C. Serre, Y. Filinchuk, G. Ferey, How hydration drastically improves adsorption selectivity for CO_2 over CH_4 in the flexible chromium terephthalate MIL-53, Angew. Chem. Int. Ed. 45 (2006) 7751–7754.

[102] T. Loiseau, C. Serre, C. Huguenard, G. Fink, F. Taulelle, M. Henry, T. Bataille, G. Ferey, A rationale for the large breathing of the porous aluminum terephtalate (MIL-53) upon hydratation, Chem. Eur. J. 10 (2004) 1373–1382.

[103] A. Millward, O.M. Yaghi, Metal-organic frameworks with expeptionally high capacity for storage of carbon dioxide at room temperature, J. Am. Chem. Soc. 127 (2005) 17998–17999.

[104] R. Morris, P. Wheatley, Gas storage in nanoporous materials, Angew. Chem. Int. Ed. 47 (2008) 4966–4981.

[105] U. Mueller, M. Schubert, F. Teich, H. Puetter, K. Schierle-Arndt, J. Pastre, Metal-organic frameworks—prospective industrial applications, J. Mater. Chem. 16 (2006) 626–636.

[106] J.R. Li, R.J. Kuppler, H.C. Zhou, Selective gas adsorption and separation in metal-organic frameworks, Chem. Soc. Rev. 38 (2009) 1477–1504.

[107] R. Kitaura, K. Seki, G. Akiyama, S. Kitagawa, Porous coordination-polymer crystals with gated channels specific for supercritical gases, Angew. Chem. Int. Ed. 42 (2003) 428–431.

[108] T. Loiseau, L. Lecroq, C. Volkringer, J. Marrot, G. Ferey, M. Haouas, F. Taulelle, S. Bourrelly, P.L. Llewellyn, M. Latroche, MIL-96, a Porous aluminum trimesate 3D structure constructed from a hexagonal network of 18-membered rings and m3-oxo-centered trinuclear units, J. Am. Chem. Soc. 128 (2006) 10223–10230.

[109] S. Surble, F. Millange, C. Serre, T. Duren, M. Latroche, S. Bourrelly, P.L. Llewellyn, G. Ferey, Synthesis of MIL-102, a chromium carboxylate metal-organic framework, with gas sorption analysis, J. Am. Chem. Soc. 128 (2006) 14889–14896.

[110] Q.M. Wang, D. Shen, M. Bulow, M.L.L. Lau, S. Deng, F.R. Fitch, N.O. Lemcoff, J. Semanscin, Metallo-organic molecular sieve for gas separation and purification, Microporous Mesoporous Mater. 55 (2002) 217–230.

[111] S. Cavenati, C.A. Grande, A.E. Rodrigues, C. Kiener, U. MuÌller, Metal organic framework adsorbent for biogas upgrading, Ind. Eng. Chem. Res. 47 (2008) 6333–6335.

[112] S. Couck, J.F.M. Denayer, G.V. Baron, J. Gascon, F. Kapteijn, An amine-functionalized MIL-53 metal-organic framework with large separation power for CO_2 and CH_4, J. Am. Chem. Soc. 131 (2009) 6326–6327.

[113] L. Bastin, P.S. Barcia, E.J. Hurtado, J.A.C. Silva, A.E. Rodrigues, B. Chen, A microporous metal-organic framework for separation of CO_2/N_2 and CO_2/CH_4 by fixed-bed adsorption, J. Phys. Chem. C 112 (2008) 1575–1581.

[114] P.L. Llewellyn, S. Bourrelly, C. Serre, A. Vimont, M. Daturi, L. Hamon, G. De Weireld, J.-S. Chang, D.-Y. Hong, Y. Kyu Hwang, S. Hwa Jhung, G. Ferey, High uptakes of CO_2 and CH_4 in mesoporous Metal-organic frameworks MIL-100 and MIL-101, Langmuir 24 (2008) 7245–7250.

[115] M. Cinke, J. Li, C.W. Bauschlicher, A. Ricca, M. Meyyappan, CO_2 adsorption in single-walled carbon nanotubes, Chem. Phys. Lett. 376 (2003) 761–766.

[116] S. Kaye, A. Dailly, O.M. Yaghi, J.R. Long, Impact of preparation and handling on the hydrogen storage properties of ZnO(1,4-benzenedicarboxylate) (MOF-5), J. Am. Chem. Soc. 26 (2007) 14176–14177.

[117] P. Küsgens, M. Rose, I. Senkovska, H. Fröde, A. Henschel, S. Siegle, S. Kaskel, Characterization of metal-organic frameworks by water adsorption, Microporous Mesoporous Mater. 120 (2009) 325–330.

[118] R. Banerjee, H. Furukawa, D. Britt, C. Knobler, M. OKeeffe, O.M. Yaghi, Control of pore size and functionality in isoreticular zeolitic imidazolate frameworks and their carbon dioxide selective papture properties, J. Am. Chem. Soc. 131 (2009) 3875–3877.

[119] H. Hayashi, A.P. Cote, H. Furukawa, M. O'Keeffe, O.M. Yaghi, Zeolite: A imidazolate frameworks, Nat. Mater. 6 (2007) 501–506.

[120] M. Eddaoudi, J. Kim, N. Rosi, D. Vodak, J. Wachter, M. O'Keefe, O.M. Yaghi, Systematic design of pore size and functionality in isoreticular MOFs and their application in methane storage, Science 295 (2002) 469–472.

[121] T. Duren, F. Millange, G. Ferey, K.S. Walton, R.Q. Snurr, Calculating geometric surface aeras as a characterization tool for Metal-Organic Frameworks, J. Phys. Chem. C 111 (2007) 15350–15356.

[122] D. Farrusseng, C. Mirodatos, Rational design and synthesis of Metal Open Frameworks for adsorption and catalysis, in: U.S. Ozkan (Ed.), Handbook of Heterogeneous Catalyst Design, Wiley-VCH, Weiheim, 2009, pp. 161–190.

[123] D. Farrusseng, C. Daniel, C. GaudilleÌre, U. Ravon, Y. Schuurman, C. Mirodatos, D. Dubbeldam, H. Frost, R.Q. Snurr, Heats of adsorption for seven gases in three metal organic frameworks: systematic comparison of experiment and simulation, Langmuir 25 (2009) 7383–7388.

[124] W. Morris, C.J. Doonan, H. Furukawa, R. Banerjee, O.M. Yaghi, Crystals as molecules: postsynthesis covalent functionalization of zeolitic imidazolate frameworks, J. Am. Chem. Soc. 130 (2008) 12626–12627.

[125] E. Richter, W. Körnbächer, K. Knoblauch, K. Giessler, Method of producing a methane-rich gas mixture from mine gas, US Patent 4,521,221 (1985) assigned to Bergwerksverband.

[126] H.E. Reinhold III, J.S. D'amico, K.S. Knaebel, Natural gas enrichment process, US Patent 5,536,300 (1996) assigned to Nitrotec.

[127] Gas Reseach Institute Topical Report: Technologies for nitrogen removal, GRI-99/0080, GRI, Chicago, USA, May 1999.

[128] PSA nitrogen rejection technology, 2005, www.nitrotec.com.

[129] Nitrogen rejection: Nitrex^{TM}, Hydrocarbon Processing, April Issue, 1998, p. 116.

[130] R.J. Buras, M.J. Mitariten, Nitrogen rejection with pressure swing adsorption: principles, design and remote control using an expert system, in: Proceed-

ings of the 44th Laurance Reid Gas Conditioning Conference, Norman, USA, 1994.
[131] H.W. Habgood, Removal of nitrogen from natural gas, US Patent 2,843,219 (1958) assigned to Canadian Patents and Development.
[132] C.C. Chao, Selective adsorption on magnesium-containing clinoptilolite, US Patent 4,964,889 (1990) assigned to UOP.
[133] K.F. Butwell, W.B. Dolan S.M. Kuznicki, Selective removal of nitrogen from natural gas by pressure swing adsorption, US Patent 6,197,092 (2001) assigned to Engelhard.
[134] Nitrogen Rejection and Carbon Dioxide Removal Made Easy, Guild Associates brochure, 2008. www.moleculargate.com.
[135] Carbon dioxide removal: Molecular Gate^{TM}, Hydrocarbon Processing Gas Processes 2006, Gulf Publishing, Houston, USA, 2006.
[136] Developments in gas separation, Guild Associates Brochure, 2007, www.moleculargate.com.
[137] M.J. Mitariten, Landfill gas upgrading process, US Patent Application 2007/0068386 (2007) submitted by Engelhard.
[138] J.J. Collins, Bulk separation of carbon dioxide from natural gas, US Patent 3,751,878 (1973) assigned to Union Carbide.
[139] S. Sircar, J.W. Zondlo, Hydrogen purification by selective adsorption US Patent 4,077,779 (1978) assigned to Air Products and Chemicals.
[140] S.P. Di Martino, Vacuum swing adsorption process with vacuum aided internal rinse, US Patent 4,857,083 (1989) assigned to Air Products and Chemicals.
[141] R. Kumar, Adsorptive process for producing two gas streams from a gas mixture, US Patent 4,915,711 (1990) assigned to Air Products and Chemicals.
[142] R. Kumar, Adsorptive process for producing two gas streams from a gas mixture, US Patent 5,026,406 (1990) assigned to Air Products and Chemicals.
[143] M.W. Seery, Bulk separation of carbon dioxide from methane using natural clinoptilolite US Patent 5,938,819 (1999) assigned to Gas Separation Technology.
[144] Carbon dioxide rejection technology, 2005, www.nitrotec.com.
[145] V.A. Malik, S.L. Lerner, D.L. MacLean, Electricity, CH_4 and Liquid CO_2 production from landfill gas, Gas Sep. Purif. 1 (1987) 77–83.
[146] E. Pilarczyk, K.D. Henning, K. Knoblauch, Natural gas from landfill gases, Resourc. Conserv. 14 (1987) 283–294.
[147] K. Seki, K. Mochidzuki, A. Sakoda, Adsorptive separation and storage of methane from biogas, in: Proceedings of the 9th International Conference on Fundamental of Adsorption, Giardini Naxos, Italy, 2007.
[148] B.G. Keefer, D.G. Doman, Flow regulated pressure swing adsorption system, US Patent 6,063,161 (2000) assigned to SoFinoy Societte Financiere d'Innovation.
[149] QuestAir M3100/M3200^{TM} methane purification PSA systems, QuestAir Technologies Brochure, 2002.
[150] S. Alizadeh-Khiavi, J.A. Sawada, A.C. Gibbs, J. Alvaji, Rapid cycle syngas pressure swing adsorption system, US Patent Application 2007/0125228 (2007) submitted by QuestAir Technologies.
[151] Pressure swing adsorption: rapid cycle, Hydrocarbon Processing Refining Processes 2006, Gulf Publishing, Houston, USA, 2006.
[152] A. Sapre, J. Poturovic, A. Wanni, T. Melli, ExxonMobil advanced technologies: refiners solution to present and future industry challenges, in: Proceedings of the 8th International Downstream Technology Conference and Exhibition, London, Great Britain, 2007.

Langmuir
Article

pubs.acs.org/Langmuir

© 2009 American Chemical Society

Heats of Adsorption for Seven Gases in Three Metal−Organic Frameworks: Systematic Comparison of Experiment and Simulation

David Farrusseng,[*,†] Cécile Daniel,[†] Cyril Gaudillère,[†] Ugon Ravon,[†] Yves Schuurman,[†]
Claude Mirodatos,[†] David Dubbeldam,[‡] Houston Frost,[‡] and Randall Q. Snurr[‡]

[†] *Université Lyon 1, CNRS, UMR 5256, IRCELYON, Institut de recherches sur la catalyse et l'environnement de Lyon, 2 avenue Albert Einstein, F-69626 Villeurbanne, France, and* [‡] *Department of Chemical and Biological Engineering, Northwestern University, Evanston, Illinois 60208*

Received January 22, 2009. Revised Manuscript Received March 27, 2009

The heat of adsorption is an important parameter for gas separation and storage applications in porous materials such as metal−organic frameworks (MOFs). There are, however, few systematic studies available in the MOF literature. Many papers report results for only one MOF and often only for a single gas. In this work, systematic experimental measurements by TAP-2 are reported for the heats of adsorption of seven gases in three MOFs. The gases are Kr, Xe, N_2, CO_2, CH_4, n-C_4H_{10}, and i-C_4H_{10}. The MOFs studied are IRMOF-1, IRMOF-3, and HKUST-1. The data set provides a valuable test for molecular simulation. The simulation results suggest that structural differences in HKUST-1 experimental samples may lead to differing heats of adsorption.

Introduction

Metal−organic frameworks (MOFs) are promising materials for gas separation and storage applications due to their exceptional pore volume in the micro- to mesopore range and their tailorability.[1−4] Hence, there is an increasing number of studies dealing with gas adsorption in MOF materials including H_2, CH_4, N_2, and CO_2, among others.[5] However, various authors have pointed out discrepancies for reported pore volumes, adsorption isotherms, and heats of adsorption among different groups.[6,7] These differences can arise due to differences in MOF synthesis or solvent removal, as well as problems in performing the adsorption measurements with small amounts of sample. Another difficulty is that many papers report results for a single material and often only for one or two gases. To make meaningful comparisons, there is a need for systematic studies of multiple gases on the same MOF sample and for studies of a particular gas on multiple MOFs.

Systematic studies of this sort would also provide a stringent test of predictions from molecular simulation for adsorption in MOFs. Molecular simulation is becoming an important tool in MOF chemistry and material science in general, because it can provide useful insights about the relation between molecular-level structure and observed macroscopic properties, including adsorption. If simulations are sufficiently accurate, they can also be used to screen hypothetical MOFs before they are synthesized. Several reviews of molecular modeling in MOFs have appeared recently, highlighting the rapid growth of this field.[8−10]

In this work, we report low-loading heats of adsorption for Kr, Xe, N_2, CO_2, CH_4, n-C_4H_{10}, and i-C_4H_{10} in IRMOF-1 (also known as MOF-5), IRMOF-3, and HKUST-1 (also known as Cu-BTC). The IRMOF structure is made of Zn_4O tetranuclear clusters connected by rigid dicarboxylic linkers such as benzene 1,4-dicarboxylate (IRMOF-1) to generate a cubic framework. The resulting compounds show square channels, which are connected in the three dimensions. IRMOF-3 differs from IRMOF-1 by the functional amino group on the benzene 1,4-dicarboxylic linker. They have a cage size of about 15 Å at channel intersections with pore openings of about 7.5 Å. The HKUST-1 structure of formula $Cu_3(BTC)_2(H_2O)$ comprises a binuclear Cu_2 paddlewheel.[11] The Cu^{2+} ions are connected through a weak bond, and the second axial coordination site is filled by a weakly bonded water molecule which can be easily removed with a heating treatment at 383 K, rendering the Cu Lewis acid center directly accessible. HKUST-1 structure consists of two types of "cages" and two types of "windows" separating these cages.[12,13] Large cages (13.2 and 11.1 Å in diameter) are interconnected by 9 Å windows of square cross section. The large cages are also connected to tetrahedral shaped side pockets of roughly 6 Å through triangular shaped windows of about 4.6 Å (3.5 Å in the hydrated form). The data set provides a valuable test for molecular simulation. Good agreement between simulation and experiment is obtained for the IRMOFs but not for

---

*Corresponding author. IRCELYON, 2 Av. Albert Einstein, 69626 Villeurbanne, France. Tel: +33 4 72 44 53 65, fax: +33 4 72 44 53 9, david.farrusseng@ircelyon.univ-lyon1.fr.

(1) Ferey, G. *Chem. Soc. Rev*. 2008, *37*, (1), 191−214.

(2) Millward, A. R.; Yaghi, O. M. *J. Am. Chem. Soc.* **2005**, *127*(51), 17998–17999.

(3) Rosi, N. L.; Eckert, J.; Eddaoudi, M.; Vodak, D. T.; Kim, J.; , M.; Yaghi, O. M. *Science* **2003**, *300*(5622), 1127–1129.

(4) Mueller, U.; Schubert, M.; Teich, F.; Puetter, H.; Schierle-Arndt, K.; Pastre, J. *J. Mater. Chem*. **2006**, *16*(7), 626–636.

(5) Morris, R. E.; Wheatley, P. S. *Angew. Chem. Int. Ed* **2008**, *47*(27), 4966–4981.

(6) Liu, J. C.; Culp, J. T.; Natesakhawat, S.; Bockrath, B. C.; Zande, B.; Sankar, S. G.; Garberoglio, G.; Johnson, J. K. *J. Phys. Chem. C* **2007**, *111*(26), 9305–9313.

(7) Panella, B.; Hirscher, M.; Putter, H.; Muller, U. *Adv. Funct. Mater*. **2006**, *16* (4), 520–524.

(8) Snurr, R. Q.; Yazaydin, A. O.; Dubbeldam, D.; Frost, H. Molecular modeling of adsorption and diffusion in metal-organic frameworks. In *Metal-Organic Frameworks: Design and Application*, MacGillivray, L. R., Ed.; Wiley-VCH, in press.

(9) Keskin, S.; Liu, J.; Rankin, R. B.; Johnson, J. K.; Sholl, D. S. *Ind. Eng. Chem. Res*. **2009**, *48*(5), 2355–2371.

(10) Düren, T.; Bae, Y.-S.; Snurr, R. Q. *Chem. Soc. Rev*. **2009**, *38*, 1237−1247.

(11) Chui, S. S. Y.; Lo, S. M. F.; Charmant, J. P. H.; Orpen, A. G.; Williams, I. D. *Science* **1999**, *283*(5405), 1148–1150.

(12) Chmelik, C.; Kaerger, J.; Wiebcke, M.; Caro, J.; van Baten, J. M.; Krishna, R. *Microporous Mesoporous Mater*. **2008**, *117*, 22−32.

(13) Rowsell, J. L. C.; Yaghi, O. M. *J. Am. Chem. Soc*. **2006**, *128*(4), 1304–1315.

Downloaded by UNIV CLAUDE BERNARD LYON 1 on July 1, 2009
Published on June 4, 2009 on http://pubs.acs.org | doi: 10.1021/la900283t

Downloaded by UNIV CLAUDE BERNARD LYON 1 on July 1, 2009
Published on June 4, 2009 on http://pubs.acs.org | doi: 10.1021/la900283t

Table 1. Simulation Parameters for HKUST-1

atom	q [e]	ε/k	σ [Å]
Cu	1.0	2.518	3.114
O	−0.6	48.19	3.03
Ca	0.7	47.86	3.47
Cb	0.0	47.86	3.47
Cc	−0.15	47.86	3.47
H	0.15	7.65	2.85

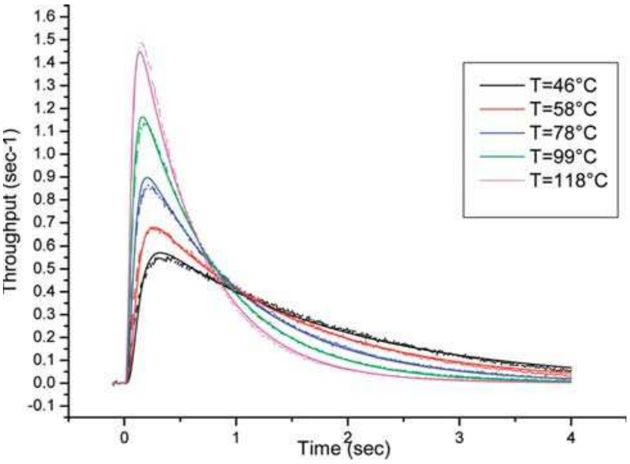

Figure 1. TAP-2 experimental data (plain line) and modeling (dash line) for Xe pulses on IRMOF-1 at various temperatures.

HKUST-1. The simulations suggest that the discrepancy may be explained by blockage of the small pockets in the HKUST-1 experimental sample.

Experimental Section

IRMOF samples were prepared by a method reported elsewhere.[4] In brief, benzene 1,4-dicarboxylic acid (H_2BDC, Aldrich, 2.5 g, 15 mmol) and $Zn(NO_3)_2 \cdot 4H_2O$ (Merck, Pro Analysis, 5.8 g, 20 mmol) are dissolved in 500 mL of DMF (Aldrich, anhydrous). The solution is heated at reflux for 18 h. The white precipitate is filtered under inert atmosphere at room temperature and washed three times with DMF. The samples were kept under inert atmosphere. Samples were characterized by XRD, ^{1}H and ^{13}C NMR, IR, and N_2 physisorption at 77 K. The BET surface areas are 1100 and 630 m^2 g^{-1}, for IRMOF-1 and IRMOF-3, respectively. The HKUST-1 sample was prepared by precipitation at room temperature. Pyridine (1.4 mmol, Aldrich, 99+%) is added dropwise to a DMF solution (Aldrich, 99.8% anhydrous) containing $Cu(NO_3)_2 \cdot 2.5H_2O$ (0.52 mmol, Riedel-deHaën, pure) and H_3BTC (0.48 mmol, Aldrich, 95%). Precipitation takes place by addition of water (30 mmol). The blue powder is filtered off and washed with DMF. The XRD pattern corresponded to highly crystalline HKUST-1, while N_2 isotherm measurements revealed very large BET surface area (1540 m^2/g) and pore volume (0.8 cc/g) in good agreement with the highest values reported elsewhere.[6]

Heats of adsorption were measured by using pulse−response experiments in an ultrahigh-vacuum reactor system referred to as a TAP reactor (temporal analysis of products).[14] The experiments are carried out by pulsing a small amount of gas (10 nmol 50 vol % in argon) over a fixed bed of adsorbent placed in a microtubular reactor and measuring the pulse responses of the gas by a mass spectrometer at the reactor exit. By modeling these pulse responses, heats of adsorption at very low coverage can be calculated. Advantages of operating in ultrahigh vacuum are (i) external mass-transfer limitations are completely absent, (ii) molecule−wall interactions dominate, and (iii) the strongest adsorption sites are probed. This technique has been used to quantify adsorption parameters including heats of adsorption and diffusion of gases over various adsorbents such as zeolites[15] and activated carbon.[16] Prior to adsorption experiments, samples were desorbed at 550 K at 100 Pa. Measurements and modeling were performed using "best of practice" procedures.[17] Adsorption experiments were carried out with Kr, Xe, N_2, CH_4, CO_2, n-C_4H_{10}, and i-C_4H_{10}.

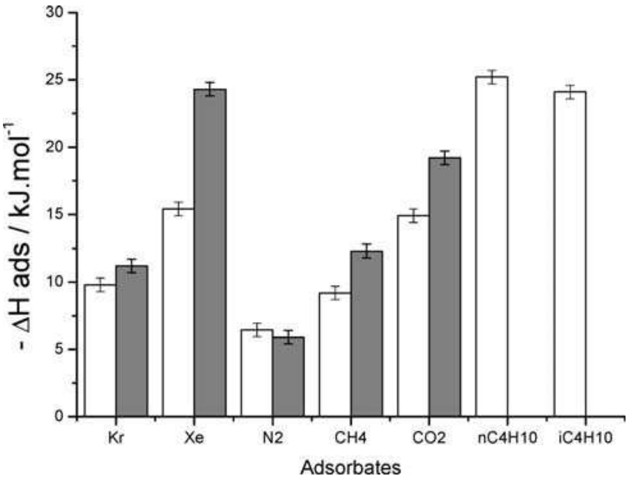

Figure 2. Isosteric heats of adsorption at very low coverages measured by TAP-2 experiments on IRMOF-1 (white) and IRMOF-3 (gray). Polarizability (Å^3) values of the gases are N_2 (1.47), Kr (2.8), CH_4 (2.6), CO_2 (2.91), Xe (4.04) from ref 36.

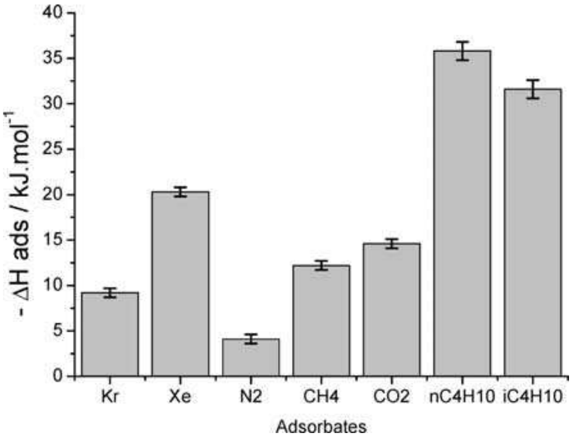

Figure 3. Isosteric heats of adsorption at very low coverage measured by TAP-2 experiments on HKUST-1.

Adsorption isotherms for CO_2 were also obtained by gravimetric measurements with a Rupprecht & Patashnick TEOM 1500 pulse mass analyzer. It consists of a microreactor with a high-resolution microbalance that generates real-time measurements of mass changes during gas−solid reactions.[18−20] The TEOM measures mass changes based on inertial forces,

---

[14] Gleaves, J. T.; Yablonskii, G. S.; Phanawadee, P.; Schuurman, Y. *Appl. Catal., A* **1997**, *160*(1), 55–88.

[15] Schuurman, Y.; Pantazidis, A.; Mirodatos, C. *Chem. Eng. Sci.* **1999**, *54* (15−16), 3619–3625.

[16] Linders, M. J. G.; van den Broeke, L. J. P.; Nijhuis, T. A.; Kapteijn, F.; Moulijn, J. A. *Carbon* **2001**, *39*(14), 2113–2130.

[17] Schuurman, Y. *Catal. Today* **2007**, *121*(3−4), 187–196.

[18] Chen, D.; Rebo, H. P.; Moljord, K.; Holmen, A. *Chem. Eng. Sci.* **1996**, *51* (11), 2687–2692.

[19] Zhu, W.; van de Graaf, J. M.; van den Broeke, L. J. P.; Kapteijn, F.; Moulijn, J *Ind. Eng. Chem. Res.* **1998**, *37*(5), 1934–1942.

[20] Giaya, A.; Thompson, R. W. *Microporous Mesoporous Mater.* **2002**, *55*(3), 265–274.

Downloaded by UNIV CLAUDE BERNARD LYON 1 on July 1, 2009
Published on June 4, 2009 on http://pubs.acs.org | doi: 10.1021/la900283t

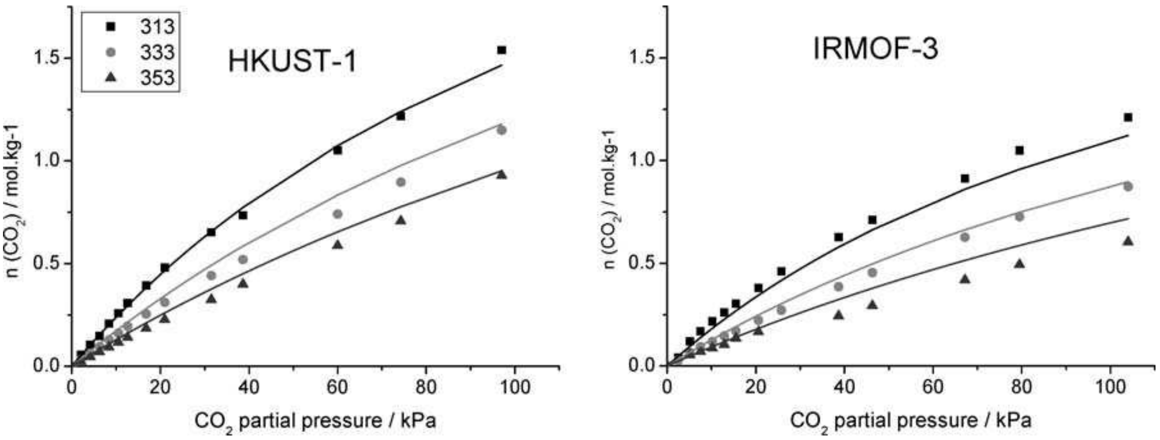

Figure 4. CO_2 adsorption isotherms obtained by gravimetric measurements (dots) and simulated data (line). IRMOF-1 data are not shown.

Table 2. Heats of Adsorption for CO_2 Measured and Simulated in This Work (kJ/mol)

$-\Delta H_{ads}(CO_2)$	gravimetric (TEOM)	pulse (TAP)	simulation
IRMOF-1	15.1 ± 0.4	14.9 ± 0.5	14.0
IRMOF-3	16.8 ± 0.3	19.2 ± 0.5	16.1
HKUST-1	12.1 ± 0.3	14.6 ± 0.5	14.9[a]/21.8

[a] pockets blocked.

presenting key advantages over conventional gravimetric microbalances: (i) a well-defined flow profile, eliminating possible (heat and mass) diffusion and buoyancy phenomena, (ii) a very fast response time resolution (0.1 s), and (iii) a high mass resolution across the entire range of pressure and temperature. The TEOM reactor was loaded with approximately 70 mg of adsorbent (sieve fraction 0.2−0.3 mm), firmly packed between two plugs of quartz wool. Prior to experiments, samples were evacuated at 550 K in He flow. When a stable baseline was reached, the reactor was cooled down to the first measurement temperature 300 K. The CO_2 uptake was measured at different CO_2 partial pressures, while the total pressure was maintained at 1 atm. The monitoring of the CO_2 partial pressure from 0.2 to 133 kPa was carried out by adjusting CO_2 and He mass flow controllers. Prior to measurements at other temperature (325, 350 K), the samples were heated again at 550 K. The CO_2 adsorption was determined from the mass change measured after the adsorption is reached, accounting for the mass change caused by the change of the gas density in the tapered element (blank experiments). Finally, heats of adsorption were calcu lated by multilinear regression using the Langmuir adsorption model.

Simulation Methods and Model

Adsorption isotherms were obtained using grand canonical Monte Carlo (GCMC) simulations.[21,22] The volume V, the temperature T, and the chemical potential μ are kept fixed; and at these conditions, the average number of molecules is computed. The chemical potential can be derived from the gas-phase pressure by using an equation of state (here Peng−Robinson). Simulations are defined in cycles, where during 1 cycle there have been N MC moves with N being the number of molecules. MC moves used for these simulations are random translation of a molecule, rotation, random reinsertion, insertion of a new molecule, and deletion of a randomly chosen existing molecule. We used 10^5 cycles. Henry coefficients and heats of adsorption at infinite dilution are obtained from NVT simulations using a single molecule. MC moves used are translation, rotation, and random reinsertion. During the simulation, the average potential energy is monitored, which is related to the heat of adsorption as $\Delta H = \langle U_{gh} \rangle - \langle U_g \rangle - RT$, where U_{gh} is the potential energy of the guest molecule inside the host framework, U_g is the potential energy of the adsorbate in the ideal gas reference state, and R is the gas constant. For the NVT simulations, we also used 10^5 cycles. Henry coefficient information is retrieved from the reinsertion MC move.[23]

The frameworks were kept rigid during the simulations with the positions taken from the crystallographic data in the literature.[11,24,25] The interactions of the adsorbates with the framework were modeled using Lennard-Jones potentials and static partial charges. The parameters for the framework were taken from the generic DREIDING model.[26] The charges for the framework were obtained from quantum mechanical calculations using the CHELPG method in *Gaussian03*.[27] Note that it has been found by several authors that simulation results for adsorption in IRMOFs are not very sensitive to precise values of the charges at room temperature.[9,10] The CO_2 molecule was modeled as a rigid molecule using Lennard-Jones parameters and charges from the TraPPE model.[28] Charge interaction was computed with the Ewald summation[21] using a relative precision of 10^{-6}. The number of unit cells was $1 \times 1 \times 1$. The Lennard-Jones interactions were truncated at 12.8 Å and tail corrections were omitted. Lorentz−Berthelot mixing rules were used to calculate mixed Lennard-Jones parameters. The charges and parameters for HKUST-1 are listed in Table 1. Similar charges for HKUST-1 were reported by Yang et al.[29] More details can be found in refs 30−33. For future investigations, we also determined the framework charges for a variety of other IRMOF structures

---

(21) Allen, M. P.; Tildesley, D. J. *Computer Simulation of Liquids*; Oxford University Press: USA, 1989.

(22) Frenkel, D.; Smit, B. Understanding Molecular Simulation (Computational Science Series, Vol *1*); Academic Press, 2001.

(23) Dubbeldam, D.; Calero, S.; Vlugt, T. J. H.; Krishna, R.; Maesen, T. L. M.; Smit, B. *J. Phy. Chem. B* **2004**, *108*(33), 12301–12313.

(24) Li, H.; Eddaoudi, M.; , M.; Yaghi, O. M. *Nature (London)* **1999**, *402*(6759), 276–279.

(25) Eddaoudi, M.; Kim, J.; Rosi, N.; Vodak, D.; Wachter, J.; , M.; Yaghi, O. M. *Science* **2002**, *295*(5554), 469–472.

(26) Mayo, S. L.; Olafson, B. D.; Goddard, W. A. *J. Phys. Chem.* **1990**, *94*(26), 8897–8909.

(27) Frisch, M. J.; Trucks, G. W.; Schlegel, H. B.; et al. *Gaussian03*; Gaussian, Inc.: Wallingford, CT, 2004.

(28) Potoff, J. J.; Siepmann, J. I. *AIChE J.* **2001**, *47*(7), 1676–1682.

(29) Yang, Q. Y.; Zhong, C. L. *J. Phys. Chem B* **2006**, *110*(36), 17776–17783.

(30) Dubbeldam, D.; Walton, K. S.; Ellis, D. E.; Snurr, R. Q. *Angew. Chem Int. Ed.* **2007**, *46*(24), 4496–4499.

(31) Frost, H.; Duren, T.; Snurr, R. Q. *J. Phys. Chem. B* **2006**, *110*(19), 9565–9570.

(32) Frost, H.; Snurr, R. Q. *J. Phys. Chem. C* **2007**, *111*(50), 18794–18803.

(33) Walton, K. S.; Snurr, R. Q. *J. Am. Chem. Soc.* **2007**, *129*(27), 8552–8556.

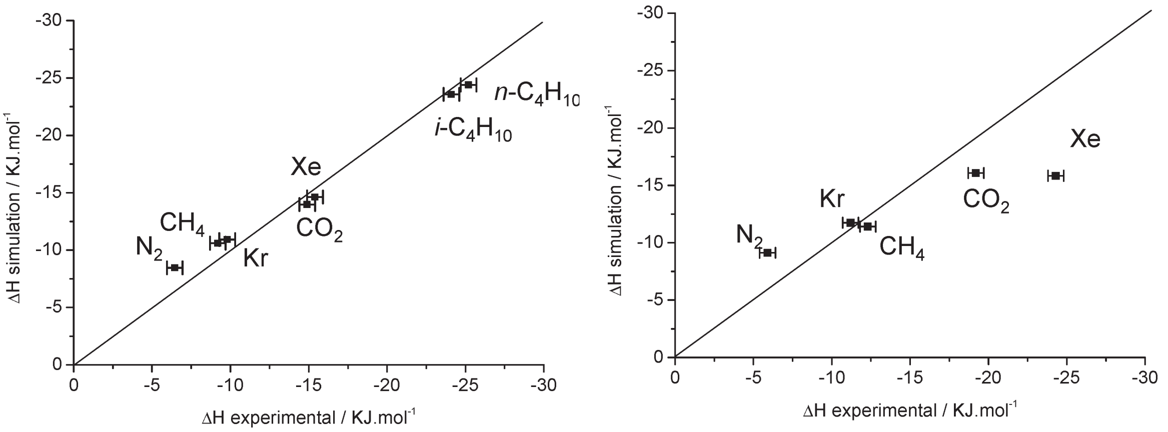

Figure 5. Comparison between low-loading adsorption enthalpies measured by TAP and calculated by Monte Carlo in IRMOF-1 (left) and IRMOF-3 (right).

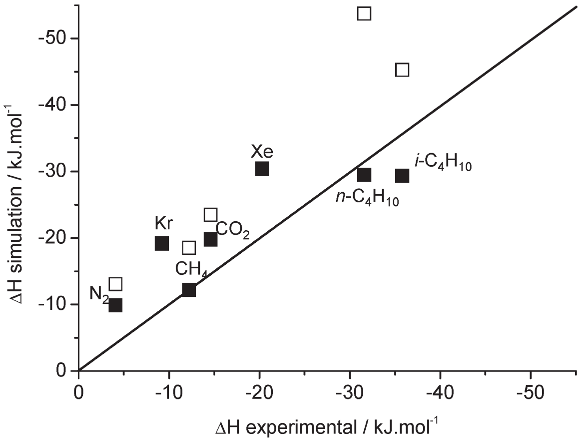

Figure 6. Comparison between adsorption enthalpies measured by TAP-2 and calculated by Monte Carlo in HKUST-1. The open symbols show Monte Carlo results where molecules can adsorb in the entire MOF structure; the filled symbols show Monte Carlo results where adsorption in the small pockets has been blocked.

Downloaded by UNIV CLAUDE BERNARD LYON 1 on July 1, 2009
Published on June 4, 2009 on http://pubs.acs.org | doi: 10.1021/la900283t

and MOF-177. These charges are reported in the Supporting Information.

Results

As an example of TAP experiments, pulse reponses for Xe on IRMOF-1 are illustrated in Figure 1. The plots show the normalized throughput of Xe after passing through the IRMOF-1 bed as function of the time. As expected, transient signals become sharper when the temperature increases, corresponding to faster Xe diffusion in the bed. The calculation of the heat was carried out by modeling the transient signals.

The isosteric heats of adsorption measured experimentally for various gases on IRMOF-1 and -3 are reported in Figure 2 . Unfortunately, experimental heats of adsorptions are usually not mentioned in the open literature for IRMOF samples, making a comparison difficult. Two studies using ^{129}Xe NMR have reported different values for Xe adsorption. Ooms and co-workers have measured a $-\Delta H$ of 12 ± 2 kJ mol^{-1} on IRMOF-1 in good agreement with our measurements, whereas Pawsey and co-workers report values in the range 5−6 kJ mol^{-1} for both IRMOF-1 and IRMOF-3.[34,35] The latter are significantly lower than with other classical nonpolar adsorbents such as carbon-based materials (usually in the range 15−20 kJ mol^{-1}). When comparing the two IRMOFs in Figure 2, we can clearly see that functionalization of the framework with amino groups leads to an increase of adsorption heats for most of the gases (Kr, Xe, CH_4, and CO_2). Millward and co-workers arrived at the same conclusion when comparing the CO_2 isotherms on IRMOF-1 and -3. For N_2, the change is not significant (in the error margin), whereas the strongest increase is observed for Xe. There is a rough correlation with the adsorbate polarizabilities. N_2, which has the weakest polarizability (α = 1.74 Å^3), shows no change, and Xe with the highest polarizability (α = 4.04 Å^3) exhibits the largest increase. These results suggest that the electric field created by the amino groups in IRMOF-3 increases the adsorption strength for more polarizable adsorbates.

Isosteric heats of adsorption for HKUST-1 are presented in Figure 3. Confidence intervals are larger for *n*- and *i*-butane because transient signals are quite broad, making the modeling less accurate. Here also in the literature, experimental heats of adsorption for HKUST-1 are scarce. For Krungleviciute et al.[37] and Wang et al.,[38] isosteric sorption enthalpies decrease sharply with the loading. Values of 14.0 and 35 kJ mol^{-1} were measured at the lowest coverage for Ar and CO_2, respectively. Our measurements for CO_2 differ significantly for HKUST-1. Finsy et al. report 50 kJ/mol for *n*-butane.[39]

Parallel to TAP experiments, CO_2 heats of adsorption were obtained by gravimetric measurements. Gas uptake was recorded from 0.2 to 133 kPa at 313, 333, and 353 K for the three MOFs as shown in Figure 4. Enthalpy values were calculated by fitting experimental data with the Langmuir model and are reported in Table 2. The gravimetric measurements confirm the consistency of the TAP results for the three MOFs. Values obtained by TAP are higher than the heats of adsorption measured by the gravimetric method. This is due to the measurement conditions: TAP data are obtained at very low coverage, whereas for gravimetric measurements, the calculation is performed over a larger range of loading.[14,18]

---

(34) Ooms, K. J.; Wasylishen, R. E. *Microporous Mesoporous Mat.* **2007**, *103* (1−3), 341–351.

(35) Pawsey, S.; Moudrakovski, I.; Ripmeester, J.; Wang, L. Q.; Exarhos, G. J.; Rowsell, J. L. C.; Yaghi, O. M. *J. Phys. Chem. C* **2007**, *111*(16), 6060–6067.

(36) Lide, D. R. Hanbook of Chemistry and Physics (84th ed); CRC Press: Boca Raton, 2004.

(37) Krungleviciute, V.; Lask, K.; Heroux, L.; Migone, A. D.; Lee, J. Y.; Li, J.; Skoulidas, A. *Langmuir* **2007**, *23*(6), 3106–3109.

(38) Wang, Q. M.; Shen, D. M.; Bulow, M.; Lau, M. L.; Deng, S. G.; Fitch, F. R.; Lemcoff, N. O.; Semanscin, J. *Microporous Mesoporous Mater.* **2002**, *55*(2), 217–230.

(39) Finsy, V.; De Bruyne, S.; Alaerts, L.; Devos, D.; Baron, G; Denayer, J. Shape selective adsorption of linear and branched alkanes in the Cu3(BTC)2 metal-organic framework, In *Stud. Surf. Sci & Catal.* Xu, R., Z. G., Chen, J., Yan, W., Eds.; 15th Int. Zeolite Conf., Beijing, China, August 12−17, 2007; pp 2048−2053.

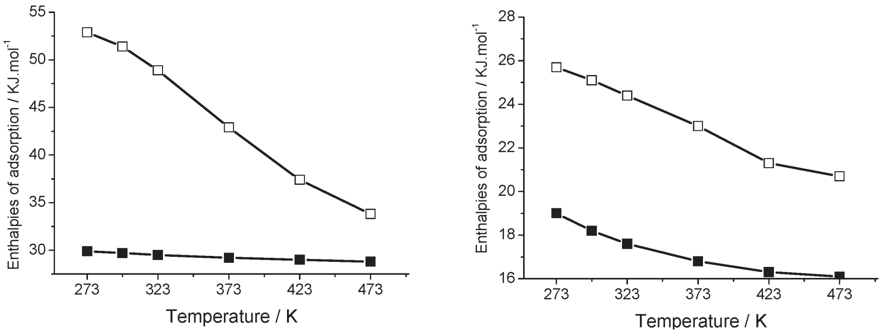

Figure 7. Enthalpies of adsorption in HKUST-1 at infinite dilution from molecular simulation for n-C_4H_{10} (left) and CO_2 (right) as a function of temperature. Two cases are shown: fully accessible HKUST-1 (open symbol) and HKUST-1 with the small pockets artificially blocked (filled symbol).

Downloaded by UNIV CLAUDE BERNARD LYON 1 on July 1, 2009
Published on June 4, 2009 on http://pubs.acs.org | doi: 10.1021/la900283t

In Figure 5, adsorption enthalpies obtained from experiment and simulation for IRMOF-1 and IRMOF-3 are compared for a variety of small gas molecules. The agreement between experiment and simulation is excellent for IRMOF-1 for all six gases. For IRMOF-3, the simulation results follow the same trend as the experiments, but the agreement is not as good. In particular, Xe and CO_2 show lower heats from simulation than from experiment.

For HKUST-1 (open symbols in Figure 6), the simulation results do not match experiment as well as for the IRMOF samples. We hypothesized that a possible explanation for this would be if molecules could access the small favorable pockets in the simulations but not in the experiments. To test this, we performed additional experiments in which the small cavities were artificially blocked using a 5 Å radius around the center of each pocket. These results (filled symbols in Figure 6) agree much better with the experimental results, suggesting that the small pockets are inaccessible in the experimental samples.

Figure 7 (open symbols) shows the temperature dependence of the heats of adsorption of n-C_4H_{10} and CO_2 in HKUST-1 predicted by simulation. There is a surprisingly large temperature dependence for these guest molecules (about 20 kJ/mol for n-C_4H_{10}). This is due to the large adsorption enthalpy in the small pockets and the fact that at higher temperature the molecules are driven out of the pockets. From simulation results, we have indeed observed that adsorbates prefer to move to the bigger pores where the adsorption enthalpy is not as favorable. This phenomenon was also reported very recently elsewhere.[40] This temperature dependence is much lower when these pockets are blocked (Figure 7, filled), and the values for the blocked case are in better agreement with experiment. A similar effect has been found as a function of loading by Chmelik et al.[12] They report that heats of adsorption for neo-pentane, n-butane, isobutene, and 2-methylbutane drop off 20 kJ mol^{-1} above 10 molecules per unit cell in HKUST-1. Our results also match well the study performed by Garcia-Perez et al.[40] considering that our calculations were performed at slightly higher temperature for consistency matters with the experimental data. The close match in size between adsorbates and the small pockets leads to a high heat of adsorption and probably explains many of the discrepancies between simulation and experiment and among experimental data sets in the literature for HKUST-1.

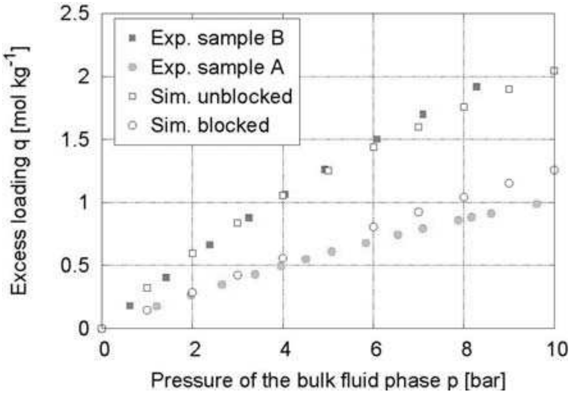

Figure 8. Simulated adsorption isotherms for N_2 at 295 K in HKUST-1 compared to experimental results of Chowdhury et al.[41]

To further investigate HKUST-1, we simulated N_2 isotherms with and without the small cavities artificially blocked. Our simulations are compared with recent experimental results from Chowdhury et al.[41] In this work, the impact of preparation methods on adsorption isotherms are revealed. The preparation methods differ in the solvent used and the temperature conditions during synthesis, as well as in the drying procedure. Samples "A" are synthesized in water/ethanol at 413 K and then dried at 358 K, whereas samples "B" are prepared in DMF/ethanol at 373 K, which are then extracted by Soxlhet technique with MeOH and then dried at room temperature. Samples "B" are clearly of higher crystallinity and purity (no Cu_2O phases), resulting in higher surface area of 1482 against 857 m^2/g for sample "B". The same authors further show that these high/low values are representative of a number of published data from different groups. It shows that two distinct classes of compounds exist, which are characterized by BET surface areas (1) around 1500 m^2/g and (2) around 700−900 m^2/g, respectively. Simulated N_2 isotherms at 295 K are compared with experimental data obtained from samples "A" and "B" in Figure 8. The results show that the simulated unblocked isotherm agrees well with the experimental isotherm obtained from sample "B", and the simulated blocked isotherm agrees well with the experimental results for sample "A". It suggests that HKUST-1 samples in group 2 have inaccessible small pockets. The presence of impurities such as acids in the cavities or strongly bonded water molecules (due to the low-temperature desorption) may be responsible for the blockage of the side pockets. In Table 3, we further compare simulated Henry coefficients with literature values for "B" samples. Here again, we note very good agreement between experimental and theoretical studies.

---

(40) García-Pérez, E.; Gascón, J.; Morales-Flórez, V.; Castillo, J. M.; Kapteijn, F.; Calero, S. *Langmuir* **2009**, *25* (3), 1725−1731.

(41) Chowdhury, P.; Chaitanya Bikkina, C.; Meister, D.; Dreisbach, F.; Gumm, S. *Microporous Mesoporous Mater.* **2008**, *117*(1−2), 406–413.

Table 3. Henry Coefficients Obtained by Simulations for Various Adsorbates at 295 K in HKUST-1 (without Pore Blocking) Compared to Two Experimental Data Sets from the Literature[38,41]

adsorbate	H_k [mol/kg/Pa] exp[38]	H_k [mol/kg/Pa] exp[41]	H_k [mol/kg/Pa] simulation
CO_2	6.24×10^{-5}	3.47×10^{-5}	6.0×10^{-5}
O_2	2.12×10^{-6}	2.8×10^{-6}	5.0×10^{-6}
Ar		2.8×10^{-6}	4.85×10^{-6}
N_2	3.09×10^{-6}	3.1×10^{-6}	3.9×10^{-6}

Conclusions

Heats of adsorption have been measured for a systematic set of gases in three common MOFs (IRMOF-1, IRMOF-3, and HKUST-1). In addition, molecular simulations have been performed for the same systems. Agreement between simulation and experiment is excellent for IRMOF-1 and good for IRMOF-3. Simulations predict a large temperature dependence of the heat of adsorption in HKUST-1, which is reduced significantly when the small pockets are blocked. The combined experimental and simulation study sheds light on discrepancies found in the literature for adsorption in HKUST-1. We hope this study will stimulate experimentalists to examine the effect of temperature on the crystal structure (including the changes upon water adsorption on Cu site) and its effect on gas adsorption.

Acknowledgment. This work was supported by TopCombi (NMP2-CT2005-515792), the U.S. National Science Foundation (CTS-0507013), and by TeraGrid computing facilities.

Supporting Information Available: Tabulated adsorption enthalpies from experiment and simulation; XRD patterns; atomic charges for a large variety of related MOFs. This material is available free of charge via the Internet at http://pubs.acs.org.

Downloaded by UNIV CLAUDE BERNARD LYON 1 on July 1, 2009
Published on June 4, 2009 on http://pubs.acs.org | doi: 10.1021/la900283t

ELSEVIER

Chemical Engineering Journal 138 (2008) 379–388

Chemical Engineering Journal

www.elsevier.com/locate/cej

High-throughput gas phase transient reactor for catalytic material characterization and kinetic studies

G. Morra [a], A. Desmartin-Chomel [a], C. Daniel [a], U. Ravon [a], D. Farrusseng [a,*], R. Cowan [b], M. Krusche [b], C. Mirodatos [a]

[a] *IRCELYON, Institut de recherches sur la catalyse et l'environnement de Lyon, Unité Mixte de Recherche 5256 CNRS-Université de Lyon 1, 2 avenue Albert Einstein, F-69626 Villeurbanne Cedex, France*

[b] *AMTEC GmbH, Annaberger Strasse 240, 09125 Chemnitz, Germany*

Received 7 May 2007; received in revised form 18 June 2007; accepted 18 June 2007

Abstract

This work presents an alternative approach for material screening, aiming at investigating under high throughput (HT) conditions key features like kinetic and thermodynamic parameters in catalysis and gas adsorption. A 16-parallel reactor was specifically designed for HT transient screening and kinetics. The fluidic system which enables parallel transient experimentation is detailed. Among its capabilities, this HT equipment allows one to evaluate (i) reaction kinetics under the same ageing conditions for a library of catalysts, and (ii) simplified aging kinetics as well for accessing proper conversion and selectivity data to be modelled. In the domain of adsorption, isotherms of pure component and gas mixtures can be measured by means of parallel breakthrough curve experimentation. The capability, versatility and limits of this equipment are demonstrated through the following case studies: (1) deactivation and kinetic study of *o*-xylene hydrogenation, (2) characterization of oxygen storage capacity (OSC) of metal/ceria-doped catalysts and (3) HT gas adsorption on microporous materials.

© 2007 Elsevier B.V. All rights reserved.

Keywords: High throughput catalysis; Combinatorial catalysis; Parallel reactor; Transient experimentation; Xylene hydrogenation; Oxygen storage; Gas adsorption; Pressure swing adsorption

1. Introduction

High-throughput (HT) screening relies on a fast testing of large libraries of compounds by using parallel reactors. This research methodology, massively applied for drug development, was extended to Material and Catalysis science in the late 1990s. Commonly, a HT research project can be carried out in two stages. The primary stage consists at screening large and as diverse as possible libraries to identify promising candidates called "hits." The latter are then optimized in a secondary screening stage with targeted libraries. The primary screening is usually characterized by a high degree of parallelization and a very fast or parallel analysis while the secondary screening is driven by higher quality data which are obtained under more realistic operating conditions and shall consider scale-up issues, fluid dynamic and process control.

Numbers of parallel experimental set-ups were developed for gas-phase reaction. An overview of current developments can be found in [1,2]. HT testing equipments for primary screening can be divided into two categories. The first ones are monolith or micro-channel type reactors in which each channel is coated with a catalyst layer having a specific composition [3–7]. The second ones are addressable arrays of thin films on wafers [8–11] or single beads [12]. In most cases, the gas phase is analysed by mass spectrometry using a sampling capillary mounted on a XY robotic actuator to test all the catalysts individually and sequentially. In contrast, HT testing equipments for secondary screening are usually fixed bed reactors with catalyst loading in the range of 20–200 mg. They consist in multi-tubular reactor modules made of steel, quartz or ceramics [13–24].

Although the secondary screening provides a quantitative evaluation of catalytic performances under operating conditions close to the real applications, much more detailed investigations on catalytic performances must be carried out before scaling up the best selected systems towards mini-pilot scale reactors. This stage, also called tertiary screening, comprises catalysts

---

* Corresponding author.
E-mail address: david.farrusseng@ircelyon.univ-lyon1.fr (D. Farrusseng).

1385-8947/$ – see front matter © 2007 Elsevier B.V. All rights reserved.
doi:10.1016/j.cej.2007.06.023

activation/deactivation studies, kinetic studies, mass and heat transfer analysis, poisoning under real inlet gases and catalyst characterization, in and/or ex situ [25,26]. Secondary and tertiary screenings are operated on a reduced number of materials. A few numbers of parallel equipments were developed for these purposes. Perez-Ramirez et al have designed a six flow reactor setup was for HT kinetic studies [27]. The key feature of the catalytic bench relies on the fluid feeding system which enables to feed each of the six reactors at a different flow rate or pressure while the proportion of reactant remains the same. This design is very well appropriate when one looks at adjusting the contact time to obtain many conversion data points in appropriate ranges for kinetic modelling. The "Spider$^{\mathrm{TM}}$" reactor, developed by Serra et al, consists of 16 parallel high-pressure reactors which can be fed independently for oil refining applications [18].

Whatever the degree of sophistication of these reactors, a key type of catalytic processes can hardly be caught correctly. They relate to catalytic instability phenomena like activation/deactivation processes occurring during steady-state operations, or catalyst behaviour under transient operating conditions which may correspond to permanently unsteady processes employing moving or fluidized bed, post-combustion, reverse flow reactors, domestic applications, etc.

If one considers for example deactivation processes, their rates depend usually on catalyst formulation and operating conditions. In a sequential testing process, the first and the last catalyst of a loaded series of six or more catalysts are evaluated at very different time on stream, depending on the time required for analysing each sample. This generally results in bias activity values [14].

A way to tackle that issue is to perform HT kinetic studies on a truly parallel system. A 16-channel reactor system equipped with a spatially resolved FTIR was developed at the University of Delaware to perform kinetic measurements under truly parallel conditions [28]. The system was successfully applied for CO oxidation and NOx storages. In contrast to sequential analysis by gas chromatography and/or mass spectrometry, this system offers the opportunity to record catalytic measurements every 4–12 s for all catalysts which then enable to have access to kinetic data under controlled and similar time-on-stream conditions.

In this paper, a 16-parallel reactor designed for HT transient screening and HT kinetics is presented. The fluidic supply that enables parallel transient experimentation and the reactor modules are described. The capability, versatility and limits of the testing units are illustrated through a series of examples: (1) deactivation under steady-state conditions and kinetic study of *o*-xylene hydrogenation, (2) characterization of oxygen storage capacity (OSC) of ceria-doped catalysts by transient redox operations, and (3) HT gas adsorption isotherms on microporous materials by transient adsorption/desorption cycles. Another successful application dealing with transient temperature runaway during temperature programmed catalytic soot combustion will be reported in a forthcoming paper.

2. Experimental

2.1. Reactor system for fast material screening

A proprietary 16 channel-multitubular reactor (Fig. 1) – which has now been commercialised as the SWITCH 16 reactor system by AMTEC GmbH [29] – was jointly developed within the frame of a joint EU program [30] by IRC-CNRS and AMTEC.

The fluidic supply consists of a combination of two separate feed delivery modules and two 16-port valves that are placed before and after the multi-channel reactor array. The reactors are made from Inconel 600 and are connected to the inlet and outlet lines using VCR fittings, and have internal diameters of 7 mm. They can be operated at up to 600 °C and 13 bars. Each feed delivery module is equipped with five mass flow

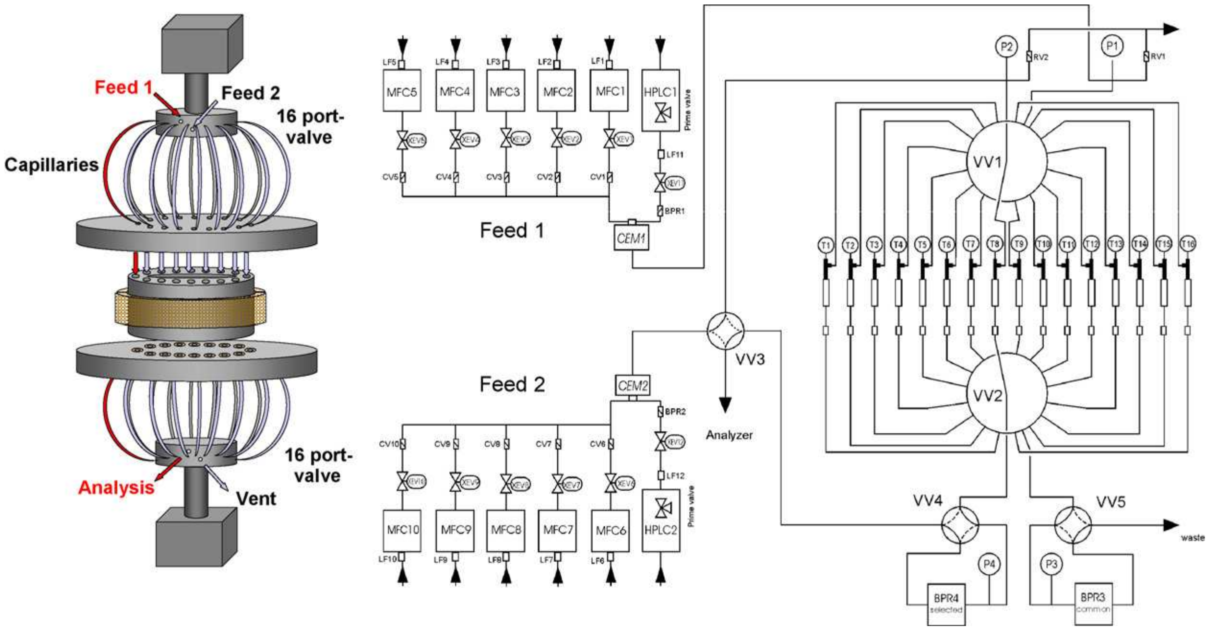

Fig. 1. Operating principle of the multi-channel reactor (left), and flow scheme (right).

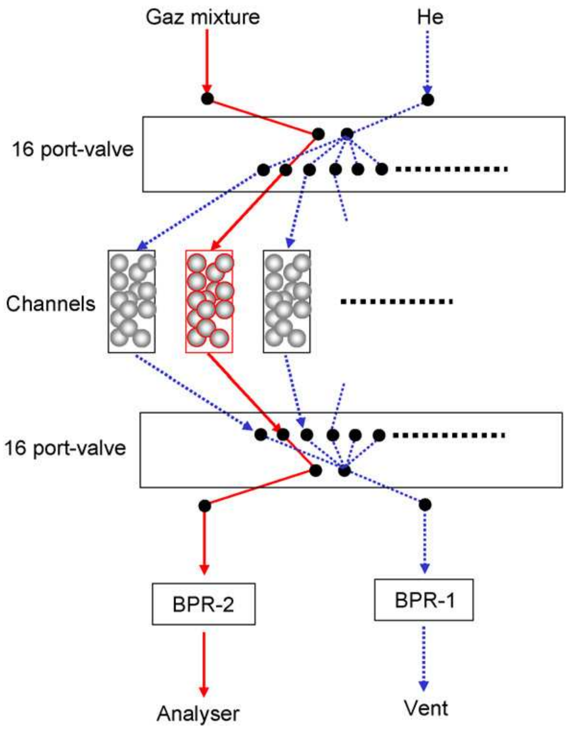

Fig. 2. Feed system scheme showing the two 16-port valve positions and flow through the selected reactor.

controllers (MFC) and a controlled evaporator mixer (CEM-Bronkorst). All the tubing and valves can be heated in order to prevent vapour condensation. The upper 16-port valve enables transient experimentation to be carried out in all 16 channels. The two 16-port valves can be synchronized so that when the upper valve switches to a given channel the lower valve selects the corresponding outlet channel which is connected to analytical systems. This system thus offers the opportunity to feed one selected reactor with a selected feed composition (Feed 2) while the 15 others are fed with a second composition (Feed 1), which can be identical to or different from Feed 1 (Fig. 2). This design has several advantages regarding testing capabilities and the type of experiments that can be carried out, that is, it is possible to evaluate catalysts under exactly the same ageing period and more specifically to measure the initial activity of each catalyst. Testing conditions can be varied in the selected channel while the other channels are maintained under standard or inert conditions, and in addition, catalyst deactivation can be studied in the selected channel while the 15 other channels are being regenerated. Finally, the design ensures that very accurate and reproducible flows are guaranteed in the selected channel by the 16-port valve. In the cases of permanent gas, the standard deviation is 0.4%. It is usually higher in the case of vapours and it depends very much of pressure, flows and nature of vapours. In the case of xylene hydrogenation the partial pressure of xylene is measured with a standard deviation of 4%. Conversion calculations are based on the partial pressure of *n*-heptane used as internal reference. There is therefore no need to use flow restrictors, which is an asset when acquiring suitable transient signals. However, in case of steady state experimentations (not reported here), flow constrictor systems can be used to guarantee equal flow distribution in the 15 other channels. Downstream, both lines are equipped with mechanical back pressure regulators (BPR) which control pressure in the common and selected lines. The back pressure regulators can be bypassed if required.

In the next presented case studies, the reaction products were monitored by gas chromatography and/or on-line mass spectrometry. GC analysis was performed by using an Agilent 3000 version QUAD instrument equipped with a four-channel module. Channel A was used for H_2, O_2, N_2, CH_4 and CO measurements (MolSieve 5A, BF PPU Plot, with Ar as carrier gas), Channel B for CO_2 and H_2O (PPU, BF PPQ, with He as carrier gas). Channel C for *cis*- and *trans*-dimethyl-cyclohexane (OV1) and Channel D for *o*-xylene quantification (Stabilwax). Mass spectrometer (SM) analysis was performed using an Inficom CPM instrument.

2.2. Case study 1: kinetic studies of o-xylene hydrogenation

2.2.1. Background and objective

Toluene and xylenes are typical model molecules used for fundamental studies on the hydrogenation of aromatic hydrocarbons which takes place in petro-chemical refinery units. In contrast with most of combinatorial studies where the catalyst optimization for higher activity or selectivity is targeted, the search of relationships between the catalyst descriptors (metal nature, dispersion, support interaction, doping effects) and the catalytic performances is the main objective when investigating model reactions. Although the model reaction of *o*-xylene hydrogenation is investigated for several decades, its mechanism is still a matter of debate. A number of conceptual reaction pathways were introduced such as the stepwise [31], rollover [32] and interfacial [33] mechanisms. Usually a kinetic model is supported by experimental data on a specific class of catalysts and the extrapolation of the derived model to other systems is always questionable. The investigation of a kinetic model which holds for diverse catalysts whatever be the active metallic sites, dopants and supports meets this above mentioned objective for searching quantitative relationships between catalyst description and catalytic performance.

Another major issue to be tackled for any kinetic study is deactivation phenomena (carbon deposits, particle growth, metal/support interaction, alloy formation or demixing) which may be specific for each tested catalyst and which cannot a priori be predicted. This issue may be even more critical during HT parallel investigation. When a catalyst is under testing, the deactivation of other catalysts is not monitored. Indeed, the choice of catalytic systems that do not deactivate with time on stream will overcome any aging issues during parallel screening [14]. However, this extremely restrictive solution cannot be envisaged in any industrial oriented project. The investigation of aging kinetics is therefore a prerequisite for handling properly reaction kinetics.

This first case study aims at acquiring a pool of kinetic data in view to further discriminate various kinetic models, while monitoring correctly the catalyst ageing all along the kinetic

Table 1
Selected catalysts which display diverse formulation, initial activity and deactivation profile in *o*-xylene dehydrogenation

Catalyst ID	Metal content (wt.%)	Support	Catalyst weight (mg)
1	0.5 Rh	Low surface Al_2O_3	30
2	0.5 Ni, 0.16 Mo	Low surface Al_2O_3	50
3	0.5 Pd	Low surface Al_2O_3	50
4	0.5 Rh, 0.19 In	High surface Al_2O_3	30
5	0.5 Pt	Low surface Al_2O_3	50
6	4 Ni, 0.77 In	Low surface Al_2O_3	100
7 (benchmark)	0.3 Pd	Low surface Al_2O_3	200

Catalyst #7 was characterized and tested in details and is used as a reference benchmark.

campaign. Only the initial part of this study will be presented here, to demonstrate the capability of the equipment.

A library of 100 bi-metallic catalysts supported on various supports was prepared and tested in the hydrogenation of *o*-xylene. For sake of clarity, only a selection of six representative catalysts is presented here (Table 1), characteristic of diverse catalytic properties (high/low activity and deactivation shapes) and catalyst formulation (metals and supports). Results on the whole library will be reported elsewhere.

2.2.2. Methodology

The deactivation study was first carried out by testing the catalysts one by one for about 1 h, that is, contacting each one with the reacting mixture while the others are maintained under H_2/N_2 flow. The switching protocol described in the experimental section was used for this purpose. Several equations were investigated to model the observed deactivation profiles. Then, kinetic data were obtained by varying H_2 partial pressure and contact time (total flow) for a given catalyst at a given temperature. When the whole set of experimental conditions is completed, the catalyst is placed in the initial conditions applied for deactivation studies and analyses are performed. Next, the selection valve switches to the next catalyst. At the end of the cycle (16 catalysts), the whole heating block is set to the next temperature dwell and the next cycle is started as soon as the temperature is stabilized.

2.2.3. Testing conditions

For the initial deactivation study, catalysts are tested with a stream of 0.5%(mol) *o*-xylene, 5%(mol) heptane, 25%(mol) hydrogen and nitrogen as diluent (Feed 2). The other channels are maintained under H_2/N_2 flow (Feed 1). The catalysts are previously reduced under H_2 at 400 °C for 2 h.

For the kinetic study, reactors are loaded with 50, 100, 200 or 400 mg of catalysts depending on their previously measured activity. The H_2 partial pressure was varied from 0.5%(mol) to 48% (mol), the temperature from 100 to 200 °C and the total flow from 20 $\mathrm{mL_{CNTP}}$/min to 50 $\mathrm{mL_{CNTP}}$/min. Each GC analysis was duplicated.

Generally speaking, it was observed that conversion can attain the thermodynamic equilibrium for one catalyst but is below detection limits for a second one although the two tested systems have “similar” compositions. As an example, the doping of Pd/alumina catalyst with Ge can multiply the activity by a factor 20 [34]. This parameter sensitivity causes experimental issues when one wants to investigate kinetics. As a consequence, the catalyst mass in the channel, that is, contact time, must be adjusted with respect to the initial activity in order to measure conversion and selectivity in appropriate ranges (outside diffusion regime but being large enough to be correctly measured) for further kinetic modelling.

2.2.4. Kinetic modelling

In order to test different kinetic models, a catalyst (catalyst #7) which does not deactivate and shows low conversion in the experimental conditions was selected as reference catalysts. A large dataset of more than 200 data points was collected and used as benchmark for model discrimination study and to simulate the impact of deactivation rates on the kinetic parameters.

About 10 different existing models and derivatives were investigated, from simple power-law to more advanced models based on diverse mechanism steps. For the present study, the selected model (referred to as Cin1) assumes that the adsorption of reactants is competitive and H_2 does not dissociate. It can be described by the following steps:

$$\left.\begin{array}{r} A + * \xleftrightarrow{K_A} A* \\ H_2 + * \xleftrightarrow{K_H} H_2^* \\ A^* + 2H_2^* \xleftrightarrow{K_{AH_4}} AH_4^* \end{array}\right\} \text{Equilibrated,}$$

$$(r_1) AH_4^* + H_2^* \xrightarrow{k_1} C + 2*,$$

$$(r_2) AH_4^* + H_2^* \xrightarrow{k_2} T + 2*$$

where A stands for the aromatic, C and T for *cis*-DMCH and *trans*-DMCH, respectively [32,35,36].

A rate equation for *o*-xylene conversion was built accordingly and it was also checked that no diffusion limitations occurred under the testing conditions. For that, the criterion $\tau = -\ln(1 - X)/k$, where τ is contact time; X, conversion; k, rate constant, was found to be fulfilled for all tested catalysts.

2.3. Case study 2: oxygen storage capacity measurements on ceria-doped catalyts

2.3.1. Background and objective

Ceria-based mixed oxides ($Ce_xM_{1-x}O_y$) are versatile solid oxygen exchangers. At high temperatures (400–800 °C) the redox cycle $Ce^{3+} \Leftrightarrow Ce^{4+} + e^-$ facilitates oxygen storage and release from the bulk fluorite structure. In addition, the surface redox chemistry of ceria is sensitive even at low temperatures to crystal structure defects [37] which can be tuned by substituting some of the Ce cations with ions of different size and/or charge [38,39]. This makes them ideal candidates for catalytic oxidation applications where their oxygen storage capacity (OSC) can be used in a dynamic way, such as the three-ways catalysis, and/or the hydrogen production under non-stationary conditions [40].

This second case study aims at showing how the effects of doping the ceria support of platinum based catalysts on OSC can be investigated using the parallel testing reactor set-up above presented, aiming at discovering new materials [41].

2.3.2. Methodology

A set of 12 catalysts containing 2 wt% Pt on $Ce_{0.9}M_{0.1}O_x$ was prepared (where M = Pb, Bi, Zr, V, W, Mo, Y, La, In, Sn, and two combinations of Zr/Bi, respectively) by impregnating platinum on various doped ceria supports. In practice, one reactor channel was loaded with a dopant free high surface area Pt/CeO_2 catalyst for comparison. The temperature was varied stepwise from 100 to 200 °C every 20 °C. OSC measurements were quantified by H_2 consumption in transient mode using the parallel reactor under isothermal conditions: Catalyst samples were oxidised in air for 15 min, then flushed with N_2 and then reacted with a reducing mixture of 10% H_2 in He while measuring continuously the hydrogen consumption by the Mass spectrometer for 3 min. While one sample was analyzed under 10% H_2 flow, the other ones were maintained under N_2 flow. After a cycle was completed, the temperature was increased by 20 °C and a new cycle started following the previous experimental sequence.

2.4. Case study 3: adsorption isotherms of microporous materials

2.4.1. Background and objective

The selective capture of carbon dioxide is a major objective for any large-scale process, CO_2 being one of the main greenhouse effect gases. For instance its separation from methane is required in the processing of natural gas. Generally, pipeline specifications for natural gas require a carbon dioxide concentration below 3%. The technology most widely used for carbon dioxide removal is amine absorption, but amine plants are costly and subjected to strong environmental constraints. An alternative, which is more recently applied, is the removal of carbon dioxide by means of an adsorption process. Pressure swing adsorption (PSA) technology has gained interest due to low energy requirements and low capital investment costs. Its main issue is to find an appropriate adsorbent which shall adsorb selectively one component over a mixture while not being adsorbed too strongly, otherwise the regeneration step can negatively affect the economy of the process. Separation by PSA can be based either on the different adsorption affinity of the components (thermodynamic separation), or on the different diffusion rates in the adsorbent (kinetic separation) [42,43]. For thermodynamic separation, the two key criteria of adsorbent effectiveness are the working capacity (WC) and the working selectivity (WS). The definition of working capacity is given in Eq. (1):

$$\mathrm{WC_A} = Q_\mathrm{A}(x, P, T)_\mathrm{ads} - Q_\mathrm{A}(x, P, T)_\mathrm{des} \tag{1}$$

where $Q_\mathrm{A},(x, P, T)_\mathrm{ads}$ and $Q_\mathrm{A},(x, P, T)_\mathrm{des}$ are the equilibrium loadings of A (mol/g) corresponding to the gas phase mole fraction (x), total pressure (P) and temperature (T) at adsorption and desorption steps, respectively. The working capacity physically represents the net amount of adsorbate transacted on and off of the adsorbent for each complete cycle, providing a good indication of the amount of adsorbent required for the separation. The working selectivity of component A relative to component B (defined in Eq. (2)) is a key indicator since it represents the separation efficiency. The operating conditions will dictate the selectivity and hence the performances of the adsorbents.

$$\alpha = \frac{\mathrm{WC_A}}{\mathrm{WC_B}} \tag{2}$$

Here, the adsorption isotherms are assumed to follow Langmuir behaviour; that is, the sorbents exhibit monolayer coverage as the saturation pressure is approached and have an energetically homogeneous surface. However, this parameter can be easily extended to other adsorption models as well. Isotherms were modelled using the Langmuir equation for a single component which can be written in the following form:

$$Q = \frac{Q_\mathrm{sat} K p}{(1 + K p)} \tag{3}$$

where $K = k\exp(-\Delta H/RT)$ and p is the partial pressure of the single component in the diluted feed.

This third case study aims at demonstrating the ability of the Switch 16 set-up for rapidly acquiring the above described key indicators for CO_2 adsorbent screening.

2.4.2. Methodology

The adsorption isotherms are calculated from breakthrough curves measurements taken at different total pressure [44]. Breakthrough curves consist at quantifying gas uptakes of an adsorbent bed in a transient operating mode. A gas mixture is sent to a selected channel for which the pressure is fixed at a given value. Partial pressures are measured on line by MS for a few minutes till the adsorbents get saturated. While adsorption measurements take place at the selected channel, the other channels are flushed under He flow to allow gas desorption for next measurements under different conditions of temperature and/or pressure.

In the reported study, channels are loaded with 200 mg of sieved adsorbents. The feed is a gas mixture of 12.5% CO_2, 12.5% N_2 in He with a total flow rate of 40 ml min^{-1}. The breakthrough curves were recorded at different total pressure from 1.4 to 6 bars. The adsorbents are zeolites supplied by ENI Technology (NaX, NaY, NaZSM5, KL, NaBeta) and purchased from Flucka for 13X or made at the laboratory (NaZSM5 with Si/Al = 27, 240). Microporous metal organic frameworks $Cu_2(BTC_3)$ and a second undisclosed compound were prepared by precipitation.

3. Results and discussion

3.1. Kinetic studies of o-xylene hydrogenation

3.1.1. Deactivation processes

The deactivation decay curves acquired for six representative catalysts over a period of several hours are reported in Fig. 3. As can be seen, the more active the systems, the more it is deactivating. Two general aging trends were observed: an initial exponential deactivation for all catalysts in the very first hours on stream, followed/or not by a linear deactivation. These two

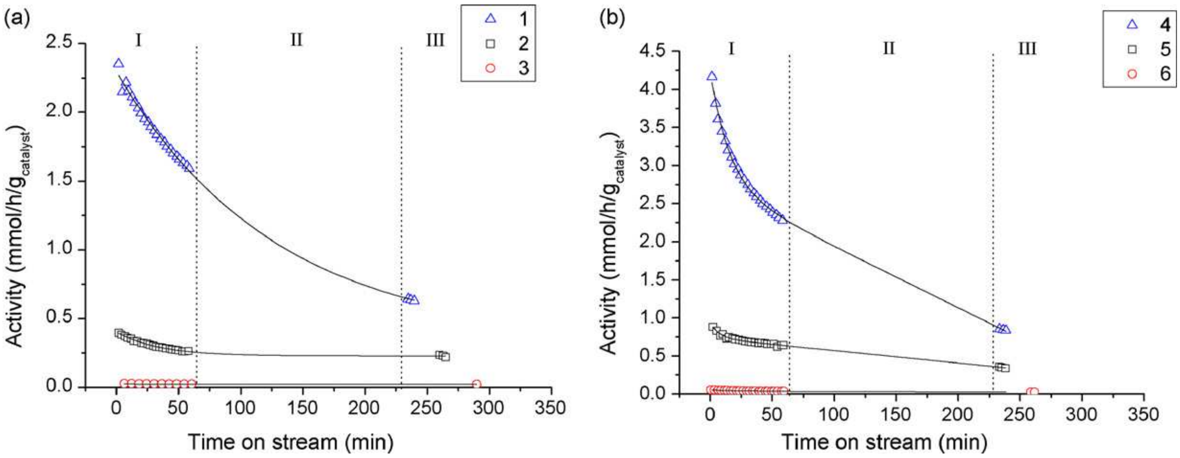

Fig. 3. Deactivation profiles during o-xylene hydrogenation for six selected catalysts. (a) Exponential (Deac1) and (b) exponential + linear (Deac2) decay models. Part I (from 0 to 60 min) corresponds to the collection of deactivation data; Part II (from 60 to 250 min), to the collection of kinetic data and Part III, to the acquisition of data in the initial deactivation conditions after 4 h on stream.

types of deactivation profiles were described by a simple exponential model (Deac1) or by a combination of an exponential and a linear model such as (Deac2)

$$A = A_\infty + k\,\mathrm{e}^{-(t/\tau)} \text{(Deac1)} \quad A = A_\infty - \nu t + k\,\mathrm{e}^{-(t/\tau)} \text{(Deac2)}$$

where A is the activity; A_∞ is the residual activity; ν is the rate of linear decrease; k is the pre-exponential factor and τ the relaxation time.

For both deactivation types, three catalysts exhibiting high (catalysts #1 and #4), medium (catalysts #2 and #5) and low activities (catalysts #3 and #6) are presented. As such, the range of initial conversions spans from 20% for catalysts #1 and #4 to 1% for catalyst #6.

Concerning the possible models for activity decay with time on stream, let us briefly recall that according to Levenspiel [45], the most general expressions are summarized in Table 2.

For the present case of o-xylene conversion, no concentration dependency was evidenced, (i.e., rate of decay was essentially independent of o-xylene, hydrogen or DMCH concentration). Additional TPO experiments performed on spent catalysts have shown that coke deposition occurred on deactivated samples. Therefore coking effects may be the cause of this activity-dependant poisoning. A mechanism by coke deposition which encapsulate the metal particles and/or block the pores by deactivation progressively the catalyst bed from top to bottom of the reactor would qualitatively fit with the observed decay curves.

Table 2
Summary of deactivation models

Activity decay	Concentration-dependence	Aging rate equation
Independent	None	$-\mathrm{d}a/\mathrm{d}t = k_\mathrm{d}a^\mathrm{m}$
Parallel	Reactant A	$-\mathrm{d}a/\mathrm{d}t = k_\mathrm{d}C_\mathrm{A}^\mathrm{n}a^\mathrm{m}$
Series	Product B	$-\mathrm{d}a/\mathrm{d}t = k_\mathrm{d}C_\mathrm{B}^\mathrm{n}a^\mathrm{m}$
Side-by-side	Feedstock impurity P	$-\mathrm{d}a/\mathrm{d}t = k_\mathrm{d}C_\mathrm{P}^\mathrm{n}a^\mathrm{m}$

a is the activity relative to fresh catalyst at a fixed point in a catalyst bed; k_d deactivation rate constant; C is the concentration of reactant A, product B or feedstock poison P; n and m are orders of decay on concentration and activity, respectively.

In addition, better fits were observed in most cases when an overlaying linear trend is added to the initial exponential model. This linear and constant deactivation, independent from activity, is assumed to be limited in time (for sake of model validity). This underlying mechanism could be a non-selective poisoning of the catalytic bed coming from a toxic component contained in the feedstock (e.g. traces of oxygen or of another pollutant). It would be classified as a side-by-side activity.

Indeed, these speculations require further analyses, such as establishing the decay rates as a function of coke contents (via advanced coke deposition kinetics acquired on an oscillating thermobalance TEOM, for instance) which might ascertain the decay origin. However, within the scope of the present study, this advanced knowledge of the aging process is not required for further discrimination of the reaction kinetics.

Table 3 presents the results of the aging modelling. As mentioned above, catalyst #7 showed no deactivation and has been used as a benchmark to test kinetics models and to simulate the deactivation impact. As previously noted, the most active catalysts show the biggest global deactivation. Although catalysts #3 and #7 have similar compositions, they thus behave quite differently in terms of deactivation (catalyst #3 activity dropped by near 20% within 5 h). This may be due to the use of different precursors (palladium (II) acetate for catalyst #3 and palladium (II) dichlorine for catalyst #7) and of different synthesis protocols.

Depending on the model (Deac1 and 2), one or two times dependency parameters can be calculated. Since the exponential decay deactivation is activity dependant, the exponential relaxation time τ can be used as a catalyst deactivation descriptor. In contrast, the linear decreasing rate ν indicates a deactivation phenomenon which is independent of the activity. As a consequence, this parameter could be used to describe the interaction of a polluting environment on a specific catalyst.

3.1.2. Deactivation and kinetic model integration

The target to develop a methodology allowing a fast access to kinetic parameters for a large number of catalysts imposes that the number of experimental conditions tested shall be limited.

Table 3
Results of deactivation kinetics

Catalyst ID	Deactivation model	Coefficient of determination (R^2)	Extrapolated activity at t_0 (mmol/h/g_{cata})	Global deactivation [$(A(t_0) - A(t_{end}))/A(t_0)$; %]	Decreasing rate ν (h^{-1}) (Deac2)	Relaxation time τ (h^{-1}) (Deac1 and 2)
#1	Deac1	0.99	2.29416	77	–	2.12
#2	Deac1	0.99	0.40329	43	–	0.57
#3	Deac1	0.99	0.0269	18	–	0.86
#4	Deac2	0.99	4.22971	80	278	0.26
#5	Deac2	0.99	0.92671	67	57	0.13
#6	Deac2	0.99	0.05593	54	1.58	0.32

In so far, kinetic parameters of the 100 catalysts were derived from 15 to 30 data points using the kinetic model presented in the section "Experimentals."

We first have investigated the ability of the model to describe catalyst performances while deactivating by using raw kinetic data, that is, not corrected from deactivation. Fig. 4 shows that the kinetic model Cin1 is able to adequately describe both deactivating (catalyst #3b) and non-deactivating (benchmark catalyst #7) systems from type Deact1. Similarly, the model predicts as well the activity for a system of type Deact2 (catalyst #6) despite a strong deactivation (about 50%) in the period where kinetic data are collected.

This means that one cannot use the standard deviation between experimental and calculated data to discriminate experiments strongly influenced by the deactivation from experiments little or not affected by deactivation.

Quantification of the impact of deactivation on kinetic parameters was studied. Kinetic parameters were calculated by applying diverse rates of deactivation on the basis of the above-described aging models (see extrapolated activity at t_0 (mmol/h/g_{cata}) in Table 2). Complete release of the methodologies and results will be published in a forthcoming publication. Nevertheless it can be pointed out here the large impact of the deactivation on the computation of kinetic parameters, the deepest effect being on adsorption entropies and enthalpies, especially widening prediction bands.

Thus, it is utmost important to take into account deactivation profiles while processing data for reaction kinetic modelling. By reprocessing the data according using appropriate deactivation models "intrinsic" kinetic parameters (ΔH, ΔS, E_a) can be calculated as catalyst descriptors.

3.2. Oxygen storage capacity measurements on ceria-doped catalysts

The results on the OSC measurements by transient parallel experimentations on various ceria-doped catalysts are shown in Fig. 5.

The reference catalyst containing 4.75 wt%Pt on high surface area ceria shows a very high OSC whatever the temperature. In contrast, the 2 wt.% Pt doped samples prepared for this study show lower OSC under the prevailing conditions, demonstrating the large impact of Pt concentration on OSC extent. As a matter of fact, it was shown elsewhere [46] that part of the Pt loading can form oxide-like clusters inside a fluorite structure, ensuring both an accelerated oxygen diffusion from bulk to surface and along the ceria surface and the storage of overstoichiometric oxygen species (including hydroxyl groups).

Among the 13 dopants, four (Pb, W, Mo and Sn) allow to increase the OSC by factors of two to three, mostly independently of the temperature within the investigated range. In contrast, vanadium doped ceria shows a continuous increase of the OSC with the temperature to attain values of 120 μmol/g.

In general, these results clearly demonstrate that solid state of ceria supports determines the level of OSC and of oxygen transfer dynamics. As a matter of fact, by doping the fluorite structure with exo-cations, various structural effects are induced, such as creating and/or stabilising oxygen vacancies [39], which affects

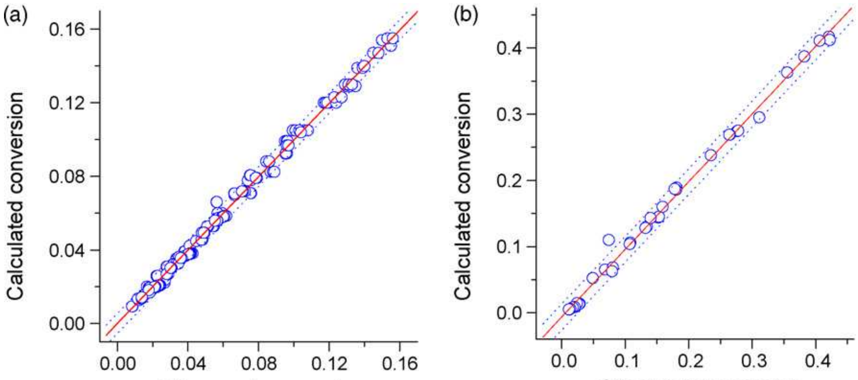

Fig. 4. Parity plots resulting from the kinetic modelling for benchmark catalyst #7 (a) and catalyst #3 (b), using non-corrected data. The dashed lines represent the 95% prediction bands.

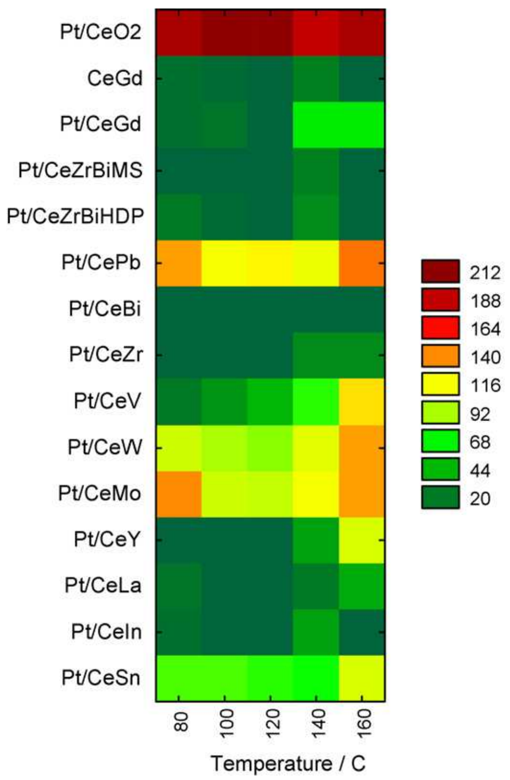

Fig. 5. Oxygen storage capacity (OSC) measurements as a function of the temperature expressed in micromol per gram of catalysts for various Pt/ceria-doped materials.

directly the intrinsic oxygen diffusion and storage capacity. In the presence of a metal, the reducible ceria provides adsorbed oxygen species that can spill over from the support to the metal particles, the reduced Ce^{3+} centres being subsequently reoxidized by gaseous oxygen (Eqs. (4) and (5)).

$$2Ce^{4+} + O^{2-} + * \rightarrow 2Ce^{3+} + O* \tag{4}$$

$$2Ce^{3+} + 1/2O_2 \rightarrow 2Ce^{4+} + O^{2-} \tag{5}$$

In the presence of hydrogen, ceria can be reduced in the bulk (Eq. (6)), creating anionic vacancies and increasing the mobility of the remaining lattice oxygen atoms. The resulting hydroxyl anions can combine to give water and O^{2-} (Eq. (7)) with the Ce^{3+} cations reoxidised by molecular oxygen to Ce^{4+} as shown above.

$$2Ce^{4+} + 2O^{2-} + H_2 \rightarrow 2Ce^{3+} + 2OH^{-} \tag{6}$$

$$2OH^{-} \rightarrow H_2O + O^{2-} \tag{7}$$

A common feature for the above mentioned doping cations favoring the OSC is that the most stable forms of the corresponding oxides are essentially amphoteric or acid except V which can be either acid or basic. By maintaining an optimized level of surface acidity, these dopants would somehow neutralize ceria basicity (hydroxyl groups) and therefore inhibit formation of stable adspecies such as formates and carbonates which would in turn inhibit oxygen mobility and spillover towards platinum particles [41]. Indeed more advanced catalyst characterization such as in situ FTIR acid–base measurements are required for supporting these assumptions, which also points out the limits of the present HT investigation.

Finally, as reported in Ref. [41], it was also observed for this catalyst library that strong relationships exist between OSC and CO preferential oxidation in a hydrogen flux (PrOx). As a general trend, it was found that the most performing CO oxidation samples exhibited the poorest OSC, indicating that excess of oxygen delivered by the system is quite detrimental for the selective oxidation of CO in the presence of hydrogen.

From an engineering point of view, the method of HT transient OSC measurements at *iso*-temperature described in the present study was proved to be efficient for assessing key features of oxygen storage and transfer dynamics in diverse materials libraries. This approach can therefore be used as an alternative guideline for optimizing primary screened formulations.

3.3. Adsorption isotherms of microporous materials

Adsorption isotherms of gas and vapours in porous materials are obtained by means of breakthrough curve measurements. The experimental procedure is very similar to the OSC measurements described above. Examples of breakthrough curves on seven different microporous materials are shown in Fig. 6. When the selected channel is fed by the gas mixture, some of the gases are preferentially adsorbed as indicated by a decrease of the partial pressure on the mass spectrometer. When the porous network is saturated, the steady-state is achieved and another breakthrough curve can be operated on the next sample. Thanks to the fluidic supply design, when one adsorbant is under testing, the other ones are desorbed under flowing sweep gas (He). As a consequence, desorption is allowed to proceed 15 times longer than adsorption. This operating mode fits well with the usual fact that desorption under sweep gas takes longer time than adsorption, especially when strongly activated adsorption takes place, which can be an issue for fast material screening.

Because of some dead volumes in the tubing and channels, a sharp decrease of the pressure is observed in the first seconds

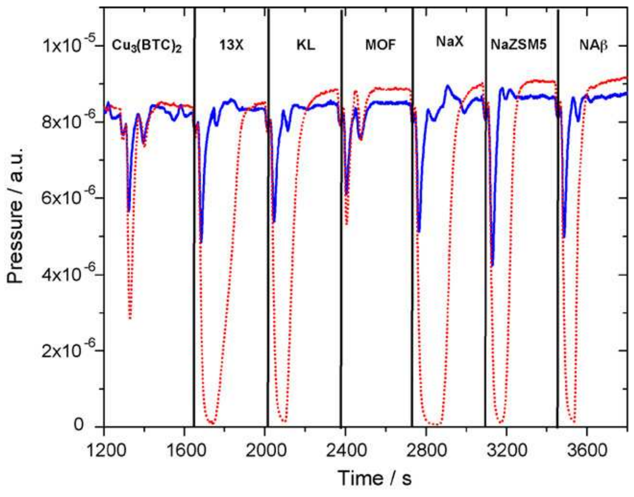

Fig. 6. N_2–CO_2 mixture breakthrough curves of seven microporous materials obtained at 100 °C and five bars total pressure: dashed lines CO_2, plain lines N_2.

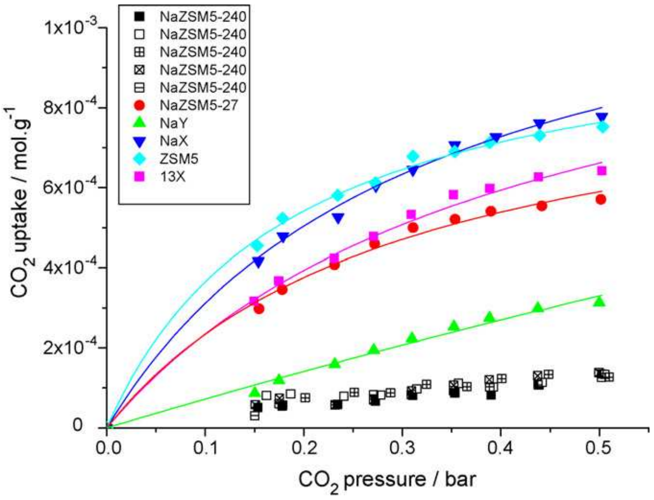

Fig. 7. CO_2 adsorption isotherms at 120 °C from a mixture $N_2/CO_2/He$ on zeolites. Five replicates of the sample NaZSM5-240 demonstrate the measurement reproducibility.

for all cases. Adsorption capacities are calculated by subtracting blank experiments performed with a non-porous SiC sample.

From breakthrough curves at different pressure, gas adsorption isotherms were established as shown in Fig. 7.

In good agreement with literature data, CO_2 is adsorbed preferentially over N_2 on zeolites with a high aluminum content such as 13X and NaX. In contrast, CO_2 adsorption is much less pronounced for NaZSM-5 with a low aluminium content and $Cu_3(BTC)_2$ metal organic frameworks due to non polar frameworks [47].

Higher CO_2 adsorption capacities are observed for HZSM5, Na-ZSM5-27 and for our reference materials NaX and 13X. The reproducibility was validated using five replicates of NaZSM5-240.

Isotherms obtained at different temperatures were modeled using Langmuir equation in order to calculate adsorption parameters. As an example, an activation energy of 20 kJ/mol was obtained for the reference 13X zeolite in good agreement with literature data.

This experimental protocol enables to measure 16 isotherms per day for pure gases or for gas mixtures. From the isotherms, working capacity and selectivity can be calculated as well according Eqs. (1) and (2) at different adsorption and desorption pressure conditions. In turn, the device authorizes a rational screening of adsorbents because it enables to evaluate different materials while defining the best process conditions for each one.

4. Conclusions and perspectives

New HT technologies offer the opportunity to increase by several orders of magnitude the number of tested samples. However, instead of screening catalysts against a single criterium such as activity or selectivity, the double approach of HT kinetic and HT characterization was privileged to obtain relevant quantitative information for further Quantitative Structure-Activity Relationship studies, thus providing new guidelines for discovery. The case studies presented here showed how to access key parameters/descriptors using HT transient methods for catalysis (hydrogenation reaction), oxygen storage capacity (redox materials) and adsorption capacity (microporous adsorbents). This double approach should facilitate the simultaneous optimization of both material and process engineering.

Acknowledgements

This work was supported by the EU FP6 Integrated Project TOPCOMBI (Project No. NMP2-CT2005-515792) and IFP-Lyon.

References

[1] A. Karlsson, et al., in: Yong Wang, Jamelyn D. Holladay (Eds.), Microreactor Technology and Process Intensification, 914, Oxford University Press, 2005, pp. 66–81.
[2] F. Schuth, et al., Top. Catal. 21 (2002) 55–66.
[3] P. Claus, D. Honicke, T. Zech, Catal. Today 67 (2001) 319–339.
[4] I. Hahndorf, et al., Chem. Eng. J. 89 (2002) 119–125.
[5] M. Lucas, P. Claus, Appl. Catal. A. 254 (2003) 35–43.
[6] U. Rodemerck, et al., Top. Catal. 13 (2000) 249–252.
[7] A. Muller, et al., Catal. Today 81 (2003) 377–391.
[8] P.J. Cong, et al., Angew. Chem. Int. Ed. 38 (1999) 508.
[9] Y.M. Liu, et al., Appl. Catal. A. 254 (2003) 59–66.
[10] M. Orschel, et al., Angew. Chem. Int. Ed. 38 (1999) 2791–2794.
[11] J. Urschey, et al., Solid State Sci. 5 (2003) 909–916.
[12] T. Zech, G. Bohner, J. Klein, Catal. Today 110 (2005) 58–67.
[13] C. Hoffmann, H.W. Schmidt, F. Schuth, J. Catal. 198 (2001) 348–354.
[14] W. Huybrechts, et al., Appl. Catal. A. 243 (2003) 1–13.
[15] C. Kiener, et al., J. Catal. 216 (2003) 110–119.
[16] P.L. Mills, J.F. Nicole, Chem. Eng. Sci. 59 (2004) 5345–5354.
[17] K.S. Oh, Y.K. Park, S.I. Woo, Rev. Sci. Instrum. 76 (2005), No. 062219.
[18] J.M. Serra, E. Guillon, A. Corma, J. Catal. 227 (2004) 459–469.
[19] N. Stoll, et al., J. Autom. Method. Manage. Chem. (2006).
[20] M.L. Bricker, et al., Scaling up of catlysts discovered from small-scale experiments, in: R.A. Potyrailo, E.J. Amis (Eds.), High-Throughput Analysis – A Tool for Combinatorial Science, Kluver Academic/Plenum Publishers, 2003, pp. 581–609.
[21] S. Bergh, High-throughput workflow development: strategies and examples in heterogeneous catalysis, in: A. Hagemeyer, P. Strasser, A. Volpe (Eds.), High-Throughput Screening in Chemical Catalysis, Wiely-VCH, Weinheim, 2004, pp. 63–86.
[22] S. Schunk, et al., Mastering the challenges of catalysts screennig in high-throughput experimentations for heterogeneously catalyzed gas-phase reactions, in: A. Hagemeyer, P. Strasser, A. Volpe (Eds.), High-Throughput Screening in Chemical Catalysis, Wiely-VCH, Weinheim, 2004, pp. 19–26.
[23] J.M. Serra, A. Corma, Two exemplified combinatorial approaches for liquid-solid and gas–solid processes in oil refining and fine chemicals, in: A. Hagemeyer, P. Strasser, A. Volpe (Eds.), High-Throughput Screening in Chemical Catalysis, Wiely-VCH, Weinheim, 2004, pp. 129–150.
[24] J.S. Paul, et al., J. Comb. Chem. 7 (2005) 407–413.
[25] J.A. Moulijn, et al., Catal. Today 81 (2003) 457–471.
[26] W.H. Weinberg, H.W. Turner, Impact of high-throughput screening technologies on chemical catalysis, in: A. Hagemeyer, P. Strasser, A. Volpe (Eds.), High-Throughput Screening in Chemical Catalysis, Wiely-VCH, Weinheim, 2004, pp. 1–15.
[27] J. Perez-Ramirez, et al., Catal. Today 60 (2000) 93–109.
[28] R.J. Hendershot, et al., Appl. Catal. A. 254 (2003) 107–120.
[29] AMTEC GmbH. www.amtec-chemnitz.de.
[30] TOPCOMBI IP. Contract No 515792-2.
[31] A. Stanislaus, B.H. Cooper, Catal. Rev. Sci. Eng. 38 (1996) 159.
[32] A.K. Neyestanaki, et al., J. Catal. 218 (2003) 267–279.
[33] V.M. Rahaman, A. Vannice, J. Catal. 127 (1991) 267–275.

[34] E. Guillon, et al., Catal. Today 65 (2001) 201–208.
[35] A.K. Neyestanaki, et al., J. Mol. Catal. A: Chem. 193 (2003) 237–250.
[36] S. Smeds, D. Murzin, T. Salmi, Appl. Catal. A. 150 (1997) 115–129.
[37] A.E.C. Palmqvist, et al., Nanostruct. Mater. 11 (1999) 995–1007.
[38] M. Mogensen, N.M. Sammes, G.A. Tompsett, Solid State Ionics 129 (2000) 63–94.
[39] G. Rothenberg, E.A. de Graaf, A. Bliek, Angew. Chem. Int. Ed. 42 (2003) 3366–3368.
[40] E.A. de Graaf, et al., Org. Process Res. Dev. 9 (2005) 397–403.
[41] D. Tibiletti, et al., J. Catal. 225 (2004) 489–497.
[42] D.M. Ruthven, S. Farooq, K.S. Knaebel, Pressure Swing Adsorption, VCH, New York, 1994, pp. 208–244.
[43] M. Ackley, S. Rege, H. Saxena, Micropor. Mesopor. Mater. 61 (2003) 25–42.
[44] J. Delgado, et al., Adsorption 12 (2006) 5–18.
[45] O. Levenspiel, Chemical Reaction Engineering, 2nd ed., 1972, 640 pp.
[46] V.A. Sadykov, et al., Solid State Phenom. 128 (2007) 239–248.
[47] Q.M. Wang, et al., Micropor. Mesopor. Mater. 55 (2002) 217–230.

MOFs as acid catalysts with shape selectivity properties

Ugo Ravon, Marcelo E. Domine, Cyril Gaudillère, Arnold Desmartin-Chomel and David Farrusseng*

Received (in Montpellier, France) 6th March 2008, Accepted 10th April 2008
First published as an Advance Article on the web 7th May 2008
DOI: 10.1039/b803953b

MOFs permit the paraalkylation of large polyaromatic compounds with nearly 100% of regioselectivity, offering new alternatives to standard zeolite catalysts.

Metal–organic frameworks (MOFs) are a class of crystalline hybrid material whose crystal structures are made up of extended 3D networks of metal ions or small discrete clusters connected through multidentate organic spacers.[1] The development of these porous coordination polymers has already opened up new perspectives in applications such as gas separation and storage.[2] The ability to tune pore size on an Angstrom scale while allowing the design of accessible metallic nanoclusters in a highly porous structure makes these compounds very attractive for catalysis.[3] The catalytic properties of HKUST-1, which uses Cu paddle wheel clusters as Lewis centres, is an outstanding proof of the concept.[4] However, we consider that published catalytic results are not in line with the generally acknowledged potential of MOFs. Indeed, only a limited number of successful catalytic studies have been reported.[5] Furthermore, the chosen catalytic reactions were usually model reactions of little industrial interest and/or reactions that did not need sophisticated catalysts in order to take place.

In contrast, the catalytic alkylation of aromatics is undertaken on a large scale in the chemical industry.[6] Among *para*-dialkylated aromatics, *para*-xylene, *para*-diisopropylbenzene, *para*-ethyltoluene, *para*-diethylbenzene, *para*- and *meta*-cymenes, and 4-*tert*-butyltoluene are very important in the fine chemical and petrochemical industries. Medium and large pore acidic zeolites are outstanding catalysts, since they combine high activity (acidic sites) and shape selectivity thanks to their micropore structures, which favour *para*-alkylation (less bulky products). Recently, the benzylation of toluene using the coordination polymer MIL-100(Fe) was reported.[7] However, shape selectivity properties were not investigated.

For the first time, we report herein MOFs that undertake an outstanding shape-selective alkylation of aromatics that outperform reference zeolites. The MOF catalysts are derived from well known IRMOF materials.[1c,3b] The cubic framework of IRMOF-1 consists of Zn_4O subunits that are linked in octahedral arrays of 1,4-benzenedicarboxylic acidic (BDC) groups to form a porous material with a channel window of about 8 Å. The topological simplicity of IRMOF-1 has lead to the preparation of a series of MOFs based on aromatic dicarboxylic acids coordinated to Zn_4O subunits. These structures, referred to as iso-reticular metal–organic frameworks (IRMOFs), have demonstrate that control over the pore size and functionality can be achieved. For instance, IRMOF-8 and IRMOF-10 are isoreticular compounds, with 2,6-naphthalenedicarboxylic acid (2,6-NDC) and 4,4′-biphenyldicarboxylic acid (4,4′-BPDC) as linkers, respectively.

The catalyst IRMOF-1 was prepared according to the method developed by Huang *et al.*, which consists of adding pure triethylamine to a solution of zinc nitrate and BDC in DMF.[8] This method was extended to the synthesis IRMOF-8 by using 2,6-NDC as the ligand.

Structural (X-ray diffraction, IR) and thermal (TDA, TGA) characterisation data for IRMOF-1 are in very good agreement with the results reported by Huang *et al.*[8] and Havizovic *et al.*[9] (Fig. 1 and Fig. 2). The sharp band at 3602 cm^{-1} can be assigned to Zn–OH species.[10] We also measured a 10% excess of Zn with respect to the theoretical formulae (elemental analysis and TGA), which leads to a global composition of $Zn_4O(BDC)\cdot 2H_2O + Zn(OH)_2$. According to Havizovic *et al.*,[9] zinc hydroxide nanoclusters that partly occupy the cavities are responsible for the structure distortion evidenced by the splitting of the diffraction peak at 9.7° (see inset to Fig. 1). On the other hand, the ^{1}H NMR spectra of different IRMOF-1 samples indicated the presence of Zn–OH–Zn species (very small peak at $\delta = -0.4$), like those encountered in $Zn_3(OH)_2(BDC)_2\cdot 2DEF$ (MOF-69c),[11,12] which contains

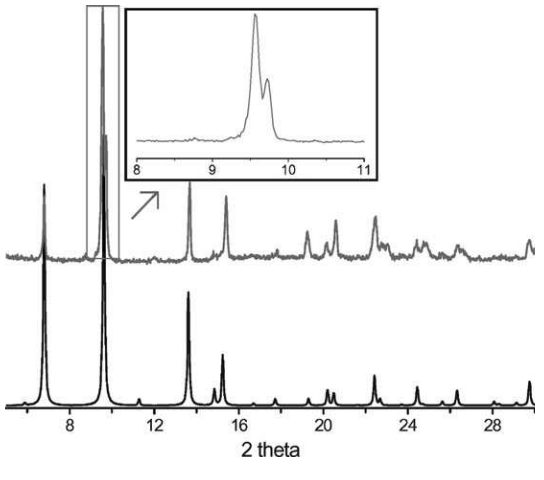

Fig. 1 Powder X-ray diffraction pattern of IRMOF-1: Top: Experimental result with zoom-in inset for the angles 8–11 (2θ). Bottom: Simulated pattern from MOF5-Zn.[9]

IRCELYON, UMR UCBL-CNRS 5256, 2, Avenue Albert Einstein, 69626 Villeurbanne, France. E-mail: david.farrusseng@ircelyon.univ-lyon1.fr; Fax: +33 (0) 4 72445365

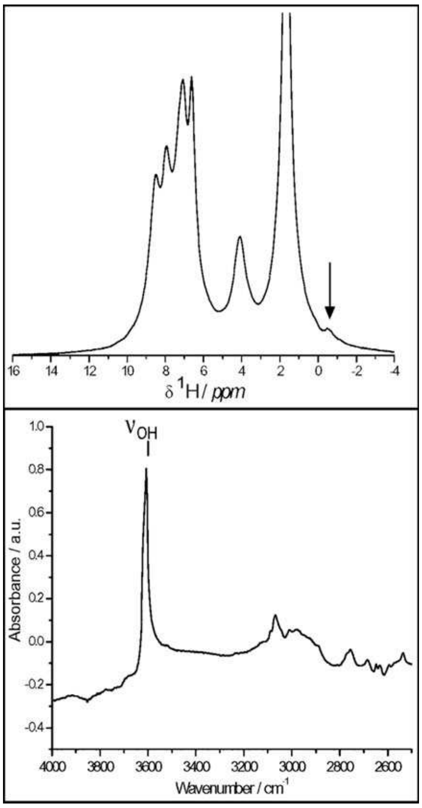

Fig. 2 IRMOF-1 short range characterization: Top: ^{1}H NMR. Bottom: *In situ* DRIFT after desorption at 220 °C.

Zn–(μ_3-OH)–Zn chains. Peak integration gave a ratio of one μ_3-OH for every 25 BDC linkers. The later phase can be formed during the synthesis of IRMOF-1, and is kinetically favoured in moisture conditions, as was the case in this study.[13] Therefore, in addition to zinc hydroxide clusters, IRMOF-1 samples also contain Zn–(μ_3-OH)–Zn chains in minor quantities, which could either be a crystalline default of the cubic structure or non-XRD detectable MOF-69c microcrystallites. Finally, it was recently demonstrated that pure IRMOF-1 undergoes a rapid phase transformation under moist conditions that is accompanied by a drastic decrease in accessible porous volume.[14]

From N_2 physisorption analysis at 77 K, the IRMOFs were determined to be microporous, and the isotherms were of type I. Their surface areas, micropore volumes and pore sizes correspond to those reported elsewhere that had similar preparation procedures to those used for IRMOF-1[8,9] and IRMOF-8 (Table 1).[15] A logarithmic plot (not shown) reveals that for IRMOF-8, N_2 adsorption occurs in two steps, revealing two distinct pore sizes. The actual calculation of the pore size using the Horvath–Kawazoe or Density Functional Theory (DFT) method is questionable, since the principal interaction potentials of the adsorbate and the adsorbent are unknown, and assumptions have to be made about pore morphology. The calculated pore diameters from the DFT method (Table 2) are therefore not fully accurate but, more importantly, allow comparison among members of a class of similar materials, which presumably have the same interaction potentials.

Table 1 N_2 physisorption results and comparison with literature data

Sample	Surface area/m^2 g^{-1a}	Pore volume/ cm^3 g^{-1}	Micropore volume/ cm^3 g^{-1b}	Pore diameter/Å^c
IRMOF-1	450	0.32	0.18	8.8
IRMOF-8	730	0.46	0.29	7.3/11.6
H-BEA	430	0.62	0.10	7.7

[a] From BET analysis.[16] [b] From t-plot analysis. [c] From DFT analysis.

In order to complete the picture of the IRMOF samples with regard to their porosity properties, the calculated sizes of their cages and channel windows from the structural data of pure crystals are reported in Table 2. For example, the window between the cages of IRMOF-1 have a van der Waals space that can accommodate a sphere of approximately 7.8 Å diameter, herein referred to as the "free-space" diameter. In contrast to zeolite pore sizes, these values shall be interpreted with care for MOF materials, especially when correlating structural features and properties. Indeed, in addition to their general flexibility, the aromatic rings of IRMOF can rotate, thus making feasible the diffusion of larger guests.[1b,7,17]

Because of size matching between alkylbiphenyl compounds and large pore zeolites, the alkylation of biphenyl is an appropriate reaction to highlight the pore shape selectivity properties in acidic catalysis.[19] The activity and selectivity of the MOF samples were tested in the alkylation of toluene and biphenyl with *tert*-butylchloride in a batch reactor. The acidic form of beta zeolite (denoted hereafter H-BEA), $AlCl_3$ and $ZnCl_2$ were used as reference catalysts. As a result, IRMOF samples were as active as H-BEA and $AlCl_3$, and reactions were complete within 2 h at 170 °C (Table 3). For toluene alkylation, IRMOF samples exhibited a high selectivity for the less bulky *para*-oriented products, whereas $AlCl_3$ produced mixtures of *ortho* and *para* compounds. On the other hand, the alkylation of biphenyl revealed an exceptional selectivity for *para*-oriented 4-*tert*-butylbiphenyl with IRMOF samples. Indeed, only traces of dialkylated products (about 1%) were detected when using the IRMOFs. In contrast, H-BEA and $AlCl_3$ showed much higher selectivities for the *ortho*-oriented product, and about 15% for the dialkylated products. In conclusion, these results reveal the outstanding pore shape selectivity properties of IRMOFs for large polyaromatics.

Measurements of conversion at different reaction times indicate that there are similar kinetics for IRMOF-1, IRMOF-8 and H-BEA at 100 °C (Fig. 3). In contrast to MIL-101(Cr), IRMOFs are active in the first minutes of

Table 2 Theoretical cage and window sizes from structural data

	Cage free-space diameter/Å	Window free-space diameter/Å
IRMOF-1^a	15.1	7.8
IRMOF-8^a	18.0	9.2
H-BEA^b	6.6	6.1

[a] Free-space diameter refers to the diameter of the largest sphere that can fit into the cage or through the window when the van der Waals radii from ref. 3*b* are assumed for all the framework atoms. [b] From ref. 18.

Table 3 Selectivity of *tert*-butylation reaction at 170 °C[a]

	Toluene			Biphenyl		
Catalyst	*para*[b]	*ortho*	di[d]	*para*[c]	*ortho*	di[d]
IRMOF-1	82	18	0	**96**	3	1
IRMOF-8	84	16	0	**95**	3	2
H-BEA	72	28	0	55	22	23
$AlCl_3$	46	54	0	51	38	11

[a] Conversions ranged from 60 to 80%. [b] *para-tert*-Butyltoluene. [c] 4-*tert*-Butylbiphenyl. [d] Sum of dialkylated products.

operation. These findings suggest that strong structural modifications are not required to create catalytic centers such as Zn–Cl[7]. Furthermore, the poor activity of $ZnCl_2$ tested as a powder at 170 °C (only 8% conversion) confirms that $ZnCl_2$ is not the catalytic specy.

After filtration, the catalysts could be re-used without any loss of activity or selectivity. XRD patterns of used IRMOF-1 did not show major modifications, whereas H^1 NMR revealed two significant changes (not shown). Firstly, integration of the broad peak at $\delta = 14$ revealed that about 20% of the carboxylate groups had been hydrolyzed to their acid form. Secondly, a very intense peak at $\delta = 3.4$ indicated the presence of a guest in the structure, which could be assigned as HCl. Indeed, very similar H^1 NMR spectra were obtained when concentrated HCl (36%) was added to fresh IRMOF-1. We suggest that the HCl, which is produced during the course of the reaction, is trapped in the framework, most likely at the oxygen containing nodes, provoking the partial hydrolysis of the host.

In order to check that the reaction takes place under heterogeneous conditions, issues of leaching were investigated. Firstly, tests in absence of solid catalysts were carried out under the same conditions, and any conversion was measured. Secondly, reaction mixtures were filtered-off after completion of the catalytic reactions, both solid catalyst and reaction solution being recovered separately. When a new reaction was started by adding fresh reactants to the recovered solution, any additional conversion was detected. This is consistent with the fact that HCl is trapped in the framework, making the filtrate HCl-free. Finally, we have observed that the reaction takes place at 50 °C with IRMOF-1. Under these conditions of pressure and temperature, the IRMOF samples were not soluble in decane, indicating that the reactions did not proceed in a homogeneous phase.

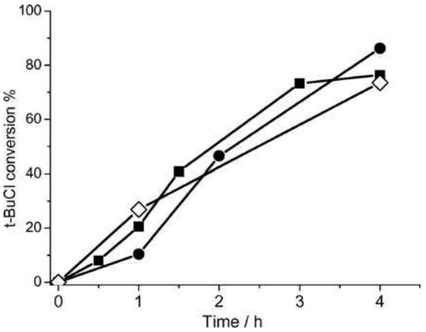

Fig. 3 Kinetic studies of toluene alkylation at 100 °C using IRMOF-1 (●), IRMOF-8 (■) and H-BEA (◇).

The exact catalytic centre is still unknown. As described earlier, acidic centres may arise either from zinc hydroxide clusters, from the presence of MOF-69c, or from structural Zn–OH defects formed at the synthesis step or upon water adsorption. Further experiments are ongoing in order to identify and assess these acidic sites.

From the experimental and theoretical data, there is, in principle, no steric hindrance to monoalkylated products diffusing out of the porous solids, including H-BEA. Even very bulky products, such as the dialkylated product 4,4′-di-*tert*-butylbiphenylene (12.5 × 5.0 Å), can be formed in large amounts in H-BEA.[19] Therefore, the shape selectivity properties observed for the IRMOF samples cannot arise from diffusion hindrance of the most bulky products, since the pore windows are even larger. For the reaction to take place, we suggest that the biphenyl is absorbed in a specific manner, allowing the formation of a transition state for the *para*-oriented product. Once alkylated, it can not be activated in the same manner because of steric hindrance, and double alkylation cannot proceed. Because of the porous structure similarities of IRMOF-1 and IRMOF-8, it is not surprising that similar selectivities are obtained.

In conclusion, we have demonstrated for the first time that MOFs can be used to undertake very shape-selective (almost 100%) catalytic alkylations of large molecules. This discovery may open new perspectives for the C–C coupling of polyaromatics or biomolecules that are too large to be addressed by zeolites.[20]

Saturation of the metal ion coordination sphere in coordination polymers is often argued to be a limitation of MOFs for catalytic applications.[21] We believe that the engineering of structural defects in MOF materials may lead to the generation of a new class of catalysts with different acidities and hydrophobic properties than are encountered in zeolites.

Original MOFs exhibiting M–OH functions and 100% regioselectivity have been recently discovered in our laboratory, and our findings will be published shortly. The investigation of other alkylating agents is also in progress.

We thank Dr C. Mirodatos for his support and IRCELYON Scientific Services.

Experimental

Synthesis

All chemicals were used as received: DMF (Aldrich, 99.8%), $Zn(NO_3)_2\cdot 6H_2O$ (Riedel-deHaën, pure), triethylamine (Riedel-deHaën, pure), BDC (Sigma Aldrich, 98%), 2,6-NDC (Alfa Aesar, 98%), $AlCl_3$ (Sigma-Aldrich, 99.99%) and anhydrous $ZnCl_2$ (Alfa Aesar). IRMOF-1 was prepared according to a procedure published by Huang *et al.*[8] A pure solution of 4.4 ml triethylamine (31.6 mmol) was added with stirring to a mixture of 660 mg (4.0 mmol) BDC and 2.4 mg (8.1 mmol) of $Zn(NO_3)\cdot 6H_2O$ dissolved in DMF. The white precipitate was recovered by filtration, washed with DMF and heated at 130 °C in air. H-BEA samples were obtained from Na-form (ENI Technology, Si/Al = 23 : 1) by ammonium exchange

(10 wt% NH_4COOCH_3 dissolved in water) at 80 °C for 4–5 h, followed by calcination at 550 °C for 3 h. This procedure was repeated twice.

Characterization

Samples were analyzed by X-ray diffraction (Bruker D5005), DRIFT (Magna 550 Nicolet, SpectraTech cell, ZnSe windows, MCT detector), N_2 absorption measurements (Micrometrics ASAP 2010 M) and chemical analysis (Spectroflame ICP-OES). IRMOF samples were further characterized by TG/TD analysis (Setaram-type SETSYS Evolution 12). For ^{1}H NMR (DX 400BRUCKER) MAS technique: 30 kHz spinning rate, pulse duration 3 μs and repetition time 16 s. Peaks: δ −0.4 (Zn–(μ_3-OH)–Zn), δ 1–3 (DMF), δ 4–5.5 (H_2O) and δ 6–10 (C_6H_6).

Catalytic alkylation

Toluene (Chimie-Plus, 99%), biphenyl (Alfa Aesar, 99%), decane (Alfa Aesar, 99%), *tert*-butylchloride (Alfa Aesar 98 + %) and mesitylene (Aldrich, 98%) were used as received. The reactants were dissolved in decane. The reaction was carried out with an aryl : *tert*-butylchloride ratio of 2 : 1. Typically, a mixture of 2 ml (18.8 mmol) of toluene, 1 ml of *tert*-butylchloride (9.2 mmol) and 7 ml of decane were placed in a 48 ml Teflon-lined autoclave (Top Industrie). 30 mg of catalysts were desorbed at 130 °C and 10^{-5} bar. After 2 h of stirring at 170 °C, the solid was recovered by room temperature filtration, and the filtrate was analysed by gas chromatography (HP 6890N equipped with a 30 m HP5 column), using 5% mesitylene as the internal standard.

Catalyst re-use and leaching tests

After the completion of reactions, the solid catalysts were first filtered off. The filtrate and recovered solid were then treated separately so as to investigate leaching issues and undertake reuse, respectively. Fresh reactants in the same ratio as those used in the previous tests were then added to the filtrate. The solution mixture (in absence of solid) was then heated to 170 °C for 2 h. Any conversion was then measured. On the other hand, the recovered solid was washed with water, ethanol and acetone prior to post-reaction characterization and reuse.

References

1 (*a*) J. L. C. Rowsell and O. M. Yaghi, *Microporous Mesoporous Mater.*, 2004, **73**, 3–14; (*b*) M. J. Rosseinsky, *Microporous Mesoporous Mater.*, 2004, **73**, 15–30; (*c*) O. M. Yaghi, M. O'Keeffe, N. W. Ockwig, H. K. Chae, M. Eddaoudi and J. Kim, *Nature*, 2003, **423**, 705–714; (*d*) A. K. Cheetham, G. Ferey and T. Loiseau, *Angew. Chem., Int. Ed.*, 1999, **38**, 3268–3292; (*e*) O. M. Yaghi, H. L. Li, C. Davis, D. Richardson and T. L. Groy, *Acc. Chem. Res.*, 1998, **31**, 474–484; (*f*) M. Higuchi, S. Horike and S. Kitagawa, *Supramol. Chem.*, 2007, **19**, 75–78.

2 (*a*) C. Sanchez, B. Julian, P. Belleville and M. Popall, *J. Mater. Chem.*, 2005, **15**, 3559–3592; (*b*) S. Kitagawa, R. Kitaura and S. Noro, *Angew. Chem., Int. Ed.*, 2004, **43**, 2334–2375; (*c*) C. Janiak, *Dalton Trans.*, 2003, 2781–2804; (*d*) D. Maspoch, D. Ruiz-Molina and J. Veciana, *Chem. Soc. Rev.*, 2007, **36**, 770–818; (*e*) C. Serre, C. Mellot-Draznieks, S. Surble, N. Audebrand, Y. Filinchuk and G. Ferey, *Science*, 2007, **315**, 1828–1831.

3 (*a*) G. Ferey, C. Mellot-Draznieks, C. Serre, F. Millange, J. Dutour, S. Surble and I. Margiolaki, *Science*, 2005, **309**, 2040–2042; (*b*) M. Eddaoudi, J. Kim, N. Rosi, D. Vodak, J. Wachter, M. O'Keefe and O. M. Yaghi, *Science*, 2002, **295**, 469–472.

4 (*a*) K. Schlichte, T. Kratzke and S. Kaskel, *Microporous Mesoporous Mater.*, 2004, **73**, 81–88; (*b*) L. Alaerts, E. Seguin, H. Poelman, F. Thibault-Starzyk, P. A. Jacobs and D. E. De Vos, *Chem.–Eur. J.*, 2006, **12**, 7353–7363.

5 For recent reviews on catalytic MOFs, see: (*a*) G. Ferey, *Chem. Soc. Rev.*, 2008, **37**, 191–214; (*b*) U. Mueller, M. Schubert, F. Teich, H. Puetter, K. Schierle-Arndt and J. Pastre, *J. Mater. Chem.*, 2006, **16**, 626–636.

6 C. Perego, S. Amarilli, A. Carati, C. Flego, G. Pazzuconi, C. Rizzo and G. Bellussi, *Microporous Mesoporous Mater.*, 1999, **27**, 345–354.

7 P. Horcajada, S. Surble, C. Serre, D. Y. Hong, Y. K. Seo, J. S. Chang, J. M. Greneche, I. Margiolaki and G. Ferey, *Chem. Commun.*, 2007, 2820–2822.

8 L. M. Huang, H. T. Wang, J. X. Chen, Z. B. Wang, J. Y. Sun, D. Y. Zhao and Y. S. Yan, *Microporous Mesoporous Mater.*, 2003, **58**, 105–114.

9 J. Hafizovic, M. Bjorgen, U. Olsbye, P. D. C. Dietzel, S. Bordiga, C. Prestipino, C. Lamberti and K. P. Lillerud, *J. Am. Chem. Soc.*, 2007, **129**, 3612–3620.

10 J. H. Liao, T. J. Lee and C. T. Su, *Inorg. Chem. Commun.*, 2006, **9**, 201–204.

11 N. L. Rosi, M. Eddaoudi, J. Kim, M. O'Keeffe and O. M. Yaghi, *Angew. Chem., Int. Ed.*, 2001, **41**, 284–287.

12 T. Loiseau, H. Muguerra, G. Ferey, M. Haouas and F. Taulelle, *J. Solid State Chem.*, 2005, **178**, 621–628.

13 S. Hausdorf, F. Baitalow, J. Seidel and F. Mertens, *J. Phys. Chem. A*, 2007, **111**, 4259–4266.

14 M. Sabo, A. Henschel, H. Froede, E. Klemm and S. Kaskel, *J. Mater. Chem.*, 2007, **17**, 3827–3832.

15 Y. W. Li and R. T. Yang, *J. Am. Chem. Soc.*, 2006, **128**, 726–727.

16 K. S. Walton and R. Q. Snurr, *J. Am. Chem. Soc.*, 2007, **129**, 8552–8556.

17 A. J. Fletcher, K. M. Thomas and M. J. Rosseinsky, *J. Solid State Chem.*, 2005, **178**, 2491–2510.

18 M. D. Foster, I. Rivin, M. M. J. Treacy and O. D. Friedrichs, *Microporous Mesoporous Mater.*, 2006, **90**, 32–38.

19 (*a*) D. Mravec, P. Zavadan, A. Kaszonyi, J. Joffre and P. Moreau, *Appl. Catal., A*, 2004, **257**, 49–55; (*b*) R. Millini, F. Frigerio, G. Bellussi, G. Pazzuconi, C. Perego, P. Pollesel and U. Romano, *J. Catal.*, 2003, **217**, 298–309; (*c*) J. Horniakova, D. Mravec, J. Joffre and P. Moreau, *J. Mol. Catal. A: Chem.*, 2002, **185**, 249–257; (*d*) Y. Sugi, S. Tawada, T. Sugimura, Y. Kubota, T. Hanaoka, T. Matsuzaki, K. Nakajima and K. Kunimori, *Appl. Catal., A*, 1999, **189**, 251–261.

20 (*a*) E. Armengol, M. L. Cano, A. Corma, H. Garcia and M. T. Navarro, *J. Chem. Soc., Chem. Commun.*, 1995, 519–520; (*b*) S. B. Pu, J. B. Kim, M. Seno and T. Inui, *Microporous Mater.*, 1997, **10**, 25–33.

21 F. X. Llabrés i Xamena, A. Corma and H. Garcia, *J. Phys. Chem. C*, 2007, **111**, 80–85.

This journal is © The Royal Society of Chemistry and the Centre National de la Recherche Scientifique 2008

Microporous and Mesoporous Materials 129 (2010) 319–329

Contents lists available at ScienceDirect

Microporous and Mesoporous Materials

journal homepage: www.elsevier.com/locate/micromeso

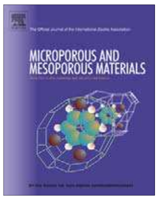

Engineering of coordination polymers for shape selective alkylation of large aromatics and the role of defects

Ugo Ravon [a], Marie Savonnet [a], Sonia Aguado [a], Marcelo E. Domine [a], Erwann Janneau [b], David Farrusseng [a,*]

[a] Université Lyon 1, CNRS, UMR 5256, IRCELYON, Institut de recherches sur la catalyse et l'environnement de Lyon, 2 Avenue Albert Einstein, F-69626 Villeurbanne, France
[b] Université Lyon 1, Laboratoire Multimatériaux et Interfaces, F-69622 Villeurbanne, France

ARTICLE INFO

Article history:
Received 13 April 2009
Accepted 3 June 2009
Available online 13 June 2009

Keywords:
Metal-organic frameworks
MOF-5
IRMOF
MIL-53
MOF-69
Shape selective catalysis

ABSTRACT

For economic and environmental reasons, there is a strong incentive to replace of homogeneous by green and efficient heterogeneous processes in catalysis. The Friedel-Crafts alkylation of aromatics is a marking example. Numbers of homogeneous catalysts (such as HF, H_2SO_3, and $AlCl_3$) have been replaced by H-form zeolites. However, large pore zeolite can not accommodate bulk aromatic molecules and/or alkylating agents avoiding the reaction to take place within the porous network. Due to their larger pore size, metal-organic frameworks (MOFs) open the doors to the alkylation of very large poly-aromatic compounds. We report different approaches for the design of acid shape selective MOFs. The first refers to a "zeolite mimetic" approach. It deals with the design of porous Zn or Al based MOF exhibiting bridging –OH species (MOF-69, MIL-53 Al) like those found in zeolites [Si–O(H)–Al]. The second approach aims at synthesizing MOF materials having structural defects to generate active catalytic centers. Two different synthetic strategies were investigated, either by fast precipitation or by the partial substitution of dicarboxylic by mono-carboxylic acid linkers. Acid centers have been characterized by solid ^1H NMR and Diffuse Reflectance IR. The mono-alkylation of biphenyl with *tert*-BuCl is achieved with 100% of para-selectivity, well superior to H-MOR and H-BEA reference zeolites.

© 2009 Elsevier Inc. All rights reserved.

1. Introduction

MOF materials can be regarded as a "new" class of catalytic materials at the frontier between active 3D inorganic frameworks like zeolites and surface organo-metallic compounds taking into account their porous structure and their accessible metallic nanoclusters, respectively. The possible organization and functionalization of active sites on the nanoscale provides the basis to develop materials specifically adapted to catalytic challenges like complex chemo-, regio- or stereo-selectivity. Although the later properties are still rarely reported for MOFs, the rapidly increasing studies on these materials with different design clearly demonstrate the versatility of metal-organic frameworks for catalysis [1,2]. MOF materials exhibiting paddle–wheel type nodes [3] have shown Lewis type catalytic activities such as cyanosilylation [4], terpene isomerization [5], alkene hydrogenation [6,7] and alcohol aerobic oxidation [8,9]. In addition, the organic moiety can be functionalized by reactive centers such as chiral basic groups [10] or metallo complexes [11].

For economic and environmental reasons, there is a strong incentive to replace of homogeneous by green and efficient heterogeneous processes in Catalysis. The alkylation of aromatics also known as Friedel-Crafts reaction is a marking example. Olefins, different types of alcohols, and also alkyl- and aryl-chlorides are applied as alkylating agents on a wide range of large scale processes in industry [12]. Numbers of strong mineral acids (such as HF, H_2SO_3, among others) and also Lewis acids (such as $AlCl_3$, $FeCl_3$, $ZnCl_2$, among others), commonly used as homogeneous catalysts for this reactions, have continuously been replaced by H-form zeolites [13]. Thus, the shape selective β-methylation of naphthalene with methanol over mordenite (0.64×0.70 nm) to produce mainly 2,6-dimethylnaphthalene is one of the major examples in acid catalysis [14]. The high selectivity to the β-mono-methylation and/or β-di-methylation is mainly due to the larger size of the 1- and 3-oriented products which strongly limits their diffusion through the porous systems of medium pore size zeolites. However, large pore zeolite can not accommodate bulky aromatic molecules and/or alkylating agents making the reaction impossible to take place within the porous network. Due to their larger pore size, metal-organic frameworks (MOFs) open the doors to the alkylation of very large poly-aromatic compounds. Recently, Horcajada et al. [15] have reported the catalytic activity of two different MIL-101 (Fe, Cr) for Friedel–Crafts benzylation. We have very recently shown in a short account that microporous zinc carboxylate frameworks show outstanding shape selectivity properties on similar alkylation type reactions [16].

---

[*] Corresponding author. Tel.: +33 4 72 44 53 65; fax: +33 4 72 44 53 9.
E-mail address: david.farrusseng@ircelyon.univ-lyon1.fr (D. Farrusseng).

1387-1811/$ - see front matter © 2009 Elsevier Inc. All rights reserved.
doi:10.1016/j.micromeso.2009.06.008

The first objective of this work is to explore different strategies to develop MOF materials exhibiting M–OH Brønsted sites for catalytic alkylation. Two main routes are investigated. The first route deals with the selection of MOF materials for which –OH groups are part of the structure as those found in H-form of zeolites. This solution can therefore be regarded as a design by zeolite mimetic approach (Fig. 1). The two compounds MIL-53(Al) [17] and MOF-69C [18] discovered by Ferey and co-workers, have been selected for testing. Both of them have well structurally identified hydroxyl groups as indicated in their formulae Al(OH)(bdc) and $Zn_3(OH)_2$(bdc), respectively. The compound MIL-53(Al) is built from infinite chains of corner-sharing $AlO_4(\mu_2\text{-}OH)_2$ while MOF-69C consists of chains of $ZnO_2(OH)_2$ tetrahedron and $ZnO_4(OH)_2$ octahedron and with μ_3-OH as bridging species. The second route aims at creating defaults in a MOF network leading to nodes that are coordinated to –OH terminal groups, instead to a linker as they should be in a perfect structure. Here also, two strategies have been investigated (Fig. 2). We have anticipated that a synthesis by very fast precipitation may lead to crystalline compounds for which a fraction of linkers are missing in the network while still maintaining a robust structure. The second strategy consists in synthesizing MOF materials from a mixture of poly-dentate and mono-dentate linkers which shall yield “defects” at the nodes which are adjacent to the mono-dentate linkers. Because, MOF-5 or IRMOF family materials do not contain –OH groups with respect to the pure crystalline structure, we have selected MOF-5 as parent material to create –OH species as structural defects.

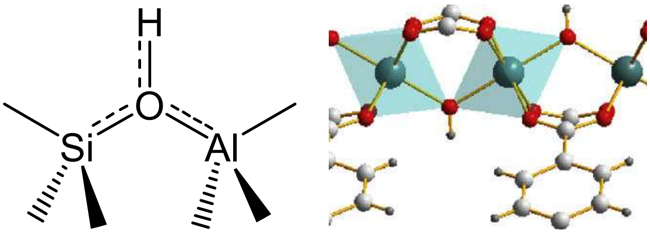

Fig. 1. MOF selection by zeolite mimetic approach. Scheme of Brønsted centers in zeolites showing μ_2 – bridging hydroxyl (left); Inorganic chain of MIL-53 showing μ_2 hydroxyl groups as potential acid centers (right).

A second objective is to address the properties of MOF for catalytic shape selectivity. Many metal-organic frameworks exhibit pore size and pore windows which exceed large pore zeolites such as beta (BEA) and mordenite (MOR). It is reasonable to envision that analogous shape selectivity effects can be also observed for MOF materials provided that the dimension of the micropores match well enough to discriminate between molecular sizes of different reagents, products or transition states involved in a particular process [19]. In this work, we have studied the alkylation of toluene and *tert*-butylbenzene, as well as larger aromatics such as naphthalene and biphenylene in order to better highlight pore-shape selectivity (Fig. 3). For the same reason, we reasoned that the *tert*-butyl group being much bulkier than the isopropyl usually studied, may be more suitable to observe larger degrees of shape selectivity. In this frame, the selection of IRMOF [20] and MOF-69 [21] materials were good candidates to investigate since their pore size can be tuned by selecting dicarboxylate ligands of different length.

2. Experimental

2.1. Synthesis

2.1.1. Solvothermal synthesis (MOF-5 solvo)

The synthesis of MOF-5 solvo was performed as reported by Sabo et al. [22]. Typically, 8.32 g (31.824 mmol) of $Zn(NO_3)_2{\cdot}4H_2O$ and 1.76 g (10.594 mmol) of 1,4-benzenedicarboxylic acid (H_2dbc) (Aldrich 99.7%), were dissolved in 100 ml of dried diethylformamide (DEF). The solution was heated at 100 °C in a Teflon-lined stainless-steel autoclave, the solid filtered off, washed and finally exchanged with $CHCl_3$ in argon flow. Finally, the material was evacuated and handled in a glove box for transferring in Schlenk type vessel.

2.1.2. Slow precipitation synthesis (MOF-5 basf)

The preparation of MOF-5 basf followed the procedure reported by Mueller et al. [23]. Typically, 3.22 g (10.8 mmol) of $Zn(NO_3)_2{\cdot}6H_2O$ (Riedel–Dehaën, pure) and 0.66 g (3.97 mmol) of H_2dbc were dissolved in 100 ml of DMF (Aldrich, 99.8% anhydrous and used as received). After 4 h of stirring at 130 °C, the solid was

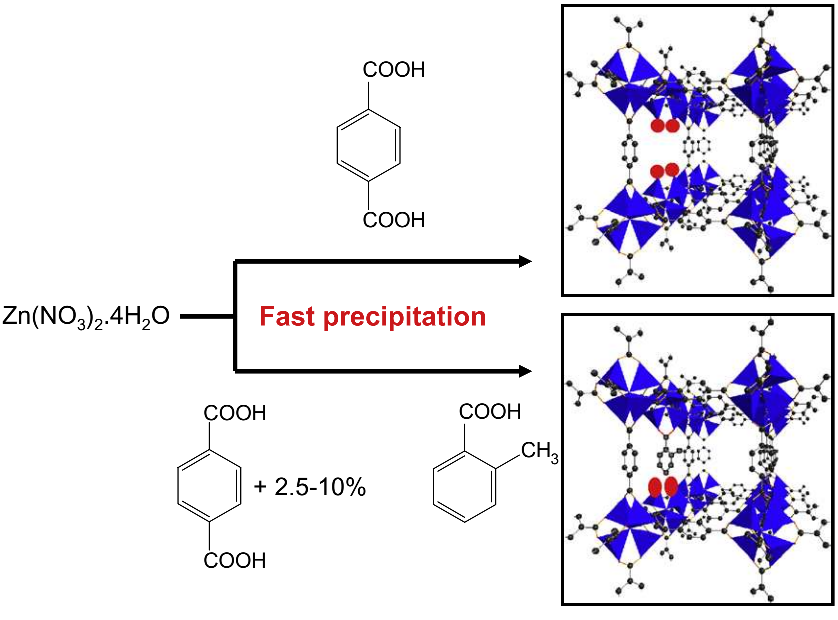

Fig. 2. Scheme of the two synthesis routes to generate structural defects; missing ligand (top), isomorphous substitution by a mono-carboxylic acid (bottom).

filtered off, washed three times with DMF and dried at 130 °C under vacuum during 3 h. It shall be pointed out that chemicals used here have different grade from the chemical used by the original authors. As a matter of fact, we do not claim that this sample, denoted hereafter MOF-5 basf, has the same properties than those reported in the original publication.

2.1.3. Fast precipitation synthesis (MOF-5 pre)

The precipitation method followed the recipe described by Huang et al. [24]. The precursors H_2(dbc) 0.66 g (3.97 mmol) and $Zn(NO_3)_2{\cdot}6H_2O$ 2.4 g (8.1 mmol) were solubilized in 80 ml of DMF (Aldrich, 99.8% anhydrous, used as received). The precipitation took place instantaneously at room temperature upon drop wise addition of 3 ml (31.6 mmol) of pure Et_3N (Riedel–Dehaën, pure). After 90 min of stirring, the white powder was filtered and washed three times with DMF. The samples were heated at 130 °C overnight under dry air flow. This procedure was extended to synthesize the isoreticular compounds IRMOF-3, Zn-MOF-8 and Zn-MOF-10 by using 2-aminoterephthalic acid, naphthalene 2,6-dicarboxylic acid and the biphenyl-4,4′-dicarboxylic acid, respectively [20].

A similar experimental procedure was applied to prepare a series of samples with an isomorphous substitution of di- by mono-carboxylate linkers. The precipitation takes place in a mixture of mono- and dicarboxylic acid, namely 2-methyl-toluic acid and H_2dbc (Fig. 2). Three samples were prepared by varying the di- to mono-carboxylic acid ratio from 2.5, 5 to 10 wt% in order to yield ZnMOF-5 (2.5), ZnMOF-5 (5) and ZnMOF-5 (10), respectively.

2.1.4. Synthesis of MOF-69 samples

The synthesis of MOF-69C, $Zn_3(OH)_2$(1,4-dbc)$_2{\cdot}$(DEF)$_2$, followed the method described by Loiseau et al. [18]. In a Teflon-lined stainless-steel bombs, H_2dbc (0.33 g, 1.99 mmol) and $Zn(NO_3)_2{\cdot}6H_2O$ (1.77 g, 5.96 mmol) were dissolved in 35 ml of DEF (Alfa Aesar, 99%). Deionized H_2O (1.17 ml) was added to the reaction solution, and the mixture was heated at 100 °C during 20 h. The crystals were collected and washed twice with DEF (30 ml) and acetone (30 ml). They were then dried at 100 °C in air. These experimental procedures were extended to the synthesis of MOF-69A, MOF-69B with 4,4′-biphenyl-dicarboxylic acid and 2,6-naphthalene-dicarboxylic acid as linkers, respectively.

2.1.5. Reference materials and catalysts

MIL-53(Al) was purchased from Aldrich (Basolite A100). The acid form of beta (H-BEA, Si/Al = 23) and mordenite (H-MOR, Si/Al = 10) zeolites were obtained from the commercial Na-forms (Fluka) by ammonium exchange following by calcination treatment. The ion exchange was carried out with 10 wt% solution of NH_4COOCH_3 in water at 80 °C during 4–5 h followed by calcination treatment at 550 °C during 3 h. This procedure was repeated twice. Both $AlCl_3$ (Aldrich 99.9%), and $ZnCl_2$ (Alfa Aesar, anhydrous, 98+%) were used as received and as reference Lewis acids. All MOF samples synthesized and used as catalysts in this study are summarized in Table 1.

2.2. Characterization

X-ray diffraction (XRD) patterns were recorded on Brucker D5005. The N_2 adsorption/desorption isotherms were measured on an ASAP 2010M from Micromeritics. Before the measurement, the sample was degassed for 3 h at 130 °C. The specific surface was determined by BET method, the pore volume by *t*-plot analysis, and the pore diameter by DFT. The samples were further characterized by TG/TD analysis with a Setaram – Type Setsys Evolution 12. Inductively Coupled Plasma (ICP) emission spectrometry was used for the analysis of the bulk chemical composition of

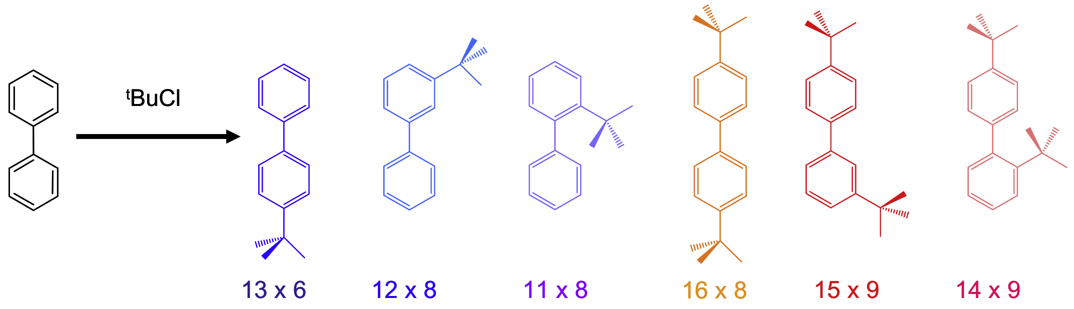

Fig. 3. Major products expected from the *tert*-butylation of biphenyl. Molecular size are indicated for 4-*tert*-butylbiphenylene, 3-*tert*-butyl-biphenylene, 2-*tert*-butyl-biphenylene, 4,4′-di*tert*-butyl-biphenylene, 3,4′-di*tert*-butyl-biphenylene, 2,4′-di*tert*-butyl-biphenylene (from left to right) Data were obtained with the software "CS Chem 3D-Pro Molecular Modeling and Analysis – 2001 CambridgeSoft" from the minimum energy configuration of each structure by performing the molecular dynamics calculations by the MM2 method.

Table 1
Summary of MOF samples synthesized and used as catalysts in this study.

Sample name	Basic structure	Linker	Synthesis method	Reference
MOF-5 solvo	MOF-5	H_2dbc	Solvothermal	[22]
MOF-5 basf	MOF-5	H_2dbc	Basf procedure	[23]
MOF-5 pre	MOF-5	H_2dbc	Fast precipitation	[24]
ZnMOF-5 (2.5)	MOF-5	H_2dbc + 2-methyl toluic acid (2.5%)	Fast precipitation	This study
ZnMOF-5 (5)	MOF-5	H_2dbc + 2-methyl toluic acid (5%)	Fast precipitation	This study
ZnMOF-5 (10)	MOF-5	H_2dbc + 2-methyl toluic acid (10%)	Fast precipitation	This study
MOF-69A	MOF-69	4,4′-Biphenyl-dicarboxylic acid	Solvothermal	This study
MOF-69B	MOF-69	2,6-Naphthalene-dicarboxylic acid	Solvothermal	This study
MOF-69C	MOF-69	H_2dbc	Solvothermal	[18]
IRMOF-3 pre	IRMOF-3	2-Aminoterephtahlic acid	Fast precipitation	This study
Zn-MOF-8	MOF-69	2,6-Naphthalene-dicarboxylic acid	Fast precipitation	This study
Zn-MOF-10	MOF-69	4,4′-Biphenyl-dicarboxylic acid	Fast precipitation	This study

the samples. DRIFT analysis was carried out on a Nicolet Magna 550 equipped with a MCT detector. The samples were loaded in a DRIFT Spectratech cell equipped with ZnSe windows. A thin layer of SiC sieved at 200–400 μm was first loaded to improve thermal exchange. Then SiC was cover up with the samples. Water desorption was followed by heating the cell to 220 °C under 50 ml min^{-1} of He. The cell was then cold down to room temperature and scans were performed in He flow. Solid state ^1H NMR analysis was carried out with a DX-400 Brucker in static conditions to allow quantification. Liquid ^1H NMR (Brucker Avance 250) was used to quantify the substitution of di- to mono-carboxylate for the samples ZnMOF-5 (2.5), (5) and (10). After the synthesis, the samples were digested in $DCl/D_2O/DMSO$-d_6 mixture, thus liberating the linkers in solution on the acid forms. The toluic acid was selected as mono-carboxylic acid because the methyl groups enable to distinguish chemical shifts between the two linkers. The integration of the characteristic signals of the two linkers allows the quantification of the respective amount of mono- and di-carboxylate linkers for the three samples.

2.3. Catalytic aromatic alkylation

Toluene (Ahimie-plus, 99%), biphenylene (Alfa Aesar, 99%), *tert*-butylbenzene (Alfa Aesar, 99%), naphthalene (Alfa Aesar, 99.6%), *n*-decane (Alfa Aesar, 99%), *tert*-butylchloride (*t*-BuCl) (Alfa Aesar 98+%) were used as received. The alkylation reactions were carried out in *n*-decane with an aromatic:*t*-BuCl molar ratio of 2:1. The catalytic sample (30 mg) was activated at 130 °C under 10^{-5} bar, unless specific conditions were given. As en example, a mixture of 1.7 g (18.8 mmol) of toluene, 0.851 g (9.2 mmol) of *t*-BuCl and 5.18 g of *n*-decane was placed in a 48 ml Teflon-lined autoclave (Top Industries) and heated to reaction temperature (100 °C or 170 °C) under stirring with autogeneous pressure. After 2 h of reaction, the solid was recovered by filtration at room temperature. The reaction mixtures were analyzed by gas chromatography with a HP 6890 N equipped with a HP-5 capillary column (30 m length). The toluene conversion was calculated by taking into account the initial concentration (100% excess). Identification of the different isomer configurations was performed by GC–MS (HP 6890 equipped with HP-5/HP-1 capillary columns, a HP 5973 quadrupolar detector – ionic impact at 70ev, and NIST02 library). In order to check that the reaction takes place in heterogeneous conditions leaching issues were investigated. Fresh reactants were added to the liquids recovered from reaction mixture and a new reaction run was performed.

3. Results

3.1. Structural characterization

The MOF-69C, $Zn_3(OH)_2(bdc)_2{\cdot}2DEF$, belongs to the rod-like type of metal open framework [25]. It consists of chains of $ZnO_2(OH)_2$ tetrahedrons and $ZnO_4(OH)_2$ octahedrons and μ_3-OH as bridging species (Fig. 4). MOF-69C exhibit 1D diamond-shaped channel with pores of diameter close to 0.85 nm. The XRD patterns reveal a mixture of mainly $Zn_3(OH)_2(bdc)_2{\cdot}2DEF$ (MOF-69C) and $Zn_3(OH)_2(bdc)_2{\cdot}DEF$ (Fig. 5). The latter is obtained after removing on molecule of DEF by heating at 170 °C in air. The powder-pattern can be indexed in a monoclinic unit-cell, space-group $P2_1/n$ [$a = 17.590(2)$, $b = 19.659(2)$, $c = 11.992(1)$, $\beta = 97.9(1)$] with a volume of 4107.4(7) $Å^3$, similar to that of the parent compound. MOF-69A and MOF-69B, which are made from di-carboxybiphenylate and di-carboxynaphthalate linkers, respectively, are isostructural to MOF-69C [21,26]. Within these units, there are tetrahedral and octahedral Zn(II) centers bound to 4 and 2 carboxylate groups, respectively. For MOF-69A, the channel dimensions are of 12.2 Å along an edge and 16.6 Å along the diagonal.

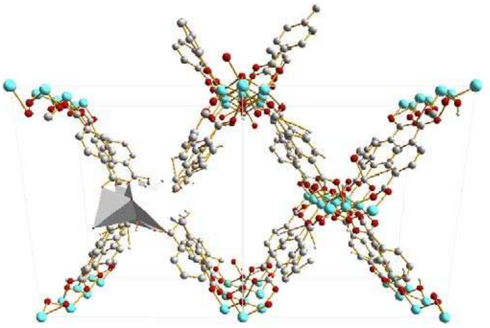

Fig. 4. MOF-69C rod-like porous structure (molecules of DEF omitted for clarity).

The powder X-ray diffraction patterns of the samples MOF-5 solvo (see Ref. [22]), MOF-5 basf, and IRMOF-3 match very well with the IRMOF cubic structure (Fig. 6). For the samples prepared by precipitation, namely MOF-5 pre, ZnMOF-5 series with 2.5%,

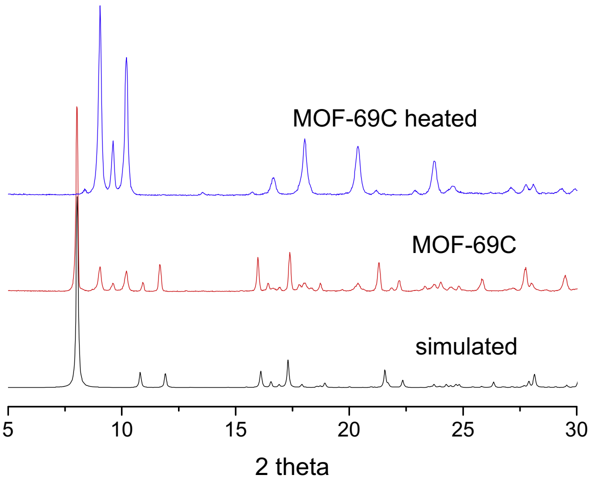

Fig. 5. Powder X-ray diffraction patterns of simulated MOF-69C (bottom), $Zn_3(OH)_2(bdc)_2{\cdot}2DEF$ (MOF-69C) (center), and of $Zn_3(OH)_2(bdc)_2{\cdot}DEF$ (top).

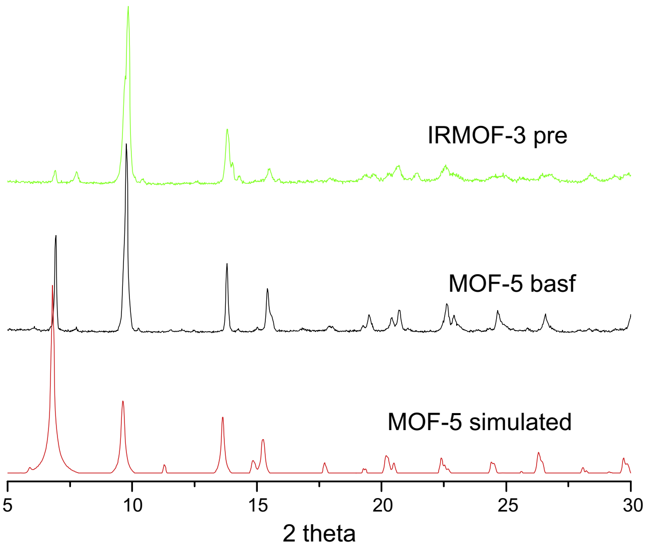

Fig. 6. Powder X-ray diffraction patterns of MOF-5 basf (center) and IRMOF-3 pre (top) samples compared with the simulated pattern (bottom).

5% and 10% of mono-carboxylic acid, XRD patterns do match with the cubic structure however with a much lower level of crystallinity. We also observe a net splitting of the peak at 9.6 (220) for MOF-5 pre which may indicate a distorted structure of lower symmetry according to Hafizovic et al. [27]. This split is sample depending and most of the time we can observe a non symmetrical peak instead such in the case of MOF-5 basf, ZnMOF-5 (2.5%, 5% and 10%). For the later series (Fig. 7), we can observe one additional signal at 8.9° which is relatively intense which upon heating at 130 °C gains of intensity. This phase can be attributed to $Zn(bdc)\cdot xH_2O$ (called N phase) which was identified by Thirumurugan et al. as the intermediate phase between $[Zn(H_2O)_2(bdc)]$ (VI) and $[Zn(H_2O)(bdc)]$ (VII) upon heating at moderate temperature [28].

The indexation of the X-ray powder-pattern of the samples Zn-MOF-8 and Zn-MOF-10 (data not shown) reveal that MOF-69 type phases have been obtained instead of expected IRMOF structures. For Zn-MOF-10 the cell parameters are 20.180(1), 18.562(1), 12.164(1), 90 95.34(5), 90 in space-group *C*2/*c*, which is identical to that of MOF-69B. The cell parameters for Zn-MOF-8 show similar values: 21.59(2), 20.88(4), 11.94(2), and 90 96.10(2), 90 and the systematic absences also suggest *C*2/*c* as a space-group. The synthesis of MOF-5 is known to be very sensitive to the conditions, especially regarding the water concentration in the media [29,30]. For instance, MOF-69C has been obtained by Loiseau et al. instead of the MOF-5 as initially expected [18]. Our finding indicates that this synthesis sensitivity is also found for the homologues IRMOF-8 and -10. The synthetic conditions applied here are more favourable for obtaining MOF-69 series against IRMOF structures.

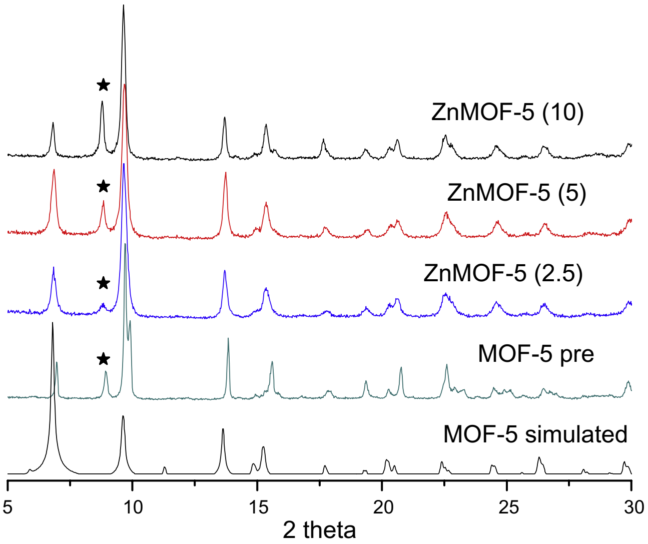

Fig. 7. Powder X-ray diffraction patterns of MOF-5 based samples prepared by precipitation (MOF-5 pre) and with increasing rate of mono-carboxylic acid ZnMOF-5 (2.5), (5), and (10), respectively. The symbol * indicates $Zn(bdc)\cdot xH_2O$ (N phase).

In order to characterize hydroxyl groups, short range DRIFT and ^1H NMR studies were carried out. From the DRIFT spectra (Fig. 8), we can clearly observe a common intense signal at about 3600 cm^{-1} for MOF-69C, MOF-5 pre, MOF-5 basf samples, and also for Zn-MOF-8. This signal can be attributed to Zn–OH species such as found in $Zn_5(OH)_4(bdc)_3\cdot 2DMF$ [31]. The presence of this –OH band is expected for MOF-69 samples since μ_3-OH specie is found in the structure. However, for pure IRMOF samples, this band should not appear. On other hand, the intensity of the hydroxyl band is much weaker for IRMOF-3 suggesting higher purity while the two intense signals centered at 3500 and 3390 cm^{-1} correspond to the both stretching and bending vibrational modes of $-NH_2$ species, respectively. The nature of the hydroxyl centers as characterized by DRIFT results are also confirmed by solid ^1H NMR studies. For MOF-69C, the intense and broad signal at −1 ppm can be assigned to Zn-(μ_3-OH)-Zn chains as reported in Loiseau et al. [18] (Fig. 9). Similarly, the presence of Zn–OH–Zn species is also revealed for MOF-5 samples in a much lower amount however (small peak at $\delta = -0.4$ ppm). Depending on the sample preparation, the peak integrations lead to μ_3-OH: bdc ratio from 10 to 25 for MOF-5 solvo and MOF-5 pre, respectively.

From XRD, DRIFT and ^1H NMR studies, we did not observe structural changes for IRMOF-3 upon air exposure, neither at long rand (phase transformation) or short range (hydroxyl groups) as also reported by Gascon and Kapteijn [32].

The partial substitution of the 1,4-benzene-di-carboxylate by mono-carboxylate linkers is followed by liquid ^1H NMR measurements after sample digestion (Fig. 10). The presence of the distinctive aromatic resonances at δ(ppm) = 7.21 (m, 2 H, H_{1-1}, H_{1-3}), 7.44 (t, 1 H, $^1J_{HH} = 6.5$ Hz, H_{1-2}) and 7.72 (d, 1 H $^1J_{CH} = 6.5$ Hz, H_{1-4}) indicates the presence of toluic acid in liquid phase which find its origin in the porous framework. Depending on the percentage of mono-carboxylic acid used in the synthesis, the peak integration reveals di-carboxylate: mono-carboxylate ratios between 1:17 and 1:53. As revealed by DRIFT, the substitution of di- to mono-carboxylate linkers is accompanied by additional signals in the hydroxyl region which could be additional Zn–OH species; the strongest being at 3580, and 3530 cm^{-1}. We also observe that for the sample with the lowest level of substitution (2.5) the intensities of the later IR bands are weaker.

In summary, DRIFT and ^1H NMR results confirm the presence of Zn–OH species in MOF-5 basf sample and MOF-5 prepared by precipitation that could, in principle, be addressed to Brønsted acid type. Pyridine adsorption measurements from room temperature to 200 °C followed by FTIR were carried out in order to characterize

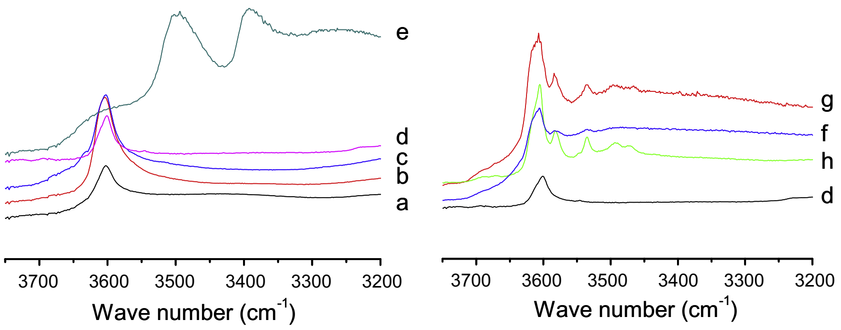

Fig. 8. DRIFT spectra recorded after drying at 220 °C under N_2 flow. Key: Zn-MOF-8 (a), MOF-5 basf (b), MOF-69C (c), MOF-5 pre (d), IRMOF-3 (e), ZnMOF-5 (2.5) (f), ZnMOF-5 (5) (g), ZnMOF-5 (10) (h).

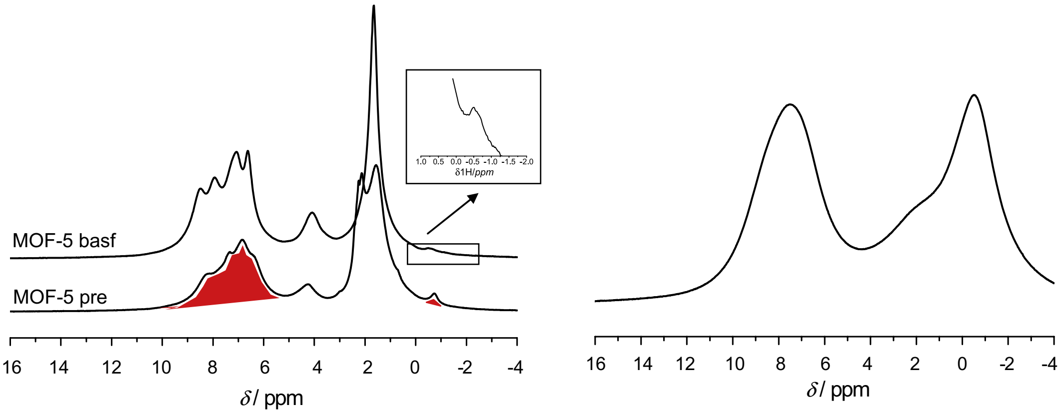

Fig. 9. Solid ^{1}H NMR of MOF-5 samples prepared by basf and precipitation methods (left) and MOF-69C (right).

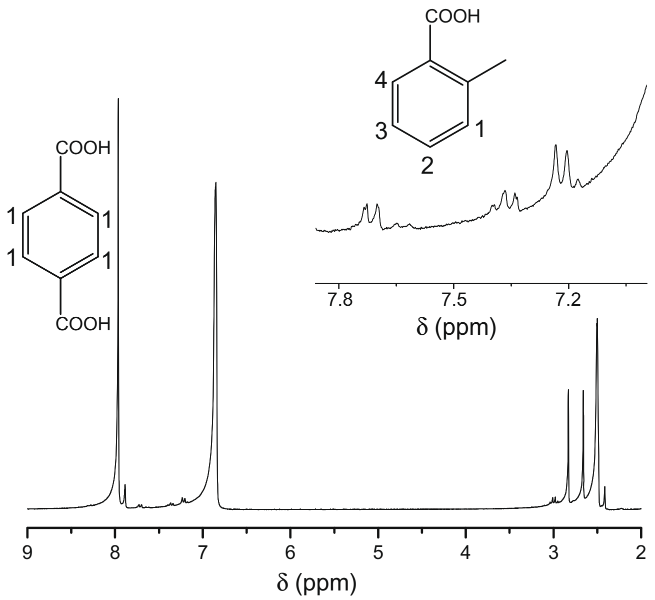

Fig. 10. Liquid ^{1}H NMR of digested ZnMOF-5 (2.5).

the nature and the strength of the acid sites. Any significant adsorptions were measured even at low temperature neither for MOF-5 pre nor for MIL-53 (Al). However, the adsorption of pyridine in low amount can not be ruled out since the signals could be masked by the intense bands of carboxylates. Although deeper investigations are requested to further characterize the acid centers, we can conclude that the acidity of identified Zn–OH is much weaker than surface hydroxides of reference oxides such as silica–alumina. For the same reason, the presence of certain amount of Lewis acid sites could not be ruled out.

3.2. Porous structure characterization

The results of N_2 physisorption experiments (Fig. 11) show that samples prepared either by precipitation or basf methods are microporous materials. Surface areas, micropore volumes and pore sizes are also reported in Table 2. The very high surface area (>2600 m^2 g^{-1}) and micropore volume (>1.3 cm^3 g^{-1}) of the MOF-5 sample prepared by solvothermal technique (MOF-5 solvo) are in good agreement with already reported values [33]. This demonstrates the high quality of the solids with respect to its structure since the presence of other non porous phases would result in a proportional decrease of the surface area and pore volumes. For the samples prepared by precipitation, surface areas, micropore volumes and pore sizes correspond to those reported elsewhere with similar preparation procedures for MOF-5 [24,27] and IR-MOF-8 [34]. Logarithmic plots (Fig. 11) show that for Zn-MOF-8 nitrogen adsorption occurs in two steps revealing two distinct pore sizes. Surprisingly, there are major surface area discrepancies between MOF-69 series. Because of structural similarity in terms of pore size and geometry with MIL-53, we would have expected much larger porous volume for MOF-69C. In contrast, their analogues with longer linkers, naphthyl (MOF-69B) and biphenyl (MOF-69A) carboxylates yield surface higher areas values.

3.3. Catalytic testing

Alkylations of aromatic compounds can be performed with either Brønsted or Lewis acid catalysts, the later being preferable

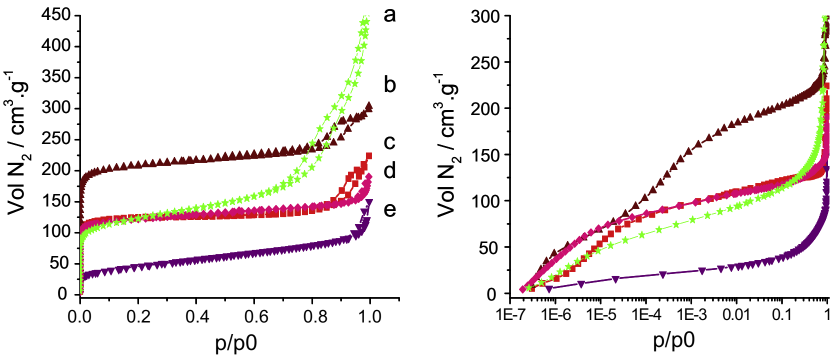

Fig. 11. N_2 adsorption/desorption isotherms at 77 K in log scale (left) and linear scale (right) for: H-BEA (a), Zn-MOF-8 (b), IRMOF-1 (c), IRMOF-3 (d) and Zn-MOF-10 (e).

Table 2
N_2 physisorption results.

Sample	Surface Area ($m^2 g^{-1}$)[a]	Pore volume ($cm^3 g^{-1}$)	Micropore volume ($cm^3 g^{-1}$)[b]	Pore diameter (Å)[c]
MOF-5 solv	2600	0.3	1.31	–
MOF-5 basf	400	–	–	–
MOF-5 pre	450	0.32	0.18	8.8
MOF-69A	270	–	–	–
MOF-69B	970	–	–	–
MOF-69C	45	–	–	–
IRMOF-3	426	0.25	0.16	7.3
Zn-MOF-8	730	0.46	0.29	7.3/11.6
Zn-MOF-10	160	0.17	0.02	8.7
H-BEA	430	0.62	0.10	7.7

[a] From BET analysis.
[b] From *t*-plot analysis.
[c] From DFT analysis.

when linear alkyl-halides are used as alkylating agents [35]. Because the reactivity of alkylated aromatics are higher than the parent aromatics, both Brønsted and Lewis acids usually perform un-desired poly-alkylations. In order to limit this issue, the aromatic compound is commonly fed in high excess with respect to the alkylating agent, thus enhancing selectivity and workup operations [36]. In our case, we did consider that an aromatic: *tert*-BuCl ratio of 2:1 would be appropriate to highlight different behaviours of different catalysts towards the selective mono-alkylation while minimizing analytical issues due to the liberation of HCl.

The alkylation of four aromatic substrates, toluene, *tert*-butylbenzene, naphthalene and biphenylene has been carried out. For sake of conciseness and clarity, only the results on the alkylation of toluene and biphenylene are only reported here. The catalytic conversion of *tert*-butylbenzene gives similar insights than those obtained with the toluene while naphthalene is alkylated selectively in β-position (2-*tert*-butyl-naphtahlene as main mono-alkylated product) whatever the catalysts employed; thus hindering structure–activity relationships to be proposed. A first series of screening has been carried out at 170 °C, a relatively elevated temperature, in order to discriminate active from non active formulations (Table 3). Except for IRMOF-3 and MIL-53(Al), all other tested MOF samples convert toluene in the range of 70–80% which are intermediate values with respect to reference catalysts (H-BEA and $AlCl_3$). Note that the H-BEA sample is a non-dealuminated zeolite which contains moderate to strong Brønsted acidity and accompanied with Lewis centers. Furthermore, all MOF samples exhibit high selectivity to the less bulky para-oriented products (80–85%) slightly superior to H-BEA whereas $AlCl_3$ produces mixtures of ortho- and para-isomers in nearly equal ratio. The obtained results on the catalytic alkylation of biphenylene confirm the later trends. MOF samples, at the exception again of IRMOF-3 and MIL-53(Al), are as active as H-BEA zeolite and show exceptional selectivity to the para-isomer 4-*tert*-butylbiphenylene. Indeed, only traces of di-alkylated products (<1%) are detected whereas much higher selectivity to the ortho-oriented product and about 15% towards di-alkylated products are measured for H-BEA and $AlCl_3$.

After these preliminary tests, catalytic experiments at 100 °C were carried out in order to better discriminate the activity of MOF catalysts and also to better highlight shape selectivity properties. As a matter of fact, MOFs conversion values are now more spread (from 8% to 62%) (Table 4). At this temperature also, both IRMOF-3 and MIL-53(Al) are not active whatever activation procedures which were applied. We can see major activity differences on MOF-5 samples depending on the synthesis procedure. The most crystalline and porous MOF-5 (MOF-5 solvo) sample shows the lowest catalytic activity in contrast to all other MOF-5 type samples including the samples with mixture of mono- and di-carboxylate linkers (ZnMOF-5 samples). On the other hand, it appears that the generation of additional defects by mono-acid substitution (ZnMOF-5 samples) does not affect significantly catalytic performances with respect to MOF-5 sample prepared by precipitation (MOF-5 pre). We also observe significantly lower activities for MOF-69 type samples; the lowest activity being for MOF-69C which has also the lowest surface area. Surprisingly, Zn-MOF-8 and -10 show the highest catalytic activities, although they have similar structure than MOF-69B and MOF-69A, respectively. Kinetic studies confirm the ranking of MOF activities with Zn-

Table 3
Catalytic results for the *tert*-butylation of toluene and biphenylene at 170 °C after 6 h.

Catalyst	Toluene conversion	Selectivity			Biphenylene conversion	Selectivity		
		Para [a]	Ortho	Di [c]		Para [b]	Ortho	Di [c]
MOF-5 solvo	n.a.	–	–	–	n.a.	–	–	–
MOF-5 basf	73	84	16	0	n.a.	–	–	–
MOF-5 pre	73	82	18	0	37	90	6	4
IRMOF-3 [d]	0	–	–	–	0	–	–	–
Zn-MOF-8	86	84	16	0	38	97	3	0
Zn-MOF-10	86	82	18	0	39	99	1	0
MOF-69C	81	81	19	0	33	89	7	4
MIL-53(Al) [d]	0	–	–	–	0	–	–	–
H-BEA	90	72	28	0	70	66	18	16
H-MOR	n.a.	–	–	–	15	75	0	25
$AlCl_3$	64	46	54	0	64	50	35	15
$ZnCl_2$	8	77	23	0	n.a.	–	–	–

Selectivity [a] 4-*tert*-butyltoluene, [b] 4-*tert*-butylbiphenylene, [c] sum of di-alkylated products, [d] MIL-53 (Al) samples were tested as made or after being activated either at 220 °C under N_2 flow or at 170 °C under vacuum (10^{-5} mbar). In all cases, meta-isomers were not detected. However, the presence of minor quantity of meta-isomers can not be rule out. Key: n.a. not analyzed.

Table 4
Catalytic results for the *tert*-butylation of toluene and biphenylene at 100 °C after 2 h.

Catalyst	Toluene conversion	Selectivity			Biphenylene conversion	Selectivity		
		Para	Ortho	Di		Para	Ortho	Di
MOF-5 solvo	13	90	10	0	n.a.	–	–	–
MOF-5 basf	47	89	11	0	n.a.	–	–	–
MOF-5 pre	40	88	12	0	28	100	0	0
ZnMOF-5 (2.5)	30	85	15	0	n.a.	–	–	–
ZnMOF-5 (5)	46	86	14	0	n.a.	–	–	–
ZnMOF-5 (10)	36	86	14	0	n.a.	–	–	–
MOF-69C	8	90	10	0	n.a.	–	–	–
MOF-69A	15	89	11	0	n.a.	–	–	–
MOF-69B	23	90	10	0	n.a.	–	–	–
Zn-MOF-8	47	90	10	0	13	100	0	0
Zn-MOF-10	62	92	8	0	10	100	0	0
MIL-53 (Al)	0	–	–	–	n.a.	–	–	–
H-BEA	67	72	28	0	30	55	25	20
H-MOR	5	85	15	0	5	81	0	19
$AlCl_3$	n.a.	–	–	–	55	47	34	19

MOF-10 > MOF-5 pre > MOF-69C (Fig. 13). In contrast to the wide range of activities, selectivity values are very similar for all porous zinc carboxylates samples whatever their synthesis procedures. The para-selectivity for the toluene alkylation is plotted as a function of the conversion in Fig. 12. It clearly shows that high level of selectivity for zinc carboxylate frameworks can be maintained at high conversion in contrast to tested zeolites. Indeed, we note that H-BEA catalyst is much less selective with respect to Zn-MOF-10 with similar conversion. However, we must mention that selectivity for H-form zeolites, such as BEA and MOR can be enhanced by dealumination of samples in order to produce stronger Brønsted acid sites and extra framework Al species [37,38]. In addition, di- and poly-alkylation products as well as *trans*-alkylation products can be decreased in a large amount by a post-synthesis silanization treatment [39,40]. Thus, silanized H-MOR shows enhanced selectivity (90%, at 10% of conversion) to the corresponding mono-alkyl-isomer in the naphthalene alkylation with iso-propyl-bromide at 200 °C during 1 h [39]. In this sense, our results obtained for Zn-MOF-8 and Zn-MOF-10 in the naphthalene alkylation with *t*-BuCl at 170 °C during 2 h are readily comparable to those reported in literature using modified mordenite zeolites [39]. Thus, 100% of 2-*tert*-butylnaphthalene is produced at 42% and 23% of conversion when Zn-MOF-8 and Zn-MOF-10 are used as catalysts, respectively (data not shown).

The main outcome of the biphenylene alkylation is the 100% selectivity in the para-oriented product. It has to be emphasized also that reference catalysts (H-BEA, H-MOR, $AlCl_3$) yield high amount of di-alkylated products in contrast to MOF catalysts.

Isomerization test reactions have been performed to investigate product reactivity in the MOF. In absence of alkylaton agent, 4-*tert*-butyltoluene does not isomerize on MOF compounds at 100 °C in contrast to acid zeolites. It means that when the para-allkylation is performed in the course of the reaction the product does not react further, likely because of the weak acidity of investigated MOFs. This result may explain the superior selectivity of MOF materials. Summarizing, those results point out outstanding pore-shape selectivity properties of microporous zinc carboxylate open frameworks for large poly-aromatics.

3.4. Catalyst post characterization and leaching tests

After filtration and washing with *n*-decane under inert atmosphere, MOF-5 pre sample can be re-used without any loss of activity or selectivity. Solid ^{1}H NMR spectrum of used precipitated MOF-5 reveals the presence of a guest in the structure which can be assigned to $H_3O^+Cl^-$ (very intense peak at $\delta = 3.4$ ppm). Indeed, very similar ^{1}H NMR spectra are obtained when concentrated HCl (36%) is added to fresh MOF-5 samples. We suggest that the HCl,

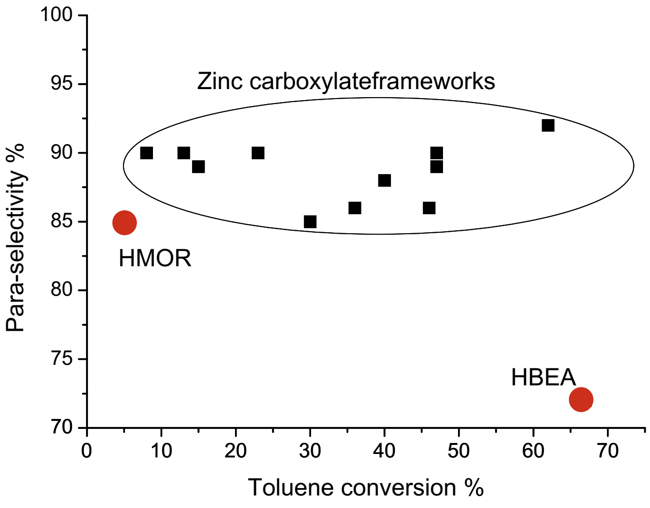

Fig. 12. Conversion-selectivity plot on toluene alkylations with *tert*-butyl chloride at 100 °C during 2 h.

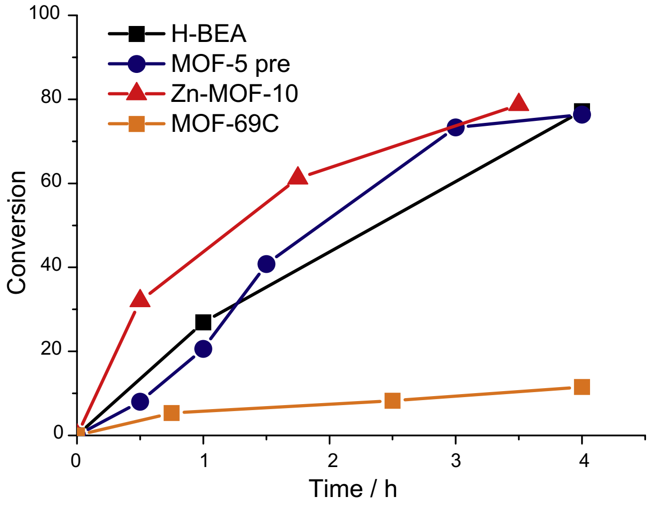

Fig. 13. Kinetic curves for different catalytic samples in the *tert*-butylation of toluene at 100 °C.

which is produced in the course of the reaction, is trapped into the framework, likely, at the oxygen containing nodes. The hydration of the sample, which provokes the rapid formation of $H_3O^+Cl^-$, arises from the sample cell which is not tight against ambient air. We believe that this aqueous HCl formation is responsible of a partial hydrolysis of the framework as indicated by a very broad peak at $\delta = 14$ ppm and the change of the XRD pattern (Fig. 14). Because the linkers from the solid framework are also made form aromatics species, we were wondering whether the alkylation could take place on the terephthalate linkers as well. Any data from solid NMR supports this hypothesis.

In order to check that the reaction takes place in heterogeneous conditions, leaching issues were investigated. Firstly, tests in absence of solid catalysts were carried out in same conditions and any conversions were measured. Secondly, reaction mixtures were filtered off after the completion of catalytic reactions, both solid catalyst and liquid being recovered separately. When a new reaction was started by adding fresh reactants to the recovered liquid, any additional conversion was detected. This is consistent with the fact that HCl is trapped into the framework making the filtrate HCl free. Finally, we have observed that the reaction takes place at 50 °C with precipitated MOF-5. In these conditions of pressure and temperature, IRMOF samples are likely not soluble in *n*-decane indicating that the reaction does not proceed in homogeneous phase.

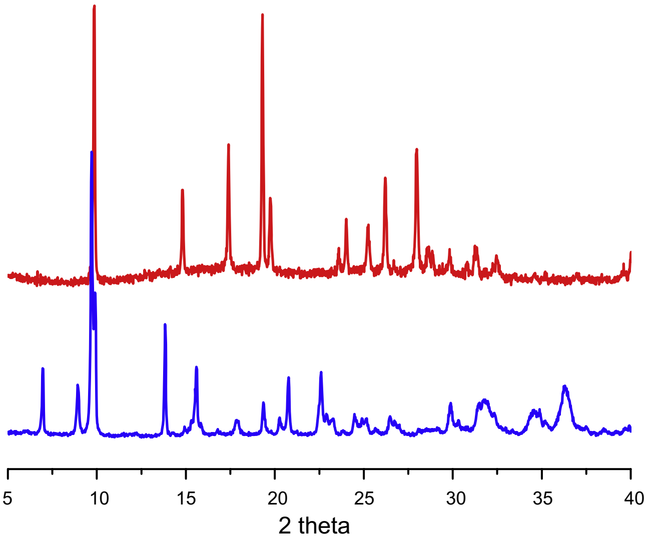

Fig. 14. Powder X-ray diffraction patterns of MOF-5 pre before (bottom) and after reaction (top).

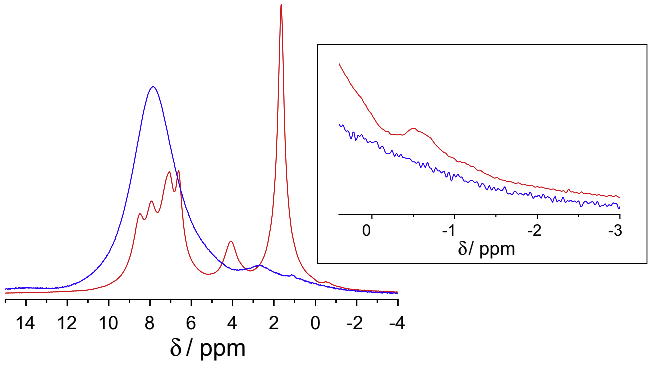

Fig. 15. Solid ^1H NMR post characterization after running the alkylation with toluene-d_8.

3.5. Post characterization of H–D exchange in the course of the reaction

In order to ascertain the key role of Zn–OH species in the catalytic properties of zinc carboxylate open frameworks, alkylation on toluene-d_8 was carried out with precipitated MOF-5 at 100 °C. After reaction, the sample was recovered as indicated above and characterized by solid state ^1H NMR measurements (Fig. 15). Apart the aromatic signal arising from the linker, we can observe a broad peak placed at $\delta = 3$ ppm which may be assigned to $DH_2O^+Cl^-$ trapped in the network. But more importantly, the characteristic Zn–O(H)–Zn peak at $\delta = 0.4$ ppm has disappeared suggesting an H–D exchange with the toluene-d_8 while the reaction takes place.

4. Discussion

The intriguing non activity of IRMOF-3 and the very low activity of pure MOF-5 (MOF-5 solvo with the highest surface area) clearly indicate the key role of Zn–OH species in the catalytic properties. Obviously, all samples exhibiting a sharp IR band at 3600 cm^{-1} are active whereas IRMOF-3 is not active. We suggest that the very low activity of pure MOF-5 arises from its partial hydrolysis in the reaction media which may contain about 0.02% of water (*tert*-butyl chloride was used as received). The ZnOH–ZnOD exchange in the course of the reaction when using toluene-d_8 also supports that Zn–OH species are the actual catalytic centers. Furthermore, the fact that there is no evidence of alkylations on the aromatic linkers, clearly suggests that the catalyst centers are bewared by the framework itself. Finally, we can rule out the role of Zn–Cl as catalytic species that would arise from structural modifications since kinetic studies show that MOF catalysts are active in the first minutes on operation in contrast to MIL-101(Cr) [15]. Furthermore, the poor activity of $ZnCl_2$ tested as a powder at 170 °C (only 8% conversion) confirms that $ZnCl_2$ is not the catalytic specie. We therefore conclude that Zn–OH species, that are part of the framework, are likely responsible from the catalytic activity of the zinc carboxylate open frameworks. The non activity of MIL-53(Al) may suggest that the acidity of bridging μ_2-OH is not strong enough to catalyze the reaction. Unfortunately, the adsorption of pyridine measured by IR did not allow a proper quantification of the acid site strength. On the other hand, preliminary molecular modeling results (DFT) [41] indicate a very low acidity of MIL-53(Al) which is in agreement with pyridine adsorption and catalytic results. On the other hand, the presence of uncoordinated Zn at the surface or at crystalline defects with Lewis feature can not be ruled out. These centers may also be involved in the reaction pathway. As a matter of fact, Horcajada et al. [15] proposed that benzylation of benzene over MIL-101(Fe) type materials could be catalyze on both Lewis and Brønsted acid sites.

Structural (X-ray diffraction, IR) and thermal (TDA, TGA) characterization data (not shown) for precipitated MOF-5 are in very good agreement with the results reported by Huang et al. [24] and Hafizovic et al. [27]. We also measured a 10% excess of Zn with respect to the theoretical formulae (elemental analysis and TGA), which leads to a global composition of $Zn_4O(bdc)\cdot 2H_2O + Zn(OH)_2$. According to Hafizovic et al. [27], zinc hydroxide nanoclusters that partly occupy the cavities could be responsible for the structure distortion evidenced by the splitting of the diffraction peak at 9.7. However, authors point out that other structural change would result in the same distortion. On the other hand, the ^1H NMR spectra obtained for different precipitated MOF-5 samples indicated the presence of 3–5% of Zn–OH–Zn species, like those found for $Zn_3(\mu_3OH)_2(bdc)_2\cdot 2DEF$ (MOF-69C). Phase transformation from MOF-5 to MOF-69C has been well characterized since very recently [29,30]. The later phase can be formed during the synthesis of

MOF-5, and is kinetically favoured in moisture conditions, as was the case in this study. Therefore, in addition to zinc hydroxide clusters, precipitated MOF-5 samples also contain Zn–(μ_3OH)–Zn chains in minor quantities, which could either, be a crystalline default of the cubic structure or non-XRD detectable MOF-69C microcrystallites. Finally, it was recently demonstrated that pure MOF-5 undergoes a rapid phase transformation under moist conditions to MOF-69C that is accompanied by a drastic decrease inaccessible porous volume [22,42].

They are many more Zn–OH–Zn species in MOF-69 samples than in MOF-5 type samples as confirmed by solid ^{1}H NMR studies. In addition, MOF-69A and B show comparable and higher surface areas than MOF-5 type samples, suggesting equal or even enhanced site accessibility. The fact that precipitated MOF-5 samples have superior activity than MOF-69 type samples, although they have a much lower number of sites, indicate that (i) Zn–μ_3OH–Zn species have a moderate activity and/or other kind of Zn–OH (as described above) exist in precipitated MOF-5 which are much more active. In summary, catalytic centers may arise either from Zn hydroxide clusters or from the presence of Zn–OH–Zn type species [i.e. $Zn_3(\mu_3OH)_2(bdc)_2\cdot 2DEF$ found in MOF-69C], or structural defects as Zn–OH species formed at the synthesis step or upon water adsorption.

Obviously, the action of water content at the synthesis stage and/or the action of the moisture when handling the MOF-5 samples are responsible from the generation of structural defects as Zn–OH species. In addition to the later, the isomorphous substitution of di-carboxylate by mono-carboxylate linkers creates other types of Zn–OH species. Unfortunately, their characterization, quantification and role in catalysis are made difficult by the high sensitivity of MOF-5 against moisture.

The pore size distribution calculated by Horvath–Kawazoe or Density Functional Theory (DFT) methods can be only indicative values, since the principal interaction potentials of the adsorbate and the adsorbent are unknown and assumptions have to be made about the pore morphology. The numerical values of the pore diameters calculated from the DFT method (Table 5) are therefore not fully accurate but, more importantly, allow a comparison among members of a class of similar materials which presumably have the same interaction potentials. In order to complete the picture of MOF samples with regard to their porous properties, calculated sizes of cages and channel windows from structural data of pure crystals are reported in Table 5. For example, the window between the cages of IRMOF-1 have a van der Waals space that can accommodate a sphere with a diameter of approximately 7.8 Å, herein referred as the "free-space" diameter. In contrast to zeolite pore sizes, these numbers shall be interpreted with care for MOF materials, especially when one wants to correlate structural features and properties. Indeed, in addition to their general flexibility properties the aromatic rings of IRMOF can rotate thus making feasible the diffusion of larger guests [43,44].

From experimental and theoretical data, there is in principle no steric hindrance for mono-alkylated products to diffuse out of all porous solids, including H-BEA. Even very bulky products such as the di-alkylated product 4,4′-di-*t*-butylbiphenylene (16 × 8 Å) can be formed in large amounts in H-BEA [45–48]. Therefore, the shape selectivity properties observed for IRMOF sample can not arise from diffusion hindrance of the most bulky products since pore windows are even larger. For the reaction to take place we suggest that the biphenylene is absorbed in a specific manner to allow the formation of the transitions state for the para-oriented product. Once alkylated, it can not be activated in the same manner because of steric hindrance and double alkylation can not proceed.

Table 5
Theoretical cage and window sizes from structural data.

	Cage free space diameter (Å)	Window free space diameter (Å)
IRMOF-1[a]	15.1	7.8
IRMOF-8[a]	18.0	9.2
H-BEA[b]	6.6	6.1

[a] "Free-space" diameter refers to the diameter of the largest sphere that can fit in the cage or through the window when van der Waals radii are assumed for all frameworks atoms from Ref. [20].

[b] From Ref. [49].

5. Conclusions

The MOF design by a "zeolite" mimetic approach leads us to select microporous structures exhibiting bridging hydroxyls (MOF-69, MIL-53). By NMR and IR characterization, we have demonstrated the key role of Zn–OH species to generate catalytic properties. Although Zn–OH groups can be created by isomorphous substitution of di- by mono-carboxylate linkers, the impact on the catalytic performances can be hardly assessed. Indeed, MOF-5 prepared by precipitation, without taking special care to control neither water concentration nor moisture, already shows a few percent of Zn–OH as structural defects while the overall cubic structure is maintained.

This study illustrates the rational design of MOF to generate single site Brønsted acid catalysts. The construction by building block approach enables to regard MOF material as extended molecules. However, they are by essence solids. With this respect, they are quite similar to zeolites and thus there are accompanied with characterization issues such as the identification and quantification of defects. As clearly shown in this study, short range characterization shall be systematically carried out in order to identify actual catalytic centers. On the other hand, we believe that the engineering of structural defects in MOF materials may lead to the generation of a new class of catalysts with different acidity and hydrophobic properties than encountered in zeolites. In this sense, other alkylating agents of high industrial relevance and also much more catalyst demanding in terms of acidity strength, such as alcohols and alkenes, are now under study.

We have also demonstrated that MOFs can undergo 100% shape selective catalytic alkylations of large aromatics molecules. This discovery lead us to generate a new class of Brønsted acid MOFs which are more acid and can perform alkylation and isomerization at room temperature [41].

Acknowledgments

We thank C. Daniel and C. Lorenz for DRIFT and NMR investigations. We also thank Prof. S. Kaskel and Dr. A. Henschel for having provided high surface area MOF-5 samples.

References

[1] G. Ferey, Chemical Society Reviews 37 (2008) 191.
[2] D. Farrusseng, C. Mirodatos, in: U. Ozkan (Ed.), Handbook of Catalyst Design, Wiley-VCH, Weinheim, 2009.
[3] S. Vagin, A. Ott, B. Rieger, Chemie Ingenieur Technik 79 (2007) 767.
[4] K. Schlichte, T. Kratzke, S. Kaskel, Microporous and Mesoporous Materials 73 (2004) 81.
[5] L. Alaerts, E. Seguin, H. Poelman, F. Thibault-Starzyk, P.A. Jacobs, D.E. De Vos, Chemistry – A European Journal 12 (2006) 7353.
[6] W. Mori, T. Sato, T. Ohmura, C.N. Kato, T. Takei, Journal of Solid State Chemistry 178 (2005) 2555.
[7] W. Mori, S. Takamizawa, C.N. Kato, T. Ohmura, T. Sato, Microporous and Mesoporous Materials 73 (2004) 31.
[8] C.N. Kato, W. Mori, Comptes Rendus Chimie 10 (2007) 284.
[9] C.N. Kato, M. Ono, T. Hino, T. Ohmura, W. Mori, Catalysis Communications 7 (2006) 673.
[10] J.S. Seo, D. Whang, H. Lee, S.I. Jun, J. Oh, Y.J. Jeon, K. Kim, Nature 404 (2000) 982.
[11] K.S. Suslick, P. Bhyrappa, J.H. Chou, M.E. Kosal, S. Nakagaki, D.W. Smithenry, S.R. Wilson, Accounts of Chemical Research 38 (2005) 283.

[12] G.A. Olah, Friedel–Crafts Chemistry, Wiley, NY, 1973.
[13] J.S. Beck, A.D. Dandekar, T.F. Degnan, in: M. Guisnet, J.-P. Gilson (Eds.), Zeolites for Cleaner Technologies. Catalytic Science Series, vol. 3, Imperial College Press, London, 2002, p. 223.
[14] A. Corma, Journal of Catalysis 216 (2003) 298.
[15] P. Horcajada, S. Surble, C. Serre, D.Y. Hong, Y.K. Seo, J.S. Chang, J.M. Greneche, I. Margiolaki, G. Ferey, Chemical Communications (2007) 2820.
[16] U. Ravon, M.E. Domine, C. Gaudillère, A. Desmartin-Chomel, D. Farrusseng, New Journal of Chemistry 32 (2008) 937.
[17] F. Millange, C. Serre, G. Ferey, Chemical Communications (2002) 822.
[18] T. Loiseau, H. Muguerra, G. Ferey, M. Haouas, F. Taulelle, Journal of Solid State Chemistry 178 (2005) 621.
[19] E. Armengol, A. Corma, H. Garcia, J. Primo, Applied Catalysis, A: General 149 (1997) 411.
[20] M. Eddaoudi, J. Kim, N. Rosi, D. Vodak, J. Wachter, M. O'Keefe, O.M. Yaghi, Science 295 (2002) 469.
[21] N.L. Rosi, M. Eddaoudi, J. Kim, M. O'Keeffe, O.M. Yaghi, Angewandte Chemie, International Edition 41 (2002) 284.
[22] M. Sabo, A. Henschel, H. Froede, E. Klemm, S. Kaskel, Journal of Materials Chemistry 17 (2007) 3827.
[23] U. Mueller, M. Schubert, F. Teich, H. Puetter, K. Schierle-Arndt, J. Pastre, Journal of Materials Chemistry 16 (2006) 626.
[24] L.M. Huang, H.T. Wang, J.X. Chen, Z.B. Wang, J.Y. Sun, D.Y. Zhao, Y.S. Yan, Microporous and Mesoporous Materials 58 (2003) 105.
[25] N.L. Rosi, M. Eddaoudi, J. Kim, M. O'Keeffe, O.M. Yaghi, CrystEngComm 4 (2002) 401.
[26] N.L. Rosi, J. Kim, M. Eddaoudi, B. Chen, M. O'Keeffe, O.M. Yaghi, Journal of the American Chemical Society 127 (2005) 1504.
[27] J. Hafizovic, M. Bjorgen, U. Olsbye, P.D.C. Dietzel, S. Bordiga, C. Prestipino, C. Lamberti, K.P. Lillerud, Journal of the American Chemical Society 129 (2007) 3612.
[28] A. Thirumurugan, C.N.R. Rao, Journal of Material Chemistry 15 (2005) 3852.
[29] S. Hausdorf, F. Baitalow, J. Seidel, F. Mertens, Journal of Physical Chemistry A 111 (2007) 4259.
[30] S. Hausdorf, J. Wagler, R. Mossig, F. Mertens, Journal of Physical Chemistry A 112 (2008) 7567.
[31] J.H. Liao, T.J. Lee, C.T. Su, Inorganic Chemistry Communications 9 (2006) 201.
[32] J. Gascon, F. Kapteijn, Journal of Catalysis 261 (2009) 75.
[33] A.R. Millward, O.M. Yaghi, Journal of the American Chemical Society 127 (2005) 17998.
[34] Y.W. Li, R.T. Yang, Journal of the American Chemical Society 128 (2006) 726.
[35] K. Smith, G.M. Pollaud, I. Matthews, Green Chemistry (1999) 75.
[36] Y. Du, S. Liu, Y. Ji, Y. Zhang, F. Liu, Q. Gao, F.-S. Xiao, Catalysis Today 131 (2008) 70.
[37] R. Anand, R. Maheswari, K.U. Gore, B.B. Tope, Journal of Molecular Catalysis A: Chemical 193 (2003) 251.
[38] A.B. Halgeri, J. Das, Applied Catalysis, A: General 181 (1999) 347.
[39] P. Moreau, A. Finiels, P. Geneste, J. Solofo, Journal of Catalysis 136 (1992) 487.
[40] C.T. O'Connor, K.P. Möller, H. Manstein, Journal of Molecular Catalysis A: Chemical 181 (2002) 15.
[41] D. Farrusseng, submitted for publication.
[42] S. Kaye, A. Dailly, O.M. Yaghi, J. Long, Journal of the American Chemical Society 129 (2007) 14176.
[43] M.J. Rosseinsky, Microporous and Mesoporous Materials 73 (2004) 15.
[44] S. Kitagawa, K. Uemura, Chemical Society Reviews 34 (2005) 109.
[45] J. Horniakova, D. Mravec, J. Joffre, P. Moreau, Journal of Molecular Catalysis A: Chemical 185 (2002) 249.
[46] R. Millini, F. Frigerio, G. Bellussi, G. Pazzuconi, C. Perego, P. Pollesel, U. Romano, Journal of Catalysis 217 (2003) 298.
[47] D. Mravec, P. Zavadan, A. Kaszonyi, J. Joffre, P. Moreau, Applied Catalysis, A: General 257 (2004) 49.
[48] Y. Sugi, S. Tawada, T. Sugimura, Y. Kubota, T. Hanaoka, T. Matsuzaki, K. Nakajima, K. Kunimori, Applied Catalysis, A: General 189 (1999) 251.
[49] M.D. Foster, I. Rivin, M.M.J. Treacy, O.D. Friedrichs, Microporous and Mesoporous Materials 90 (2006) 32.

DOI: 10.1002/cctc.200((will be filled in by the editorial staff))

Acid centres investigation of MIL-53 (Al, Ga) for Brønsted-type catalysis: in-situ FTIR and ab initio Molecular Modelling.

Ugo Ravon[a] ,Gerald Chaplais[b], Céline Chizallet[c], Behnam Seyyedi[d], Francesca Bonino[d],Silvia Bordiga[d] Nicolas Bats[c], and David Farrusseng*[a]

The intrinsic properties of Metal-Organic Frameworks with regards to their isolated centres, regular cavities, dynamic flexibility and framework polarity make them very attractive for catalysis[1]. However, the general lack of short range characterizations and mechanism investigations hinders the rational design of MOF for catalytic applications. Indeed, very little is known on the nature and strength of potential catalytic centres. HKUST-1 for which the Cu paddlewheel were characterized as hard Lewis centres is a rare exception [5]. Ferey and coll. have reported the catalytic activity of two different MIL-100 (Fe, Cr) for Friedel-Crafts benzylation[3]. Despite their identical $M_3OF_{0.85}(OH)_{0.15}(H_2O)_2(btc)_2$ structures, the Fe^{3+} catalyst shows much higher catalytic activity and even surpasses HBEA and HY zeolites. Because the structure possesses different potential catalytic centres namely redox (Fe-O), Brønsted and Lewis acids, the relation between the structure and the activity can be hardly proposed [4, 5]. We have recently shown that $Zn_3(OH)_2(bdc)$ (also called MOF-69C) [6] which exhibit μ_3-OH species [7] is 100% shape selective for the tertbutylation of large aromatics [8]. We had anticipated that bridging OH groups which are present in number of rod-like 1D structure would generate a Brønsted-type acid catalyst [9]. Among this 1D class, the MIL-53 structure is the most studied (Fig. 1). It is built from infinite chains of corner-sharing $MO_4(\mu_2\text{-}OH)_2$ (M=Al, Cr, Fe, Ga) [11] making diamond type channels [15] in the open form.

The objective of this study is to assess the acid properties of MIL-53(Al) and IM-19 (also called MIL-53(Ga)) [11, 12] for acid catalysis. It deals with the identification of the nature of the intermediate in model Friedel-Crafts alkylations and the characterization of acid centres by combined Infra-Red (IR) and Density Functional Theory (DFT) studies.

MIL-53(Al) (Vol_{micro} = XXX $cm^3.g^{-1}$, particle size= 1-10 μm) and MIL-53(Ga) (Vol_{micro} = 0.47 $cm^3.g^{-1}$, particle size= XXX μm) were prepared according to procedure described in [13] and [12, 14], respectively. Brønsted and Lewis acidities of MIL-53(Al) and MIL-53(Ga) were evaluated by IR spectroscopy by following the modification of spectroscopic features of CO (Fig. 2). Before the measurements, samples were heated at 280 °C in air for 24h and then at 250 °C in primary vacuum. IR spectra collected were recorded at 100 K upon decreasing the partial pressures of CO probe molecule. IR peak positions and shifts have been simulated by DFT in order to propose assignments.

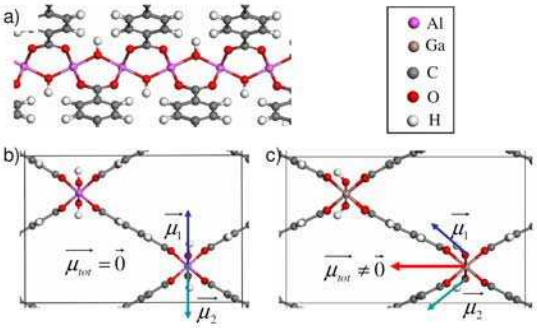

Figure 1: Unit cells optimized by DFT of MIL-53, (a) view of the Al-(OH)-Al chains, (b) perpendicular view of MIL-53(Al), (c) and of MIL-53(Ga), with representations of the dipolar moments of OH groups.

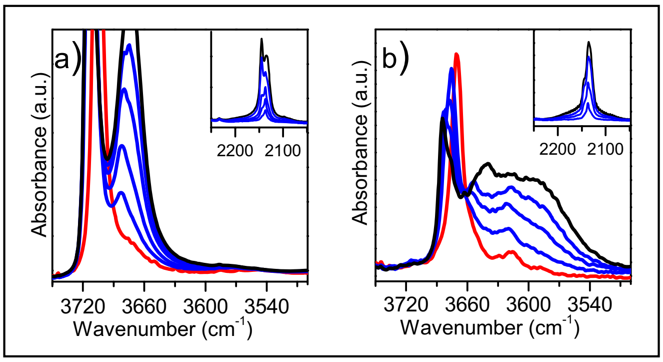

Figure 2: FTIR spectra of CO adsorbed at 100 K on MIL-53(Al) (a) and MIL-53(Ga) (b): red curves report spectra collected at RT in vacuo; black curves are due to spectra collected at 100 K in presence of 40 mbar of CO; blue curves show spectra collected at decreasing coverage and increasing temperatures.

Theoretical calculations are in very good agreement with experimental data for ν(OH) bands; 3709 (th) and 3704 cm^{-1} (exp) for MIL-53(Al); 3663 (th) and 3669 cm^{-1} (exp) for MIL-53(Ga). Upon CO adsorption [15] (Figure 2) small red shifts appear in the –OH vibration regions. A larger and broader shift is observed for

[a] *Université Lyon 1, CNRS, UMR 5256, IRCELYON, Institut de recherches sur la catalyse et l'environnement de Lyon, 2 avenue Albert Einstein, F-69626 Villeurbanne. Fax: +33 4 72 44 53 99; Tel: +33 4 72 44 53; E-mail: david.farrusseng@ircelyon.univ-lyon1.fr*
[b] *Université de Haute Alsace, Ecole Nationale Supérieure de Chimie de Mulhouse, Laboratoire de Matériaux à Porosité Contrôlée, UMR CNRS 7016, 3 rue Alfred Werner, F-68093 Mulhouse, France*
[c] *IFP-Lyon, BP 3, 69360 Solaize, France*
[d] *Department of Inorganic, Physical and Materials Chemistry and NIS Centre of Excellence, Università di Torino, Via P. Giuria 7, 10125*

MIL-53(Ga) ($\Delta\nu$=-50/-100 cm^{-1}) with respect to MIL-53(Al) ($\Delta\nu$(OH)= - 30/-50 cm^{-1}). Surprisingly a parallel perturbation in the CO stretching region is not present. In fact, for both MIL-53 (Al) and MIL-53(Ga), the main absorptions are detected around the CO liquid-like frequency (*ca.* 2140 cm^{-1}): doublets at 2145-2137 cm^{-1} and 2147-2137 cm^{-1}, respectively. These bands are reversible only upon prolonged outgasing, thus indicating that they are associated to some stable adducts. Theoretical calculations on both compounds evidenced four main adsorption modes for CO with stabilities in the same range (see supporting information):

1- The traditional "C adduct" -OH···CO
2- A reverse "O adduct" -OH···OC
3- A bridging adduct -OH···OC···OH- at the centre of the cavity
4- A “benzene adduct” B···CO, where B is the aromatic ring.

Among them, the “C adduct” is the most stable. It leads to the highest $\Delta\nu$(OH) and very small blue shifts in the CO region (2145 cm^{-1}), in agreement with experiments. The three other modes induce very small calculated $\Delta\nu$(OH) and slightly negative CO shifts (from 2142 to 2131 cm^{-1}), which may explain the lower frequency component of the experimental doublet.

As a synopsis, experiments combined to molecular modelling in the OH-region let us conclude that the Brønsted acidity [7, 20, 21]}, even if very mild, follows the order: MIL-53(Al) < MIL-53(Ga). DFT calculations also show that in the absence of host molecule, OH groups of MIL-53(Al) are straight, as usually admitted, but they are all tilted in the same direction for MIL-53(Ga) (Fig. 1 c), which induces a non zero dipolar moment. Note that only the MIL-53(Al) sample shows a small presence of Lewis sites (band at 2230 cm^{-1}), likely due to the external surface of the material.

Friedel & Crafts alkylation reactions were carried out following procedure described in [17]. We and others have demonstrated that the reaction with MOF proceed via an heterogeneous mechanism [8, 18]. The reaction pathway of alkylation by halides depends on the kind of catalysts. Three mechanism types are known, namely basic [19], redox [20] and acid [21]. The nature of the reaction intermediate, and thus the mechanism, can be identified using established principles developed by March (eq1)[22]. In short, the reaction rate of a substrate is directly correlated to the stability of the reaction intermediate everything else equal. From Hammett equation, the charge of the intermediate can be identified by varying the substituants on the aromatic ring and measuring respective reaction rates ; k^A and k^B are reaction rates for two different aromatic substrates (A and B), σ^A and σ^B are the corresponding Hammett constants and ρ is a characteristic parameter of the reaction giving indications on the charge of the intermediate.

$$\log\left(k^A / k^B\right) = \left(\sigma^A - \sigma^B\right)\rho$$

For MIL-53(Ga), the initial reaction rates of monosubsitued benzenes (cyano-, chloro-, bromo-, methyl) with tBuCl were measured at 100°C [17]. They are plotted as function of the Hammett constant of the corresponding substituant using benzene as reference ($\sigma^B = \sigma^0 = 0$). As expected from the Hammett equation, we can observe a linear relationship between the reaction rates and the Hammett constant of the substituant (Fig. 3). The negative slope (ρ=-3) clearly indicates that the intermediate is positively charged. According to Hammett principle, the more electron donor is the substituant, the more the intermediate is stable and thus the higher the reaction rate. Thus, we suggest that the intermediates are protonated forms of the aromatic substrates as it is found for acid zeolites such as HY [21] (Fig.3).

The MIL-53(Ga) is very active even at low temperature (1.8x10^{-4} mol.g^{-1}.s^{-1} at 373K and 6.9x10^{-6} mol.g^{-1}.s^{-1} at 298K) with respect to other Zn based MOFs and reference zeolites [8] (see kinetics in Supporting Information). For fast reactions in microporous zeolites such as the benzylation of toluene on K-Clays, the diffusion rate of the reactants governs the activity [23]. Coq and Figeras [21] have demonstrated that the activity of acid zeolites (HY, HBeta, HZSM-5) is mainly correlated to the volume of mesopores and to micropore size. We suggest that the higher activity of MIL-53(Ga) with respect to zeolites likely arises from the much faster diffusion of the reactants in the porous network. First, MIL-53(Ga) exhibits micropore volume (0.47-0.48 cm^3.g^{-1} [11, 12]) which is 50% larger than Y zeolite and much larger pore aperture of 13Å x13Å [12] against 7.4Å for Y zeolites [24]. Second, favourable packing of the subtrates via π stacking with the MOF linker may afford more appropriate 1:1 ratio of the substrates in the porous network [25, 26]. Finally, MIL-53(Ga) shows outstanding para-selectivity (90%) in the alkylation of large aromatics such as biphenyl (see SI), comparable with Zn-based MOFs [8, 17, 18].

In contrast, MIL-53(Al) did not show any catalytic activities whatever different activation procedures investigated, the different sources used (Basolite A100 was also tested) or different reaction conditions (higher temperature). This is in line with observations of Alaerts et al who have not observed reactions when investigating adsorption on MIL-53(Al) with various aromatics including benzene chloride [26].

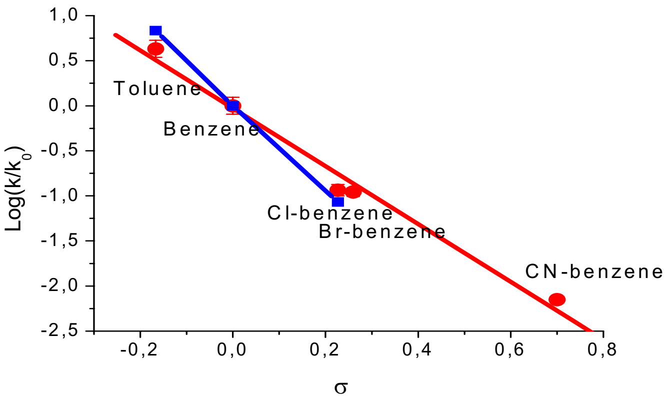

Figure 3: Plot of the activities as a function of the Hammett constant of the corresponding aromatic substrates. MIL-53(Ga) (dots), HY (square) from Coq et al[21].

The absence of catalytic activity in MIL-53(Al) may be due to the very low acidity as determined by CO adsorption. However the high catalytic activities of the Ga form might not only arise from the mild acidity of the Ga-μ_2OH-Ga species alone. We suggest that the tilted OH groups as evidenced by DFT calculations (fig. 1), induces a much stronger stabilization of the positively charged intermediates than the non-polar MIL-53(Al). In addition, further stabilisation by π stacking between the aromatic intermediates and the ring of the linker can not be rule out [25, 26]. Beyond these results, this study demonstrates that MOFs can achieve very high activity and shape selectivity owing their well isolated acid sites and large micropore volume allowing fast diffusion of reactants.

† Electronic Supplementary Information (ESI) available: Kinetics of toluene alkylation over MIL-53(Ga) and other reference catalysts. Yield of the alkylation of biphenyl. Calculated CO adsorption modes, adsorption energies and IR shifts. See DOI: 10.1039/b000000x/

Experimental and Methodological Section

Spectra were collected in transmission mode at 2 cm^{-1} resolution on self-supporting wafer, in controlled atmosphere, on a IFS28 Bruker spectrometer. The alkylation reactions were carried out in *n*-decane with an aromatic:*t*-BuCl molar ratio of 2:1. Catalysts were activated at 130 °C under 10^{-5} bar, unless specific conditions were given. As en example, a mixture of 1.7 g (18.8 mmol) of toluene, 0.851 g (9.2 mmol) of *t*-BuCl and 5.18 g of *n*-decane was placed in a 48 ml Teflon lined autoclave (Top Industrie) and heated to reaction temperature under stirring with autogeneous pressure. For activity measurements at low conversion, 10mg of catalyst were used for the alkylation with toluene and benzene whereas 100mg were used for halogeno- and cyano-benzene. The Hammett slopes (ρ) of MIL-53(Ga) and HY can not be directly compared since they have been obtained in different test conditions (temperature and solvant).

Investigation of leaching issues and post-characterisation were carried out as reported in [8]. Any leaching and structural modifications could be detected.

Periodic Density Functional Calculations are performed in the framework of the Generalized Gradient Approximation of Perdew and Wang PW91[27], with the VASP 4.6 code[28]. The interaction between core and valence electrons are described by the projector augmented-waves (PAW)[29]approach with energy cutoff of 520 eV to account for most accurate geometries (convergence criterion: energy differences lower than 10-7 eV/atom), adsorption energies and vibrational frequencies. The shape and dimensions of the cell have been fully optimized. The harmonic O-H and C≡O stretching wavenumbers are calculated calculated numerically (at the 3x1x2 k-points set), with a displacement of ± 0.005 Å around the equilibrium position. The anharmonicity corrections for O-H frequencies are performed by manual 1D exploration of the potential energy surface, along the axis of the vibrator, at constant position of its centre of mass, in the range [-0.3; +0.4 Å] around the equilibrium O-H bond length. Subsequently, the one-dimensional Schrödinger equation is solved numerically, based on a sixth order fit of the potential energy curve as implemented in the ANHARM module[30].

Acknowledgements

We thank the European program NanoMOF (FP7-NMP) and computational facilities from IDRIS and CINES (project n° x2010086335). We also thank Dr. F. Figueras for discussions.

Keywords: MOF • acid catalysis • CO adsorption • aromatic alkylation • Metal-Organic Framework

[1] a) U. Mueller, M. Schubert, F. Teich, H. Puetter, K. Schierle-Arndt, J. Pastre, *J. Mater. Chem.* **2006**, *16*, 626; b) L. Q. Ma, C. Abney, W. B. Lin, *Chem. Soc. Rev.* **2009**, *38*, 1248; c) J. Lee, O. K. Farha, J. Roberts, K. A. Scheidt, S. T. Nguyen, J. T. Hupp, *Chem. Soc. Rev.* **2009**, *38*, 1450; d) D. Farrusseng, S. Aguado, C. Pinel, *Angew. Chem., Int. Ed.* **2009**, *48*, 7502.

[2] L. Alaerts, E. Seguin, H. Poelman, F. Thibault-Starzyk, P. A. Jacobs, D. E. De Vos, *Chemistry-a European Journal* **2006**, *12*, 7353.

[3] P. Horcajada, S. Surble, C. Serre, D. Y. Hong, Y. K. Seo, J. S. Chang, J. M. Greneche, I. Margiolaki, G. Ferey, *Chemical Communications* **2007**, 2820.

[4] A. Vimont, J. M. Goupil, J. C. Lavalley, M. Daturi, S. Surble, C. Serre, F. Millange, G. Ferey, N. Audebrand, *J. Am. Chem. Soc.* **2006**, *128*, 3218.

[5] A. Vimont, H. Leclerc, F. Mauge, M. Daturi, J. C. Lavalley, S. Surble, C. Serre, G. Ferey, *J. Phys. Chem. C* **2007**, *111*, 383.

[6] T. Loiseau, H. Muguerra, G. Ferey, M. Haouas, F. Taulelle, *J. Solid State Chem.* **2005**, *178*, 621; N. L. Rosi, M. Eddaoudi, J. Kim, M. O'Keeffe, O. M. Yaghi, *CrystEngComm* **2002**, *4*, 401.

[7] N. L. Rosi, J. Kim, M. Eddaoudi, B. L. Chen, M. O'Keeffe, O. M. Yaghi, *J. Am. Chem. Soc.* **2005**, *127*, 1504.

[8] U. Ravon, M. Savonnet, S. Aguado, M. E. Domine, E. Janneau, D. Farrusseng, *Microporous Mesoporous Mater.* **2010**, *129*, 319.

[9] A. Corma, *J. Catal.* **2003**, *216*, 298.

[10] F. Millange, C. Serre, G. Ferey, *Chemical Communications* **2002**, 822.

[11] C. Volkringer, T. Loiseau, N. Guillou, G. Ferey, E. Elkaim, A. Vimont, *Dalton Trans.* **2009**, 2241.

[12] G. Chaplais, A. Simon-Masseron, F. Porcher, C. Lecomte, D. Bazer-Bachi, N. Bats, J. Patarin, **2009**, Phys. Chem. Chem. Phys, *11,* 5241.

[13] T. Loiseau, C. Serre, C. Huguenard, G. Fink, F. Taulelle, M. Henry, T. Bataille, G. Ferey, *Chemistry-a European Journal* **2004**, *10*, 1373.

[14] Patent WO2009115683

[15] A. Zecchina, G. Spoto, S. Bordiga, *PCCP* **2005**, *7*, 1627.

[16] a) A. Buzzoni, S. Bordiga, G. Ricchiardi, C. Lamberti, A. Zecchina, G. Bellussi, *Langmuir* **2003**, *12*, 930; b) F. Bonino, A. Damin, S. Bordiga, C. Lamberti, A. Zecchina, *Langmuir* **2003**, *19*, 2155.

[17] U. Ravon, M. E. Domine, C. Gaudillere, A. Desmartin-Chomel, D. Farrusseng, *New J. Chem.* **2008**, *32*, 937.

[18] P. K. Thallapally, C. A. Fernandez, R. K. Motkuri, S. K. Nune, J. Liu, C. H. F. Peden, *Dalton Trans.* **2010**, *39*, 1692.

[19] H. Pines, J. A. Vesely, V. N. Ipatieff, *J. Am. Chem. Soc.* **1955**, *77*, 554.

[20] K. Bachari, J. M. M. Millet, B. Benaïchouba, O. Cherifi, F. Figueras, *J. Catal.* **2004**, *221*, 55.

[21] B. Coq, V. Gourves, F. Figuéras, *Applied Catalysis A: General* **1993**, *100*, 69.

[22] *Advanced Organic Chemistry*, J. March, Wiley (4th Ed), **1992**.

[23] T. Cseri, S. Bekassy, F. Figueras, E. Cseke, L. C. Demenorval, R. Dutartre, *Applied Catalysis A-General* **1995**, *132*, 141.

[24] E. Armengol, A. Corma, H. Garcia, J. Primo, *Applied Catalysis A-general* **1997**, *149*, 411.

[25] L. Alaerts, M. Maes, L. Giebeler, P. A. Jacobs, J. A. Martens, J. F. M. Denayer, C. E. A. Kirschhock, D. E. De Vos, *J. Am. Chem. Soc.* **2008**, *130*, 14170.

[26] L. Alaerts, M. Maes, M. A. van der Veen, P. A. Jacobs, D. E. De Vos, *Phys. Chem. Chem. Phys.* **2009**, *11*, 2903.

[27] J. Perdew, Y. Wang, *Phys. Rev. B* **1992**, *45*, 13244.

[28] G. Kresse, J. Hafner, *Phys. Rev. B* **1994**, *49*, 14251.

[29] G. Kresse, D. Joubert, *Phys. Rev. B* **1999**, *59*, 1758.

[30] I. N. Senchenya, E. Garrone, P. Ugliengo, *J. Mol. Struct* **1996**, *368*, 93.

Received: ((will be filled in by the editorial staff))
Published online: ((will be filled in by the editorial staff))

Entry for the Table of Contents

COMMUNICATION

In contrast to MIL-53(Al), MIL-53 (Ga) (IM-19) is extremely active and selective for the alkylation of aromatics. The reaction proceeds through the protonation of the aromatic substrate. CO adsorption and molecular modelling show that the bridging μ$_2$-OH of MIL-53(Ga) exhibits stronger Brønsted-type acidity than MIL-53(Al).

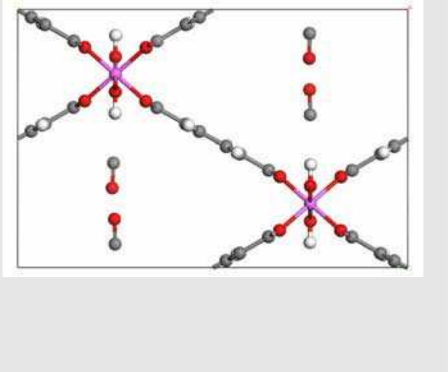

*Ugo Ravon , Gerald Chaplais , Céline Chizallet, Behnam Seyyedi, Francesca Bonino, Silvia Bordiga, Nicolas Bats , and David Farrusseng **

Page No. – Page No.

Acid centres investigation of MIL-53 (Al, Ga) for Brønsted-type catalysis: in-situ FTIR and ab initio Molecular Modelling

RESUME en français

Cette thèse s’inscrit dans un projet Européen TOPCOMBI de 22 partenaires. Plus spécifiquement, ce travail est le résultat d’une collaboration entre ENI (Italie), ITQ (Espagne), Repsol (Espagne) et IRCELYON (France).

Ce travail est composé de 2 thématiques différentes dont les améliorations peuvent s’obtenir en trouvant de nouveaux matériaux adaptés aux besoins.

Les demandes énergétiques mondiales sont et seront en constante hausse ces prochaines années. Dans l’optique de pallier à ce besoin, de nouvelles ressources doivent être trouvées et d’autres optimisées. Les énergies fossiles font parties des ressources les plus utilisées dans le monde. Parmi c’est 3, le gaz naturel semble être le plus prometteur du point de vu du rendement énergétiques ou de l’impact écologique. Cependant, de nombreux champs de gaz ne peuvent pas être traités car trop petit ou trop contaminés pour être économiquement viable. L’un des moyens pour les rendre attractifs est d’abaisser le coût de purification en utilisant de nouvelles techniques de séparation comme le système PSA. Cependant, il n’existe pas à l’heure actuelle d’adsorbant efficace pour permettre une purification économique viable.

De nos jours, les réactions d’alkylation représentent un intérêt économique très important. Les procédés industriels sont généralement effectués par des réactions acides homogènes ou non. A la vue des nouvelles restrictions écologiques, certains procédés de catalyse homogène doivent être remplacés par des réactions catalytiques hétérogènes possédant les mêmes rendements. Pour ce faire, de nouveaux matériaux à caractères acide ont été utilisés : les zéolithes. En revanche la faible taille de pores de ces composés empêche les réactions d’alkylation sélective de molécules trop grosse comme les composés poly-aromatiques.

Depuis une vingtaine d’année, de nouveaux composés cristallins microporeux ont vu le jour. Les MOFs, Metal Organic Frameworks. Ces composés ont la particularité d’être obtenus avec différents cations métalliques et ligands organiques. Ces combinaisons donnent une très grande diversité de ces composés au niveau des réactivités, du volume poreux et de la taille des pores. Dans ce travail, nous avons essayé d’obtenir différents matériaux avec des caractéristiques précises afin de pouvoir les utiliser dans des procédés de purification du méthane ou dans la catalyse acide. Pour ce faire, nous avons mis en place un protocole de synthèses de MOFs à haut débit ainsi que d’un protocole de caractérisation adapté à nos besoins. Les différents composés remplissant les différents critères étant testés dans les réactions adéquates.

TITRE en anglais

The development of new materials such MOFs for CO2 capture and alkylation of aromatic compounds.

RESUME en anglais

This thesis is a European project TOPCOMBI of 22 partners. More specifically, this work is the result of collaboration between ENI (Italy), ITQ (Spain), Repsol (Spain) and IRCELYON (France).

This work consists of 2 different themes which improvements can be obtained by finding new materials tailored to the needs.

The global energy demands are and will be constantly rising in the coming years. In order to meet this need, new resources must be found and further optimized. Fossil fuels are among the most used resources in the world. Among this 3, natural gas appears to be the most promising point of view of energy efficiency and ecological impact. However, many gas fields cannot be treated because there are too small or too contaminated to be economically viable. One way to make them attractive is to lower the cost of purification using novel separation techniques such as the PSA system. However, there is no currently effective adsorbent to allow a viable economic cleansing.

Today, the alkylation reactions represent a very important economic interest. Industrial processes are typically carried out by homogeneous acid reactions or not. Seeing the new environmental restrictions, some homogeneous catalytic processes must be replaced by heterogeneous catalytic reactions with the same yields. To do this, new materials to acid characters were used: the zeolites. However the small size of pores of these compounds prevents selective alkylation reactions of molecules too large compounds such as poly-aromatic.

For twenty years, new microporous crystalline compounds have emerged. The MOFs, Metal Organic Frameworks. These compounds have the characteristic to be obtained with different metal cations and organic ligands. These combinations give a wide variety of these compounds at the level of reactivity, pore volume and pore size. In this work, we tried to get different materials with specific characteristics in order to use them in methods for purification of methane in acid catalysis. To do this, we have established a protocol for the synthesis of MOFs with high speed and a characterization protocol suited to our needs. The different compounds fulfilling the various criteria being tested in the appropriate responses.

DISCIPLINE

Chimie physique et catalyse

MOTS-CLES

MOF, Synthèse, catalyse hétérogène, adsorption

INTITULE ET ADRESSE DE L'U.F.R. OU DU LABORATOIRE :

IRCELYON 2 av A.Einstein 69626 Villeurbanne